QUEEN'S UNIVERSITY BELFAST

DOCTOR OF PHILOSOPHY

Gold nanostars

From catalytic and SERS properties to the development of smartphone-based and portable biosensing approaches for food contaminants

Lou Franco, Javier

Award date:
2022

Awarding institution:
Queen's University Belfast

Link to publication

Terms of use
All those accessing thesis content in Queen's University Belfast Research Portal are subject to the following terms and conditions of use

- Copyright is subject to the Copyright, Designs and Patent Act 1988, or as modified by any successor legislation
- Copyright and moral rights for thesis content are retained by the author and/or other copyright owners
- A copy of a thesis may be downloaded for personal non-commercial research/study without the need for permission or charge
- Distribution or reproduction of thesis content in any format is not permitted without the permission of the copyright holder
- When citing this work, full bibliographic details should be supplied, including the author, title, awarding institution and date of thesis

Take down policy
A thesis can be removed from the Research Portal if there has been a breach of copyright, or a similarly robust reason.
If you believe this document breaches copyright, or there is sufficient cause to take down, please contact us, citing details. Email: openaccess@qub.ac.uk

Supplementary materials
Where possible, we endeavour to provide supplementary materials to theses. This may include video, audio and other types of files. We endeavour to capture all content and upload as part of the Pure record for each thesis.
Note, it may not be possible in all instances to convert analogue formats to usable digital formats for some supplementary materials. We exercise best efforts on our behalf and, in such instances, encourage the individual to consult the physical thesis for further information.

Download date: 15. jul. 2024

Gold Nanostars: From Catalytic and SERS Properties to the Development of Smartphone-based and Portable Biosensing Approaches for Food Contaminants

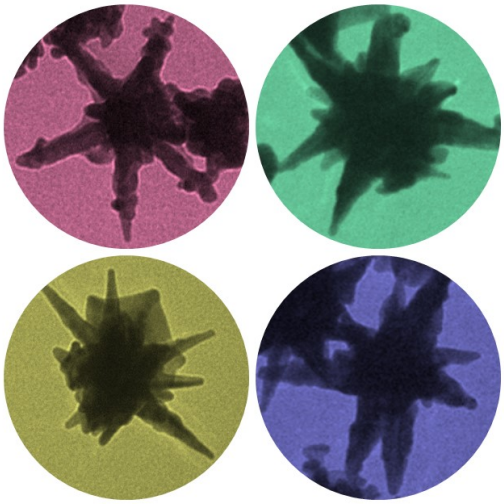

A thesis presented to

The Faculty of Medicine, Health and Life Sciences

School of Biological Sciences

Queen's University Belfast

For the Degree of

Doctor of Philosophy (PhD)

By

Javier Lou Franco MSc.

September 2021

Acknowledgements

First of all, I would like to thank my principal supervisor, Cuong Cao, for offering me the opportunity to join the FoodSmartphone project and providing scientific support throughout the thesis. It has been a great experience learning from you, who always had a bunch of suggestions to solve any scientific problem that arose in the project. A big thank-you to Chris Elliott too, for always offering a warm welcome at IGFS, sharing your expertise in the field of food safety and providing excellent contacts within the scientific community and food production sector to push our research to the next level.

Also, it has been a pleasure sharing this time with everyone working in Cuong's group: Claire and Casy that introduced me to this lab when I arrived in Belfast to start this thesis, Natasha and Brendan that have shared the struggle of working with gold nanostars and *Mycobacterium bovis*, Matthew and Jamie that always had great (and sometimes crazy) ideas of things to try. A huge thank-you to all of you, this thesis wouldn't be the same without all your help! I've also been very lucky to share part of these years with everyone that joined our group for part of their studies, like Bhaskar or Zoe. Likewise, it has been a pleasure sharing time and space with everyone at the office, lab or anywhere else in the School of Biological Sciences (whether we met at work or at the Jeggy Nettle).

On the other hand, I'm also thankful to the great FoodSmartphone Consortium, all the PhD students that composed it and their respective research groups, who made this project possible. Specially to Michel Nielen, for co-ordinating this project; to Mª Pilar, Pablo and Roger, in CSIC, for hosting me during my secondment; and Luis, in Zeulab, for offering me the possibility even if it was eventually truncated due to covid pandemic. Anyway, we still enjoyed 2 of 3 years travelling to conferences, meetings and summer schools in Prague, Wageningen or Miami.

Y por último, no puedo cerrar esta sección de agradecimientos sin dedicar unas líneas a todos los que me habéis apoyado desde España, empezando por mi familia que siempre me ha animado a seguir formándome y me ha apoyado en todas las decisiones, aunque significara irme 3 años a vivir fuera. También a todos los amigos a los que me he tenido que conformar con ver en verano y navidades, pero que hemos mantenido el contacto pese a la distancia.

¡Gracias!

Abstract

Gold nanoparticles have long been explored and used throughout history for many purposes, from decoration in ancient times to biomedical applications nowadays. Recent progress in the field of nanotechnology has enabled us to better understand these materials and provided necessary technological tools for controlling their synthesis and functionalisation. As a result, it has been observed that nanomaterials possess many interesting properties not found in bulk materials, deriving from the quantum size effect. Among them, their nanozyme activity and their Surface-Enhanced Raman Spectroscopy (SERS) properties have been thoroughly studied and characterised in this thesis. For that purpose, gold nanostars have been synthesised following a seed-mediated bottom-up approach, which enables to control the optical and morphological properties of the resulting nanoparticles. Gold nanostars have shown potential to replace biological enzymes as catalysts while behaving as excellent substrates for Raman enhancement studies due to the high presence of Raman *hot spots* within their anisotropic structure. However, it has been revealed that differences in the morphological properties or in the surface nature of gold nanostars strongly affect both their nanozyme and SERS properties, boosting or hindering these activities. These findings are of special relevance for certain applications, such as the development of diagnostic devices based on these mechanisms.

On the other hand, smartphones have emerged as ideal readout systems which, in combination with gold nanostars conjugated with specific biorecognition elements define a new type of point-of-care (POC) sensors barely explored until now, satisfying many conditions required for on-site applications of diagnostic devices. A direct and obvious application where gold nanostar-based sensors can play an important role is found in the food safety field, a field that still relies, sometimes exclusively, on hygiene protocols instead of on sensing devices. This is due to many factors, including the lack of portable, user-friendly and robust sensing assays, making virtually not possible to test food for contaminants everywhere where necessary. In this line, almost 400 contamination cases of milk products have been notified in the last decade in the EU, being the dairy sector of special interest in Northern Ireland as it represents 25.7% of its farm output and comes second in terms of gross turnover. Among these contamination events, microbiological cases are the most worrying, given that they can cause both spoilage of the foodstuff and a wide range of human diseases if consumed. Together with the necessity of producing more food than ever before as the world population grows, it has become essential to test food to discard any contamination event before food reaches the consumers.

Prior to the biosensor development, a literature review was performed leading to the creation of a novel online sensors classification system. Over 900 sensors retrieved form the literature and market were analysed to build an interactive platform providing state-of-the-art information on sensors targeting various food contaminants. They have been classified according to their portability, capability to quantify the analyte, user-friendliness or capability to perform multiplex analyses. Not only this has served as an interesting tool to be used by any person involved in the field, but also has provided us with a clear picture of the benefits and drawbacks of each analytical method. Besides, it has further strengthened the idea of incorporating gold nanomaterials to enhance the sensor capabilities.

Along this thesis, gold nanostars have proved that new strategies for sensing are possible, which eventually may lead to POC sensors that replace costly lab-based analyses. Several assays targeting food contaminants (such as *Mycobacterium bovis* or Hg^{2+} ions) are herein introduced. The former combines the use of antibodies as biorecognition elements and the peroxidase-like activity of gold nanostars as signal transducers, leading to a colourimetric signal that can be read and quantified using a smartphone camera to predict the presence of *M. bovis* in the concentration range $10^4 – 10^6$ CFU/mL. Hg^{2+} ions detection, on the other hand, relies on the SERS properties of gold nanostars, which can be further enhanced in combination with their nanozyme activity or exploiting the synergistic effect observed using gold-silver bimetallic nanoparticles. Sensitivities of 0.2 and 0.1 ppb, respectively, have been achieved using these approaches.

Overall, the latest findings related to the optical and spectroscopic properties of gold nanostars are reported in this thesis, together with a thorough study of current methodologies being used for sensing food contaminants. This has resulted of paramount importance for successfully developing diagnostic devices targeting food contaminants. The implications and extent of these findings are yet to be evaluated, considering that the full potential of anisotropic gold nanoparticles and bimetallic nanostructures is only beginning to be understood. However, the incorporation of smartphones as readout systems for POC sensing seems to have just undertaken a path of no return.

List of figures

Figure C1. 1 Foodborne hazards based on Disability-Adjusted Life Years at the global level. Reproduced from WHO [6]. 3

Figure C1. 2 (a) Milk production by country in 2017. (b) Average milk consumption per capita in 2017, measured in kg per person per year. This includes milk equivalents of dairy products (excluding butter). Figure reproduced from UN FAO. 5

Figure C1. 3 Main microbiological hazards reported in scientific literature for dairy products processed at the dairy factory. The most important hazards are bolded. Figure reproduced from [31]. 8

Figure C1. 4 AuNPs synthesised with different shapes following bottom-up approaches: (a) spheres, (b) rods, (c) prisms, (d) bipyramids, (e) stars, (f) cubes, (g) polygon-shaped nanocrystals, (h) cages, (i) gold@silica hybrid nanoparticles. Reproduced from Lou-Franco et al. [97]. 14

Figure C1. 5 LSPR phenomenon generated by the interaction of incident light with conduction electrons from the surface of non-anisotropic spherical AuNPs (a) or anisotropic rod-shaped AuNPs in their longitudinal mode (b) and transversal mode (c). Reproduced from [101]. 15

Figure C1. 6 Raman and fluorescence spectroscopy responses depending on the distance AuNP – dye. Preferred SERS (top) and SEF (bottom) configurations to maximise spectroscopic enhancement. 17

Figure C1. 7 Chemical reactions catalysed by AuNPs. Reproduced from Lou-Franco et al. [97].. 18

Figure C1. 8 (a) Comparison of the peroxidase-like activity of different shaped and sized AuNPs using TMB substrate. (b) Comparison of the peroxidase-like activity of AuNPs stabilised with different coating layers. Reproduced from Lou-Franco et al. [97]. 19

Figure C1. 9 Peroxidase-like activity of AuNPs used as clinical diagnostic tools. (a) AuNPs grown on graphene sheets used to develop a "off-on" colourimetric sensor [159]. (b) Nanohybrid composed of AuNPs and CNTs acting as colourimetric influenza virus detection [156]. (c) Rod-shaped Au-Pt core/shell NPs used for measles virus detection [154]. (d) Magnetic nanobeads combined with AuNPs for separation and detection of influenza virus [155]. (e) User-friendly device for hemoglobin and red blood cells detection in urine samples [152]. (f) Gold-loaded nanoporous ferric oxide NPs used for direct exosome detection [158]. (g) Fluorometric and colourimetric detection of dopamine based on AuNCs [166]. Reproduced from Lou-Franco et al. [97]. 25

Figure C1. 10 Gold nanozymes applied for tumour therapy. (a) Peroxidase-like activity is combined with photodynamic and photothermal therapies for tumour imaging and localised treatment [187]. (b) Various enzymatic activities are combined to generate ROS inside the cell after directing the NPs to the affected tissue [189]. Reproduced from Lou-Franco et al. [97]. 30

Figure C1. 11 Gold nanozymes used as ROS scavengers for cell protection. (a) Catalase-like activity of amine-terminated dendrimer-entrapped AuNCs used for neuronal protection against oxidative damage [196]. (b) Light mediated reversible modulation of ROS levels using mesoporous NPs loaded with AuNPs [195]. Reproduced from Lou-Franco et al. [97]. 34

Figure C2. 1 Analytical methods commonly used for detection of microbiological contamination in food. 51

Figure C2. 2 Comparison of sensitivities achieved by different techniques commonly used in the detection of microbiological contamination in food. 53

Figure C2. 3 Layout of TEST classification system following a 5 criteria hierarchal system. Branches leading to no information are marked "[0]" in the decision tree in every case where the criteria combination has not been translated into an available (or potentially available) commercial sensor. 61

Figure C2. 4 Website layout showing the outcome of a TEST search using the parameters "pathogen" AND "non expert" AND "portable" AND "qualitative" AND "singleplex", resulting in 3 e-docs targeting E. coli, Listeria and Salmonella contaminations. 63

Figure C3. 1 Reaction pathways leading to noble metal NPs with different shapes, starting with the reduction of a metallic salt to form nuclei through aggregation which, passed a certain size, become seed. These have a certain structure (single crystal, singly twinned or multiply twinned). Green, orange and purple colours represent {1,0,0}, {1,1,1} and {1,1,0} facets, respectively. The parameter R is defined as the ratio between the growth rates along the {1,0,0} and {1,1,1} directions. Figure reproduced with permission from [315]. 68

Figure C3. 2 UV-Vis analyses of AuNSt-NaCit synthesised using different amounts of seeds (ranging from 40 to 300 μL) which leads to different optical properties. Inside the graph, an image showing the visual differences in the AuNSt samples. 76

Figure C3. 3 AuNSt samples stabilised with varying concentrations of sodium citrate O/N and analysed by UV-Vis to characterise the aggregation process before washing the samples..... 78

Figure C3. 4 Stability study of citrate-capped AuNSt, varying citrate concentrations from 10^{-6} to 10^{-1} M. 79

Figure C3. 5 AuNSt samples are analysed by UV-Vis spectroscopy before any surface modification "AuNSt (initial)", after stabilisation with citrate "Citrate-capped" and after replacing the citrate coating with varying concentrations of (a) 11-MUA and (b) 16-MHA. 81

Figure C3. 6 UV-Vis spectra of AuNSt functionalised with different coating molecules. 82

Figure C3. 7 Molar extinction coefficient values (ε) of AuNSt depending on their LSPR wavelength. 83

Figure C3. 8 TEM images of AuNSt samples. Top and centre images correspond to AuNSt synthesised using 50 µL of seeds, captured using magnification between X50k – X120k. Bottom images correspond to AuNSt synthesised using 500 µL of seeds and exhibiting a 550 nm LSPR (left) and using 75 µL of seeds resulting in a 739 nm LSPR (right). Same magnification is used in both cases (X40k).. 85

Figure C3. 9 Zetasizer analyses of AuNSt. (a) Size analysis of AuNSt with different optical properties performed by DLS and manual measurement of TEM images using ImageJ software. (b) ζ-potential analysis of AuNSt coated with different stabilising agents (sodium citrate, PEG, OEG, 11-MUA). 86

Figure C3. 10 The RI sensitivity of AuNSt was calculated using water – glycerol mixtures and measuring their UV-Vis spectra (a) to observe the plasmon shift and then plot it against the RI variation (b). 87

Figure C3. 11 UV-Vis spectroscopy analysis of TMB oxidation. 200 pM AuNSt coated with different molecules were mixed with 0.1 mM TMB in an aqueous solution containing 6% H_2O_2. The spectra were collected after 20 min of reaction. 88

Figure C3. 12 Characterisation of the peroxidase-like activity of AuNSt depending on the size and surface modifications. (a) Kinetic analysis of AuNSt-NaCit with different sizes in the presence of varying concentrations of TMB (0 – 0.5 mM) and 6% H_2O_2. (b) Comparison of the turnover number observed for AuNSt-NaCit with different sizes. (c) Kinetic analysis of AuNSt coated with different stabilising molecules in the presence of varying concentrations of TMB (0 – 0.5 mM) and 6% H_2O_2. (d) Comparison of the turnover number observed for AuNSt coated with different stabilising molecules. Data in a and c are fitted to a Hill equation while a one-way ANOVA is performed to analyse data in b and d..... 90

Figure C4. 1 Direct immunoassay for streptavidin detection fitted to a calibration line between 0 – 3 µg/mL range. 102

Figure C4. 2 Colour signal generated after mixing fixed concentrations of AuNSt and $AuCl_4^-$ with a varying concentration of L-AA in a high (a) and low (b) concentration range. TMB was added to all samples to determine their potential as peroxidase-mimics. 105

Figure C4. 3 (a) Spectroscopic characterisation of upper threshold concentrations for L-AA and $HAuCl_4$ mixed with TMB 0.3 mM to discard signal generation in negative samples. (b) Effect of the gold salt concentration in the restoration of the peroxidase-like activity of enlarged AuNSt (500 pM). .. 106

Figure C4. 4 (a) 500 pM AuNSt were enlarged with a fixed concentration of L-AA ($5 \cdot 10^{-6}$ M) and a varying concentration of Au^{3+} (from 10^{-4} to $2 \cdot 10^{-4}$ M) prior to the addition of TMB 0.3 mM. oxTMB formation is characterised by measuring A_{370nm}. (b) Samples enlarged for 5 minutes with the highest concentration of Au^{3+} ($2 \cdot 10^{-4}$ M) and $5 \cdot 10^{-6}$ M L-AA led to TMB oxidation regardless of the presence of AuNSt, whereas only samples containing AuNSt led to oxTMB when the enlargement time was increased to 30 minutes (c). 107

Figure C4. 5 HR-TEM image of AuNSt after 30 min of reaction with $HAuCl_4$ $2 \cdot 10^{-4}$ M and L-AA $5 \cdot 10^{-6}$ M in PB 10 mM. 108

Figure C4. 6 UV-Vis analysis of oxTMB generated by AuNSt after undergoing or skipping an enlargement step. All samples contained 500 pM AuNSt. 109

Figure C4. 7 (a) RGB app layout after uploading a picture taken with the smartphone for analysis. The red square limits the area to be measured, while the results are shown on top in different colour spaces. (b) Data acquisition approach for each AuNSt concentration, analysing each replica in 3 separate areas of the well. ΔRGB values were calculated as shown in the Equation. (c) Calibration curves obtained using a Dose-Response model from Red, Green and Blue channel values and ΔRGB to quantify the presence of AuNSt are compared with the linear fit obtained using lab-based spectrophotometer equipment to measure $A_{370\ nm}$. 112

Figure C4. 8 (a) Colourimetric analysis of the peroxidase-like activity of silver enlarged AuNSt at a fixed concentration of AuNSt (50 pM) and varying the concentration of the silver enhancement solutions provided with the kit (no dilution, 2 times and 10 times dilution). (b) Images for further analysis are taken with the smartphone and the signal generated by the oxidation of TMB measured by UV-Vis spectroscopy. (c) Calibration curves obtained from Red, Green and Blue channel values to quantify the presence of AuNSt. 115

Figure C4. 9 (a) Smartphone Modulated Colorimetric Reader used for this work. (b) Components of the modulated smartphone reader, including a phone case, light-box connector, light box, assay platform adaptor and bottom panel. (c) Light box seen from the top, displaying an aperture from which an external light source can be introduced in the system. (d) Inside of the light box containing a modified pH strip prepared for analysing blue (d) and red (e) solutions. 118

Figure C5. 1 Immunochemical assay used to select suitable biorecognition elements to include in the biosensing assay for M. bovis detection. (a) Antibodies tests. (b) Peptide-binder tests. 128

Figure C5. 2 Calibration line obtained for the sandwich immunoassay developed to detect M. bovis using R44 as capture antibody and 1F11 as detection antibody..... 129

Figure C5. 3 UV-Vis analysis of AuNSt prior and after their surface modification with 1F11 antibody using the DTT reduction method. 130

Figure C5. 4 Sensitivity and selectivity analyses of the proposed system to detect M. bovis. (a) Calibration curve of the assay. M. bovis samples ranging from 10^3 to 10^6 CFU/mL were tested and the A_{370} values measured, plot and fitted to a Dose-Response curve. (b) Selectivity assay where different bacteria at the same concentration (10^5 CFU/mL) were analysed and the results compared through a one-way ANOVA. 132

Figure C5. 5 Operating steps using "QuantColorimetryApp". (a) A calibration image needs to be fed to the app first. (b) Each colour is associated to a certain known bacterial concentration. (c) The trained system is saved in the app, which coexists with systems for different applications. (d) A new image from a different assay is uploaded to the app for predicting the concentration of target analyte. 133

Figure C5. 6 Smartphone-based detection of M. bovis. (a) Two different smartphone apps are used to analyse the images taken with the smartphone. After calibrating them, both apps were capable of predicting the concentration of M. bovis present in several samples ranging from 10^3 to 10^6 CFU/mL. (b) Predictions observed using the spectrophotometer and comparison of the accuracy in the predictions with both smartphone apps. 135

Figure C6. 1 (a) SERS. The incident light induces a surface plasmon resonance, resulting in an enhanced electromagnetic field at the vicinity of AuNPs leading to an augmented scattering effect. (b) TERS. A plasmonic tip enhances the electromagnetic field within a confined volume at the tip-sample

junction, creating a lightning rod effect. ω_p: plasmon frequency, ω_S: scattered frequency. Figure reproduced from [396]. 139

Figure C6. 2 (a) UV-Vis analyses measuring $A_{370\ nm}$ after 20 min of reaction of AuNSt in the presence of a minimal concentration of TMB and in the absence of TMB (negative control). The samples are analysed in triplicate. (b) Raman spectroscopy analyses of the same samples analysed by UV-Vis spectroscopy. Raman measurements were performed using a laser power of 20 mW, wavelength source 785 nm, 10 exposures with an integration time of 5 s and a 10x objective lens. 144

Figure C6. 3 (a) 10 µM of R6G were mixed with AuNSt stabilised with different moieties and measured by Raman spectroscopy. (b) oxTMB generated by AuNSt was measured by Raman spectroscopy. Raman measurements were performed using a laser power of 10 mW, wavelength source 785 nm, 10 exposures with an integration time of 5 s and a 10x objective lens. 146

Figure C6. 4 (a) AuNSt-NaCit with different plasmonic properties were analysed by Raman spectroscopy to detect the presence of oxTMB. Raman measurements were performed using a laser power of 2 mW, wavelength source 785 nm, 10 exposures with an integration time of 5 s and a 10x objective lens. (b) Table summarising the amount of oxTMB generated by each AuNSt sample and the Raman signal produced. 147

Figure C6. 5 Raman spectra of decreasing concentrations of Rhodamine 6G in the presence and absence of AuNSt-NaCit. Raman measurements were performed using a laser power of 5 mW, wavelength source 785 nm, 10 exposures with an integration time of 5 s and a 10x objective lens. 149

Figure C6. 6 (a) AuNSt samples coated with a varying concentration of BDT are shown in an image and further UV-Vis spectroscopy analyses shown in the graph, together with spectra obtained after adding Ag to produce Au-Ag bimetallic NPs. (b) Spectra obtained by Raman spectroscopy for each of the BDT-based nanostructures. Raman measurements were performed using a laser power of 25 mW, wavelength source 785 nm, 10 exposures with an integration time of 5 s and a 10x objective lens. (SN: Supernatant) 152

Figure C6. 7 AuNSt coated with 4-MBA before and after performing the silver reduction step were analysed by (a) UV-Vis spectroscopy and (b) Raman spectroscopy. Raman measurements were performed using a laser power of 25 mW, wavelength source 785 nm, 10 exposures with an integration time of 5 s and a 10x objective lens. (SN: Supernatant) 154

List of schemes

Scheme C3. 1 Optically tuneable AuNSt are synthesised and characterised in this Chapter to study their potential as nanozymes and Raman enhancers for sensors development. 71

Scheme C3. 2 Synthesis and functionalisation of AuNSt following a seed-mediated growth. 73

Scheme C4. 1 Streptavidin-functionalised AuNSt after performing a gold enlargement step to restore their peroxidase-mimicking activity, enabling them to generate a colourimetric signal. 97

Scheme C5. 1 Assay mechanism proposed for the smartphone-based colourimetric detection of M. bovis. 123

Scheme C5. 2 DTT reduction method used to conjugate AuNSt to 1F11 antibodies. The antibody fragments generated lead to functional (green) and non-functional (red) binding sites. 126

Scheme C6. 1 Mechanism for Hg^{2+} sensing in environmental water samples [439]. 155

Scheme C6. 2 Mechanism for Hg^{2+} sensing through SERS using AuNSt-BDT-AgSAT. 156

List of tables

Table C1. 1 Clinical biosensors exploiting the catalytic properties of AuNPs. 27

Table C1. 2 Other non-clinical biosensors exploiting the catalytic properties of AuNPs. 41

Table C2. 1 Synopsis of commercially available kits for microbiological contaminants in foodstuff. 59

Table C2. 2 Number of sensors described in the scientific literature for microbiological food contamination classified according to the TEST criteria. 62

Table C3. 1 Summary of spectroscopic differences between AuNSt samples prepared with varying volumes of seeds. (FWHM: Full Width at Half Maximum) 77

Table C3. 2 Results after replacing citrate-capped AuNSt with bifunctional alkane chains of varying length (11 and 16 C chains). (Agg. Indicates aggregation) 81

Table C3. 3 Michaelis-Menten parameters obtained from the kinetic analyses of different types of AuNSt in relation to their peroxidase-like properties. The data shown in the table are the average of triplicate values 91

Table C4. 1 Set of conditions used for functionalising AuNSt with streptavidin following a one-pot approach. 101

Table C4. 2 Analysis of the supernatant of streptavidin functionalised AuNSt using a direct immunochemical assay. 103

Table C4. 3 The capability of silver-enlarged AuNSt to oxidise TMB and generate a blue colour was characterised spectrophotometrically. 113

Table C6. 1 Assignment for the main Raman bands [162,423] obtained for two Raman active probes used in this Chapter: R6G and oxTMB. 145

Table C6. 2 Assignment for the main Raman bands [435,436] obtained for two Raman active probes embedded in Au-Ag bimetallic NPs. 150

Table C6. 3 Compilation of spectroscopic data obtained from AuNSt coated with several concentrations of Raman probes BDT and 4-MBA, before and after (Ag) applying a silver growth step. (→) indicates plasmon redshift, (←) indicates plasmon blueshift..... 154

Table C6. 4 Comparison of analytical performance of two different approaches discussed in this Section for Hg sensing in water samples exploiting SERS activity of AuNSt. 157

List of abbreviations

11-MUA	11-Mercaptoundecanoic acid
16-MHA	16-Mercaptohexadecanoic acid
4-MBA	4-Mercaptobenzoic acid
AA	Ascorbic acid
AEF	Analytical enhancement factor
AgNP	Silver nanoparticles
AgSAT	Silver satellites
ANOVA	Analysis of variance
AuNP	Gold nanoparticles
AuNRs	Gold nanorods
AuNSt	Gold nanostars
BCG	Bacillus Calmette-Guérin
BDT	Benzene-1,4-dithiol
bTB	Bovine tuberculosis
CFU	Colony-forming unit
COPD	Chronic obstructive pulmonary disease
CTAC	Cetyltrimethylammonium chloride
CTC	Charge-transfer complex
DALY	Disability-adjusted life year
DLS	Dynamic Light Scattering
EC	Electrochemistry
EF	Enhancement factor
EFSA	European Food Safety Authority
ELISA	Enzyme-linked immunosorbent assay
EM	Electromagnetic (theory)
EPA	Environmental Protection Agency
EPEC	Enteropathogenic *Escherichia coli*
ETEC	Enterotoxigenic *Escherichia coli*
FAO	Food and Agriculture Organization
FDA	Food and Drug Administration
FWHM	Full width at half maximum
HCV	Hepatitis C virus
HIV	Human immunodeficiency virus
HRP	Horseradish peroxidase
HR-TEM	High-resolution transmission electron microscopy
HSV	Hue, Saturation, Value (colour space)
HTST	High-temperature short-time (processing)
ICA	Immunochromatographic assay
IFN	Interferon
IR	Infrared
LAB	Lightness, Chromatic axes A/B (colour space)
LAMP	Loop-mediated isothermal amplification
LFD	Lateral flow device
LOC	Lab-on-a-chip

LOD	Limit of detection
LSPR	Localised surface plasmon resonance
MAE	Mean absolute error
MOF	Metal-organic framework
MRL	Maximum residue level
MSN	Mesoporous silica nanoparticle
MTBC	Mycobacterium tuberculosis complex
N/A	Not available, not applicable
NaCit	Sodium citrate
NIR	Near-infrared
NP	Nanoparticle
O/N	Overnight
OEG	Oligo(ethylene glycol)
oxTMB	Oxidised TMB
PB	Phosphate buffer
PBDE	Polybrominated diphenyl ethers
PCB	Polychlorinated biphenyls
PCR	Polymerase chain reaction
PDT	Photodynamic therapy
PEG	Poly(ethylene glycol)
PFU	Plaque-forming unit
PO	Peroxidase
POC	Point-of-care
PPC	Post-pasteurisation contamination
qPCR	Real-time PCR
R6G	Rhodamine-6-G
RASFF	Rapid Alert System for Food and Feed
RCA	Rolling circle amplification
rcf	Relative centrifugal force
RDM	Raw drinking milk
RGB	Red, Green, Blue (colour space)
RI	Refractive index
RIU	Refractive index unit
ROS	Reactive oxygen species
RS	Raman spectroscopy
RT	Room temperature
SAM	Self-assembled monolayer
SEF	Surface enhanced fluorescence
SERRS	Surface enhanced resonant Raman scattering
SERS	Surface enhanced Raman scattering
SM	Single molecule
SMCR	Smartphone Modulated Colorimetric Reader
SN	Supernatant
SOD	Superoxide dismutase
SPR	Surface plasmon resonance
STEC	Shiga toxin-producing *Escherichia coli*
TB	Tuberculosis
TBEV	Tick-borne encephalitis virus

TEM	Transmission electron microscopy
TERS	Tip enhanced Raman spectroscopy
TEST	The end-user sensor tree
TMB	3,3’,5,5’-Tetramethylbenzidine
UHT	Ultra-high-temperature (processing)
VOC	Volatile organic compounds
WHO	World Health Organisation
ε	Molar extinction coefficient

Contents

Acknowledgements i

Abstract ii

List of figures iv

List of schemes x

List of tables xi

List of abbreviations xiii

Chapter 1 Introduction & Literature Review 1

1.1 Food contamination 2

1.1.1 Background 2

1.1.2 Milk contamination 4

1.1.3 EU Regulation & Current situation 9

1.1.4 Mycobacterium bovis 11

1.2 Gold nanoparticles 12

1.2.1 Optical properties 14

1.2.2 Spectroscopic properties 16

1.2.3 Catalytic properties 17

1.2.4 Applications & Smartphone readout systems 20

1.3 Gold nanozymes – a review 21

1.3.1 Abstract 21

1.3.2 Biomedical applications of gold nanozymes 22

1.3.3 Other applications of gold nanozymes 35

1.4 Thesis aims and objectives 42

Chapter 2 Developing a novel classification system for sensors targeting microbiological food contaminants: TEST – The End-user Sensor Tree 43

2.1 Introduction 44

2.1.1 Abstract 44

2.1.2 TEST – An end-user friendly sensor database 44

2.2 Methods 46

2.2.1 Classification of sensors 46

2.3 Results and discussion 48

2.3.1 Analytical methods 48

2.3.2 Sensitivity 51

2.3.3 Commercial sensors 54

2.3.4 Construction of TEST tree and e-docs 60

2.4 Conclusions 64

Chapter 3 Gold nanostars: Synthesis and characterisation of their peroxidase-like activity 65

3.1 Introduction 66

3.1.1 Gold Nanostars Synthesis 69

3.1.2 Objectives 70

3.2 Methods 72

3.2.1 Reagents and chemicals 72

3.2.2 Synthesis of AuNSt 72

3.2.3 Functionalisation of AuNSt 73

3.2.4 Characterisation of AuNSt 73

3.2.5 Peroxidase-mimicking activity of AuNSt 74

3.3 Results and discussion 75

3.3.1 Synthesis of AuNSt 75

3.3.2 Stabilisation of AuNSt with different functional groups 77

3.3.3 Characterisation of AuNSt 82

3.3.4 Peroxidase-mimicking activity of AuNSt 87

3.4 Conclusions 92

Chapter 4 Colourimetric applications of AuNSt and smartphone-based quantification 94

4.1 Introduction 95

4.1.1 Colour quantification through smartphones 96

4.1.2 Objectives 97

4.2 Methods 98

4.2.1 Reagents and chemicals 98

4.2.2 AuNSt functionalisation with streptavidin 98

4.2.3 Gold enlargement of AuNSt 99

4.2.4 Silver enlargement of AuNSt 99

4.2.5 HR-TEM 99

4.2.6 Colour analysis using “RGB Color Detector” 99

4.2.7 Colour analysis using “QuantColorimetryApp” 100

4.3 Results and discussion 101

4.3.1 Inhibition of peroxidase-like activity of streptavidin-functionalised AuNSt 101

4.3.2 Autocatalytic enlargement of AuNSt 103

4.3.3 Smartphone-based quantification 110

4.3.4 Development of a smartphone modulated colourimetric reader 116

4.4 Conclusions 119

Chapter 5 Smartphone-based detection of *Mycobacterium bovis* 120

5.1 Introduction 121

5.1.1 Bovine tuberculosis 121

5.1.2 *M. bovis* current detection approaches 122

5.1.3 Objectives 123

5.2 Methods 124

5.2.1 Reagents and chemicals 124

5.2.2 Binding immunoassay 1D 124

5.2.3 Sandwich immunochemical assay 124

5.2.4 DTT reduction 125

5.2.5 Indirect immunochemical assay 126

5.3 Results and discussion 127

5.3.1 Characterisation of *M. bovis* binders 127

5.3.2 Immunochemical assay for *M. bovis* detection 128

5.3.3 AuNSt conjugation to 1F11 129

5.3.4 Retrieving peroxidase-like activity of AuNSt for *M. bovis* detection 130

5.3.5 Smartphone calibration for colour analysis 133

5.3.6 Smartphone-based detection of *M. bovis* 134

5.4 Conclusions 136

Chapter 6 Gold nanostars and SERS 137

6.1 Introduction 138

6.1.1 Raman Spectroscopy, SERS and SERRS 138

6.1.2 AuNPs as Raman enhancers 140

6.1.3 Objectives 141

6.2 Methods 142

6.2.1 Reagents and chemicals 142

6.2.2 Raman Microscopy Analyses 142

6.2.3 Synthesis of Au-Ag bimetallic NPs 142

6.3 Results and discussion 143

6.3.1 Potential of SERS for biosensing 143

6.3.2 Characterisation of AuNSt as Raman enhancers 144

6.3.3 Au-Ag bimetallic NPs 149

6.3.4 Published studies 155

6.4 Conclusions 158

Chapter 7 Thesis conclusions 160

List of publications arising from this thesis 166

References 169

Appendices 202

Chapter 1 Introduction & Literature Review

1.1 Food contamination

Food contamination is a persistent health issue that we have become used to deal with [1]. Some of them are natural-occurring contaminants, including biological contaminants like bacteria or viruses that find in a certain animal or food matrix the perfect environment to grow. Also, physical or chemical contaminants such as toxins derived from these living organisms or heavy metals can pose a threat to our health. However, many of these contaminants have an anthropogenic source, such as pesticides, veterinary drugs or nanoplastics. As a result, the more the food industry is developed, the more different contaminants we will encounter (https://ec.europa.eu/food/safety_en). With a world population quickly approaching 8,000 million people as of 2020, producing safe and contaminant-free food has become a real challenge. According to several sources (such as the Australian Commonwealth Scientific and Research Organization or the World Wildlife Foundation), in the next 50 years we will have to produce as much food as we have ever produced in human history to feed a growing world population. In such large numbers, even rare contamination events become a threat, even more if the effects of globalisation are considered, as a punctual contamination event can reach more people than ever.

1.1.1 Background

The late 1990s was marked by a series of food crises involving bovine spongiform encephalopathy (BSE), *Salmonella* or dioxins contaminations that undermined consumers' confidence in the food supply system. The EU response to this food crisis was to create the European Food Safety Authority (EFSA) in 2002 [2], an organisation aiming to assess the risk of food contamination and produce scientific reports to advice regarding European policies and legislation related to food safety. In parallel, the Rapid Alert System for Food and Feed (RASFF) created in 1979 enables information to be shared efficiently between its member, thus notifying any food related risk as soon as possible to prevent it from being harmful to consumers [3]. According to the most recent scientific report by the World Health Organization (WHO) [4] unsafe food causes more than 200 diseases ranging from diarrhoea to cancer, which accounts for an estimated 600 million people falling ill and 420,000 deaths every year. Moreover, it is estimated that about 40% of the foodborne disease burden is carried by children under 5 years of age. These data shed some light on the magnitude of the problems in food contamination.

Recent studies have reviewed the main contaminants found in food that pose a threat to human health, which are mainly divided into microbiological and chemical agents [5]. The first group

encompasses bacteria (e.g. *Salmonella*, *Campylobacter*, *Escherichia coli*, etc.), viruses (e.g. Norovirus, Hepatitis A, etc.), parasites (e.g. trematodes, toxoplasma, etc) or worms (e.g. cestodes, nematodes). Despite this last group of worms not leading to fatal outcomes, microbiological contaminants overall account for over 90% of foodborne deaths according to WHO estimates [6]. On the other hand, common chemicals include pesticides (e.g. carbamates, organophosphates), mycotoxins (e.g. aflatoxin, ochratoxin) or environmental pollutants (e.g. persistent organic pollutants, dioxins, heavy metals). In order to properly evaluate the actual health impact each of these contaminants has, the Disability-Adjusted Life Years (DALY) metric was introduced in the 90s, calculated as the years of life lost due to a premature death caused by a certain disease plus the number of years lived with disability or poor health due to that condition. This way, the health impact of non-fatal diseases can be fairly compared to those commonly leading to death [6]. Various microbiological and chemical food contaminants are compared in terms of DALYs in Figure C1.1, showing that microbiological contaminants remain the principal threaten for our health.

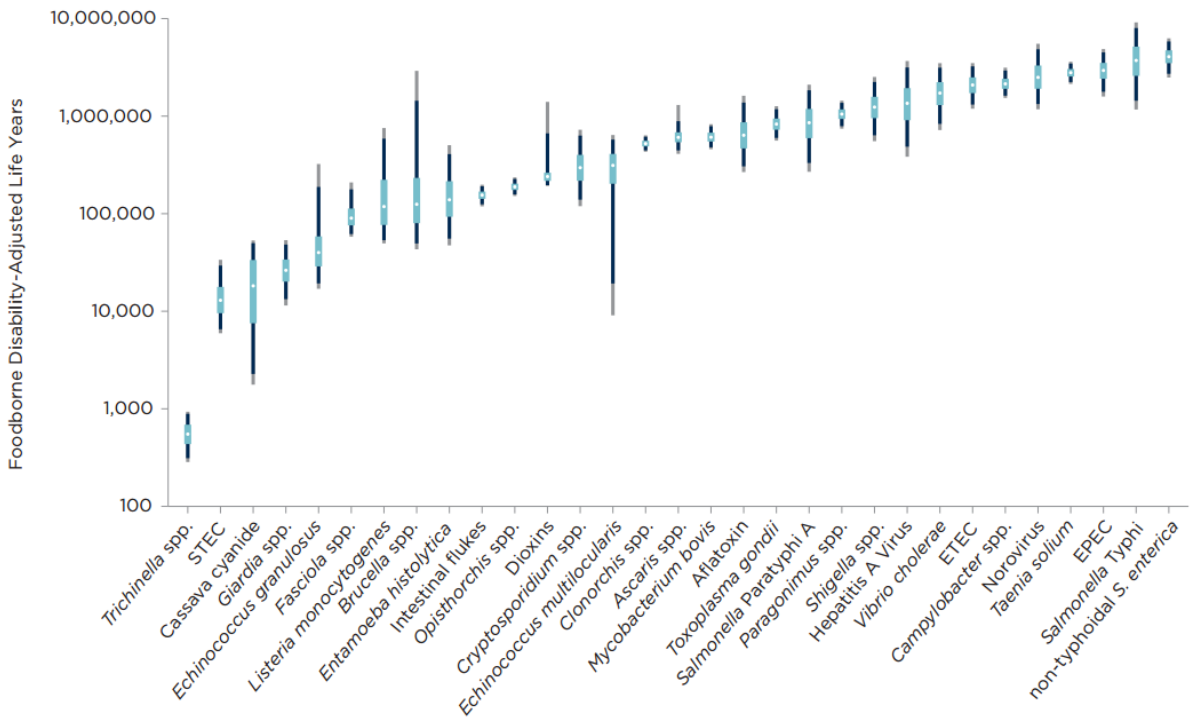

Figure C1. 1 Foodborne hazards based on Disability-Adjusted Life Years at the global level. Reproduced from WHO [6].

Notes: White dots indicate the median burden, black boxes the inter-quartile range (50% UI), black lines the 5 and 95 percentiles (90% UI) and grey lines the 2.5 and 97.5 percentiles (95% UI). Note that the y-axis is on a logarithmic scale. Abbreviations: EPEC = Enteropathogenic Escherichia coli; ETEC = Enterotoxigenic E. coli; STEC = Shiga toxin-producing E. coli.

Therefore, the current work will revolve around the study of microbiological contaminants in particular, given the high incidence they have in the consumers' health. On the other hand, the dairy sector represents 25.7% of Northern Ireland's farm output, surpassing the cattle sector, and comes second in terms of gross turnover (£ 1,008 m in 2015) only surpassed by the "beef and sheep meat" combined sector (£ 1,265 m in the same period) [7]. Accordingly, there is a need to address the important issue if microbiological contamination in milk products, thus satisfying both food safety data and economic demands.

1.1.2 Milk contamination

Milk is a highly nutritious food, essential for humans during the first stage of our lives. The importance of dairy products as nourishment lays in their rich nutritional value, which at the same time explains the enormous diversity of microbial contaminants that find in milk products the perfect media to grow [8]. Some of these contaminants lead to food spoilage, whereas some others pose a serious threat to our health. Many attempts have been made to try to regulate and control the situation, but none of them has managed to satisfy everyone involved in the milk supply chain [9]. From hygiene measures introduced during milk handling to precautionary measures such as pasteurisation or routine analyses in finished dairy products, this problematic remains unresolved. All this leads to the present work, aiming to develop novel diagnostic tools to tackle this global issue.

The origin of this problem can be dated back to the Neolithic, i.e. in the 7th millennium BC [10]. Before this time, milk consumption was reserved for infants as only them could digest lactose, a major constituent of mammalian milk. This was due to lactase (an essential enzyme for milk digestion) being down-regulated after the weaning period was completed. However, the emergence of lactase persistence, a genetic adaptation in the regulation of the lactase gene, enabled continued digestion of milk. This Darwinian event can be located in time and place either by detecting the presence of milk fats in archaeological vessels and ceramics [11,12] or by detecting proteins such as β-lactoglobulin (a major whey protein of cow and sheep's milk) in archaeological dental calculus [13]. These analyses show that dairy products were likely to start being consumed around the sea of Marmara [14], rapidly spreading the habit throughout Europe. Soon after that, different dairy products started to be produced [15], bringing with it the diversity of microbial contaminants that are reported nowadays to be associated with them [8].

The risk derived from milk consumption changed drastically in the 19th century with Louis Pasteur invention of the pasteurisation process, which became a virtually mandatory step of milk production.

It generally consists in heating milk to 72 ˚C for 15 seconds to eliminate potential pathogens and extend the shelf-life of the product. After the implementation of the process, the percentage of foodborne illness outbreaks associated with milk dropped enormously. According to the Food and Drug Administration (FDA) claims, before 1938 25% of all food-related outbreaks in the US were related to milk, whereas the implementation of pasteurisation made this percentage drop below 1% in 2011 [16].

Nowadays, the global dairy industry plays an important role within the food field (https://www.fao.org/faostat/). Milk production and consumption are widely spread around the globe, which has resulted in a boost in trade between different countries. A constant 8.6% share of dairy products is used for international trade, which highlights the importance of standardising basic regulations on milk products and the need to facilitate the flow of information between different countries. According to the Food and Agriculture Organization of the United Nations (FAO), the total milk production in 2016 reached 821.8 million tonnes (Figure C1.2), being a fifth of it (168.3) produced by the EU (data provided by FAOSTAT). Germany and France are the main producers within the EU, accounting for 36.5% of it. It should be pointed out that about one third of this milk is used for cheese production (37%), another third for butter production (30%) and the rest processed into other products, including cream, drinking milk, powder or others (FAOSTAT).

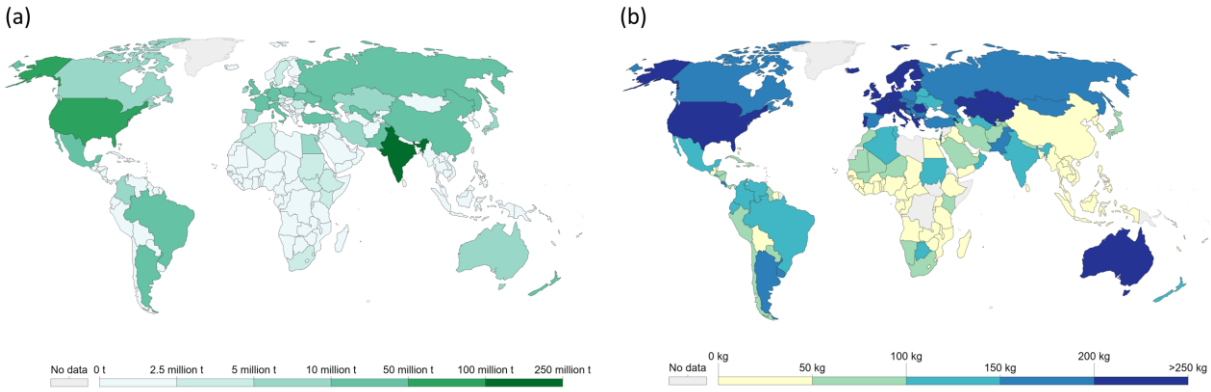

Figure C1. 2 (a) Milk production by country in 2017. (b) Average milk consumption per capita in 2017, measured in kg per person per year. This includes milk equivalents of dairy products (excluding butter). Figure reproduced from UN FAO.

Milk is known to support a rich microbiota due to its high nutritional content, despite being virtually sterile in healthy udder cells. These microorganisms colonise milk from different sources including the teat surface, air, milking equipment, feed, soil, faeces or grass [17–19]. And they can play a number of different roles, beneficial such as facilitating dairy fermentations and promoting health, or detrimental such as causing food spoilage and human disease [20]. Among these, there is an especial interest in

controlling those that lead to spoilage (economic impact) and those that cause disease (health impact).

1.1.2.1 Spoilage microorganisms

Milk is generally stored at refrigeration temperatures thus reducing the growth of bacteria. However, psychrotolerant microorganisms can grow and reproduce in low temperatures (below 7 ˚C) despite their optimal temperature for growth being between 15-20 ˚C [21]. *Pseudomonas* spp. represent no more than 10% of the microflora of freshly drawn milk, but they can constitute up to 70-90% in raw milk stored at low temperature for less than 10 days, due to the selective advantage for the growth of psychrotrophic bacteria provided by low temperature storage [22]. Therefore bacteria such as *Pseudomonas fluorescens*, *Pseudomonas gessardii*, *Pseudomonas fragi* or *Pseudomonas lundensis* become the most common cause of milk spoilage in dairy products, via the production of extracellular enzymes, such as lipases that degrade milk fat causing rancidity or proteases that degrade casein generating a grey colour and bitter off-flavours [23–25]. However, the pasteurisation process has a big impact in the reduction of the microbiological load, including spoilage psychrotrophic microorganisms. As a result, the main two spoilage groups remaining will be thermoduric microorganisms (heat-resistant) and those introduced through post-pasteurisation contamination (PPC). The former group includes important spore-forming bacteria such as *Clostridium* or *Bacillus* spp. [26,27], some of which are resistant to pasteurisation and have the potential to survive and grow at refrigeration temperatures. As for the latter group, PPC events are generally caused by the same types of bacteria already mentioned, which can be divided in four groups: *Pseudomonas (P. fluorescens*, *P. putida)*, coliforms (*Enterobacter*, *Klebsiella)*, non-coliform non-*Pseudomonas* gram-negatives (*Flavobacterium*, *Acinetobacter*) and gram-positive spore-formers (*Bacillus cereus*, *Paenibaciullus*) [28]. These contaminations often occur due to problems associated with hygienic design of equipment in dairies, inadequate cleaning and sanitisation procedures or control of plant air. Moreover, the formation of biofilms can lead to persistent contamination issues, as they may attach to processing equipment and become resistant to cleaning and sanitation [29]. Fungi groups such as yeasts and moulds complete the diverse number of microorganisms that cause spoilage of milk products. On the other hand, strategies to reduce the spoilage rate include reducing the pH by fermenting lactose to lactic acid, adding approved preservatives, introducing a desirable microflora not leading to spoilage effects and outcompeting undesirable microorganisms thus restricting their growth, reducing the water activity by adding salts or sugars, limiting available oxygen within package or freezing [8].

1.1.2.2 Foodborne pathogens

On the other hand, there are some microbiological contaminants that instead of food spoilage lead to human disease, causing from fever, nausea, diarrhoea, vomiting or stomach cramps [30] to other more serious conditions such as tuberculosis. They are generally called foodborne pathogens and, in the case of dairy products, the most common include *Listeria monocytogenes*, *Salmonella* spp., *Escherichia coli*, *Campylobacter* spp. or *Staphylococcus aureus* [31]. There are many sources from which these bacteria can contaminate dairy products, such as the mammary gland or associated lymph nodes of infected cows, milking and processing equipment, raw milk tankers, the environment or personnel. Again, pasteurisation is the main barrier to prevent these pathogens reaching the consumer. However, spores of pathogens like *Clostridium botulinum* or *Bacillus cereus* are resistant to this process [32], similarly to heat-stable enterotoxins produced by *S. aureus* [33]. Others, for example, *L. monocytogenes*, *Yersinia enterocolitica* and *Brucella* spp. are able to survive and multiply at refrigeration temperatures, posing a threat to human health in the event of an insufficient pasteurisation or PPC. Furthermore, zoonotic bacteria such as *Coxiella burnetii* and *Mycobacterium bovis*, causative agents of Q fever and tuberculosis, can infect cows or other mammals and transfer to raw milk. In these cases, pasteurisation will be an effective barrier as their main source is the cattle, therefore it is unlikely to introduce these bacteria through a PPC event [20]. Overall, the main situations leading to a human infection by milk-borne pathogens can be classified in two groups: consumption of unpasteurised or insufficiently pasteurised milk and other foodstuff derived from it, such as cheese produced from raw milk; PPC, mostly related to the introduction of contaminated raw milk into processing plants that lead to the generation of persistent biofilms [34]. Figure C1.3 shows below the main milk-borne pathogens associated to each stage of the dairy processing.

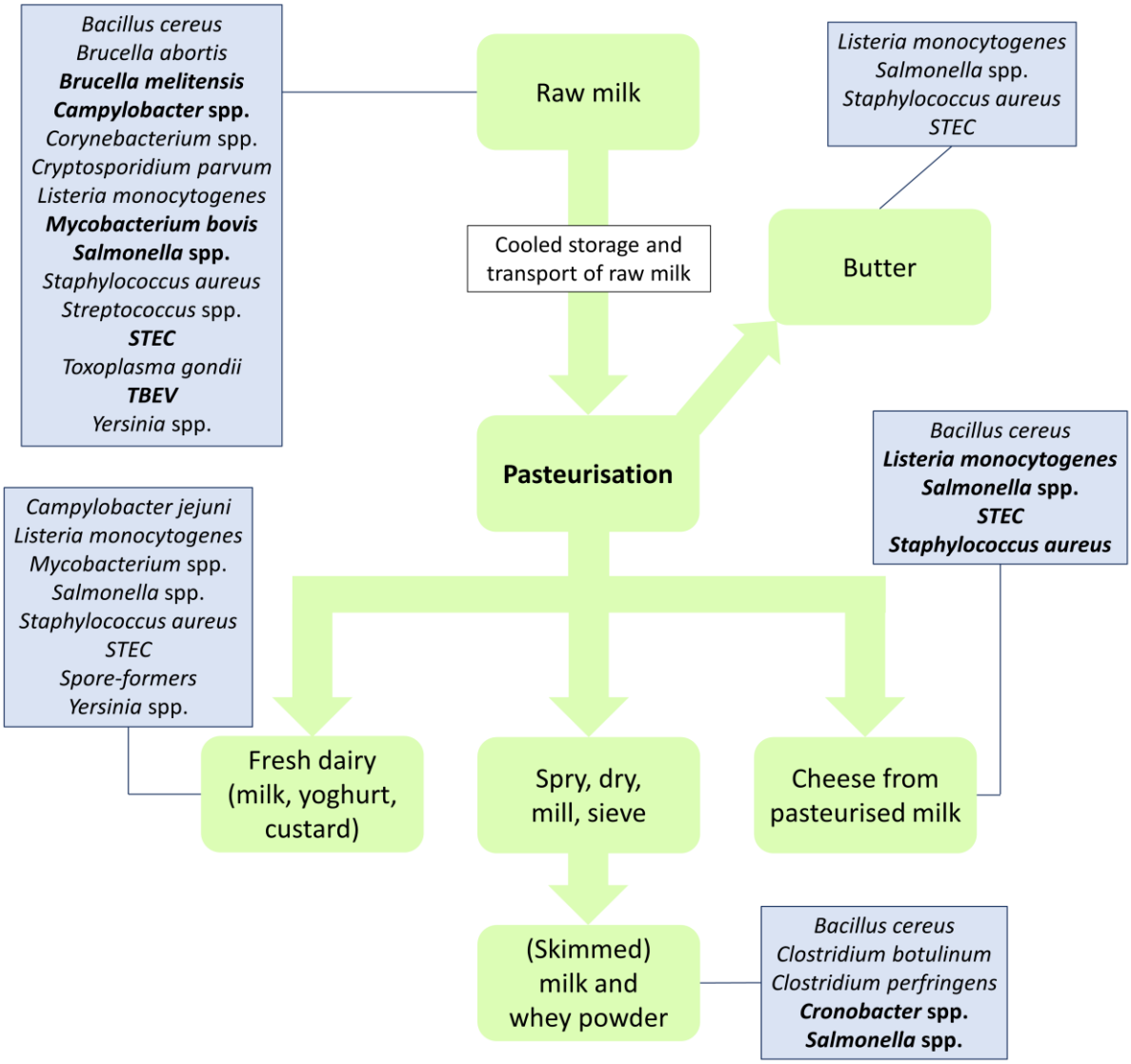

Figure C1. 3 Main microbiological hazards reported in scientific literature for dairy products processed at the dairy factory. The most important hazards are bolded. Figure reproduced from [31].

STEC: Shiga toxin-producing *Escherichia coli*, TBEV: Tick-borne encephalitis virus

There is evidence that suggests that almost 50% of fluid milk in the US shows PPC, generally caused by gram-negative bacteria that can rapidly grow at refrigeration temperatures of 6 ˚C leading to spoilage that can be sensorially detected within 7-10 days of processing [28]. This way, developing rapid and user-friendly biosensors to test and ensure that milk products are free of microbiological contaminants becomes a necessity.

1.1.3 EU Regulation & Current situation

Extensive regulation exists in the EU and elsewhere regarding food safety. In the case of milk products intended for human consumption, pasteurisation remains the most efficient procedure to avoid microbiological contaminants being present in the final product. This is stated in the regulatory document entitled "*COUNCIL DIRECTIVE 2002/99/EC of 16 December 2002 – laying down the animal health rules governing the production, processing, distribution and introduction of products of animal origin for human consumption*". In there, different pasteurisation processes are indicated to eliminate health risks linked to milk depending on the pH of the milk: simple high-temperature – short-time pasteurisation (HTST) if the milk has a pH below 7.0, or double HTST if the pH is higher. Alternatively, ultra-high temperature (UHT) processes can be applied in either case.

However, raw milk consumption has gained popularity in recent years due to claims on enhanced nutritional values, taste and health benefits, despite many of these claims not being backed by scientific evidence [35–38]. Further discussion on this topic was presented as a scientific dissemination article in *New Food magazine* (https://www.newfoodmagazine.com/article/100417/milk-pasteurization-could-tuberculosis-be-slipping-into-our-breakfast-bowls/).

At present, raw drinking milk (RDM) is legally distributed by dairies and it can be easily purchased directly on-farm, through the Internet or vending machines located around many countries in the EU [39], thus targeting a wider range of consumers. This situation has brought a lack of uniformity in regulatory terms, as laws regarding RDM differ enormously between different countries. As a general rule, according to the *Regulation (EC) No 853/2004* [40], cows' RDM produced in Europe must contain ≤ 100,000 colony-forming units (CFU)/mL for total bacteria plate count (at 30 ˚C) and ≤ 400,000 CFU/mL for somatic cells. Moreover, it must come from animals belonging to a herd officially free of brucellosis and tuberculosis and comply with the numerous hygiene measures stated in the aforementioned Regulation.

Despite all the hygiene and security measures put in place to prevent any microbial contamination in milk products, there are still many cases that escape the surveillance and put the consumer at risk [31]. The scope of this threaten is manifest in the RASFF portal, where all notifications relevant to the area are reported and classified according to the hazard and the product affected. The number of notifications related to microbial contaminants in milk products in the EU in the last decade (2010-2019) reaches an impressive 392 cases, being *Listeria monocytogenes*, *Escherichia coli* and *Salmonella* spp. the most frequent pathogens reported [41]. Only 40 of these notifications were classified as "not serious", which mostly included milk products infested with moulds. This notification system not only

pursues to convey awareness of the current state of food contamination, but it has also become a key tool to ensure the flow of information within the EU or otherwise in the event of any food-related risk arising [42]. This is of paramount importance considering the large distance that separates farm and fork. According to Friends of the Earth Europe, the largest environmental network in Europe, imported milk products in Spain travel an average of 836 miles, whereas Walmart, an important American retail corporation, estimated that food travels on average 1,500 miles before it reaches consumers. In a food system that does not follow political borders, international flow of information such as the one provided by RASFF to track any sort of contamination becomes essential [42]. The following reported notifications illustrate some food scandals recently occurred in the EU that led to important health issues:

I. Multi-country outbreak of Shiga toxin-producing *Escherichia coli* infection associated with haemolytic uraemic syndrome (April 2016): it affected a Romanian milk processing establishment that would export cheese to several EU countries (specifically Belgium, Germany, Italy and Spain). There were 25 cases affecting mostly young children, of which 19 developed the mentioned syndrome and 3 died [43]. The alert notification was followed by the recall of the company products in the countries affected to avoid further cases.

II. Multi-country outbreak of *Salmonella Agona* infections linked to infant formula (January 2018): in this case, the outbreak took place in France and the product affected powdered milk. 39 infants were infected, from which 37 in France, 1 in Spain and 1 in Greece. Recalled products had been distributed to 13 EU countries and 54 third countries, which shows the magnitude of these problems not only for their health threat, but also for their economic implications. *Salmonella agona* is the tenth most commonly reported Salmonella serotype in the EU. However, its isolation from food samples has been mostly linked to pig and broilers meat, rather than dairy products [44].

III. Multi-country outbreak of *Salmonella Poona* infections linked to consumption of infant formula (March 2019): contaminated infant formula that had been processed in Spain and distributed by France eventually affected 32 infants and young children (30 in France, 1 in Belgium and 1 in Luxembourg). This case exemplifies the difficulties that sometimes entails trying to track such a contamination within the common market, as there was not a clear contamination point to target. Recalls and public messaging to alert the public of affected countries were the main two measures that followed this incident [45].

1.1.4 Mycobacterium bovis

M. bovis is a slow-growing, aerobic, acid-fast, Gram positive bacterium that causes tuberculosis (TB) in cattle and other mammals such as goats, deer or badgers [46]. It is member of the *Mycobacterium tuberculosis* complex (MTBC), which also includes different species classified depending on the animal that constitutes their main reservoir: *M. tuberculosis* (humans), *M. africanum* (humans, limited to West Africa), *M. microti* (voles), *M. caprae* (sheep and goats) or *M. pinnipedii* (seals). However, all these bacteria can infect humans with various degrees of success [47,48], causing zoonotic TB and coursing with virtually identical symptoms to those of TB. According to the WHO [49], in 2016 there were 10.4 million new cases of TB worldwide, accounting for 1.7 million deaths. In this context, *M. tuberculosis* (and *M. africanum*) and *M. bovis* have the greatest impact, being the latter responsible for about 10 – 15% of TB cases in developing countries and 1 – 2% in developed countries [50]. Officially, this translated into 147,000 cases of zoonotic TB in humans in 2016, although considering the difficulties in distinguishing it clinically from TB, the true burden of zoonotic TB is thought to be underestimated [51]. Humans become infected with *M. bovis* mainly by consuming raw milk from infected cows or dairy products made from raw milk, such as cheese and yoghurt where the bacteria can remain viable for up to 14 days, or up to 100 days in butter [52]. Current methods to detect *M. bovis* include culture approaches which can take up to 90 days to give a result due to its slow growth nature [50], or PCR approaches which require trained personnel and expensive equipment [53]. Nevertheless, most efforts to avoid this contamination have been placed at the animal level, using either *in vivo* intradermal tuberculin tests (skin tests) or *in vitro* γ-interferon (γ-IFN) assays [54,55]. Both approaches are oriented to diagnose cattle as tuberculosis-free, therefore complying with EU regulations to sell raw milk. The herd must be checked annually using either test. However, the difficulties in the standardisation of these approaches, the lack of reproducibility of the former and the presence of non-specific responses in the latter have risen valid concerns about the safety of commercialising and consuming raw milk [55,56]. Moreover, wildlife such as badgers are well known to be an important reservoir of *M. bovis* implicated in the spread of bovine TB (bTB) in the UK and Ireland [57], which can easily infect animals from a TB-free herd. As a result, outbreaks of tuberculosis have occurred in Ireland [58] and elsewhere in the past years, leading to serious health conditions to those affected. In consideration, rapid, reliable and user-friendly sensing devices are required to detect the presence of *M. bovis* in milk products to provide further protection to the general consumer.

1.2 Gold nanoparticles

Metallic nanoparticles and gold nanoparticles (AuNPs) specifically have attracted the interest of the scientific community due to their excellent physical, chemical and biological properties derived from their "nano" size. Generally, the term nanoparticle includes particles of any shape with at least one of their dimensions in the 1 – 100 nm range [59]. The main reasons that can be highlighted for using gold instead of other metals nanoparticles include the good stability observed in AuNPs [60], the relative ease with which gold surfaces can be chemically modified [59] or their lower toxicity for biomedical applications [61]. However, it was their optical effects which first attracted interest in colloidal gold in ancient times, being used in Chinese ceramics to sharp reddish colours in 400 BC [62], in the famous Lycurgus Cup of Roman origin combined with Ag NPs to achieve a dichroic effect in 400 AD [63], or in Persian artwork to obtain shinning effects in 900 AD [64]. Few to none applications were described in the following years until the thirteenth century, when European alchemists started to propose AuNPs for medicinal use. However, it was in the nineteenth century that some potential of AuNPs could be foreseen, with J. A. Chrestien using gold to treat seven syphilis patients [65], Michael Faraday producing metallic gold colloids while mounting thin sheets of gold leaf onto microscope slides [66] and Robert Koch discovering the in vitro bacteriostatic properties of gold [67]. Thereafter, John Turkevich published a detailed study of the process of nucleation and growth of colloidal gold [68] and Richard Feynman gave his famous lecture "*There's plenty of Room at the Bottom: An Invitation to Enter a New Field of Physics*" [69] in which the potential implementations of nanomaterials were discussed, paving the way to the wide range of applications found nowadays.

It is interesting to note that properties of materials in the nanoscale differ enormously from the ones found in the bulk material, as a result of quantum-size effects. Many studies ever since have revolved around these new properties, either physical, chemical or biological, to characterise and understand how gold nanomaterials behave [60,70–72]. These include optical properties, like Surface Plasmon Resonance (SPR), spectroscopic properties, like Surface-Enhanced Raman Spectroscopy (SERS) or catalytic properties, like peroxidase-mimicking. As a result, AuNPs can be exploited for different purposes, from biosensors development to biomedical, environmental or food related applications. A critical step, however, for achieving successful applications is the synthesis of gold nanomaterials, as the mentioned properties they possess are dependent on the NP size, shape and surface chemistry. Two approaches are widely used for the fabrication of gold nanostructures: bottom-up and top-down. The former relates to techniques such as chemical synthesis, self-assembly or molecular fabrication, involving the nucleation of gold atoms and their growth into colloidal AuNPs from a molecular precursor. The latter refers to methods such as photolithographic micropatternings, pyrolysis and

attrition [73]. Micropatterning techniques employ a light, electron or ion beam to selectively pattern nanostructures from precursor resist materials, like photolithography [74], electron beam lithography [75], soft lithography [76], nanocontact printing [77], nanoimprint lithography [78], nanosphere lithography [79], colloidal lithography [80] or scanning probe lithography [81]. Pyrolysis approaches bring under high pressure and burn a vaporous precursor to generate ashes that are further processed to produce nanoparticles [82–84]. And attrition (or milling) methods consist in grinding macro- and microscale materials to generate particles of nanometric dimensions [85]. The fabrication conditions required and the expensive equipment needed are the main limitations faced by top-down approaches. Specifically, lithography approaches are neither cost nor time-effective, pyrolysis requires a high amount of energy and attrition methods carry an inherent imperfection in the shape and size of the nanostructures obtained. Logically, thus, bottom-up approaches have emerged as a simpler alternative enabling to produce AuNPs with a diverse range of sizes and shapes, such as spheres [68,86], rods [87,88], cubes [89], prisms [90,91], stars [92], cages [93], polygons [94] and many others [95,96] (Figure C1.4). Bottom-up methods include chemical reduction, microemulsion, laser ablation microwave irradiation and green or biological methods [85]. They can produce homogeneous nanostructures with well-defined crystallographic and surface structures, but they often require reactants that are toxic and can negatively affect biological applications. Overall, however, bottom-up approaches have become the preferred method for syntheses in most nanozyme studies.

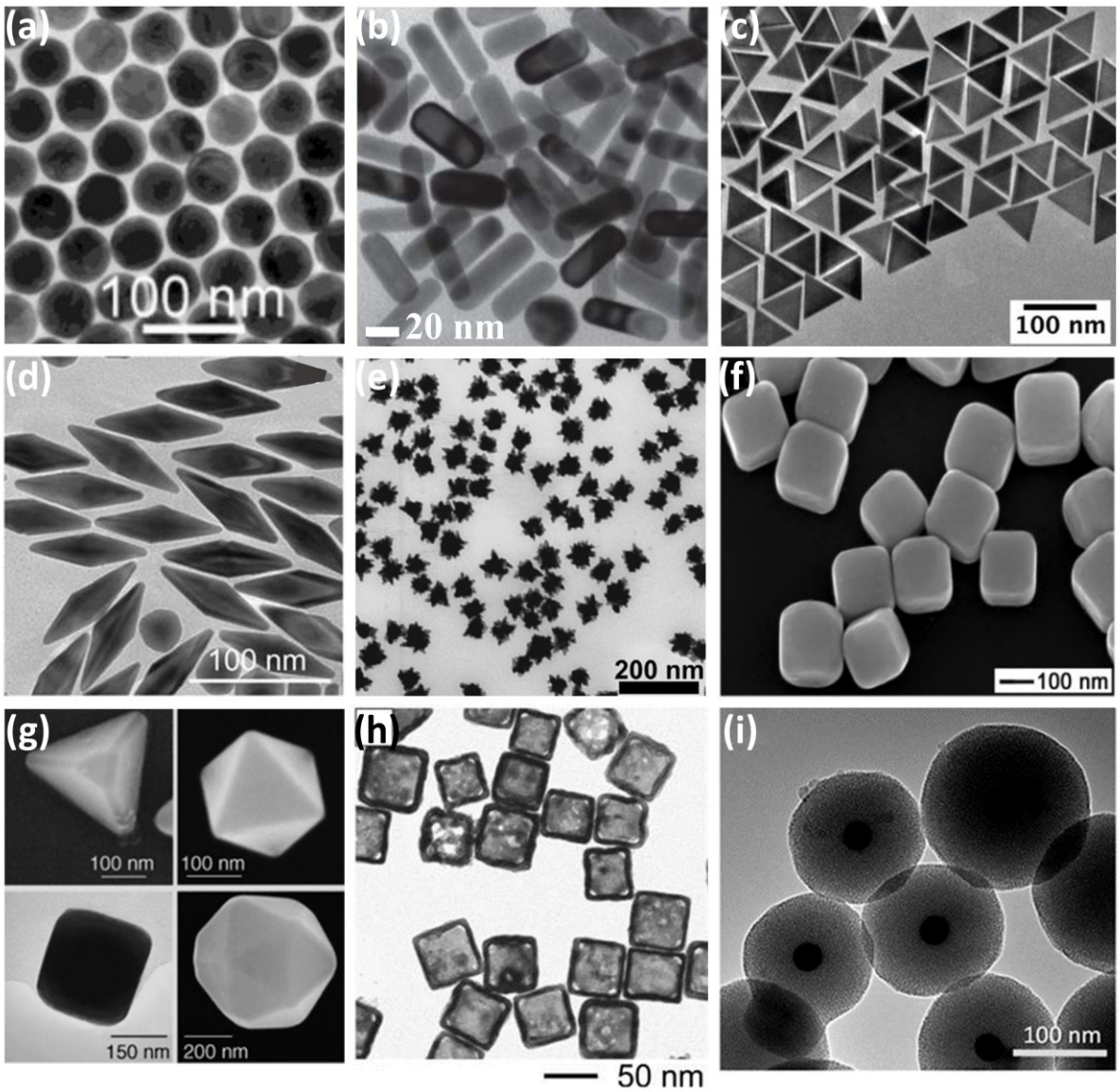

Figure C1. 4 AuNPs synthesised with different shapes following bottom-up approaches: (a) spheres, (b) rods, (c) prisms, (d) bipyramids, (e) stars, (f) cubes, (g) polygon-shaped nanocrystals, (h) cages, (i) gold@silica hybrid nanoparticles. Reproduced from Lou-Franco et al. [97].

1.2.1 Optical properties

From the shinning effects observed in Chinese and Persian artworks in ancient times to the dichroic effect observed in the Lycurgus cup in Roman times, the interaction of light with metallic nanoparticles has long attracted interest. It was not until the middle 1800s that Faraday's investigations followed by Mie's and Maxwell-Garnett's theories started to shed some light on the optical properties behind these visual effects [98]. When metallic nanoparticles are exposed to light, the oscillating electromagnetic field of the light induces a coherent collective oscillation of the conduction band electrons. As the electron cloud is displaced from the nuclei and the particle surface becomes

polarised, a restoring force arises due to Coulomb attraction between the nuclei and the electrons, causing the electron cloud to oscillate in a restricted manner [62,99]. The amplitude of these oscillations reaches a maximum at a specific frequency, which varies depending on the nanostructure size, shape, composition or environment [100]. This phenomenon is known as Localised Surface Plasmon Resonance (LSPR) or surface plasmon, whose location in the electromagnetic spectrum can be visualised as a strong absorption band at the frequency where the incident light is in resonance with the oscillation of the conduction electrons. For isotropic NPs (like spherical NPs) there is only one band in the visible range since their plasmonic properties remain unvaried all along their surface. This is not the case for anisotropic NPs (like nanorods, nanostars, nanoprisms, etc.), where several absorption bands appear due to their asymmetry, which modifies their plasmonic properties in line with the direction from which the incident light interacts with them (Figure C1.5) [101]. Thus, NPs with two different axis lengths will present both longitudinal and transversal LSPR modes [102], corresponding to oscillations along the length and the width of the NP, respectively, and leading to two different absorption peaks.

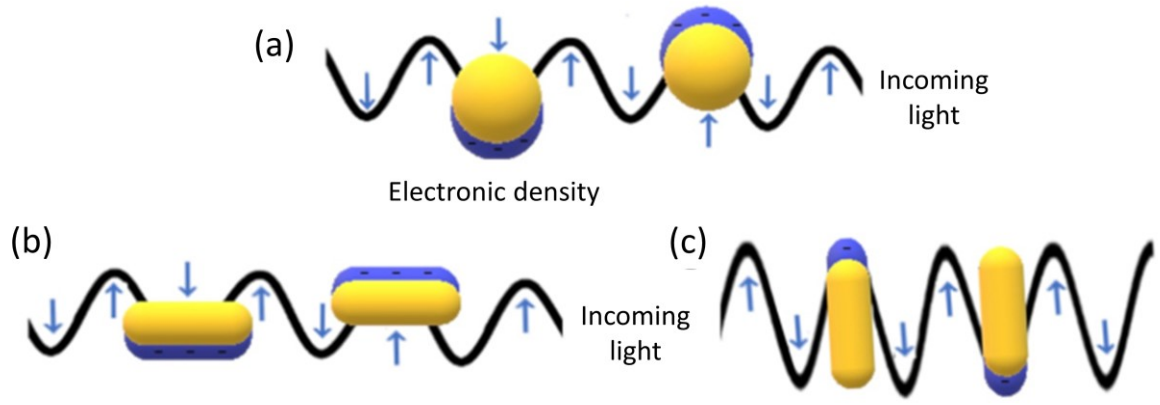

Figure C1. 5 LSPR phenomenon generated by the interaction of incident light with conduction electrons from the surface of non-anisotropic spherical AuNPs (a) or anisotropic rod-shaped AuNPs in their longitudinal mode (b) and transversal mode (c). Reproduced from [101].

This resonant oscillation yields extraordinarily high absorption coefficients and scattering properties while also increases the electromagnetic field at the NP surface, leading to a wide range of properties that are exploited in the biological, chemical and physical fields [60]. The increases in absorption and scattering have been exploited for LSPR biosensing, whereas the increase of the electromagnetic field is used for surface-enhanced Raman spectroscopy (SERS) applications, as it is discussed in Section 1.2.2. LSPR biosensing has some advantages compared to other approaches, including their high sensitivity via detection of refractive index changes, no labelling requirement as sensing mechanism

records spectral shifts due to binding events, good reproducibility and low cost [103]. Many LSPR sensors are therefore described in the literature using gold nanomaterials to detect medical biomarkers in a ultra-sensitive manner [104,105].

Another very interesting and direct example of the LSPR is the photothermal effect. When AuNPs are irradiated at their LSPR, photons are converted into phonons, which lead to a phonon-phonon relaxation and subsequently to an increase in the system temperature and conduction to its surrounding. That is, the energy is released in the environment of the nanostructure as local heat. This phenomenon has already been used for developing thermal sensors [106], applying photothermal therapies in medicine [107] or even imaging applications in diagnostics [108].

1.2.2 Spectroscopic properties

The excitation of surface plasmons produces very strong electromagnetic fields in the NPs surface, thus acting as tinny antennas and leading to signal enhanced properties in many spectroscopic techniques. Among these, Raman spectroscopy [109] or fluorescence spectroscopy [110,111] have already been widely used for developing ultra-sensitive biosensors. The former, Surface-Enhanced Raman Scattering (SERS), is based in the inelastic scattering of photons after interacting with molecules located near the surface of NPs (a distance below 20 – 30 Å) where high electric field intensities (or *hot spots*) are created [112]. The latter, Surface-Enhanced Fluorescence (SEF), requires some spacing between the AuNPs and the fluorophore to avoid fluorescence quenching caused by the energy transfer between the fluorophore and the metal (Figure C1.6). In both SERS and SEF, the highest enhancement is usually reached when there is a good overlap between the excitation source wavelength, the NPs LSPR and the optical properties of the analyte to be measured.

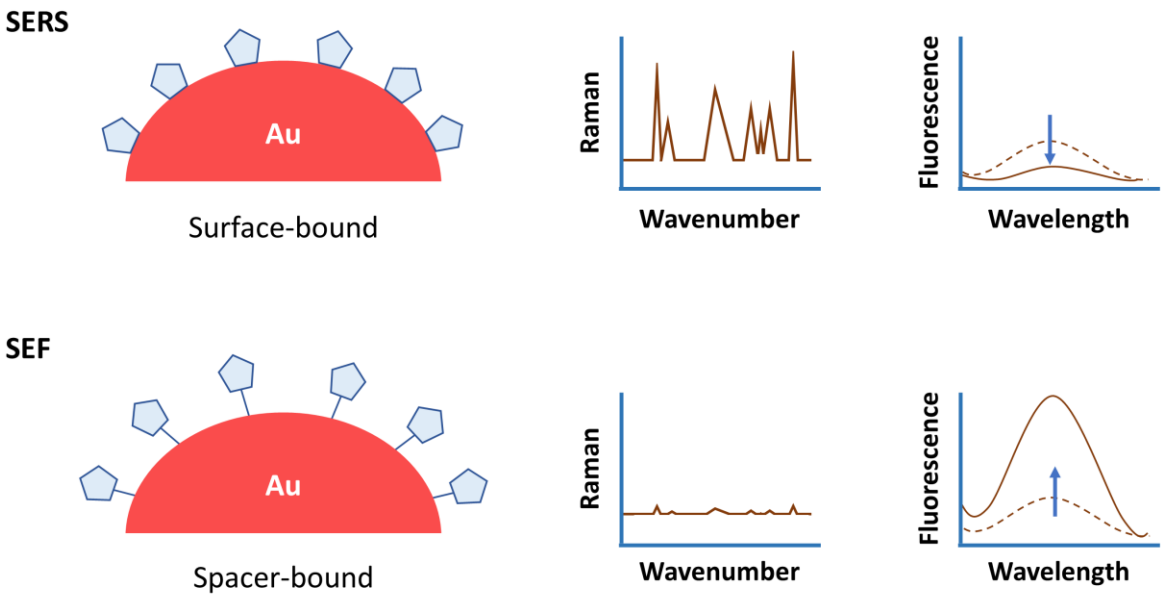

Figure C1. 6 Raman and fluorescence spectroscopy responses depending on the distance AuNP – dye. Preferred SERS (top) and SEF (bottom) configurations to maximise spectroscopic enhancement.

For this work, SERS has been chosen as the approach to use for analyte detection as it does not show the quenching problematic and it offers a wider versatility in terms of multiplexing, while the use of different fluorescent dyes may lead to overlapping signals difficult to distinguish. In this context, a high confinement of the electromagnetic energy has been observed at the junctions between NPs in dimers [113] or clusters [114], creating extremely effective SERS hot spots that have also been reported at the sharp edges or tips of anisotropic NPs [115,116].

1.2.3 Catalytic properties

The presence of an electronically active surface on metallic nanomaterials explains the fact that they behave as catalytic centres, being capable to boost chemical reactions similarly to chemical catalysts or biological enzymes [117,118]. These properties were already observed and reported in AuNPs in the 1970s [119] and 1980s [120,121], when gold colloids were used as catalysts for the oxidation of carbon monoxide and proved that they were much more active and stable than conventional catalysts used at that time. Ever since then, many applications have been explored using the different catalytic activities that AuNPs possess, illustrated in Figure C1.7 (i.e. oxidase [122], glucose oxidase [123,124], peroxidase [125], catalase [126,127], superoxide dismutase [126], and reductase [128]). For this reason, Paolo Scrimin's group coined the term *nanozyme* [129] in analogy to the nomenclature of

catalytic polymers (*synzymes*) previously reported [130]. The same logic followed for the enhancement of spectroscopic properties applies here, as it has been observed that the sharp tips of anisotropic AuNPs (pyramids) provide active sites with high surface energy that help overcoming the activation energy required to oxidise ethanol [131]. Several parameters are known to affect the catalytic properties of AuNPs, like the size, morphology, surface chemistry, functional layers, or even external parameters such as pH or temperature of the surrounding media.

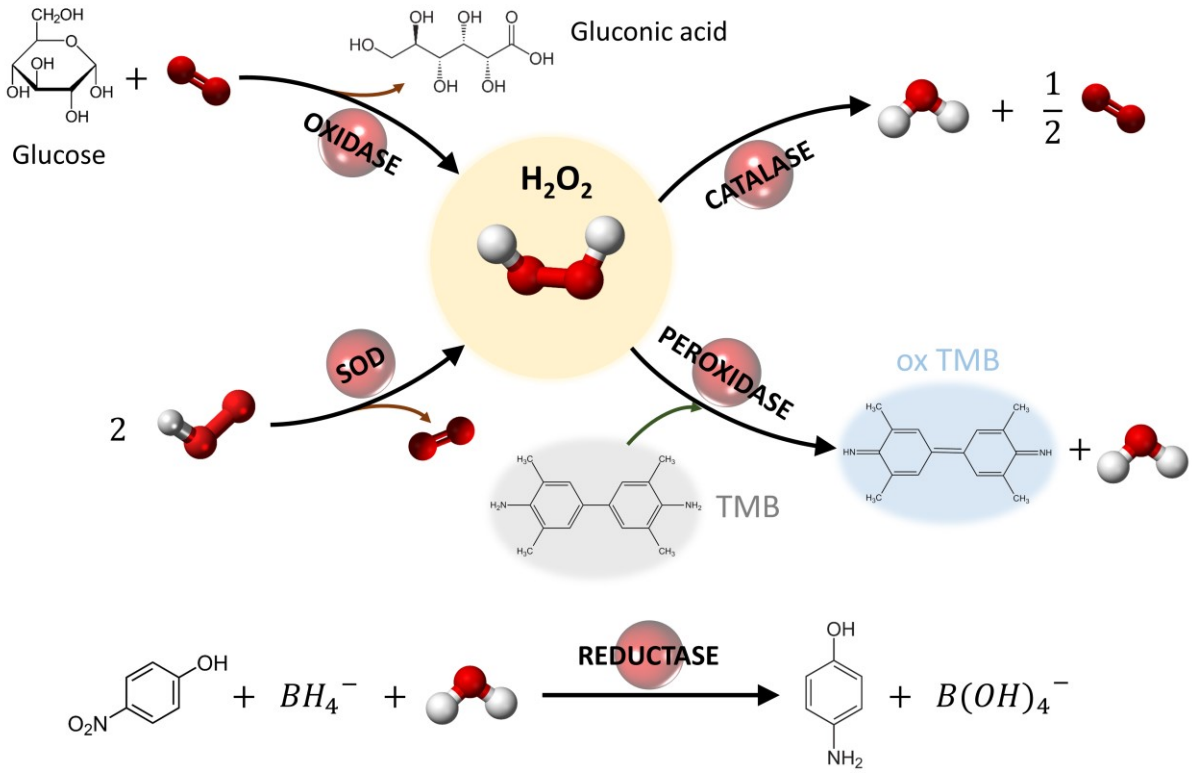

Figure C1. 7 Chemical reactions catalysed by AuNPs. Reproduced from Lou-Franco et al. [97].

1.2.3.1 Size and shape dependence

Low-coordinated gold atoms located at corner sites of the nanomaterial are known to play a major role in the catalytic properties of AuNPs, due to the presence of an electron-rich plane at the interface [132]. As a result, small AuNPs around 2 nm in diameter or a height of six atomic monolayers have been found to be optimum for reactions like the oxidation of CO [133], since they have a high proportion of exposed atoms. However, the shape of the NP also plays an important role and previous studies suggest that higher surface-to-volume ratios lead to enhanced catalytic properties [134] (Figure C1.8a).

1.2.3.2 pH and temperature dependence

Similar to biological enzymes, the nanozyme activity is also controlled by the pH and temperature of the surrounding media. This way, 3,3',5,5'-tetramethylbenzidine (TMB) oxidation catalysed by AuNPs happens at an optimum rate at pH values between 3.5 – 4 and temperatures between 40 – 50 ˚C [135,136], being these conditions dependent on the substrate. Moreover, some studies have reported that differences in the pH of the media can cause AuNPs to switch their catalytic functionality, boosting their peroxidase-like activity or catalase-like activity depending on this parameter [137]. The temperature, on the other hand, not only affects the reaction rate, but also can induce thermodynamic transitions in the stabilising layer of AuNPs that alters the 3-dimensional structure of the NP surface, therefore hindering or boosting the substrate diffusion and the reaction rate [138].

1.2.3.3 Surface nature dependence

Finally, since the nanozyme activity is a surface phenomenon, any chemical or physical modification at the interface also affects the catalytic properties of AuNPs. Many studies have therefore proved that the peroxidase-like activity of unmodified AuNPs is significantly reduced when these are amino-modified or citrate-capped [139] (Figure C1.8b).

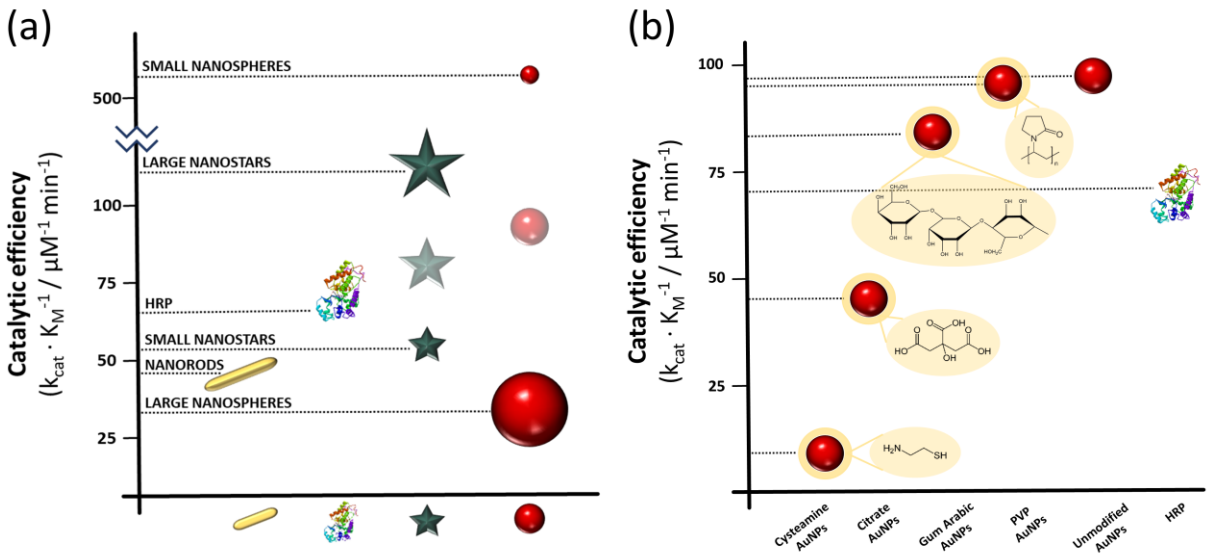

Figure C1. 8 (a) Comparison of the peroxidase-like activity of different shaped and sized AuNPs using TMB substrate. (b) Comparison of the peroxidase-like activity of AuNPs stabilised with different coating layers. Reproduced from Lou-Franco et al. [97].

1.2.4 Applications & Smartphone readout systems

All these properties, either optical, spectroscopic or catalytic, have opened a wide range of possibilities regarding potential applications. Among these we can highlight biomedical applications, which include diagnosis and analytical sensors, drug delivery, photodynamic therapy, gene therapy or imaging. Beyond the biomedical field, applications in catalysis, water remediation, nanoelectronics or non linear optics have also been developed [60]. In this project, AuNPs have been studied and exploited in relation to their potential to improve diagnostic devices for biosensing applications. Specifically, using their nanozyme and spectroscopic enhanced activities. On the other hand, smartphones have become an important ally for portable data processing and user-friendly analysis thanks to the rapid development of their platforms, existing nowadays almost 4 billion smartphone users spread all over the globe (Statista, 2021). In addition, they are all equipped with a camera that provides the perfect tool for *in situ* colourimetric analyses. As a result, many examples of new biosensors can be found using smartphones to quantify colourimetric signals [140–142] or fluorescent signals [143], among others, existing as well a wide review of the field [144,145].

The work presented in this thesis will thus revolve around the application of AuNPs to generate colourimetric signals in a proportional manner to the concentration of the target analyte (food contaminant in this case) and the application of smartphones to quantify said signal using their camera, aiming to develop fully portable sensing devices.

1.3 Gold nanozymes – a review

The section herein presented consists in a comprehensive study of the biomedical, environmental and food safety related applications of gold nanozymes. It represents a section of the work published as a review article (Javier Lou-Franco, Bhaskar Das, Christopher Elliott and Cuong Cao. "Gold Nanozymes: From Concept to Biomedical Applications." *Nano-Micro Letters* 13, no. 1 (2021): 1-36.). This work falls under the scope of the first thesis aim (listed in Section 1.4) “Prepare an updated review on the fundamentals of gold nanozymes and their application in the biomedical field”.

1.3.1 Abstract

In recent years, gold nanoparticles have demonstrated excellent enzyme-mimicking activities which resemble those of peroxidase, oxidase, catalase, superoxide dismutase or reductase. This, merged with their ease of synthesis, tunability, biocompatibility and low cost, makes them excellent candidates when compared with biological enzymes for applications in biomedicine or biochemical analyses. Herein, over 200 research papers have been systematically reviewed to present the recent progress on the fundamentals of gold nanozymes and their potential applications. The review reveals that the morphology and surface chemistry of the nanoparticles play an important role in their catalytic properties, as well as external parameters such as pH or temperature. Yet, real applications often require specific biorecognition elements to be immobilized onto the nanozymes, leading to unexpected positive or negative effects on their activity. Thus, rational design of efficient nanozymes remains a challenge of paramount importance. Different implementation paths have already been explored, including the application of peroxidase-like nanozymes for the development of clinical diagnostics or the regulation of oxidative stress within cells via their catalase and superoxide dismutase activities. The review also indicates that it is essential to understand how external parameters may boost or inhibit each of these activities, as more than one of them could coexist. Likewise, further toxicity studies are required to ensure the applicability of gold nanozymes *in vivo*. Current challenges and future prospects of gold nanozymes are discussed in this review, whose significance can be anticipated in a diverse range of fields beyond biomedicine, such as food safety, environmental analyses or the chemical industry.

1.3.2 Biomedical applications of gold nanozymes

The most successful applications of gold nanomaterials in biomedicine relate to their use as visible optical indicators incorporated in lateral flow assays, i.e., the underlying technology used in pregnancy tests. With the discovery of the many nanozyme properties, a new path was unlocked, leading to a wide range of biomedical applications hitherto unexplored. Considering the little information reported so far *in vivo* for nanoparticles toxicity and distribution, it is not surprising that most applications are related to diagnostics *ex vivo*, which are reviewed in this section.

1.3.2.1 Biosensing and biosensors development: clinical diagnostics

For many diseases and physiological conditions such as cancer, diabetes or neurodegeneration, the best cure is an early detection that could be achieved by the implementation of biosensors [146–148]. Many diagnostic tools have already become part of our lives: pregnancy or glucose tests can be bought in pharmacies, whereas antidoping, legal highs or explosive tests are commonly carried out in police controls or at immigration ports. Many other forms of biosensors are being developed and soon will be as common as the previous ones (e.g., detection of clinically important biomarkers such as creatinine and phenylalanine or monitoring of environmental pollutants) [149]. Ever since AuNPs were discovered to possess peroxidase-mimicking activity, they have been used as signal transducers capable to generate a colourimetric signal. Despite the fact that they can catalyse for various substrates such as TMB, 2,2'-azino-bis(3-ethylbenzothiazoline-6-sulphonic acid) (ABTS) or o-phenylenediamine (OPD) [139,150], gold nanomaterials have mostly been applied for the oxidization of TMB, a substrate catalysed by HRP widely used in immunological assays (i.e., ELISA). Many examples can be found in the literature for sensors applied in biomedicine that use the peroxidase-like activity of gold nanomaterials to oxidize TMB and generate a colourimetric signal [151–157]. Due to the ease of surface modification with specific ligands, gold nanomaterials could allow the development of these diagnostic tools for diverse targets, such as viruses [154–156], exosomes [158], red blood cells [152], amino acids or even ions [151]. Apart from coloured products, gold nanozymes can catalyse for the conversion of different substrates into fluorescent, luminescent or Raman active products. Alternatively, some systems use the electrons produced in the reaction to develop electrochemical sensors. All these possibilities are discussed in this section. Hybrid systems based on Au with other nanomaterials could lead to an enhanced catalysis. The applicability of this phenomenon in the biosensor field was first reported by Liu et al., who described the synergism between catalytic active graphene and AuNPs to detect specific DNA molecules (Figure C1.9a) [159]. A similar strategy was followed by Ahmed and co-workers, who immobilized AuNPs on the surface of carbon nanotubes to

enhance the peroxidase-like activity of the resulting nanohybrid, which developed a more intense colour in less time. This system (Figure C1.9b) could effectively detect influenza virus A (H3N2) in human serum with a sensitivity of 3.4 PFU mL^{-1} (i.e., plaque-forming units per mL) [156], 100 times higher than reported conventional ELISA assays and 500 times higher than commercial immunochromatography kits (ImunoAce Flu, TAUNS Laboratories, Inc., Numazu, Shizuoka, Japan). These synergistic effects for oxidizing TMB were also observed with Au–Pt core/shell nanorods for detection of measles virus (Figure C1.9c) [154]. Furthermore, Oh et al. [155] developed a different sensor including a capturing step with magnetic nanoparticles for the detection of influenza virus A (H1N1) in human serum (Figure C1.9d). Following this approach, a similar limit of detection (LOD) was observed without making use of synergistic catalytic effects. Several studies have attempted to explain the mechanism by which the synergistic effect occurs. Liu et al. [159] proposed that the attractive interaction between carbon 2p (from reduced graphene) and Au 5d (from AuNP) orbitals around the carbon vacancy and defect would explain not only the strong covalent interfacing, but also the observed favourable H_2O_2 adsorption, thus enhancing its reduction. Similar charge transfer mechanisms have been proposed to explain this synergism in bimetallic nanoparticles [160].

Due to their simplicity and unnecessity of laboratory-based requirements, all these systems have a clear potential to become portable sensors and to be applied for point-of-care (POC) diagnostics. A good example has been developed by Wu et al. (Figure C1.9e) to detect occult blood in urine, commonly linked to a serious health condition such as chronic nephrotic syndrome or urinary system tumours. It consists of a flexible container with two tiny containers inside it, one with TMB and H_2O_2 reagents for the colourimetric reaction and the other with buffered AuNPs. After adding the urine sample to the flexible tube this is bended to break the tiny containers inside and develop the colourimetric reaction only in the presence of Fe^{2+} ions, which restore the peroxidase-like activity of AuNP capped with a purine derivative, otherwise remaining inactive. This system permits to detect either haemoglobin or red blood cells presence in urine due to their high content in Fe^{2+}, by using a colour chart that enables a fast and visual detection [152]. This system, however, remains qualitative, providing a semi-quantitative estimation in the best-case scenario. This limitation could be circumvented using a smartphone camera, which would permit to quantify the colour intensity by means of a calibration curve previously built. It is curious to see that, to date, only one publication [161] is obtained when the terms “gold nanozyme” AND “smartphone” are searched in Scopus database. The proposed method to detect mercury ions in environmental water samples is further discussed in Section 1.3.3.1.

Gold nanozymes are used for the development of not only colourimetric sensors but also electrochemical detection platforms. The electrochemical approaches have been shown to have great

repeatability, accuracy and robustness, while advancements in miniaturization have made the design of portable and quantitative sensors possible. Boriachek et al. [158] used gold-loaded ferric oxide nanocubes functionalized with an exosome-associated antibody to allow magnetic isolation of the captured target, whereas the peroxidase-like activity of the encapsulated AuNPs could generate a colourimetric signal. Abreast of the colourimetric output, the reaction happened on a screen-printed carbon electrode; therefore, the electroactive diimine generated during the TMB oxidation process [162] could also be quantified through chronoamperometry (Figure C1.9f). In the same line, other research groups have used screen-printed gold electrodes modified with aptamers specific for cardiac troponin I, a well-known standard biomarker for the early detection of Acute Myocardial Infarction [163]. This system uses bimetallic Cu@Au nanozymes (capable of oxidizing hydroquinone to benzoquinone) immobilized on magnetic metal organic framework nanocatalysts. Similar to other synergistic effects described above, the outstanding catalytic activity of the resulting nanohybrid allows highly sensitive detection through differential pulse voltammetry.

Finally, gold nanozymes can also be harnessed in other sensing approaches based on fluorimetry and spectroscopy for the detection of urinary spermine [164], HIV and HCV [165] or dopamine [166] (Figure C1.9g). Due to complicated optical components required, the spectroscopic methods often lack portability; thus, their development and practical implementations are more limited. In case of SERS-based systems, Hu et al. developed a system that uses the peroxidase activity of AuNPs to detect the lactate and glucose levels in living rats' brains, which are associated with ischaemic stroke. While there are some portable Raman spectrometers available on the market (such as QE Pro-Raman by Ocean Insight or TruScan™ GP analyser by ThermoFisher), there is still a long way for engineering and optimizing the systems for POC diagnostics.

Together with a vast range of approaches for surface modifications and bioconjugations, it is evident that enzyme-mimicking activities of AuNPs and Au nanohybrid structures can allow versatile biosensor platforms generating either a colourimetric, electrochemical, fluorescent or spectroscopic measurable signal. As it is a new field, only a few examples have been described in the literature regarding gold nanozymes applied for clinical biosensors used in real samples. A summary is presented in Table C1.1.

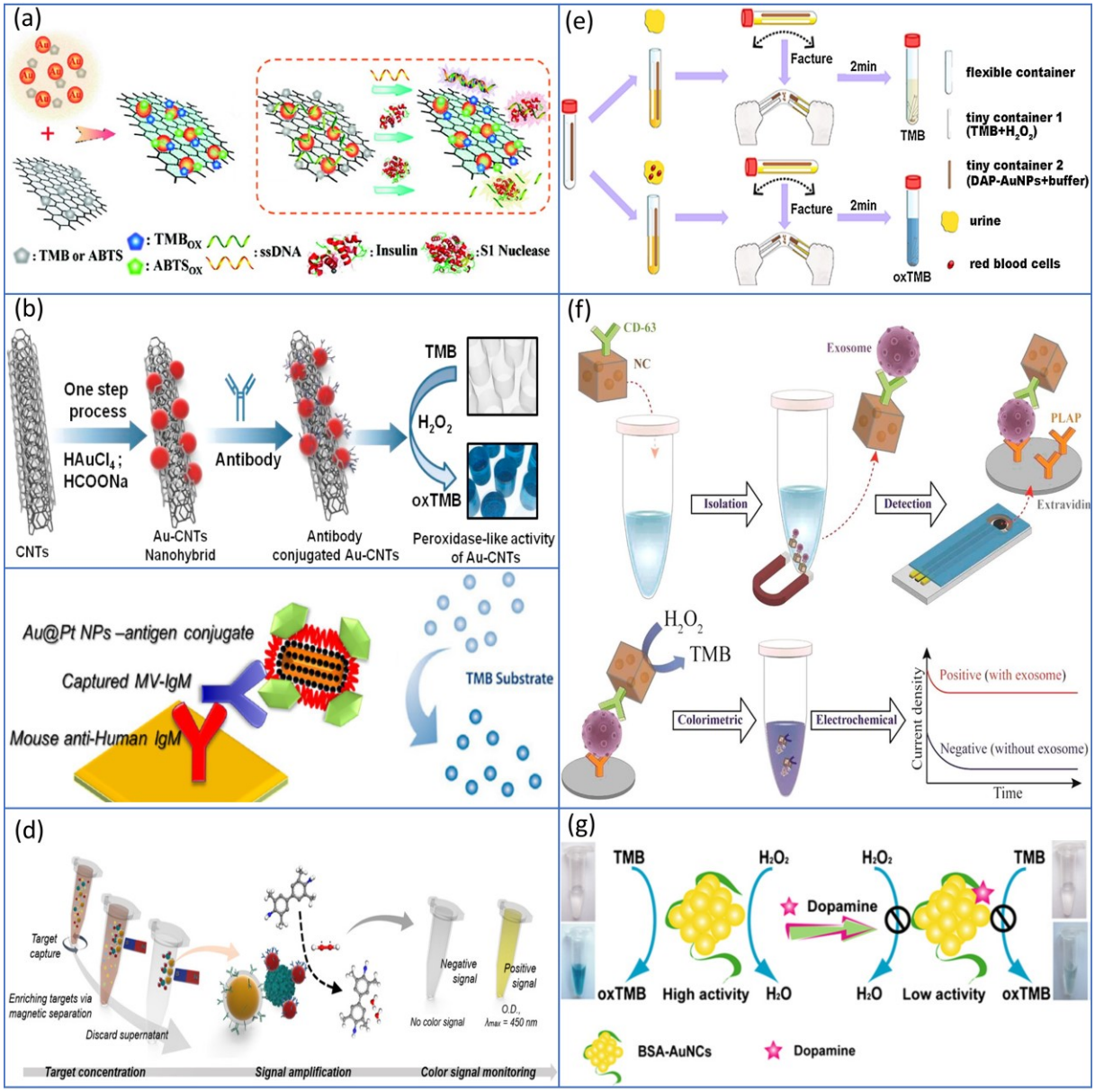

Figure C1. 9 Peroxidase-like activity of AuNPs used as clinical diagnostic tools. (a) AuNPs grown on graphene sheets used to develop a "off-on" colourimetric sensor [159]. (b) Nanohybrid composed of AuNPs and CNTs acting as colourimetric influenza virus detection [156]. (c) Rod-shaped Au-Pt core/shell NPs used for measles virus detection [154]. (d) Magnetic nanobeads combined with AuNPs for separation and detection of influenza virus [155]. (e) User-friendly device for hemoglobin and red blood cells detection in urine samples [152]. (f) Gold-loaded nanoporous ferric oxide NPs used for direct exosome detection [158]. (g) Fluorometric and colourimetric detection of dopamine based on AuNCs [166]. Reproduced from Lou-Franco et al. [97].

Target	Nanomaterial	Activity	Outputs	Sample	LOD	Ref
Hemoglobin & red blood cells	AuNPs	Peroxidase	Colourimetric	Human urine	0.96 nM & $1.6 \cdot 10^6$ cells/L	[152]
Heparine & heparinase	Gold nanoclusters	Peroxidase	Colourimetric	Diluted serum	0.3 & 0.06 µg/mL	[167]
Cu^{2+} & histidine	Gold nanoclusters	Peroxidase	Colourimetric	Human serum, blood	0.1 nM & 20 nM	[151]
Pseudomonas aeruginosa	AuNPs	Peroxidase	Electrochemical	Drinking water	60 CFU/mL	[168]
Placental cell-derived exosomes	Au-loaded Fe_2O_3 nanocubes	Peroxidase	Colourimetric, electrochemical	Cell culture media	$8 \cdot 10^6$ vesicles per million cells per 24 h (10^3 exosomes/mL)	[158]
Spermine	Ag-Au bimetallic NPs	Oxidase & Peroxidase	Fluorescence	Urine	0.87 nM	[164]
Rubella virus (IgM antibodies)	Au-Pt core/shell nanorods	Peroxidase	Spectroscopic, colourimetric	Human serum	10 ng/mL	[169]
Cysteine & homocysteine	Au-Pt NPs	Peroxidase	Spectroscopic, colourimetric	Human serum	3.5 & 1.6 nM	[153]
Measles virus (IgM antibodies)	Au-Pt core/shell nanorods	Peroxidase	Spectroscopic	Human serum	10 ng/mL	[154]
Influenza virus A (H1N1, H3N2)	AuNPs and magnetic nanobeads	Peroxidase	Spectroscopic, colourimetric	Spiked samples & human serum	$4.42 \cdot 10^{-14}$ g/mL & 2.5 PFU/mL	[155]
Cocaine	Multi-shaped AuNPs and ZnSeS alloyed quantum dots	Peroxidase	Spectroscopic	KCl-HCl buffer	112 nM	[170]

HIV & HCV DNA	Pt-Au bimetallic NPs	Oxidase	Fluorescence	Buffer	5 pM	[165]
Glucose & lactate	AuNPs@MOF	Peroxidase & Oxidase	SERS	Living rats' brain	4.2 & 5 µM	[171]
Murine norovirus	AuNPs	Peroxidase	Colourimetric	Human serum, shellfish homogenate	200 PFU/mL	[172]
Dopamine	Au nanoclusters	Peroxidase	Fluorescence, colourimetric	PC12 cells	10 nM	[166]
Xanthine	Au nanoclusters	Peroxidase	Spectroscopic	Urine & serum	20 nM	[173]
Influenza virus A (H3N2)	AuNPs – CNT hybrid	Peroxidase	Spectroscopic, colourimetric	Human serum	3.4 PFU/mL (10 PFU/mL in real samples)	[156]

Table C1. 1 Clinical biosensors exploiting the catalytic properties of AuNPs.

1.3.2.2 ROS generation

Gold nanozymes are not only applied for sensing devices, they can also be used as drug agents for therapeutics. This application has been mainly linked but not limited to small AuNPs (less than 2 nm in size), which are capable of penetrating the cells and cellular compartments and cause cytotoxicity (necrosis) by means of oxidative stress [61]. Thus, nanozymes with peroxidase-mimicking activity can catalyse the hydrogen peroxide decomposition and produce ROS [174–176]. The induced toxicity has been mainly used for tumour treatment, by first directing the nanoparticles to the targeted area and then enhancing their catalytic properties through photodynamic therapy (PDT). Despite not being a perfect photoregulation system, with clear on/off states, this approach can help reduce the off-target tissue effects. This is a common issue with many drugs being used nowadays, which reach different parts of the body and cause a non-desired effect referred to as a side effect of said drug [177]. Therefore, different nanocomplexes can be introduced in the body through the preferred administration via and after they are accumulated in the area of interest, the ROS generation process can be improved. This approach requires a smaller nanomaterial concentration to produce the same effect than the non-enhanced system, thus decreasing the drug concentration that needs to be administrated and the side effects caused by ROS generation elsewhere. However, very important external parameters govern nanozyme activities. Not only controllable parameters such as size, shape or nanoparticle surface modification, but also some others determined by the biological matrix, such as pH, temperature or the presence of interfering molecules [178]. Therefore, it becomes very important to understand the tumour microenvironment if gold nanozyme properties are to be used for a clinical treatment. Well-known characteristics such as acidity [179], hypoxia [180] and abnormally high concentrations of H_2O_2 [181,182] in the affected area are a common denominator of the disease.

Conventional PDT involves light and a photosensitizing chemical substance, which combined with molecular oxygen, leads to phototoxicity. A recent approach used platinum nanoparticles (PtNPs) decorated on photosensitizer integrated metal–organic frameworks for enhanced PDT [183]. The nanoplatform successfully used the catalase-like activity of PtNPs to convert the abundant H_2O_2 in the tumour region into O^2, thus modifying the hypoxic environment and facilitating the light-irradiated formation of cytotoxic $^1O_2$. This was the first study that exploited the nanozyme activity of metallic NPs to achieve an enhanced PDT. Different gold nanozymes have been combined with PDT ever since, paving the way for a new promising approach entirely to explore. Moreover, any laser wavelength within the therapeutic window (i.e., 650-1350 nm) can be used for this enhancement purpose, being one or another more convenient depending on the absorption profile of the nanocomplex being used. This way, 808-nm light irradiation has been used to improve the ROS generation of AuNPs embedded in porous hollow carbon shell nanospheres [174,184], whereas other studies have used 660-nm

irradiation to increase the method efficiency with AuNPs embedded in a zeolitic imidazolate framework [185] or 671 nm wavelength for hollow mesoporous organosilica nanoparticles containing AuNPs [186]. Interestingly, different nanomaterial combinations have been used, leading to different paths for generating ROS in which AuNPs can take diverse roles. Fan et al. pioneered the application of AuNPs for thermal cancer therapy combined with nanozyme activity. They encapsulated AuNPs in hollow carbon shell nanospheres and showed that, under an acidic environment, they retained the ability of ROS generation. More importantly, this process could be photoenhanced by the 808-nm laser irradiation, substantially inhibiting CT26 tumour growth in vivo [174]. This capability of ROS generation by AuNPs was confirmed by Zhang et al., who delved into the matter by using mesoporous carbon nanospheres doped with AuNPs as a drug delivery system. This nanocomplex was loaded with dye IR780 to enhance the photothermal therapy, so that when the tumour tissue was irradiated with the 808-nm laser it would also generate heat, thus further enhancing the photothermal therapy. Together with the nanozyme properties of AuNPs to decompose H_2O_2 located in the tumour cells to $^{\cdot}OH$ and cause intracellular oxidative damage, this synergistic strategy has demonstrated favourable results as a therapy for folate-overexpressed gastric cancer tumours [184]. Many others [187,188] came simultaneously to a conclusive consensus: the combination of photodynamic and photothermal therapies provides a novel approach with excellent synergistic therapeutic outcomes (Figure C1.10a). However, some other tumour treatments take advantage of different gold nanozyme properties (Figure C1.10b), either using their glucose oxidase activity [186,189] or their catalase activity [185] to alleviate the pernicious effects. The former system used a nanocarrier loaded with collagenase to degrade the collagen I fibre in the extracellular matrix and enhance the penetration of the system and O_2 infiltration, AuNPs capable of oxidizing glucose and generate H_2O_2 as a by-product and copper-based complexes to generate ROS. The latter addressed tumour hypoxia through the catalase-like activity observed in AuNPs, which takes advantage of the abundance of H_2O_2 in tumour areas to generate O_2 that can be used by a photosensitizer to increase ROS levels. It is interesting to note that while different nanozyme activities derived from the same AuNPs can be boosted or inhibited, it is just likely that they coexist up to some points. Again, the microenvironment and the surface properties of the nanocomplex will play a crucial role in this sense. No studies have been found, however, clarifying whether these synergistic effects have any impact in the final outcomes for tumour treatment.

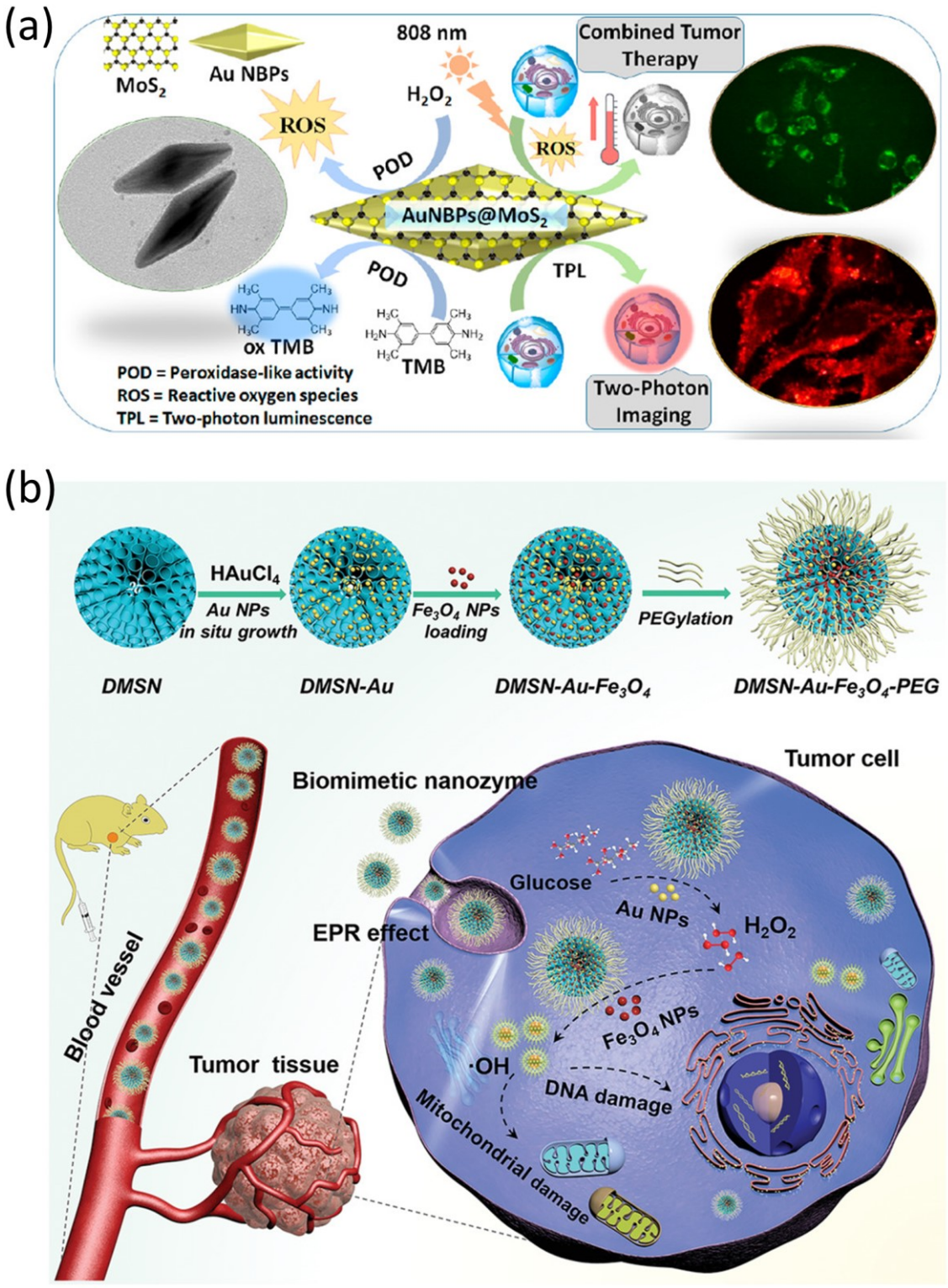

Figure C1. 10 Gold nanozymes applied for tumour therapy. (a) Peroxidase-like activity is combined with photodynamic and photothermal therapies for tumour imaging and localised treatment [187]. (b) Various enzymatic activities are combined to generate ROS inside the cell after directing the NPs to the affected tissue [189]. Reproduced from Lou-Franco et al. [97].

Likewise, ROS generation has also been used for bacterial inactivation and wound disinfection [122,190]. Qu and co-workers first reported that AuNPs embedded in mesoporous silica (MSN-AuNPs) could act as oxidase mimics [122] and were capable of generating ROS that led to antibacterial activity. This approach showed that MSN-AuNPs served as efficient and safe antibacterial agents even in the absence of H_2O_2, a powerful oxidizer which in high concentrations harms healthy tissues and delays wound healing. Microscopic analyses of *Staphylococcus aureus* and *Escherichia coli* showed that ROS generated by MSN-AuNPs could oxidize and destroy the bacterial lipid membranes, thus inhibiting the growth of both Gram-positive and Gram-negative bacteria. Further applications of MSN-AuNPs using *Bacillus subtilis* biofilms were investigated, whose antibacterial activity also resulted in an effective breakdown of existing biofilms and prevention of new biofilm formation. This was followed by a similar study, using AuNPs with ultrathin graphitic carbon nitride to take advantage of their synergistic effect and catalyse the decomposition of H_2O_2 to $^{\cdot}OH$ radicals in an efficient manner [190]. Importantly, the mentioned synergism enables to use lower concentrations of H_2O_2 to reach the required antibacterial activity, thus avoiding the side effects mentioned above. This system has been applied for bacteria killing, biofilm degradation, wound disinfection and lung infection treatment. In vitro experiments showed the nanocomplex to have bactericidal activity against both Gram-negative and Gram-positive bacteria, as well as high efficiency in breaking down biofilms and preventing new ones to be formed. These approaches provide a novel alternative to tackle the growing healthy issue caused by persistent infections [191].

In addition to the applications described, AuNPs have also been used in conjunction with α-FeOOH/porous carbon as biomimetic catalyst for Fenton reaction [192]. The proposed system used the glucose oxidase activity of AuNPs to generate gluconic acid, which helps to adjust the microenvironmental pH to promote the Fenton reaction and H_2O_2 to induce its reaction with Fe^{2+}, thus generating $^{\cdot}OH$ radicals. This reaction has many applications, especially for organic wastewater treatment [193], as the ROS formed can quickly and non-selectively degrade most organic pollutants to CO_2 and H_2O. Correspondingly, any novelty that improves its yield could have a direct application in different sectors of the environmental field.

1.3.2.3 Cell protection

Interestingly, AuNPs could also be used for ROS protective effects [194–197]. It might seem contradictory to what has just been explained, but as mentioned before, the nanozyme activity of AuNPs can be tuned or modulated depending on the surface chemistry of the nanoparticle or the microenvironment in which they are being used. This duality has been exploited to develop

antioxidant nanocomplexes for protecting certain tissues from harmful effects caused by a high ROS presence. This is important since ROS, which are known to be involved in the regulation of gene expression and cell signalling cascades, can cause serious damage within biological systems of the human body if present at high concentrations [198]. For instance, a build-up of ROS within the body can induce an inflammatory-type response leading to diseases such as chronic obstructive pulmonary disease (COPD) [199]. Additionally, brain tissue damage and central nervous system-related disorders are associated with ROS, being the attenuation of oxidative stress a promising strategy to prevent conditions such as Parkinson, Alzheimer or amyotrophic lateral sclerosis [200,201]. Most approaches propose to use antioxidant enzymes to revert this situation, but their delivery to the brain has shown major challenges, including proteolytic degradation, immunogenicity, short circulation half-time and poor permeability across the blood–brain barrier [200]. All these drawbacks open the way for alternative strategies using enzyme mimetic AuNPs as ROS scavengers.

Kunjiappan et al. [194] reported on these applications by using biologically synthesised AuNPs from *Azolla microphylla* extracts as antioxidant and hepatoprotective tools. This in vitro study compared the cell viability (among other parameters) of primary hepatocytes treated with acetaminophen (APAP) in the presence and absence of AuNPs. The study concluded that AuNPs presented antioxidant and hepatoprotective effects in APAP-treated hepatocytes by inhibiting ROS generation, scavenging free radicals and increasing the antioxidant defence enzymes. However, this empirical study did not prove the mechanisms underlying the effects observed and lacked some in vivo experiments to prove its applicability.

On the basis of previous works using iron oxide NPs [202] and platinum NPs [203], it had been observed that several nanozymes exhibited pH-switchable catalase-like and peroxidase-like activities. This effect was later demonstrated in other metallic NPs, such as gold and silver [137], being the adsorption energy between the metals and H_2O_2 the key aspect to favour one or the other reaction. Since the adsorption process is affected by the pH of the media, this explains the pH-switchable activity empirically observed. It is based on this knowledge that Liu et al. published their work to shed some light on how to circumvent the pH dependence by simply modifying the NP surface. They discovered that gold nanoclusters (AuNCs) deprived of their peroxidase-like activity while retaining their catalase- like activity under different pH values if modified with amine-terminated poly(amidoamine) (PAMAM). It was suggested that 3°-amines on the surface of the NP provided sufficient suppression of the critical mediator $^{\cdot}OH$ [196]. This system was used as a primary neuronal protection against oxidative damage (Figure C1.11a), after demonstrating that mice neurons did internalize the AuNCs by endocytosis and that these neurons showed a significantly higher survival rate when treated with H_2O_2. Other approaches have used a light-mediated modulation system to

control ROS levels in living cells, giving rise to smart nanozymes (Figure C1.11b). This was achieved by encapsulating AuNPs in azobenzene (Azo) decorated mesoporous silica NP. Under visible light, cyclodextrin (CD) interacts with Azo through host–guest chemistry, blocking the catalytic sites of the nanocomplex and inhibiting its catalase-like activity at neutral pH conditions. However, UV illumination causes an isomerization of Azo to its cis conformation, resulting in CD being released from the system and recovering the catalase-like activity to become an effective ROS scavenger [195]. This turn on/off system was tested in MCF-7 cells, whose viability was modified at will depending on the light exposure. It is noteworthy that this system has some limitations, such as a relatively low nanozyme activity in the experimental conditions or low tissue penetration capacity of UV light. This approach resembles the PDT treatments before mentioned, arguably going a step further in terms of distinction between the two possible states. Be this as it may, there is no doubt that all these systems have paved the way for a whole new generation of smart nanozymes. Countless benefits may derive from these protective effects, not only for health purposes, but also for any process involving cell viability, such as in vitro fertilization (IVF). Dashtestani et al. [197] developed apoferritin-containing gold–silver NP to be used as ROS scavengers. The nanozyme showed both SOD- and catalase-like activity, thus decomposing superoxide ions to hydrogen peroxide, which subsequently is converted into water and molecular oxygen. This nanozyme was examined as a protective agent during the cryopreservation of human sperm, to control the freeze–thaw induced oxidative stress. The results showed a significant increase in the sperm motility and viability, being both parameters essential for sperm–egg fusion and fertilization.

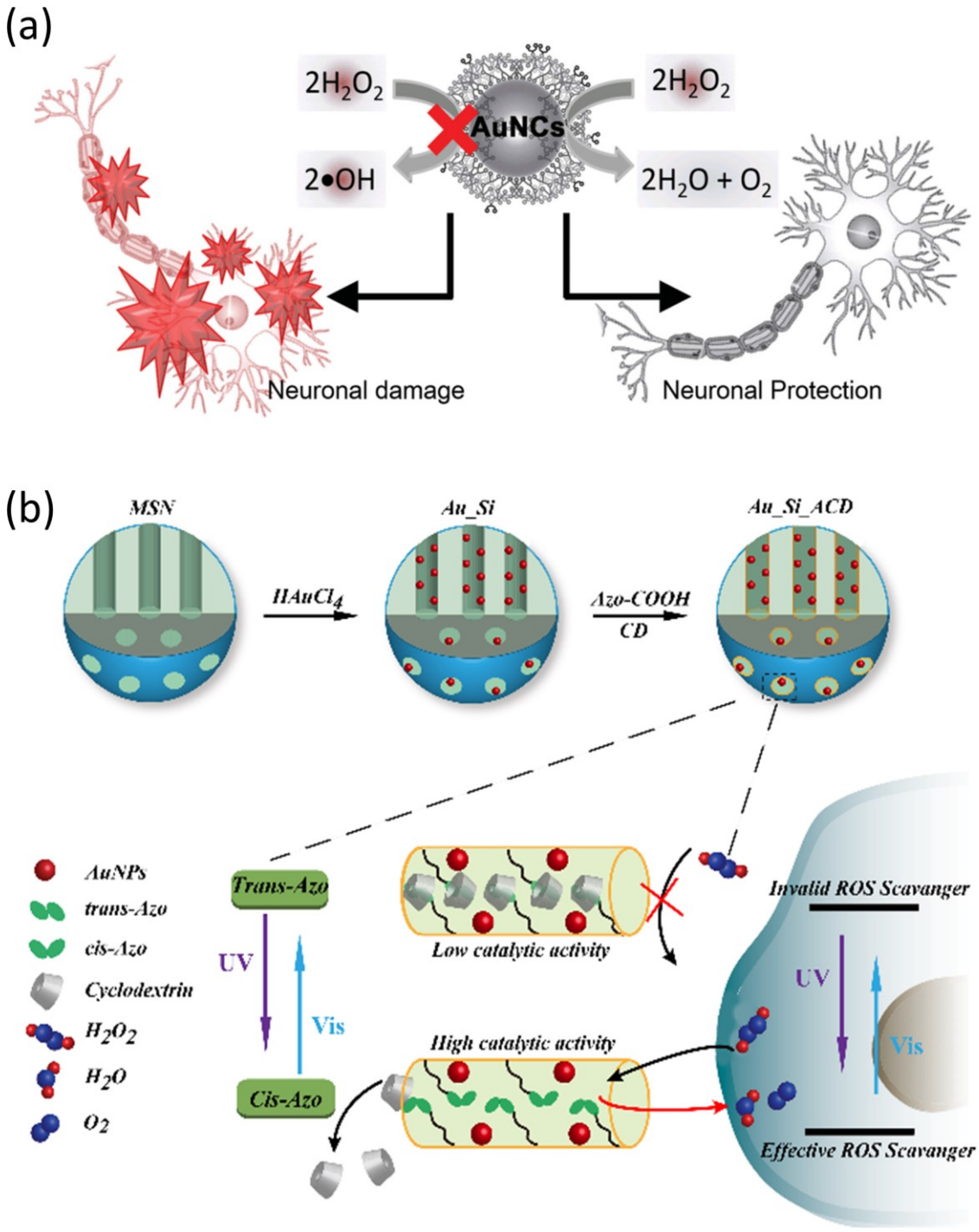

Figure C1. 11 Gold nanozymes used as ROS scavengers for cell protection. (a) Catalase-like activity of amine-terminated dendrimer-entrapped AuNCs used for neuronal protection against oxidative damage [196]. (b) Light mediated reversible modulation of ROS levels using mesoporous NPs loaded with AuNPs [195]. Reproduced from Lou-Franco et al. [97].

1.3.3 Other applications of gold nanozymes

Different options have been discussed throughout the review related to treating or diagnosing a certain biomedical condition. Conversely, little importance is often given to other matters that threaten our health in an indirect manner, such as environmental or food contamination. As a result, these conditions tend to fall by the wayside and only sporadic food- or water-related outbreaks remind us the potential risks of not diagnosing a disease in our environment. Fortunately, there is a high awareness of this within the scientific community, as our group previously reported in a comprehensive and interactive platform that reported over 900 sensors retrieved from the scientific literature and commercial market for aquatic toxins, mycotoxins, pesticides and micro-organism detection [204]. Furthermore, the catalytic properties of AuNPs can be applied to different bioprocesses with industrial or scientific interest, either for oxidizing amino acids [205], cleaving RNA [206], inducing the Fenton reaction [192] or even to catalyse enantioselective reactions [207]. Despite the fact that all these reactions can be carried out by biological counterparts, AuNPs may provide some key advantages during the process that sometimes can lead to lowering the production costs. These and other biological aspects of gold nanozymes, not strictly related to biomedicine, are discussed in this section.

1.3.3.1 Environmental applications

Most applications encompassed in this category are related to diagnostic tools to detect toxic contaminants in environmental waters. This mainly includes heavy metals [161,208–215], pesticides [216–218] or micro-organisms [168,172,219–221], for being the most common contaminants, but it could potentially include any others. Nonetheless, these are not the only examples of gold nanozyme applications in the environmental sector, especially since their catalytic activities started to be exploited for wastewater treatment to degrade or convert toxic molecules into innocuous products [222,223]. It is important to note that many of these contaminants are anthropogenic. One obvious example is the E-waste, which comprises discarded electronic devices. It was estimated that 44.7 million tonnes of E-waste were generated globally in 2016, leading to lots of contaminants being released to the environment such as heavy metals (Pb, Sb, Hg, Cd, Ni), polybrominated diphenyl ethers (PBDEs) and polychlorinated biphenyls (PCBs) [224]. Moreover, the transfer of E-waste to ground and surface water, agricultural soils, rice, fish and humans has been proved [225]. A constant exposure to these contaminants brings harmful health effects with it. Far from being reduced, E-waste numbers are expected to keep growing, thus increasing the health threat.

Moving to the detection mechanisms themselves, the peroxidase-like activity of gold nanozymes is again the preferred approach for developing a sensor. Interestingly, many sensors for Hg detection have been reported in the literature using AuNP nanozyme activity [161,208–210,212]. The reason behind it is that mercury can form an Au–Hg amalgam on the surface of the AuNP that enhances its peroxidase-like activity. This system has proved to be very sensitive and, more importantly, selective towards Hg. Slight differences can be found between all these systems, whose sensitivity ranges between 0.15 and 6 nM. The best LOD was found using an Au/Fe_3O_4/GO hybrid material that not only could detect Hg^{2+} in river and tap water samples, but would also allow for an efficient and quick Hg removal by deposition of Hg^0 on the nanohybrid surface and its subsequent collection using an external magnetic field [209]. On the other hand, higher LOD (40 times less sensitive than the previous example) corresponds to a portable and paper-based approach that can be measured using a smartphone camera [161]. This approach has the particularity of being the only one that combines gold nanozymes with smartphones in any way. Recently, Logan and co-workers have lowered the LOD values reported for Hg detection using highly stable oligo ethylene glycol (OEG)-functionalized AuNPs [215], whose nanozyme activity was recovered in the presence of the metal. A tenfold increased sensitivity was observed using this approach, which reached 10 pM in tap and bottled water, while the sensitivity for saline solution was 65 pM. Despite most sensors described in this section target Hg ions, other systems have been developed to detect specifically Ce^{3+} [226] making use of its redox recycling ability to enhance TMB oxidation or Ag^+ [227] taking advantage of its ability to inhibit the nanozyme activity after being reduced onto AuNPs.

Other nanozyme sensors have been developed for malathion detection, a widely used pesticide in agriculture. These make use of the sulphanyl group from malathion molecules and its strong affinity for AuNP surfaces, thus quenching their peroxidase-like activity [218]. This inhibitory approach was first tested with AuNR [216], reaching a LOD of 1.78 µg/mL (though 10 times higher than the permissible levels of malathion in water). Then, a similar system using palladium–gold bimetallic nanorods [218] managed to lower the LOD down to 60 ng/mL, well below the permissible levels, showing no cross-reactivity with analogous organophosphates or metal salts despite the lack of a biorecognition element in the system. Again, the synergistic effect of nanohybrids shows the great potential they have in this field.

Alternatively, gold nanozymes can be used for water treatment instead of diagnostics. This sometimes involves catalytic properties from AuNPs that have barely been mentioned herein: reductase properties. Such a system becomes a quite interesting approach for reducing the toxicity of water contaminants in industrial wastewaters before they are released to the environment. p-Nitrophenol (PNP) is a contaminant susceptible to this approach. It is widely used in petrochemical synthesis and

its presence in industrial wastewaters might lead to liver and kidney damage, anaemia or systemic poisoning in the receiving bodies [228]. Fe_3O_4/Au core–satellite nanocubes have been recently used to reduce PNP into para-aminophenol (PAP) [223], a product that has many useful applications such as analgesic drugs, photographic developer or even hair dyeing agents [229]. Other applications have made use of the AuNP dehydrogenase activity to degrade estradiol [222], which pollutes wastewaters and has been reported to feminize wild fish [230] and interfere with the human endocrine system [231].

1.3.3.2 Food safety applications

In a similar manner to environmental applications, food diagnostics remains of paramount importance due to the implications that a contamination in this matrix has for human health. The array of contaminants that can be found in food is diverse, as much as the variety in food products. This includes micro-organisms, pesticides, antibiotics or toxins among others. The biomedical consequences of consuming contaminated food go from diarrhoea to cancer, potentially causing more than 200 diseases. According to the WHO (2019) an estimated 600 million people fall ill after consuming contaminated food, while 420,000 die every year as a result of it, being children under 5 years of age who mostly suffer these consequences [232]. Moreover, since food supply chains cross-national borders, any contamination can reach far more people than ever. Taking all this into account, diagnosing food contamination on time remains an issue of high biomedical relevance. Some gold nanozyme-based sensors have been developed targeting microbiological contaminants: *Escherichia coli* O157:H7 [233], *Pseudomonas aeruginosa* [168] and murine norovirus [172]. The first system is based on a sandwich-type immunochromatographic assay that uses Au–Pt bimetallic NPs to enhance the colour signal generated through their peroxidase-like activity. The second approach is based on the inhibition of the peroxidase-like activity of AuNPs: the NP are coated with a *Pseudomonas*-binding aptamer, which blocks the NP surface from developing the catalytic reaction, unless the target bacteria are present in the sample and sequester the aptamers, thus resuming the peroxidase activity. With the help of a disposable carbon screen-printed electrode, this simple system allows for the detection of 60 CFU/mL in 10 min. The same approach has been used to detect murine norovirus in shellfish homogenates, reaching an LOD of 200 PFU/mL. However, the detection in this case is not electrochemical but colourimetric, showing the potential of this approach for point-of-care diagnostics, which remains an important goal considering that norovirus is the leading cause of viral foodborne outbreaks globally. In any case, this technology had been developed and applied for the detection of the pesticide acetamiprid [217] and the antibiotic kanamycin [234,235] long before.

As mentioned in the previous section, children are especially sensitive to some of these contaminations. A clear example of this can be found in the melamine scandal happened in 2008 in China, when milk was illegally adulterated with this chemical. Melamine is a nitrogen-rich organic compound that has sometimes been illegally added to food products to increase the apparent protein content, thus masking a dilution in protein in the final product. This fraud should have been detected by routine tests implemented to ensure milk quality. However, these tests were either not carried out properly or ineffective [236,237]. As a result, about 300,000 people were poisoned due to the high concentration of melamine, which caused many infants to develop kidney stones leading to renal failure and death of 6 babies [238]. Ever since, the number of publications related to melamine detection experienced a tenfold increase. Deng et al. [239] further demonstrated the versatility of gold nanozymes by developing a colourimetric sensor able to detect 0.02 mg L^{-1} of melamine in infant formula. This visual and straightforward system made use of the intrinsic binding of melamine to AuNPs to cause their aggregation and inhibit their peroxidase-like activity. This mechanism has the advantage of its simplicity, but as any sensor lacking a biorecognition element, the resulting specificity may be a matter of concern in complex matrixes. This LOD was reduced down to 8.51 nM by Li et al. [240], who used SERS properties of popcorn-like Au–Ag NPs to detect in a more sensitive manner the oxidized product generated by the bimetallic nanomaterial, oxTMB. They took advantage of the interaction between melamine and H_2O_2, which reduces the availability of the substrate for the peroxidase reaction of TMB, thus decreasing the colour generation in the presence of melamine. Interestingly, oxTMB is a Raman active compound, while anisotropic NPs are strong Raman enhancers [241,242]. This can be exploited to detect the presence of melamine in milk powder with better sensitivity than the traditional colourimetric approach.

Similar frauds have occurred with different additives, not necessarily linked to fatal consequences. This is the case of unauthorized use of ascorbic acid (also known as vitamin C). In meat products, the ascorbic acid prevents the formation of nitrosamines that lead to the discolouration of the meat during storage [243], a sign of spoilage. In agreement with the “no adulteration” policy in this matter, Xu et al. [244] developed a sensor based on Au/Cu bimetallic NR for the determination of ascorbic acid in vitamin drink samples, reaching a LOD of 25 µM. Again, the inhibition of the peroxidase-like activity of AuNPs is the approach used, combined with the synergistic effect observed between Au and Cu, which results in a catalytic activity 4.5 times higher than Au NR.

More sophisticate systems have taken advantage of this peroxidase-like activity of gold nanozymes using an indirect approach to detect the presence of a significant biomarker of a certain condition. McVey et al. [219] developed a gold nanozyme sensor to determine the presence of proteolytic enzymes in human urine, where they may be related to diabetic kidney disease if elevated, and in cow

milk, where their presence may be indicative of an infection by micro-organisms causing bovine mastitis. Protein coating of the AuNP surface blocks the TMB oxidation, while the presence of protease in the sample hydrolyses the protein and resumes the peroxidase-like activity of the AuNPs. Some of these environment- and food-related examples are summarized in Table C1.2.

Target	Nanomaterial	Activity	Outputs	Sample	LOD	Ref
Hg^{2+}	g-C_3N_4-Au nanocomposites	Peroxidase	Colourimetric	Water	3 nM	[208]
Glucose	AuNPs	Glucose Oxidase	Photoelectrochemical	-	0.46 µM	[245]
Hg^{2+}	Au/Fe_3O_4/GO hybrid material	Peroxidase	Colourimetric	Water	0.15 nM	[209]
Acetamiprid	AuNPs	Peroxidase	Colourimetric	-	1.8 ppm	[217]
Kanamycin	AuNPs	Peroxidase	Colourimetric	-	1.49 nM	[234]
Glucose	Au-Ni/g-C_3N_4 nanocomposites	Peroxidase	Colourimetric	-	1.7 µM	[246]
Hg^{2+} & Ag^{+}	Au-Pt core/shell NPs	Peroxidase (inhibition)	Colourimetric	Lake water	3.5 & 2 nM	[210]
Malathion	Pd-Au nanorods	Peroxidase (inhibition)	Colourimetric	Tap water	60 ng/mL	[218]
Kanamycin	AuNPs	Peroxidase	Electrochemical	Standard & honey	0.06 & 0.73 nM	[235]
Nitrite	AuNCs/RGO nanocomposites	Peroxidase	Colourimetric & electrochemical	Sausages	2 & 0.7 µM	[247]
H_2O_2 & Glucose	AuNPs@DNA hydrogel	Peroxidase, Glucose oxidase	Spectroscopic, colourimetric	Serum	1.7 & 38 µM	[248]
Malathion	Au nanorods	Peroxidase	Spectroscopic, colourimetric	Tap water	1.78 µg/mL	[216]

Hg^{2+}	AuNPs	Peroxidase	Colourimetric (smartphone)	Tap water	1.2 µg/L (≈ 6 nM)	[161]
H_2O_2	GO/AuNPs	Peroxidase	Spectroscopic & electrochemical	-	2 µM & 1.9 nM	[249]
Hg^{2+} & Pb^{2+}	AuNPs/BiOI nanocomposites	Peroxidase	Fluorescence	Water (tap, river, lake, sea)	Nanomolar range	[211]
Ce^{3+}	AuNPs	Peroxidase	Spectroscopic	Tap water	2.2 nM	[226]
Ag^{+}	AuNPs	Peroxidase (inhibition)	Spectroscopic	Lake water	10 nM	[227]
Ascorbic acid	Au/Cu nanorods	Peroxidase	Spectroscopic	Vitamin drink	25 µM	[244]
Protease	AuNPs	Peroxidase	Colourimetric, spectroscopic	Milk	44 ng/mL	[219]
Hg^{2+}	AuNPs	Peroxidase	Colourimetric, spectroscopic	Water	0.3 nM	[212]
Melamine	Popcorn-like Au-Ag NPs	Peroxidase	Colourimetric, SERS	Milk powder	8.51 nM	[240]
Murine norovirus	AuNPs	Peroxidase	Colourimetric	Human serum, shellfish homogenate	200 PFU/mL	[172]
Pseudomonas aeruginosa	AuNPs	Peroxidase	Electrochemical	Drinking water	60 CFU/mL	[168]
Escherichia coli O157:H7	Pt-Au porous NPs	Peroxidase	Colourimetric	-	100 CFU/mL	[233]

Table C1. 2 Other non-clinical biosensors exploiting the catalytic properties of AuNPs.

1.4 Thesis aims and objectives

The overall objective of the present thesis is to further investigate how gold nanostars can be incorporated into biosensors with a view to achieving a better analytical performance. Current knowledge on gold nanostars synthesis and properties has therefore been thoroughly reviewed in order to avoid scientific enigmas already solved, thus tackling novel barriers that prevent gold nanostars from being widely used in the field of biosensing. On the other hand, considering the utmost importance point-of-care diagnostic devices have nowadays and the global spread of smartphones, an important part of this thesis revolves around the quantification of colourimetric signals generated by gold nanostars using smartphone cameras, which have already become powerful allies for diagnosis. Finally, all the information collected from this investigation is put into practice to develop biosensing mechanisms with special relevance in the field of food safety, doing our bit in pushing the next generation of diagnostic devices towards a reality.

To that end, the following thesis aims are proposed:

1. Prepare an updated review on the fundamentals of gold nanozymes and their application in the biomedical field.
2. Develop a user-friendly sensor database for microbiological contaminants in food.
3. Synthesise AuNSt with different optical properties and functionalities to apply in the development of colourimetric and spectroscopic sensors.
4. Characterise the peroxidase-like activity of AuNSt and their capability to act as Raman enhancers.
5. Optimise the application of smartphone cameras for the quantification of a colourimetric signal generated by AuNSt.
6. Develop a smartphone-based sensor for the detection of *Mycobacterium bovis*.
7. Study the potential of bimetallic NPs for the development of ultra-sensitive sensors using SERS.

Chapter 2 Developing a novel classification system for sensors targeting microbiological food contaminants: TEST – The End-user Sensor Tree

Nelis, J.L.D., Tsagkaris, A.S., Zhao, Y., **Lou-Franco, J.**, Nolan, P., Zhou, H., Cao, C., Rafferty, K., Hajslova, J., Elliott, C.T. and Campbell, K., 2019. The end user sensor tree: An end-user friendly sensor database. *Biosensors and Bioelectronics*, *130*, pp.245-253.

2.1 Introduction

2.1.1 Abstract

Detailed knowledge regarding sensor-based technologies for the detection of food contamination often remains concealed within scientific journals or divided between numerous commercial kits which prevents optimal connectivity between companies and end-users. To overcome this barrier The End-user Sensor Tree (TEST) has been developed. TEST is a comprehensive, interactive platform including over 900 sensor-based methods, retrieved from the scientific literature and commercial market, for aquatic-toxins, mycotoxins, pesticides and microorganism detection. Key analytical parameters are recorded in excel files while a novel classification system is used which provides, tailor-made, experts' feedback using an online decision tree and database introduced here. Additionally, a critical comparison of reviewed sensors is presented alongside a global perspective on research pioneers and commercially available products. The lack of commercial uptake of the academically popular electrochemical and nanomaterial-based sensors, as well as multiplexing platforms became very apparent and reasons for this anomaly are discussed.

2.1.2 TEST – An end-user friendly sensor database

In an attempt to evaluate the state of the art of biosensors related to food safety, a collaborative work was performed to collect as many sensing assays as possible (commercialised or otherwise) and create an online and interactive database where these would be organised according to various parameters: type of contaminant, level of expertise, portability, quantification and number of analytes. This work was published as a research article in *Biosensors and Bioelectronics* under the title "The end user sensor tree: An end-user friendly sensor database" [204]. The End-user Sensor Tree (TEST) was developed aiming to provide an organised classification of sensors that would help the end-user find the relevant sensor for each situation, while increasing the visibility of those sensors struggling to overcome the valley of death towards commercialisation. All the information extracted from over 900 detection systems (633 research reports and 309 commercial sensors) was sorted in e-docs accessible through an online decision tree (http://test.foodsmartphone.net/), where the user can select the desired criteria the biosensor needs to have. The first branch level relates to the target contaminant that needs to be detected, divided into aquatic toxins, mycotoxins, pesticides or microorganisms. Since the latter constitutes my main contribution to the work, further discussion on this section will revolve around the TEST approach for microorganism detection systems. Besides, this work falls within

the second thesis aim (listed in Section 1.4) “Develop a user-friendly sensor database for microbiological contaminants in food”, which provides a clear picture of the strengths and limitations of current sensors used in this field. This literature review exercise, thus, will not only be useful for the classification of sensors in the TEST platform, but it will also be relevant for other studies throughout this thesis. The second level gives the user the option to choose whether the analyses need to be performed by an expert or a non-expert, as many commercial systems still require trained personnel and therefore are generally not accessible for *in situ* analyses. Next, the decision tree divides the sensors depending on their portability, setting semi-portable systems as those that can be transported in a car. On the next branch, the quantification capabilities are divided (i.e. qualitative sensors, semi-quantitative or quantitative). And a final branch divides the remaining sensors complying all the selected filters into singleplex or multiplex.

2.2 Methods

2.2.1 Classification of sensors

A critical step for the creation of TEST database was the search criteria to collect literature. This was done following two approaches. The first one concerned the academic literature and it exploited Scopus database to extract the most relevant information shared in the five years prior to this study, ensuring that only peer reviewed articles were considered. A general keyword structure was used to search for relevant information, with minor modifications depending on the food contaminant that was targeted. In the case of microbiological contamination of food, the following keyword search was used to investigate the literature:

(("pathogen" OR "spoilage") AND ("portable" OR "instrument" OR "sensor" OR "device" OR "platform") AND ("sensing" OR "testing" OR "analysis" OR "detection" OR "measurement" OR "monitoring") AND ("food" OR "dairy" OR "milk"))

Moreover, four conditions were applied to this search for a better target:

- Original research published between 2013 – 2018
- Published in peer reviewed journals
- Cited at least twice, or published in the last six months
- Written in English

This search resulted in 505 scientific articles, whose abstracts were analysed for relevance, being the selected articles (158 for pathogens and 39 for spoilage organisms) comprehensively analysed.

The second approach followed to build TEST database included the search for commercial sensors, for which the lack of scientific databases led to a less uniform search. Thus, the search was based on using cross-referencing, recent reviews discussing the topic [250] and manual Google searches using a large variety of keywords.

All this information was classified in an Excel table based on the different criteria previously mentioned: expertise needed, portability of the assay, quantification capability and multiplexing. Furthermore, other sensor's parameters were collected in these tables, including limit of detection (LOD), type of sensor, technique in which the sensor is based, biorecognition and transducer elements and target contaminant among others. This classification enabled the critical comparison of sensors that is discussed hereafter.

a) Expertise needed: an expert is defined as a scientist or technician with specialised skills to perform an analytical test or evaluate the results, whereas the "non-expert" category would include tests that can be performed by any person following simple instructions.
b) Portability: this category is divided in three sections. Portable sensors include test strips or lab-on-a-chip devices (LOC), generally small enough to be transported in a pocket. Semi-portable sensors correspond to those that can be used for in-field analyses but require a car to be transported due to their bigger dimensions (i.e. electrochemical (EC) instruments). Finally, non-portable sensors include bulky lab-based equipment such as spectrophotometers and mass spectrometers, or small equipment that require lab conditions to be run (PCR-based assays).
c) Quantification: for microbiological contamination, only bacterial plating has been considered as a precise measure leading to a true quantification of microorganisms. Therefore, most sensors are classified either as semi-quantitative or qualitative. The former group includes PCR-based sensors, EC approaches or any other assay capable of producing an accurate calibration curve within a realistic working range. Any other sensor is classified as qualitative, including those that have a binary response (presence/absence of the contaminant) or poor semi-quantitation (high contamination, low contamination or negative).
d) Multiplexing: it includes those sensors capable of detecting more than one target analyte in a single working cycle. Alternatively, those sensors which target a single analyte are classified as singleplex.

2.3 Results and discussion

Ideal diagnostic tools aim at offering portable, quantitative sensors that can be used by non-experts. However, none of the 197 sensors published in the literature satisfies these three parameters. On the contrary, most sensors are still non-portable or, in the case of being portable, show a poor quantification or require expertise to be used. After a deeper analysis, almost 20% of the sensors found targeting microbiological contaminants can be used by people with no scientific skills. Most of these are also classified as portable and colourimetric sensors, already automated and optimised to be used following simple instructions. In this category we can find isothermal techniques, such as Loop-mediated isothermal amplification (LAMP) which have been integrated in centrifugal microfluidic devices where no manipulation other than the sample loading is required [251]. Despite not being very sensitive, their easy handle has boosted their development. A similar situation is observed with test strips [252,253], which represent the most common type of portable sensors for non-experts. On the other hand, around two thirds of the reported sensors are still lab-based, which represents a big obstacle for food analysis. This is especially notorious in EC sensors which, despite reaching very good sensitivities, are generally lab-based and very few examples approach portability [254,255].

2.3.1 Analytical methods

Effects of microbiological contamination in food ranges from sensorial aspects that make the consumer reject the product to serious threats to human health in the case of foodborne pathogens. And whereas a lax regulation may apply to the former, there is a much stricter regulation regarding the presence of dangerous pathogens. This explains why the bulk of research publications relate to foodborne pathogens (80%) in the field of microbiological contamination of food (Figure C2.1). It is also interesting to note that one quarter of all the sensors analysed are based on PCR-like techniques. Half of these follow conventional approaches, taking advantage of the privileged position PCR has recently taken in regards to detection and “quantification” of bacteria not only in the food field, but elsewhere. However, conventional PCR displays important limitations such as the impossibility to be performed *in situ* by non-trained personnel. As a result, and in the pursue of fully portable and reliable biosensor’s development, several isothermal amplification techniques have arisen in recent years to offer an alternative, although none of them solves the issues related to the presence of PCR inhibitors in the sample matrix [256] or the necessity to conduct lengthy enrichment steps to provide enough target DNA to detect the bacterial presence. These isothermal amplification approaches include

Recombinase Polymerase Amplification (RPA) biosensors [257–259], Rolling Circle Amplification (RCA) biosensors [260] or Loop-mediated Isothermal Amplification (LAMP) biosensors [251,261]. These methods present the advantage of being portable in most of the cases, yet reaching good sensitivities around 100 CFU/mL in food matrixes [258]. This LOD value is similar to those observed using conventional PCR approaches, such as quantitative PCR (qPCR) adapted to microfluidic platforms which pursue portability [262]. To achieve higher sensitivities these approaches can be coupled to enrichment steps, thus detecting 1-3 CFU/g in food and feed after 24 h enrichment in combination with LAMP [263] or 1.3 – 1.9 CFU/g in chicken after 2 h enrichment and 1.3 – 1.9 CFU/mL in milk after 4 h of enrichment, both combined with helicase-dependent amplification (HDA) [264]. Therefore, either the assay's time or sensitivity has to be sacrificed using these approaches.

Besides PCR-based detection methods, a big group encompasses EC assays (19%). Within this group we find voltammetric [254,265,266], impedimetric [267–276], piezoelectric [277–281] or magnetic [282–284] sensors. Most of these devices have proven to be very sensitive, however their portability is quite reduced and, in many cases, require lab-based equipment or trained personnel. Miniaturisation and automation of these approaches at a reasonable price is the bottleneck encountered in EC sensing devices. Some interesting advances can already be appreciated in EC approaches such as the one proposed by Benerjee and co-workers [285]. They developed a system based on iron oxide NPs coated with poly(acrylic acid) embedded with a fluorescent dye and conjugated to an antibody specific to detect *E. coli* O157:H7 in water and milk samples. The sensor combines magnetic relaxation and fluorescence measurements, therefore enabling for accurate quantification in a wider range as each approach shows a high accuracy at different bacterial concentrations. Following this dual-modal approach, they were able to detect the presence of the bacteria between 1 – 20 CFU per 300 µl of real sample (i.e. 4 – 67 CFU/mL) via magnetic relaxation and concentrations between 20 – 100 CFU (i.e. 67 – 334 CFU/mL) using fluorescence emission data. This detection mechanism takes less than 1 hour to be performed and it is highly sensitive, competing in these aspects with gold standard techniques such as qPCR. However, this system is non-portable as of yet, despite its potential due to the growing presence of portable and relatively inexpensive benchtop relaxometers and fluorescence emission readers.

Finally, a wide range of other analytical methods are used apart from PCR and EC approaches, including optical techniques like Surface Plasmon Resonance (SPR) [286–288], spectroscopic such as Surface-Enhanced Raman Spectroscopy (SERS) [289,290], or ELISA [291–293] and immunochromatographic tests [252,253] which can be combined with nanomaterials to improve their sensitivity. All these analytical techniques for foodborne pathogen detection are organised in Figure

C2.1 according to the amount of sensors that have been described in the literature in recent years (since 2013).

The scenario found for food spoilage microorganisms detection, on the other hand, shows a completely different story. This category accounts for 20% of the recently developed biosensors. These sensors generally target a series of specific metabolites responsible for the spoilage effects rather than a specific microorganism. Among these metabolites, biogenic amines can be highlighted, as their presence over a certain threshold is used as an indicator of undesired microbial activity happening in food [294]. These metabolites can be formed by the microbial decarboxylation of amino acids present in food, typically producing histamine, tyramine, cadaverine, 2-phenylethylamine, spermine, spermidine, putrescine, tryptamine and agmatine [295]. Their presence in food products can lead not only to unpleasant sensorial properties, but also to consumers suffering allergic reactions. Apart from biogenic amines, Volatile Organic Compounds (VOCs) are also commonly produced by psychrotrophic strains, generating a species-dependent profile of VOCs as a result of these bacteria's metabolism during refrigerated storage. VOCs include different types of alcohols, aldehydes, ketones, sulphur compounds or hydrocarbons [296]. Due to the large number of metabolites targeted for food spoilage detection, there is a huge diversity of analytical techniques used. These include electronic noses, chromatography, spectroscopy or hyperspectral imaging techniques which are generally coupled to chemometrics or simulation software to predict fingerprints for spoiled food. Furthermore, sensitivity is not among the main aspects pursued in spoilage detection, as a high concentration of the target metabolite is needed to produce the undesired effect in the food, which opposes to the situation of food pathogens where a small number of bacteria can lead to a serious disease. Thus, the approaches used for each situation will vary accordingly.

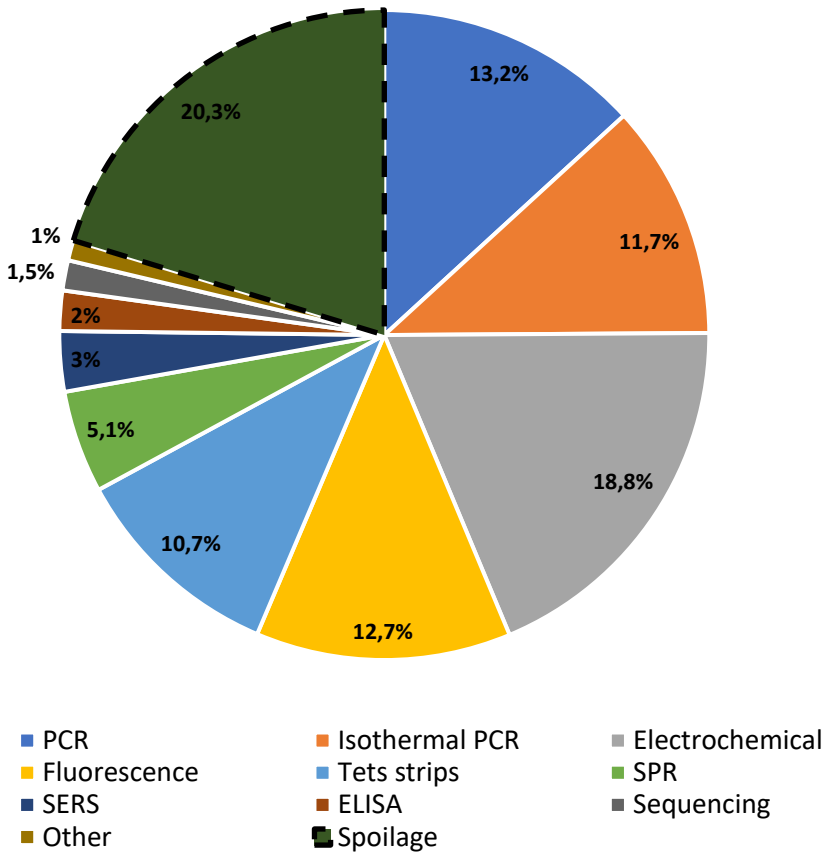

Figure C2. 1 Analytical methods commonly used for detection of microbiological contamination in food.

2.3.2 Sensitivity

One of the most important parameters in biosensing technologies is the sensitivity of the method. Generally, there is a maximum allowed concentration for the presence of a specific analyte, which is set by the legislation. In the food analysis field, this depends on the concentration needed by a specific contaminant to cause a harmful effect in the consumer or a sensorial spoilage of any kind that leads to an economic loss. Accordingly, there is a race for developing the assay which reaches the best limit of detection (LOD), without neglecting the rest of parameters set by the ASSURED criteria (Affordability, Sensitivity, Specificity, User-friendly, Rapid and Robust, Equipment-free and Deliverable to those who need it).

Among all the techniques discussed in the previous section, different sensitivities can be expected (Figure C2.2).

- PCR: PCR has long been the gold standard technique for detecting DNA presence and, by extension, detecting and identifying bacteria in any kind of sample. PCR-based assays represent 31% of publications related to microbiological contamination in food samples in the period 2013 – 2018. To reach the required sensitivities, they are usually combined with long enrichment steps (24 – 48 hours). Despite their many strengths, such as being specific, rapid and reliable, they can be negatively affected by the complex structure of the food matrix, which may contain PCR inhibitors and therefore a separation step prior to the analysis is almost mandatory. Furthermore, their conventional format cannot be used for point-of-care (POC) analyses. Without any further enhancement, LODs around 10^3 CFU/mL may be expected using PCR approaches after performing a magnetic separation of the food sample [297].

- ELISA: this type of assays has been widely used for clinical diagnostics. However, it has some limitations including a laborious procedure, limited multiplexing options, the necessity of laboratory equipment and a relatively high sample volume. Moreover, some issues may arise with non-specific binding, especially when analysing complex matrixes. Even if some of these aspects can be overcome by automating the process and integrating user-friendly readout systems, the sensitivity reached by this approach is generally insufficient for diagnosis: LODs around 10^4 CFU/mL can be expected for ELISA assays in food samples without pre-treatment or enhanced conditions [298].

- Paper strips: this immunochromatographic assay emerged in an attempt to meet the needs that conventional immunoassays (i.e. ELISA) could not provide in terms of portability. These are the most commonly used diagnostic assays for POC analyses. They contain coloured beads or nanomaterials to produce a coloured line in the event of a positive result. They lack good sensitivity, similar to ELISA assays, reaching 10^3 – 10^4 CFU/mL in their standard LFIA configuration [252].

- SPR: this approach is used for the study of biomolecular interactions, chemical detection or immunoassays. SPR biosensors can detect and measure any binding event happening in the surface of a metallic material by observing the change in its optical properties. In the food analysis field, SPR biosensors take advantage of immunological interactions to capture target bacteria in a similar manner as ELISA assays work. However, sensitivities are increased from around 10^4 CFU/mL generally observed in ELISA assays to 10^1 – 10^2 CFU/mL [287]. Currently

they lack portability and require lab equipment and trained personnel, thus limiting their POC application.

- EC: they account for one of the largest groups for microbiological detection in foodstuff. This category includes different techniques (potentiometry, voltammetry, coulometry) and they are highly sensitive, as it has been proved that impedimetric sensors can detect as little as 1 – 10 CFU/mL in complex matrixes such as pork sausage in a label-free, easy-to-operate, fast and on-site manner [270].

- SERS: sensors based in Raman spectroscopy show a clear dichotomy regarding ASSURED criteria. On one hand they are extraordinarily sensitive and robust sensors. On the other hand, they require expensive and bulky equipment to perform the analysis. Even though miniaturised Raman spectrometers exist, like those commercialised by Ocean Optics, they are expensive and the sample analysis and interpretation is not user-friendly. These sensors can be used to detect low levels of contaminant bacteria, around 10 CFU/mL, in food samples in less than 1 h of total assay time [289].

- Fluorescence: finally, fluorescence-based sensors show similar characteristics as SERS sensors. They are very sensitive and robust, but expensive and hardly applicable for POC analyses. And again, companies like Boditech Med have already developed miniaturised fluorescence readers in an attempt to overcome this issue. LODs under 5 CFU/mL have been reported for bacteria detection in food matrixes, completing this assay in under 2 h [299].

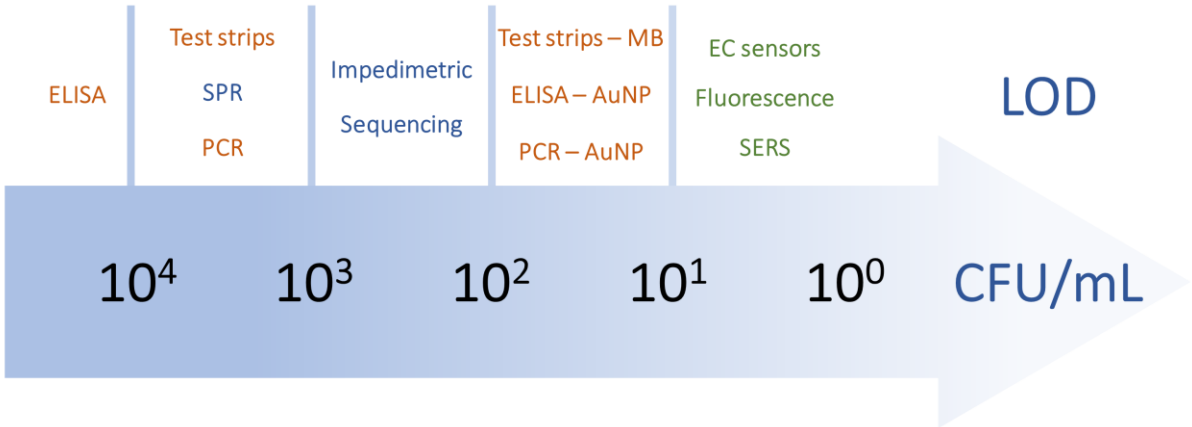

Figure C2. 2 Comparison of sensitivities achieved by different techniques commonly used in the detection of microbiological contamination in food.

It is interesting to note that the techniques that have already been adapted for POC analyses, despite not achieving ultra-sensitive detection, can be enhanced when combined with nanomaterials. Striking examples of this can be observed in the literature. Liu and co-workers developed an isothermal PCR assay combined with a lateral flow assay that was colourimetrically detected by AuNP aggregation, reaching a LOD of 20 CFU/mL for *L. monocytogenes detection* in milk and cheese samples [300]. This represents a sensitivity 2 orders of magnitude higher than what could be achieved using PCR approaches or test strips on their own. Another example of this has been done using a nanomaterial-enhanced ELISA assay, in which magnetic beads were used to capture and separate the target bacteria from the complex food matrix and then AuNPs conjugated to primary, secondary and tertiary antibodies were used for the detection together with HRP labels. The resulting network of nanomaterials and enzymes achieved an impressive enhancement capable of detecting between 3 – 15 CFU/mL for different food pathogens in real samples in less than 2 h [292]. Thus, the enhancement factor observed for ELISA assays can reach between 2 and 3 orders of magnitude. Finally, paper strips can also see their sensitivity enhanced by means of nanomaterial-based approaches. A clear example of this has been described by Suaifan and co-workers, sandwiching a peptide substrate specific for *Staphylococcus aureus* between a gold surface and magnetic beads [301]. If the bacteria was present in the sample, its proteolytic activity would cleave the peptide and therefore the magnetic beads would be released, resulting in the gold colour lying beneath being exposed and detected by the naked eye or using a smartphone. This approach managed to detect 40 CFU/mL in in food matrixes and 100 CFU/mL in environmental samples, which represents an enhancement similar to that observed for ELISA assays with and without nanomaterials.

Despite being true that similar or even better sensitivities can be observed using fluorescence or SERS based approaches, none of these fully satisfy the ASSURED criteria (they often lack being “Affordable”, “User-friendly”, “Equipment-free” and “Deliverable to those who need it”). Therefore, the possibility of enhancing sensitivities of those approaches already fitted for POC analyses by using nanomaterials as signal transducers opens a very interesting path for delivering ASSURED sensors.

2.3.3 Commercial sensors

The need of food testing *in situ* has boosted the development, validation and commercialisation of biosensors in the field of microbiological contamination. In total, 82 commercially available systems have been identified for pathogens, being most of these designed for targeting *E. coli*, *Salmonella* spp., *Listeria* spp. or *Campylobacter jejuni*. Interestingly, only lateral flow assays (and ELISA and PCR-based techniques in a semi-portable configuration) have been successfully developed and commercialised

for POC testing. This marks a clear gap between the state of research and market, generally referred to as *Valley of Death*. Immunochromatographic assays can be easily adapted to portable devices and can be used by non-trained personnel. Even so, they struggle to reach good sensitivities and are often combined with pre-enrichment steps to avoid this limitation. On the other hand, approaches like qPCR have proven their efficiency going through strict validation tests and have resulted in very good LODs, but they still require long enrichment steps and lack the portable character provided by immunochromatography. Finally, a different group of sensing assays include accelerated plating techniques (such as RAPID'Chromogenic Media Solutions, by BIO-RAD), which can be used semi-portably to identify target bacteria but also need at least 48 h of incubation to provide these results. It is worth noting that electrochemical devices are not present as commercially available kits, despite reaching very good sensitivities in short periods of time. Table C2.1 shows a compilation of commercially available kits for the detection of microbiological contaminants in food. Among 85 sensors found, only 5 of them fall in the multiplex category, being many others capable of targeting different bacteria in separate assays. Moreover, many of them require some sort of expertise and are not fully portable (i.e. PCR kits).

On the other hand, it is not easy for the end-user to find a repository collecting all the alternatives in the market regarding available sensors. As opposed to research articles that can be filtered out using scientific databases to find most of the information related to a specific topic, handsearching needs to be done to compare commercially available sensors. This results in big renowned companies being easily found among all the others. Therefore, doubts may arise on whether there is a lack of sensors availability within smaller companies due to the high costs of assay validation and standardisation or whether they exist and are just more difficult to find within this ocean of information. This situation is illustrated in Table C2.1, where companies like Neogen, BIO-RAD, Eurofins, ThermoFisher or Sigma-Aldrich are easily found, while small companies specialised in food testing might not be included.

Finally, no other techniques apart from immunochromatography, bacteria plating and ELISA- or PCR-based are reported. This seems to indicate that most sensors described in the literature have some not yet overcome limitations that hinder their commercialisation and exploitation. In the case of food spoilage commercially available sensors, they do not target a specific microorganism as it happens with foodborne pathogens, but they generally use electronic noses (i.e. Airsense Analytics) to detect a series of volatile metabolites associated to the spoilage character or a combination of microbiological techniques (catalase test, Kovac's reagent strips, selective agars) to identify the bacteria. The reason why this field is not so developed lies in the non-harmful character of these contaminations and the possibility of an accurate detection through smell.

Commercial name	Manufacturer	Analyte	Foodstuff	Detection limit	Assay duration	Test type	Company site
Peel Plate Microbial Test	Charm Sciences Inc	Aerobic bacteria *Coliforms* *Enterobacteriaceae* *E. coli*	Dairy products, meats, water and environmental samples	1 CFU (ideally)	24-48h	Bacterial plating	http://www.charm.com/
ANSR	Neogen	*Campylobacter* *E. coli* O157:H7 *Listeria* *Listeria monocytogenes* *Salmonella*	Various (food and environmental samples)	1 CFU/analytical unit or 100 CFU/mL post enrichment	20-24h 12-26h 16-26h 16-32h 10-26h	Isothermal molecular pathogen detection	http://foodsafety.neogen.com/en/
Reveal 2.0	Neogen	*E. coli* O157:H7 *Listeria* *Salmonella*	Various (food and environmental samples)	1 CFU/analytical unit or 10^4/10^6/10^6 CFU/mL post enrichment	12h 27-30h 24h	Immunochromatography	http://foodsafety.neogen.com/en/
GeneQuence	Neogen	*Listeria* spp. *Listeria monocytogenes* *Salmonella*	Various (food and environmental samples)	1-5 CFU/25g	30-48h 42-48h 24-48h	DNA hybridization + TMB	http://foodsafety.neogen.com/en/
RapidCheck	Romer Labs	*E. coli* O157 *Listeria* *Salmonella*	Various (food and environmental samples)	N/A	8-18h 24-44h 22-32h	Immunochromatography	https://www.romerlabs.com/
Chromogenic media	BioMerieux	*Listeria* *Salmonella* *Cronobacter* *Campylobacter*	Various (food samples)	<10 CFU/g	24-48h	Bacterial plating	http://www.biomerieux.com/
MICROFAST	Zeulab	*E. coli* O157	Various (food samples)	N/A	18-24h	Immunochromatography	http://www.zeulab.com/
foodproof	BIOTECON Diagnostics	*Brucella* *Campylobacter* *Clostridium* *E. coli* *Cronobacter* *Listeria*	Various (food samples)	1-10 CFU/25g	24h	Real-time PCR	https://www.bc-diagnostics.com/

		Salmonella *Vibrio* *Staphylococcus* *Bacillus cereus*					
mericon	QIAGEN	*Salmonella* spp. *Listeria*	Various (food and feed)	10 copies DNA	Preculture + 1h assay	Real-time PCR	https://www.qiagen.com/
GeneDisc Plates	Pall	*Salmonella* *E. coli* O157 *EHEC* *Listeria*	Various (food samples)	1 CFU/25g	6-18h	PCR technology	-
Sample6 DETECT HT System	IEH Laboratories	*Listeria* *Salmonella* *E. coli*	Various (food samples)	1 CFU/mL	4h 15h 24h	Phage engineering technology	http://www.iehinc.com/
iQ-Check™ Kit	BIO-RAD	*Cronobacter* *Campylobacter* *E. coli* *Enterobacteriaceae* *Listeria* *Salmonella* *Vibrio*	Various (food samples)	N/A	12-24h	Real-time PCR	http://www.bio-rad.com/
IRIS Salmonella®	Solabia Biotecnologica	*Salmonella* spp.	Milk powder, flours	1 CFU/375g, 1 CFU/125g	74-82h	Bacterial plating	http://www.solabia.com/
BACSpec™ Salmonella ELISA Kit	Eurofins	*Salmonella*	Various (food and environmental samples)	1-3 CFU/25g	34-44h (enrich) + 2h	ELISA	https://www.eurofins.com/
BACSpec™ Listeria ELISA Kit	Eurofins	*Listeria*	Various (food and environmental samples)	1-3 CFU/25g	44-52h (enrich) + 2h	ELISA	https://www.eurofins.com/
Salmonella Velox	DNA Diagnostic A/S	*Salmonella*	Raw meat, poultry, fishery products	1 CFU/25-125g	5.5h	qPCR	http://dna-diagnostic.com/
3M™ Molecular Detection Assay 2	3M Science	*Campylobacter* *Salmonella* *Listeria* *E. coli* *Cronobacter*	Various (food samples)	N/A	2h (+ enrichment)	Molecular detection	https://www.3m.com/

RapidFinder™ Salmonella Species	ThermoFisher	*Salmonella* spp. *S. Typhimurium* *S. Enteriditis*	Various (food samples)	N/A	16-22h	Real-time PCR	https://www.thermofisher.com/
Assurance GDS®	Sigma-Aldrich	*Salmonella* *Listeria* *Cronobacter* *E. coli*	Various (food samples)	N/A	21-24h	IMS + PCR	https://www.sigmaaldrich.com/
Veriflow® Campylobacter	Invisible Sentinel	*Campylobacter*	Chicken carcass rinsates	1 CFU (Zero tolerance)	26h	PCR	http://invisiblesentinel.com/
Veriflow® Listeria monocytogenes	Invisible Sentinel	*Listeria monocytogenes*	Various (food and beverage samples)	1 CFU (Zero tolerance)	24h	PCR	http://invisiblesentinel.com/
Veriflow®	Invisible Sentinel	*Salmonella* spp. *Listeria* spp. *E. coli* O157:H7 *STEC* *Alicyclobacillus* *Dekkera*	Various (food and beverage samples)	1 CFU (Zero tolerance)	24h	PCR	http://invisiblesentinel.com/
Oxoid Listeria Rapid Test	ThermoFisher	6 *Listeria* spp. (including *monocytogenes*)	Various (food samples)	2-10 CFU/g	48h enrich + 20min test	Immunochromatography	https://www.thermofisher.com/
The Hunter® Real-Time PCR System	InstantLabs Medical Diagnostics Corporation	*Listeria* spp. *E. coli* O157 *Salmonella* spp. *L. monocytogenes*	Various (food samples)	1 CFU/test portion	24h	Real-time PCR	https://instantlabs.com/
Atlas® System	Roka Bioscience	*E. coli* O157:H7 *Listeria monocytogenes* *Listeria* spp. *Salmonella* spp.	Various (food samples)	N/A	24h	Molecular detection	http://rokabio.com/
DuPont™ Lateral Flow System E. coli O157	DuPont	*E. coli* O157:H7 *Salmonella* *Listeria*	Various (food and beverage samples)	1 CFU/25g	8-20h	Immunochromatography	https://www.dupont.com/

MicroSEQ™ E. coli O157:H7 Detection Kit	ThermoFisher	*E. coli* O157:H7 *Salmonella* spp. *Listeria monocytogenes* *Listeria* spp.	Various (food samples)	1-3 CFU/25g	8-18h	PCR + TaqMan® probe	https://www.thermofisher.com/
RAPID'E.coli O157:H7 Medium	BIO-RAD	*E. coli* O157:H7	Various (food and environmental samples)	1 CFU	48h	Bacterial plating	http://www.bio-rad.com/

Table C2. 1 Synopsis of commercially available kits for microbiological contaminants in foodstuff.

2.3.4 Construction of TEST tree and e-docs

The TEST repository is based on an online decision tree which directs the user to e-docs with a fixed layout. Five different criteria have been used for classifying all the information, which are selected consecutively by the end-user to find the desired information (Figure C2.3). Thus, the TEST tree enables to choose the type of target analyte that needs to be measured (1), the level of expertise needed to perform the assay (2), the degree of portability needed (3), the accuracy in the quantification (4) and whether a singleplex or multiplex test is needed (5). Unlike the traditional classification of sensors, which divides them according to their bio-recognition and transducer elements, this classification aims at providing the end-user with a more practical non-linear approach. It contains information extracted from 942 detection systems (633 research reports and 309 commercial sensors) from which 282 target microbiological contamination (197 research reports and 85 commercial sensors).

Among the 282 systems analysed for microbiological contamination, it is interesting to note how scarce proper quantitative sensors are. Only assays based on bacterial growth are considered as such, therefore any other assay measuring a signal proportional to the presence of the contaminant is included in the “semi-quantitative” category. Consequently, only non-portable sensors are described for quantitative microbiological detection (Table C2.2). This lack of portable quantitative devices (no matter the level of expertise demanded) is indicative of the issues faced to bring a technology that satisfies the real needs of the end-users to the market. On the other hand, many scientific reports and commercial sensors describe assays both portable and qualitative, which highlights the contrast that seems to exist between portability and quantification.



Figure C2. 3 Layout of TEST classification system following a 5 criteria hierarchal system. Branches leading to no information are marked "[0]" in the decision tree in every case where the criteria combination has not been translated into an available (or potentially available) commercial sensor.

	FOOD PATHOGENS		FOOD SPOILAGE	
Type	**Expert**	**Non-expert**	**Expert**	**Non-expert**
Quant. portable	0	0	0	0
Semi-quant. portable	3	4	0	0
Qualitative portable	8	23	3	13
Quant. semi-portable	0	0	0	0
Semi-quant. semi-portable	3	1	0	1
Qualitative semi-portable	5	3	0	0
Quant. non-portable	0	0	2	0
Semi-quant. non-portable	53	0	4	1
Qualitative non-portable	55	0	15	0
TOTAL	**127**	**31**	**24**	**15**

Table C2. 2 Number of sensors described in the scientific literature for microbiological food contamination classified according to the TEST criteria.

This hierarchal classification system can be accessed online (http://test.foodsmartphone.net/) and leads the end-user to a webpage (http://testwiki.foodsmartphone.net/) where the e-docs prepared for each criteria combination explain the state of the art considering the chosen parameters (Figure C2.4). Moreover, this platform serves as an interaction point between researchers, food agencies and manufacturers, as it enables any user to upload comments and help keeping up to date the technical information.

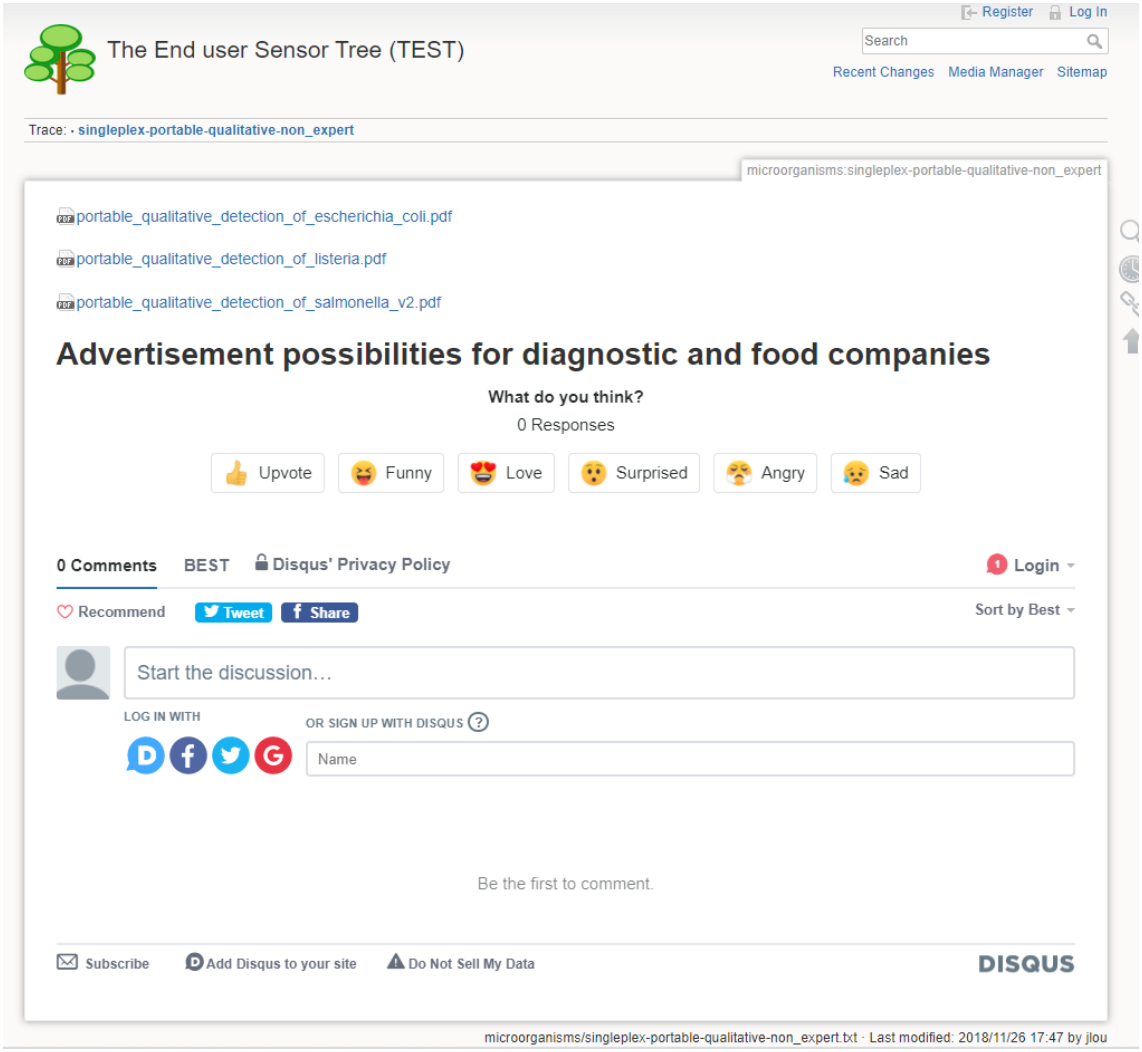

Figure C2. 4 Website layout showing the outcome of a TEST search using the parameters “pathogen” AND “non expert” AND “portable” AND “qualitative” AND “singleplex”, resulting in 3 e-docs targeting *E. coli*, *Listeria* and *Salmonella* contaminations.

2.4 Conclusions

The End-user Sensor Tree is the first interactive platform for food contaminant sensors providing a novel classification, based on end-users needs, approach, maximizing the available information for commercial sensors and sensors in development. Rapid, on-site and sensitive quantitative detection is still an almost unreachable dream with lab-based instrumental methods showing a more robust and reliable analytical performance. However, nanomaterial-enhanced and EC based sensors show great potential due to their ability to reach high sensitivity and provide semi-quantitative results. Unfortunately, these novel sensors seem still far away from being implemented in real life applications. Test strips, however, do seem to successfully bridge the perceived *valley of death* with many examples of rapid tests requiring little or no expertise. Moreover, rough quantification using a special reader or even a smartphone camera seems possible. Another step forward to rapid screening is the use of multiplexing. Unfortunately marketing of multiplex tests has equally shown little progress and scientific reports on this are lacking. Overall, it would appear, more effort from the scientific community needs to be invested in the validation of the developed systems. Perhaps capturing the market through the sales of such systems through spinoffs might further boost development. The lack of commercial novel sensors could also be an effect of the unwillingness of companies to invest into a leap into the unknown. Moreover, it is hoped that TEST will increase sensor promulgation overall and the aim is to further grow TEST into a fully comprehensive sensor platform for numerous analytes in various matrixes providing independent expert advice stretching over both the food and medical sectors. Such development can equally lead to more rapid acceptance of novel systems and provide stakeholders with a means to actively communicate and shape the future of contaminant screening together. Other enthusiasts and stakeholders may wish to contribute to this substantial quest. Ultimately, this might lead to a more time effective and delineated bottom-up biosensing environment replacing the current top-down laboratory-based system.

Chapter 3 Gold nanostars: Synthesis and characterisation of their peroxidase-like activity

3.1 Introduction

The shape and size of AuNPs play an important role in the properties of these nanomaterials. Depending on these parameters, their optical interaction with light will vary and, therefore, so will all the properties dependent on it. Mie's theory [302] explains how the particle's electric surface charge density changes with the particle diameter, leading to a shift in the plasmon absorption band to larger wavelengths as the NP size increases (i.e. redshift) (Appendix, Figure A1) . This phenomenon is observed when the size of isotropic AuNPs changes, but an even more significant plasmon shift might be observed with the slightest change in morphology [303]. This is due to a larger concentration of the electromagnetic field at the tips and protrusions of AuNPs. Moreover, the optical properties of anisotropic NPs can be tuned in the visible (Vis), near-infrared (NIR) and infrared (IR) regions of the spectrum, a wide range which cannot be obtained by changes in the diameter of spherical NPs. The fact that plasmonic properties can be tuned in the NIR is especially interesting for biomedical applications given that this range of wavelengths (650 – 1350 nm) is known as the therapeutic window and results in light having a maximum depth of penetration in biological tissues. Therefore, AuNPs whose plasmon band is set in the NIR can be excited after being administered in the body and applied for *in vivo* imaging. Advantages of anisotropic NPs, however, are not limited to NIR window applications in tissues. Others include the use of their excellent optical properties for signal enhancement in sensors development [304], their capability to efficiently convert absorbed radiation into heat in picoseconds for photothermal treatment [108], or many others including chemical catalysis [305] or drug delivery [306] applications.

The first examples of anisotropic NPs were described in 1979 and 1981, where hexagonal (icosahedral) and pentagonal (decahedral) AuNPs were synthesised by vapor deposition methods [307,308]. Since then, there has been an exponential growth in the research related to anisotropic nanomaterials, which are classified as 1, 2 or 3D nanostructures depending on the number of dimensions enabling electron motion. Nanorods, nanowires or nanotubes belong to 1D category, triangles, sheets or ribbons belong to 2D and pyramids, stars, flowers, cages or cubes belong to 3D nanostructures. Plenty of information can be found revolving around the importance of shape control in noble metal nanoparticles for achieving optimum application results [309–312]. Furthermore, not only the LSPR position is dictated by the NP morphology, but also optical features such as absorption or peak width depend on the shape, size, composition, surface charge, interparticle interactions, surface-adsorbed species and the refractive index of the surrounding medium [313]. Direct advantages of anisotropy include the

"lightning-rod effect" or a larger surface area. The former refers to an enhanced charge density localisation at tips or protrusions of metallic nanostructures, where free electrons can be excited by an electromagnetic field and create a strong electric field at these regions, explaining the high SERS activity observed for anisotropic NPs. The larger surface area observed for anisotropic NPs, on the other hand, influences their chemical reactivity and explains why they show enhanced catalytic properties as compared to isotropic NPs [303].

Many different approaches have been developed for synthesising anisotropic nanomaterials, which generally use capping agents to hinder or enhance the crystal growth in certain facets, form surfactant micelles or structural defects to physically direct the anisotropic growth or promote a directed growth through the formation of twin planes in the seed particles [303]. These approaches require less energy than vapour-phase methods, this is why solution-based syntheses are usually preferred. Typically, syntheses approaches include: seed-mediated synthesis, polyol synthesis, biological synthesis, hydro/solvothermal synthesis, galvanic replacement reactions, photochemical synthesis, electrochemical synthesis or template-mediated synthesis.

- Seed-mediated synthesis: it involves two steps, the synthesis of "seed NPs" by reducing a metal salt in the presence of a reducing and a stabilising agent, and the growth of these seeds into the desired shape by adding a growth solution containing a surfactant or shaping agent and a mild reducing agent. The surfactant molecules form suitable templates for achieving the growth in a specific shape, while the metal salt is reduced only on the surface of seeds. This is the most common approach and can be modified to alter the direction of growth as desired (Figure C3.1).
- Polyol synthesis: it involves the reduction of an inorganic salt precursor by a polyol that also acts as solvent, such as ethylene glycol, propylene glycol or glycerols among others. It is commonly used to produce Ag, Pd or Pt NPs applying high temperature (150 ˚C or higher [314]) to reduce metallic ions and induce the nucleation and growth in the solution phase. The stabiliser used, which adsorbs onto the NPs seeds, determines the morphology of the final nanostructure [315].
- Biogenic synthesis: biological systems such as bacteria, *algae* or plant extracts are capable of producing anisotropic NPs due to the presence of reducing and capping agents. For example, *Pseudomonas stutzeri* AG259 has been used to produce Ag triangular and hexagonal NPs [316], *E. coli* and extracts of lemongrass plant to produce triangular AuNPs [317,318], and green algae *Chlorella vulgaris* to generate Au nanoplates [319].

- Other approaches: it includes hydro/solvothermal synthesis, where NPs are synthesised in hot water/solvent in an autoclave under high pressure; galvanic replacement reactions, where the difference in electrochemical potential between two metals drives the formation of NPs; photochemical synthesis, which takes advantage of radiolytic and photochemical methods to reduce the metal salt precursors; electrochemical synthesis, using a two electrodes set-up where the bulk metal at the anode is reduced into a metal colloid; and template-mediated synthesis, where a nanoporous polycarbonate or alumina is used as a template on which metals such as Au are deposited through electrochemical methods [303].

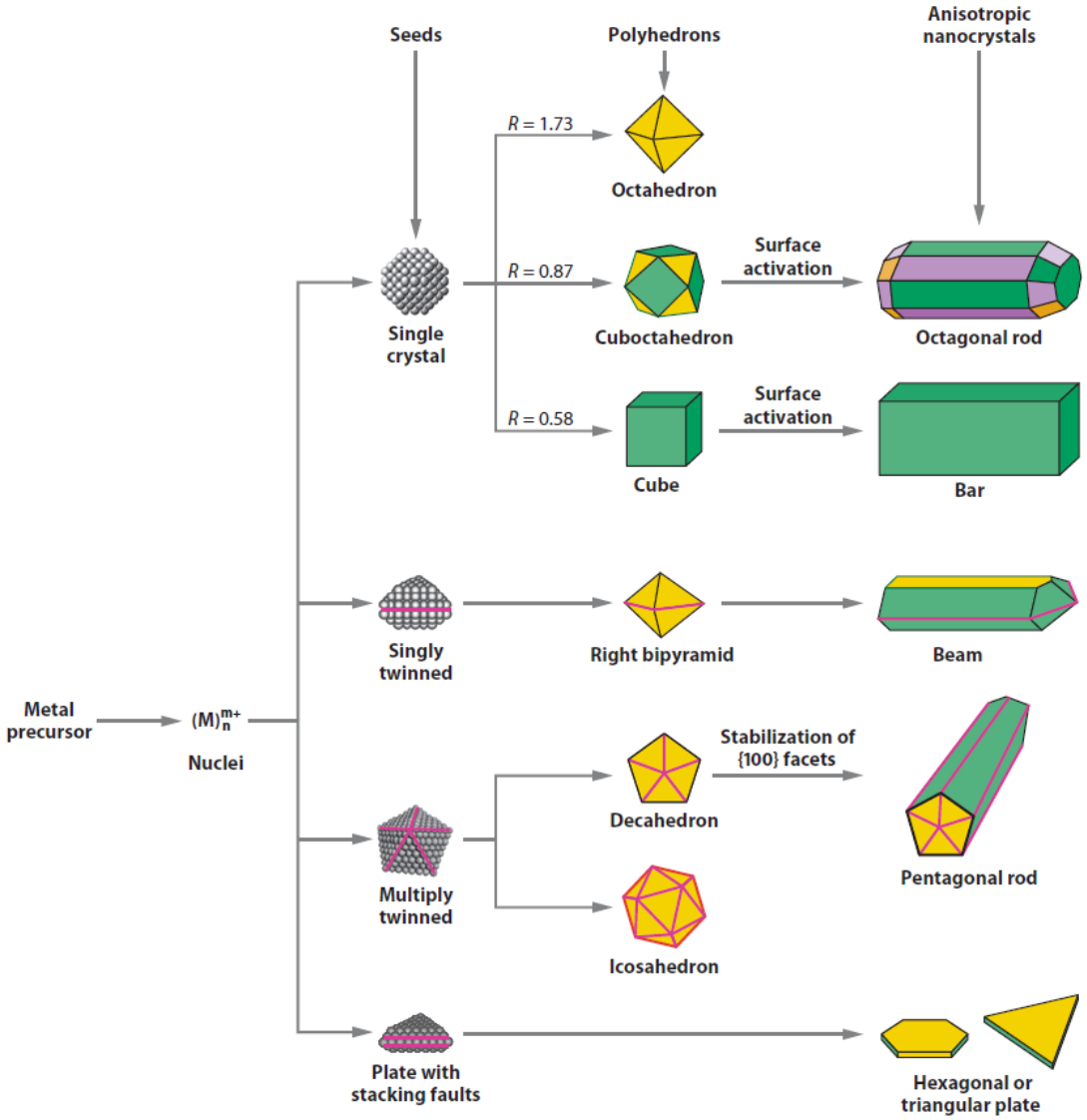

Figure C3. 1 Reaction pathways leading to noble metal NPs with different shapes, starting with the reduction of a metallic salt to form nuclei through aggregation which, passed a certain size, become seed. These have a certain structure (single crystal, singly twinned or multiply twinned). Green, orange and purple colours represent {1,0,0}, {1,1,1} and {1,1,0} facets, respectively. The parameter R is defined as the ratio between the growth rates along the {1,0,0} and {1,1,1} directions. Figure reproduced with permission from [315].

3.1.1 Gold Nanostars Synthesis

Gold nanostars (AuNSt) are among the most interesting shapes for biosensing applications since they have plasmon bands that are tunable into the NIR region and contain multiple sharp branches that act as "lightning rods" enhancing the local electromagnetic field [320]. These two properties combined with the general advantages of gold nanostructures compared with other metals (see Section 1.2) make them ideal for a wide number of applications like SERS, photodynamic/photothermal therapy, imaging or biosensing.

Many approaches have been explored for synthesising AuNSt [321], which can be classified in two main groups: seeded-growth methods and one-pot methods. Jana and co-workers pioneered the study of seed-based approaches for controlling the shape of AuNPs [322], following El-Sayed attempts in 1996 to control this parameter in PtNPs claiming its importance for catalytic applications [323]. However, these first studies suffered from a lack of monodispersity in the nanostructures obtained, leading to a mixture of shapes. Therefore, this initial method was slightly modified by El-Sayed to achieve a better control in the synthesis of gold nanorods (AuNRs) [324], which paved the way for synthesising AuNPs with all sort of morphologies. This method involves the reduction of chloroauric acid with ascorbic acid (a mild reducing agent) onto gold crystal seeds in the presence of a cationic surfactant (such as CTAB) that displays a preferential adsorption on certain seed facets, thus triggering the anisotropic growth. Many other studies have followed based on these researches to prepare star-like NPs: Carroll and co-workers applied it to prepare tripod and tetrapod AuNPs [325], Hafner and co-workers investigated the applicability of seeded-grown AuNSt for LSPR sensors by measuring their scattering spectra in different environment [326], while Hu and and co-workers first reported a modified seed-based protocol for obtaining symmetrically-branched and monodisperse AuNSt [327]. One of the main issues related to seeded-growth methods, however, is the difficulty to remove capping molecules used for directing the seeds' growth, especially for plasmonic or catalytic applications where any surface modification matters. This leads to the recent popularity gained by one-pot methods, where the metallic precursor solution is prepared in the presence of a suitable reducing agent (i.e. ascorbic acid, hydrazine) and surfactant (i.e. CTAB, PVP). Reactant concentrations and reaction times are generally critical parameters for optimising these procedures and obtain the desired nanostructure shape and size. Thus, Yacaman and co-workers have reported a very simple method for producing star polyhedral gold nanocrystals by adding a 32-fold molar excess of ascorbic acid to an aqueous solution of chloroauric acid [328]. No capping agents are required in this approach, being exclusively ascorbic acid and their oxidised derivatives that promote the preferential growth of

{1,1,1} surfaces and stabilise the resulting nanostructures. Green chemicals, such as N-2-hydroxyethylpiperazine-N-2-ethanesulphonic acid (HEPES), have also been used both as reducing and stabilising agent to yield a high proportion of multi-branched AuNPs (≈92%) with one to eight tips [329]. However, the simplicity of these sort of approaches comes at a price: a lower degree of control over the shape and size distribution of the products.

In an attempt to overcome the limitations observed in the previous syntheses approaches discussed, Vo-Dinh and co-workers presented a surfactant-free method to prepare biocompatible AuNSt with adjustable geometry and plasmonic properties by using a seed-mediated growth [320]. The Au seeds were prepared using citrate both as the reducing and stabilising agent, while the seeds growth was carried out adding silver nitrate and ascorbic acid simultaneously over an aqueous acidic solution containing a variable amount of seeds. This way, the need of using CTAB or similar surfactant molecules to stabilise either the seeds or the AuNSt could be avoided. Moreover, a thorough characterisation of how different parameters (including pH, stirring speed or reagents ratios) affected the synthesis was performed to provide information on how to modify these parameters for yielding AuNSt with different plasmonic and morphological properties. This information was used by Liz-Marzán and co-workers to optimise a AuNSt synthesis protocol [330] which has been used in this Chapter with minor modifications.

3.1.2 Objectives

In this Chapter, AuNSt were synthesised following previously reported seed-mediated protocols with tuneable optical properties. They were characterised by spectroscopy techniques and advanced microscopy and their potential for biosensing assays was studied. In this line, their surface was modified with several linkers that provided the AuNSt with different functionalities and surface properties. On the other hand, the nanozyme activity of these nanomaterials was characterised, focusing in their peroxidase-mimicking activity. The relation between AuNSt optical and surface properties with such activity was studied pursuing to provide hints on how to better develop a colourimetric or spectroscopic sensor based on AuNSt. Hence, TMB has been used as a model substrate, given that not only it becomes oxidised into a coloured product, but also this product is a Raman active molecule that can be detected in an ultra-sensitive manner within the strong electric fields created at tips and protrusions of AuNSt. Their Raman potential, however, will be discussed in Chapter 6.

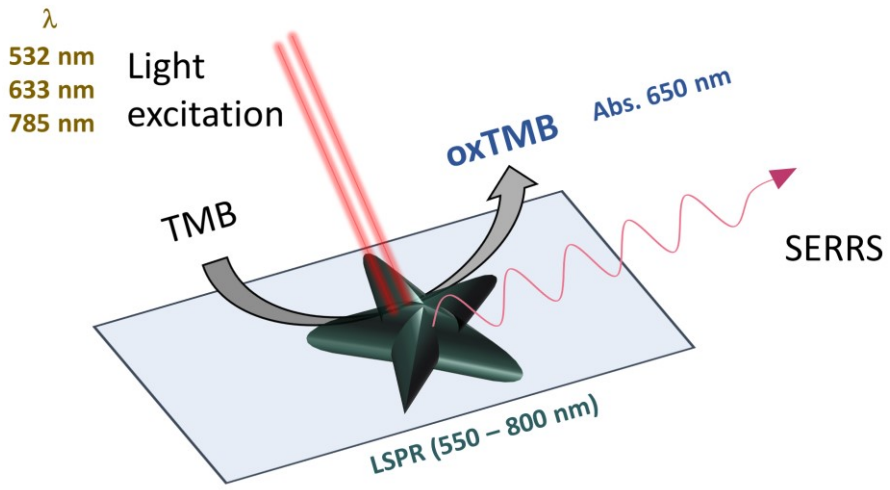

Scheme C3. 1 Optically tuneable AuNSt are synthesised and characterised in this Chapter to study their potential as nanozymes and Raman enhancers for sensors development.

3.2 Methods

3.2.1 Reagents and chemicals

Gold(III) chloride trihydrate ($HAuCl_4 \cdot 3H_2O$, 99.9%), L-ascorbic acid ($C_6H_8O_6$), silver nitrate ($AgNO_3$), hydrochloric acid (HCl), sodium citrate tribasic dehydrate ($HOC(COONa)(CH_2COONa)_2 \cdot 2H_2O$, 99%), 11-mercaptoundecanoic acid ($HS(CH_2)_{10}CO_2H$, 95%), 16-mercaptohexadecanoic acid ($HS(CH_2)_{15}CO_2H$, 90%), O-(3-Carboxypropyl)-O'-[2-(3-mercaptopropionylamino)ethyl]-polyethylene glycol (Mw 5000), O-(2-Carboxyethyl)-O'-(2-mercaptoethyl)heptaethylene glycol ($C_{19}H_{38}O_{10}S$, 95%), 3,3',5,5'-tetramethybenzidine (TMB), hydrogen peroxide (H_2O_2 30% (w/w) in H_2O), ethanol (CH_3CH_2OH) were all purchased from Sigma Aldrich (UK). TEM Formvar carbon films on nickel grids were purchased from Agar Scientific (UK).

3.2.2 Synthesis of AuNSt

AuNSt were synthesised through a seed-mediated approach, following Liz-Marzán protocol [330] with minor modifications. The mechanism includes first the synthesis of spherical gold seeds that will act as nuclei in a second step where the anisotropic growth happens, leading to the formation of star-shaped NPs (see Scheme C3.2).

3.2.2.1 Seeds synthesis

Seeds are obtained following Turkevich's method for synthesis of colloidal gold [68]. Briefly, 5 mL of 1% sodium citrate solution was added to a 95 mL of boiling 0.5 mM $HAuCl_4$ solution under vigorous stirring. After 15 min of reaction, the solution is cooled and kept at 4 ˚C. The produced seeds show a LSPR of 519 nm, confirmed by UV-Vis spectroscopy.

3.2.2.2 Seeds growth into stars

The Au seeds obtained in the previous step are used as nuclei for the AuNSt synthesis, $HAuCl_4$ as gold source, $AgNO_3$ to direct the anisotropic growth of Au branches on certain crystallographic facets and L-AA as reducing agent. A varying volume of the citrate-stabilised seed solution is added to 10 mL of 0.25 mM $HAuCl_4$ containing 10 μl of HCl (1 M) in a glass vial under moderate stirring. Immediately after that, 100 μl of 3 mM $AgNO_3$ and 50 μl of 100 mM L-AA are added and the solution is allowed to react at room temperature for 2 min. The reaction takes place very quickly: in the first ten seconds the colour change can be observed, turning from light red to blue/greenish depending on the volume of seeds used.

3.2.3 Functionalisation of AuNSt

Once synthesised, the AuNSt were stabilised with one of the following coating molecules: sodium citrate (NaCit), 11-mercaptoundecanoic acid (11-MUA), polyethylene glycol (PEG) or oligoethylene glycol (OEG). In the first case, AuNSt were incubated overnight (O/N) in 1 mM sodium citrate final concentration, under minor stirring conditions at RT. In the case of 11-MUA, citrate molecules were replaced with 11-MUA at a concentration of 100 µM in an ethanol:water 1:1 solution (v/v), under minor stirring conditions O/N at RT. Alternatively, the AuNSt were stabilised with hydrophilic polymers (PEG or OEG). Immediately after synthesis, 0.8 µM of PEG was added to the AuNSt solution and stirred continuously for 15 min at RT. Stabilisation with OEG was achieved by adding 500 µM of OEG to the AuNSt solution and stirred O/N at RT. Regardless of the stabilisation method used, the AuNSt were finally washed by centrifugation at 10 ˚C and 1200 rcf for 25 min to remove any unbound molecule and resuspended in dH_2O.

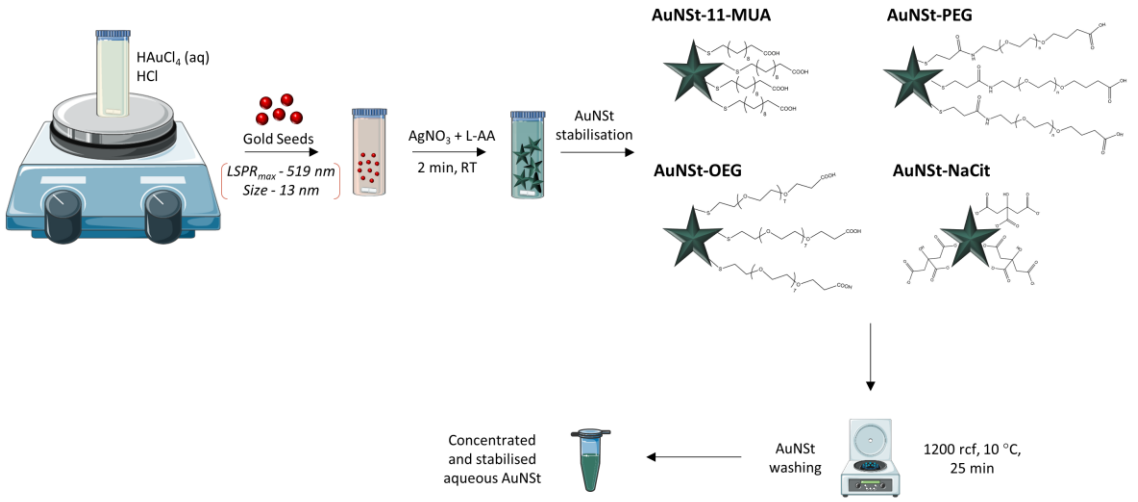

Scheme C3. 2 Synthesis and functionalisation of AuNSt following a seed-mediated growth.

3.2.4 Characterisation of AuNSt

3.2.4.1 Ultraviolet-Visible (UV-Vis) Spectroscopy

UV-Vis analyses were conducted using an Agilent Technologies Cary 60 UV-Vis spectrophotometer for large volumes (around 1 mL) or a Safire^2 TECAN microplate reader for absorbance measurements in microtiter plates, either for endpoint measurements at a single wavelength or for spectrum scans.

3.2.4.2 Transmission Electron Microscopy (TEM)

TEM imaging was conducted on a Joel JEM 1400 Plus Transmission Electron Microscope, operated at 120 kV, while high resolution transmission electron microscopy (HR-TEM) imaging was conducted on a TALOS FEI HR-TEM operated at 200 kV (ThermoFisher). Samples were prepared by drop-casting 4 µL of AuNPs onto a formvar/carbon supported nickel grid and dried O/N at RT. The images were analysed by ImageJ software to obtain a size distribution of each NPs sample.

3.2.4.3 Dynamic Light Scattering (DLS)

A Zetasizer NanoZS (Malvern) was used for obtaining a size estimation and ζ-potential values of different AuNSt samples. Briefly, 50 µL of AuNSt concentrated at 1 OD were added into a polystyrene low volume cuvette for size measurement, while 1 mL was added into a disposable folded capillary cell for ζ-potential analysis. Data were generated automatically using Malvern software.

3.2.5 Peroxidase-mimicking activity of AuNSt

100 pM of AuNSt were incubated with a varying concentration of TMB (0-0.5 mM) in 300 µl of a 6% H_2O_2 aqueous solution for 20 min at RT. After this time, the absorbance of each reaction was measured at a wavelength of 370 nm, which is representative of the charge transfer complex derived from the TMB oxidation [162,219]. These absorbance values are converted into concentration of oxTMB using the Beer-Lambert equation and plotted following the Hills model to extract the Michaelis-Menten parameters (v_{max} and K_M) that enable for comparing the catalytic efficiency of different AuNSt samples.

3.3 Results and discussion

3.3.1 Synthesis of AuNSt

3.3.1.1 Parameters affecting AuNSt synthesis

AuNSt have been synthesised to be used as transducer elements in biosensing assays. Therefore, they have been fabricated with different optical properties ranging from the visible to the NIR spectrum. In order to do so, the protocol described in Section 3.2.2 was followed with some modifications considering the role each reagent had in the synthesis process. No changes applied to the seeds' fabrication, but to the second step where seeds are grown into star-shaped NPs. Gold seeds were used as nuclei, serving as substrate for further growth, while $HAuCl_4$ served as gold source. Varying the ratio of seed to metal salt is an approach that has been long known for controlling the size of AuNPs [331]. Therefore, varying the volume of seeds used has been the main approach followed for tuning the morphological properties of the AuNSt. However, the crucial parameters leading to a controlled growth of the seeds are the reducing and capping agents. In this case, L-AA has been used as reducing agent, using a molar ratio L-AA:$HAuCl_4$ higher than 3:2, since each ascorbic molecule can donate two electrons to reduce Au^{3+}. As for the capping agent, $AgNO_3$ was used to assist the anisotropic growth, directing the branches formation on certain crystallographic facets of citrate-capped gold seeds. It might be thought that silver ions not only assist the growth, but also become reduced to form silver branches onto the gold seeds. However, elemental analyses performed by inductively coupled plasma (ICP) atomic emission spectrometers have shown that AuNPs obtained following a silver-assisted growth only contain around 2.5 – 4.5% of silver [332]. Finally, HCl is used to lower the reaction pH, promoting redshifted plasmons and potentially also influencing the anisotropic growth with chloride ions behaving similarly to iodide ions in various protocols reported [320,333]. It is important to highlight that $AgNO_3$ and L-AA must be added simultaneously. If silver ions are added too early, silver chloride is formed and it precipitates before L-AA is added. If it is added too late, large gold spheres will be formed by the reducing action of L-AA. Hence, chemical concentrations, molar ratios and addition times are of paramount importance for controlling morphological parameters during AuNSt synthesis. Others, such as stirring speed and temperature, also need to be controlled for achieving reproducible batches.

3.3.1.2 Optically tuneable AuNSt

Following the considerations discussed above, the seeds volume has been varied between 40 – 300 µL, leading the use of fewer seeds to larger NPs size if the rest of parameters are kept constant (as reported in Section 3.2.2). The resulting AuNSt were analysed by UV-Vis spectroscopy (Figure C3.2), where it can be appreciated how their optical properties can be tuned. The absorbance ratio of spherical AuNPs (A_{LSPR}/A_{450}) can be used to estimate the diameter of the seeds used for the synthesis of AuNSt [334], resulting in 13 nm sized spheres. As they grow into AuNSt, their LSPR redshifts. The smaller the shift, the fewer the morphological differences should be expected, leading to the formation of intermediate sphere/star shapes with small sizes. The larger the shift, on the other hand, the more spiky and large-sized AuNSt can be obtained. It can be appreciated in the image within Figure C3.2 that a shift in the LSPR is correlated to a colour change in the solution (from wine red seeds to purple, blue and, eventually, green for larger shifts), something that cannot be observed over such a wide range with size modifications in gold nanospheres. The peak width, on the other hand, is indicative of the sample dispersity. It can be numerically estimated with the Full Width at Half Maximum (FWHM) parameter, which can be obtained by fitting each UV-Vis spectrum to a Gaussian curve (Table C3.1). Hence, Au seeds show the smallest FWHM (47 nm) meaning that the AuNPs used as seeds are very monodisperse as compared to the resulting AuNSt, whose FWHM values are around 200 nm, indicative of a more polydisperse sample.

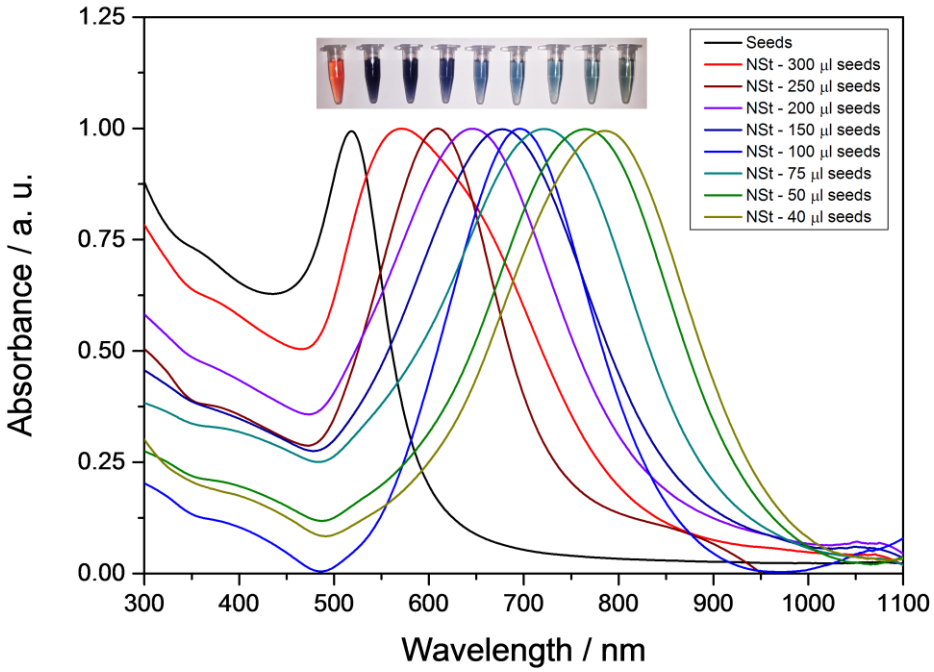

Figure C3. 2 UV-Vis analyses of AuNSt-NaCit synthesised using different amounts of seeds (ranging from 40 to 300 µL) which leads to different optical properties. Inside the graph, an image showing the visual differences in the AuNSt samples.

Sample	Seeds / µL	LSPR / nm	FWHM / nm
Seeds	-	519	47
AuNSt 1	300	571	229
AuNSt 2	250	610	141
AuNSt 3	200	645	207
AuNSt 4	150	675	210
AuNSt 5	100	695	176
AuNSt 6	75	721	229
AuNSt 7	50	758	219
AuNSt 8	40	785	220

Table C3. 1 Summary of spectroscopic differences between AuNSt samples prepared with varying volumes of seeds. (FWHM: Full Width at Half Maximum)

3.3.2 Stabilisation of AuNSt with different functional groups

In order to be used for any application, the surface of AuNSt needs to be modified to prevent NP aggregation. Otherwise, they undergo a clustering process upon interactions at short distances, which would cause the loss of any property derived from the nanoscale. Therefore, 4 different chemicals known to be capable of stabilising AuNPs in solution have been used: sodium citrate (NaCit), 11-mercaptoundecanoic acid (11-MUA), polyethylene glycol (PEG) and oligoethylene glycol (OEG). Whether AuNSt endure or not the centrifugation step that follows the synthesis to wash NPs from unused reagents indicates if a successful stabilisation has happened or not. UV-Vis spectroscopy is used to ensure that no peak shift or intensity changes occur, indicating that AuNSt are stable. However, since aggregation of AuNPs leads to the formation of larger clusters that sediment and make the colloidal solution lose its characteristic colour (i.e. changing from blue/green to light grey or colourless), a visual analysis is the fastest approach for discarding protocols that do not lead to a successful stabilisation.

- Sodium citrate: citrate is a tricarboxylic acid trianion that, once passively adsorbed onto AuNSt, provides them with a negatively charged surface that keeps the NPs stable in solution due to electrostatic repulsion, thus preventing clustering and aggregation processes. However, a too high or too low concentration of these anions can induce aggregation. Therefore, it is essential to find a suitable citrate concentration to be used to stabilise AuNSt. The protocol described in Section 3.2.3 was followed with modifications in the concentration

of sodium citrate used, ranging from 10^{-8} to 10^{-1} M. Figure C3.3 shows that when citrate concentrations below 10^{-4} M were used to stabilise AuNSt O/N, these showed aggregation signs. Furthermore, even if AuNSt samples stabilised with 10^{-4} M showed no signs of aggregation after this 12-hours process, they did not endure the washing step that follows, leaving 10^{-3} M as the lowest concentration that successfully stabilised AuNSt.

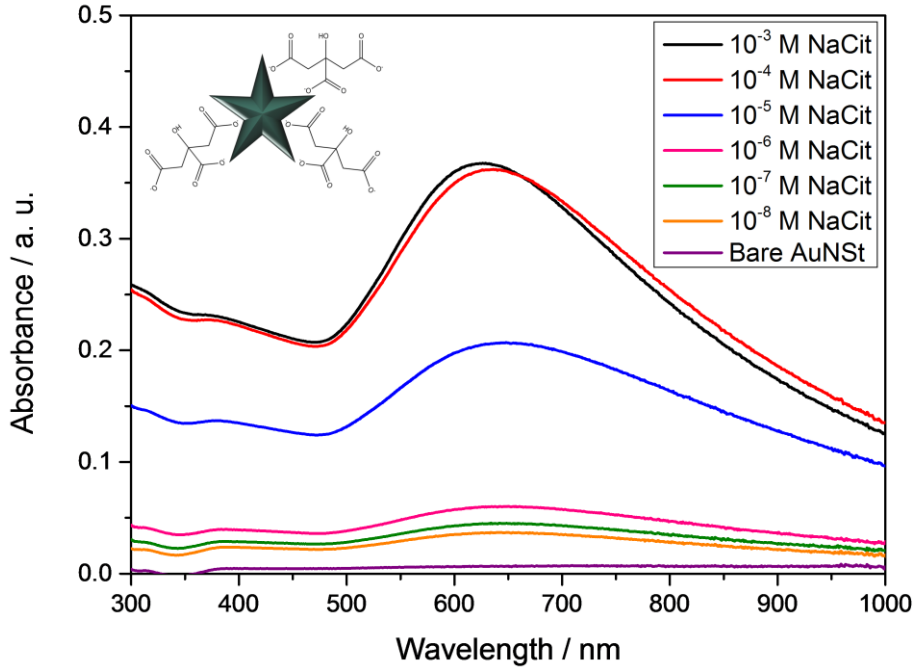

Figure C3. 3 AuNSt samples stabilised with varying concentrations of sodium citrate O/N and analysed by UV-Vis to characterise the aggregation process before washing the samples.

At the same time, higher concentrations of sodium citrate were studied as well, from 10^{-3} to 10^{-1} M. A visual analysis confirmed in all cases that while 10^{-2} M showed partial aggregation of AuNSt, it was absolute and irreversible with 10^{-1} M (Figure C3.4). Surely, no addition of citrate to the AuNSt sample before incubating them O/N and washing them by centrifugation led to quick aggregation processes observed both visually and spectroscopically. Thus, 1 mM sodium citrate was chosen as the optimum concentration for stabilising AuNSt, after which they remained stable in solution for several months.

(a)

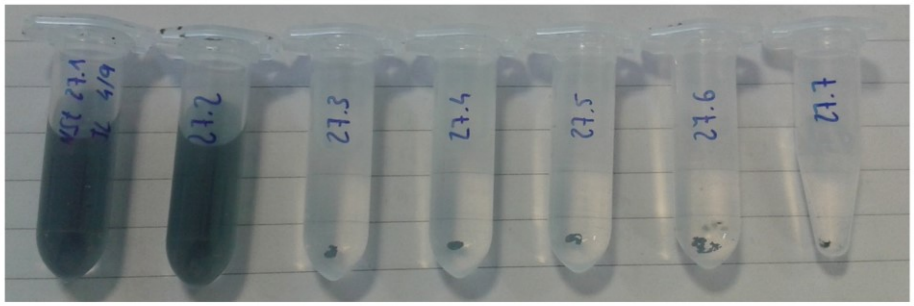

[NaCit] / mM	1	5	25	50	75	100	0
Stability	✓	✓	×	×	×	×	×
Centrifugation	~	~	×	×	×	×	×

(b)

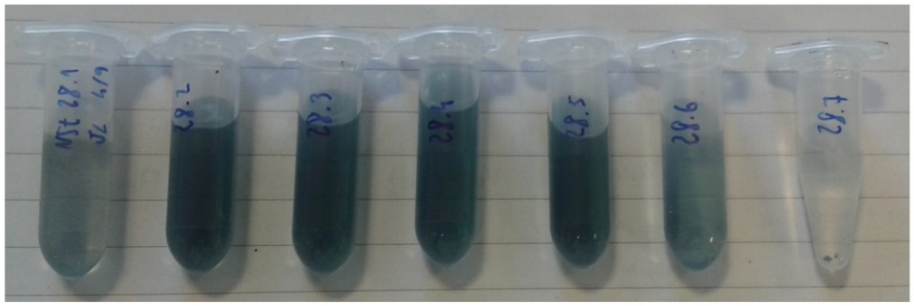

[NaCit] / mM	0,01	0,1	0,5	1	5	10	0
Stability	~	✓	✓	✓	✓	~	×
Centrifugation	×	×	~	✓	~	×	×

(c)

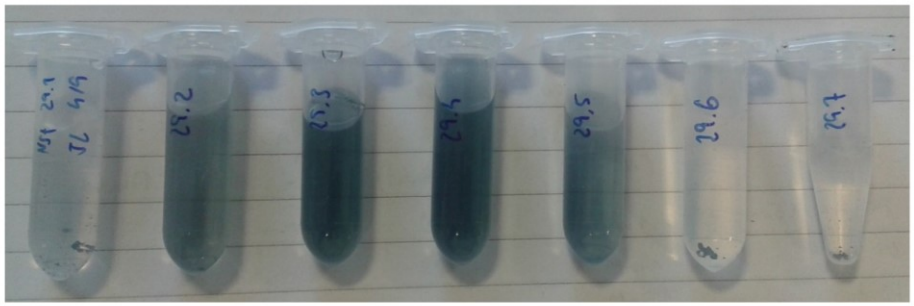

[NaCit] / mM	0,001	0,01	0,1	1	10	100	0
Stability	×	~	✓	✓	~	×	×
Centrifugation	×	×	×	✓	×	×	×

Figure C3. 4 Stability study of citrate-capped AuNSt, varying citrate concentrations from 10^{-6} to 10^{-1} M.

- 11-Mercaptoundecanoic acid (11-MUA): 11-MUA is a bifunctional alkane chain containing a carboxylic group at one end and a thiol group at the other end. It is generally used as molecule for forming a self-assembled monolayer (SAM) on AuNPs, as the thiol groups interact with gold atoms, whereas the carboxylic groups provide a negative charge to keep NPs stable in solution as well as a functional group for further surface modifications. However, due to the mostly hydrophobic nature of 11-MUA, it requires the use of a solvent with a lower relative polarity than the aqueous solutions used with citrate stabilisation. This is why it is dissolved in ethanol and added to the aqueous AuNSt sample in a relation 1:1 (ethanol:water, in volume). Following the protocol mentioned in Section 3.2.3, AuNSt are first stabilised with citrate and then citrate molecules are replaced by 11-MUA due to a higher affinity for gold of thiol groups, which displace citrate. This two-step stabilisation process is performed to prevent AuNSt from aggregating, which was the phenomenon observed when 11-MUA was directly added in an ethanol/water mixture to bare AuNSt. A spectroscopic analysis is done using different concentrations of 11-MUA and 16-mercaptohexadecanoic acid (16-MHA), which is a similar linker with an aliphatic chain containing 16 C instead of 11. The results are shown in Figure C3.5 and further detailed in Table C3.2, showing evidence that no successful stabilisation was achieved with 16-MHA. Using this linker at the lowest concentration (10^{-7} M), the absorbance at the LSPR peak (which is indicative of the AuNSt concentration) drops a 15% compared to the initial citrate-capped AuNSt, while it falls to half the initial value when 16-MHA concentration is increased to (10^{-6} M). Higher concentrations showed irreversible aggregation, indicating that no stabilisation was achieved with this linker. When 11-MUA was used, on the other hand, good absorbance values (similar to those of citrate-capped AuNSt) were observed using 10^{-5} and 10^{-4} M 11-MUA, being the latter the optimum concentration for stabilising AuNSt. The differences observed for 11-MUA and 16-MHA might be explained by the length difference in the alkane chain. Both linkers consist in two small polar groups connected by a hydrophobic chain. Therefore, the longer the chain, the smaller the solubility of these molecules in an ethanol:water solution, hindering their attachment to AuNSt.

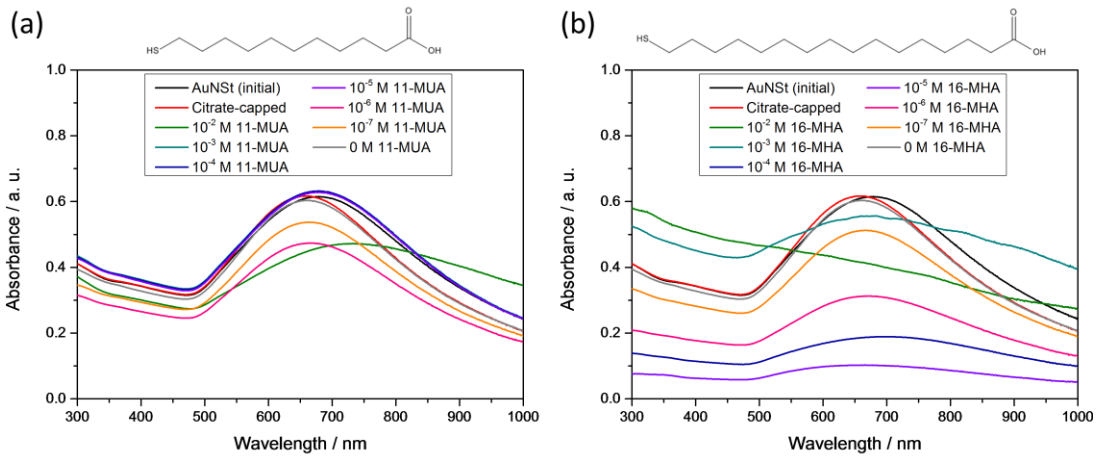

Figure C3. 5 AuNSt samples are analysed by UV-Vis spectroscopy before any surface modification "AuNSt (initial)", after stabilisation with citrate "Citrate-capped" and after replacing the citrate coating with varying concentrations of (a) 11-MUA and (b) 16-MHA.

AuNSt Sample	AuNSt in H_2O	11-MUA in EtOH	16-MHA in EtOH	[11-MUA]	[16-MHA]	LSPR	Abs_{LSPR}
1	750 µl	750 µl	-	10^{-2} M	-	731 nm	0.472
2	750 µl	750 µl	-	10^{-3} M	-	731 nm	0.472
3	750 µl	750 µl	-	10^{-4} M	-	677 nm	0.632
4	750 µl	750 µl	-	10^{-5} M	-	681 nm	0.628
5	750 µl	750 µl	-	10^{-6} M	-	665 nm	0.474
6	750 µl	750 µl	-	10^{-7} M	-	666 nm	0.538
7	750 µl	-	750 µl	-	10^{-2} M	Agg.	Agg.
8	750 µl	-	750 µl	-	10^{-3} M	Agg.	Agg.
9	750 µl	-	750 µl	-	10^{-4} M	Agg.	Agg.
10	750 µl	-	750 µl	-	10^{-5} M	Agg.	Agg.
11	750 µl	-	750 µl	-	10^{-6} M	671 nm	0.313
12	750 µl	-	750 µl	-	10^{-7} M	664 nm	0.513
13	1500 µl	-	-	-	-	659 nm	0.604

Table C3. 2 Results after replacing citrate-capped AuNSt with bifunctional alkane chains of varying length (11 and 16 C chains). (Agg. Indicates aggregation)

❖ Polyethylene glycol (PEG) & Oligoethylene glycol (OEG): another common way to stabilise AuNSt is by attaching polymers or oligomers to their surface, such as PEG and OEG. They are both bifunctional chains, containing a thiol and a carboxylic group in a similar disposition as

11-MUA. However, the presence of O atoms along these chains provide them with a higher polarity and therefore a better applicability in aqueous samples. Following previously reported protocols [330], a 5 KDa PEG polymer was used to stabilise AuNSt. As described in Section 3.2.3, an aqueous solution containing AuNSt and PEG $8 \cdot 10^{-7}$ M was softly stirred for 15 min to allow PEGylation of NPs. For OEG, $5 \cdot 10^{-4}$ M was the concentration used as reported by Logan et al. [215]. No concentration optimisation was thus needed.

To compare how each functional surface (i.e. NaCit, PEG, 11-MUA and OEG) affected the optical properties of AuNSt, the same sample was split in 4 volumes, being each of them stabilised with a different compound. Citrate-capped AuNSt showed a LSPR set at 670 nm, while the rest of modifications led to a plasmon redshift, reaching 712, 717 and 723 nm for PEG-capped, 11-MUA-capped and OEG-capped AuNSt, respectively (Figure C3.6).

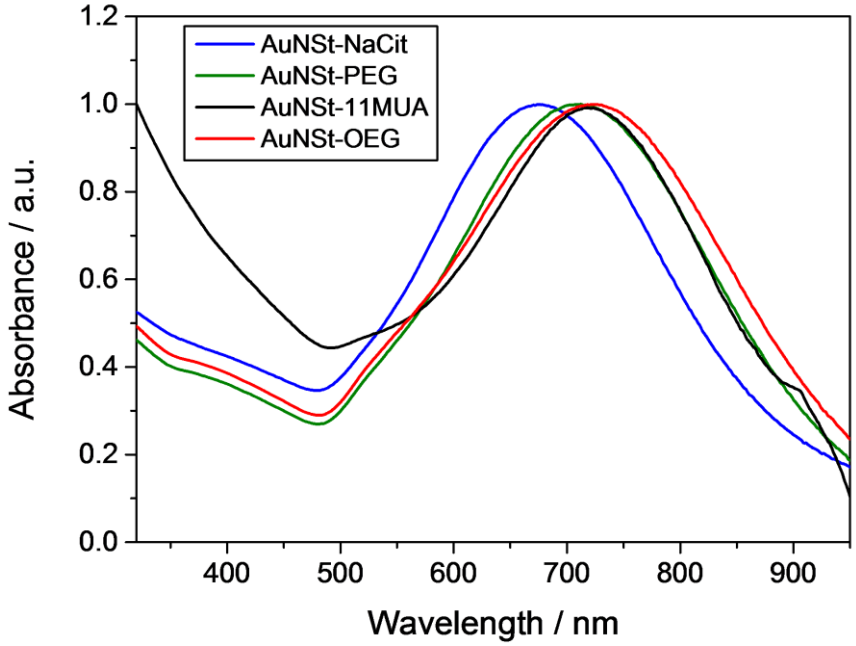

Figure C3. 6 UV-Vis spectra of AuNSt functionalised with different coating molecules.

3.3.3 Characterisation of AuNSt

3.3.3.1 Quantification of AuNSt

One of the main difficulties encountered while working with AuNSt was to reproduce conditions for experiments in which different batches of AuNSt were used. Considering the rapidity at which the synthesis takes place (therefore difficult to control) and the low volume produced per synthesis (10 mL with an optical density between 1 – 2 a. u.), it was of paramount importance

to obtain an extinction coefficient value enabling to correlate the absorbance measured with the sample molarity. In order to do so, the experimental molar extinction coefficient (ε) values calculated by de Puig and co-workers [335] were used to produce a calibration curve from which to extrapolate ε values for each synthesis (Figure C3.7). Their approach consisted in using ICP-AES to determine the amount of Au^{3+} ions unreacted after the synthesis and then use TEM microscopy and 3D modelling to determine the volume of individual AuNSt. Then they used this information to determine ε values that were correlated to a AuNSt sample with a specific LSPR. By using the equation interpolated from their experimental data, it was possible to identify ε values once a UV-Vis analysis had been done for a synthesis, and using the Beer-Lambert equation ($A = \varepsilon \cdot \ell \cdot c$) it was possible to determine their concentration.

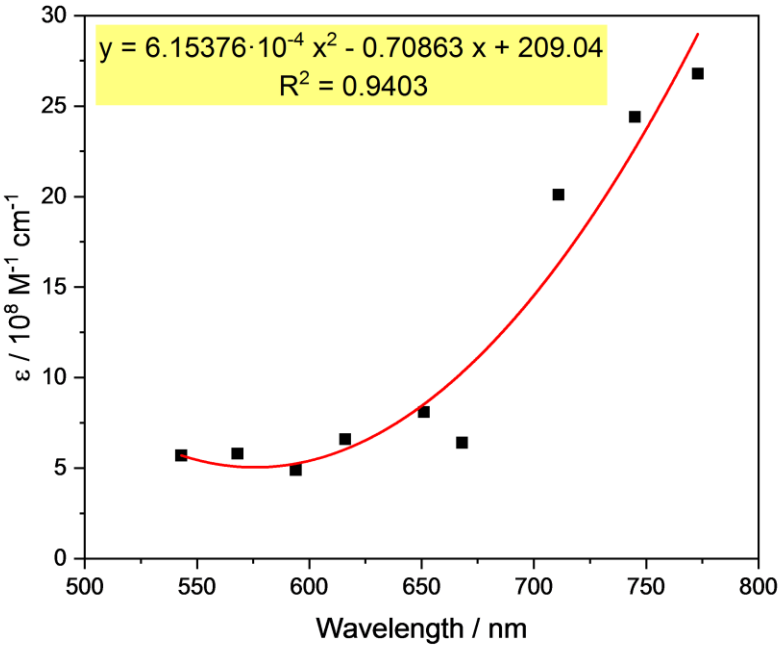

Figure C3. 7 Molar extinction coefficient values (ε) of AuNSt depending on their LSPR wavelength.

3.3.3.2 Morphological analysis, Size & ζ-potential characterisation

TEM images of AuNSt were taken as described in Section 3.2.4.2 to characterise their size and morphology. As illustrated in Figure C3.8 (top and centre images), it can be observed that AuNSt synthesised with 50 µL of seeds (and therefore exhibiting large LSPR values) have a maximum size between 100 – 200 nm if measured from tip to tip. However, the majority of AuNSt are smaller than 100 nm. They show a quite asymmetric morphology, with a varying number of tips

and protrusions grown from the original seeds. The sample polydispersity results in wider absorption peaks, as previously discussed in Section 3.3.1.2.

In order to visualise morphological differences during the growth process, two samples are compared (Figure C3.8 bottom) corresponding to AuNSt displaying LSPR values at 550 nm (bottom left) and 739 nm (bottom right). It is clear that smaller plasmon shifts represent a smaller growth from the gold seeds therefore remaining more spherical, while larger plasmon shifts lead to star-shaped NPs. Furthermore, several images from AuNSt with LSPR values tuned at 752, 713 and 692 nm were analysed using the software ImageJ to calculate their average size (over 100 AuNSt measured from tip to tip for each sample), being 105 ± 29, 103 ± 27 and 78 ± 19 nm, respectively. This exact 3 samples were also studied by DLS, whereby estimated average sizes were 98.2, 89.9 and 81.9 with polydispersity indexes of 0.192, 0.206 and 0.180, respectively (Figure C3.9a). It is interesting to note that DLS size estimations are smaller than those obtained by analysing TEM images by ImageJ, despite the fact that DLS measures the hydrodynamic size of colloids in suspension. However, DLS technique bases its calculations on the Brownian movement of a sphere in solution, therefore the size calculation for AuNSt might be a good estimation (especially for comparison from batch to batch) but cannot be considered as accurate as manual calculation from TEM images. Anyhow, both ImageJ and DLS calculations lead to similar sizes and, at the same time, provide similar results in terms of sample polydispersity.

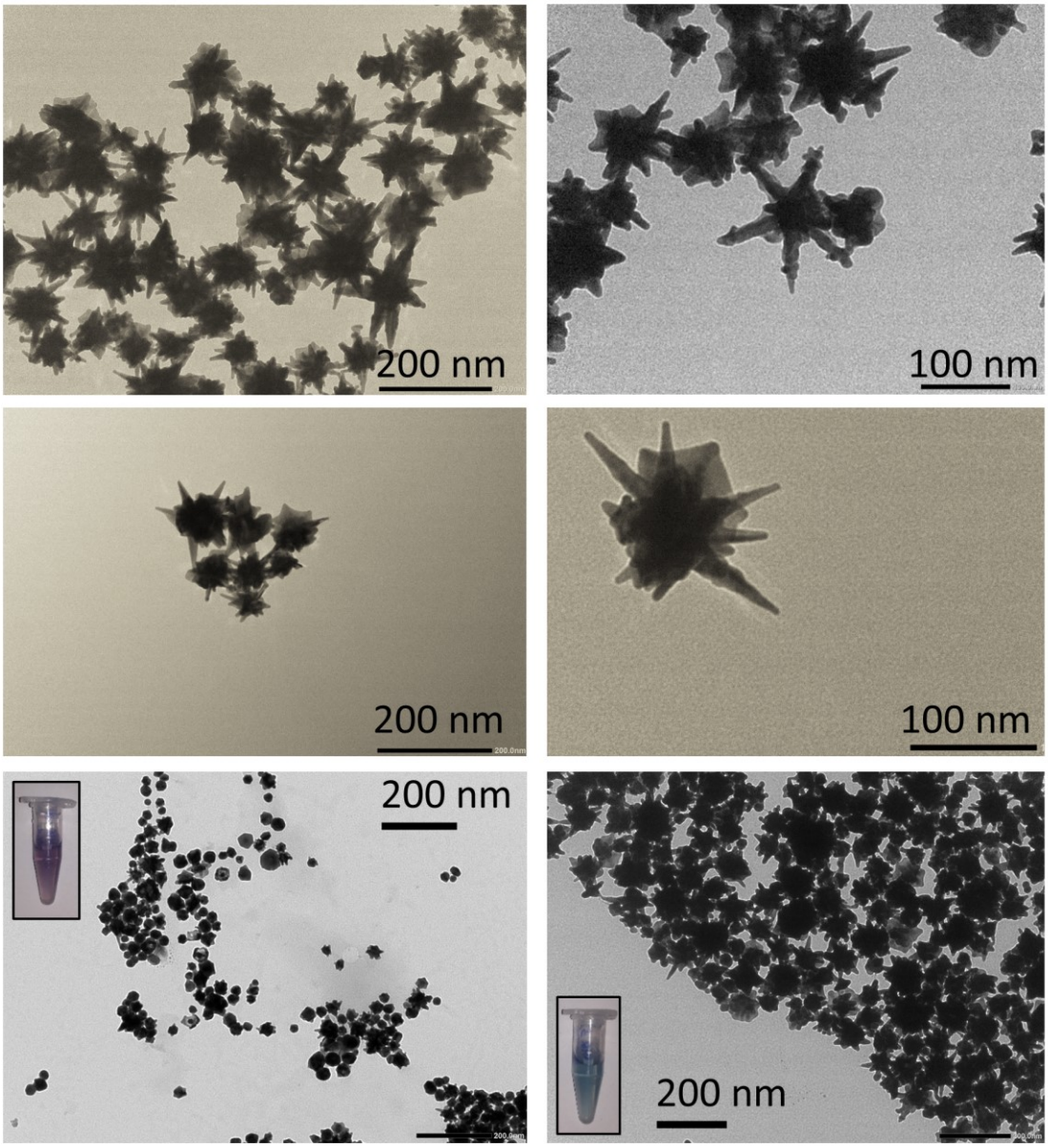

Figure C3. 8 TEM images of AuNSt samples. Top and centre images correspond to AuNSt synthesised using 50 µL of seeds, captured using magnification between X50k – X120k. Bottom images correspond to AuNSt synthesised using 500 µL of seeds and exhibiting a 550 nm LSPR (left) and using 75 µL of seeds resulting in a 739 nm LSPR (right). Same magnification is used in both cases (X40k).

In addition, a Zetasizer was also used to compare the surface charge of AuNSt stabilised with different coating molecules (Figure C3.9b). All of them show negative ζ-potential values equal or above 20 mV in absolute terms, which indicates a good NP stability due to electrostatic repulsions. Citrate-capped AuNSt showed the greater surface charge generated by the three carboxylic groups it possesses, whereas PEG-capped AuNSt showed the lowest surface charge due to the big size of this polymer and the presence of a single carboxylic group per molecule.

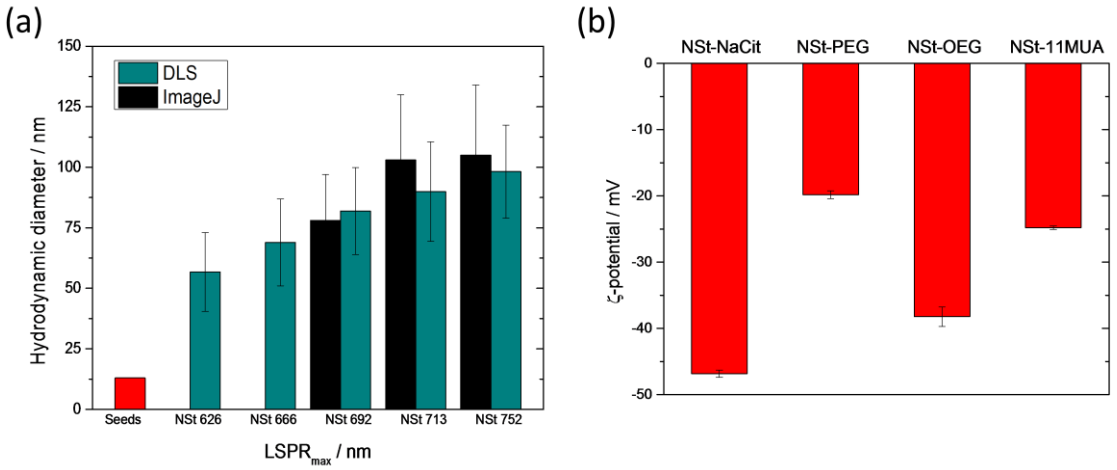

Figure C3. 9 Zetasizer analyses of AuNSt. (a) Size analysis of AuNSt with different optical properties performed by DLS and manual measurement of TEM images using ImageJ software. (b) ζ-potential analysis of AuNSt coated with different stabilising agents (sodium citrate, PEG, OEG, 11-MUA).

3.3.3.3 Refractive index sensitivity of AuNSt

To finish with the basic characterisation of AuNSt, a refractive index (RI) sensitivity study was performed. It is well known and documented that the SPR of noble metal NPs redshifts as the RI of the surrounding environment increases, which form the basis of LSPR-based colourimetric sensing approaches [336]. Hence, a nanomaterial with a high RI sensitivity will be more suitable for these type of sensing assays. To compare the performance of AuNSt with other type of NPs, water – glycerol mixtures of varying proportions were used to modify the RI of the medium and extinction spectra were recorded to observe the plasmon shift (Figure C3.10a). The plasmon peak shifted from its initial wavelength of 772 nm in an aqueous solution (100% water) to 820 nm in solutions containing 80% glycerol or above. Considering the RI for water (1.33) which increases as more glycerol is added (until 1.47, the RI of glycerol), the RI sensitivity of AuNSt can be calculated as the plasmon shift observed divided by refractive index unit (RUI). This value corresponds to the slope of Figure C3.10b, or 386 nm/RIU. This value, if compared with AuNPs of different morphologies, is only outperformed by some gold nanobranches and nanobipyramids, reaching 703 and 540 nm/RUI, respectively. However, AuNSt showed a better sensitivity than other morphologies such as gold nanospheres (44 nm/RUI), nanocubes (83 nm/RUI), nanorods (195 – 288 nm/RUI) or even certain nanobipyramids (150 – 212 nm/RUI) [336].

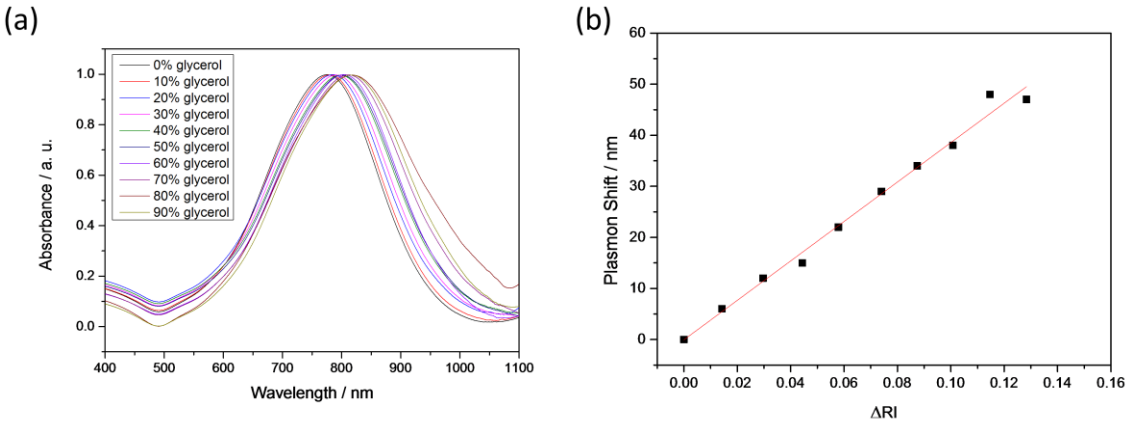

Figure C3. 10 The RI sensitivity of AuNSt was calculated using water – glycerol mixtures and measuring their UV-Vis spectra (a) to observe the plasmon shift and then plot it against the RI variation (b).

3.3.4 Peroxidase-mimicking activity of AuNSt

A detailed kinetic study was performed prior to the application of AuNSt in colourimetric biosensors, in order to understand their potentials and limitations. As it has been previously reported, AuNPs exhibit a strong peroxidase-like activity among other nanozyme activities [97]. This has been extensively studied for gold nanospheres elsewhere [219], but a deep analysis on how AuNSt behave in this matter is lacking. Thus, 200 pM of AuNSt stabilised with different molecules were incubated with TMB in an aqueous solution containing H_2O_2 6%. After 20 minutes, the samples were analysed by UV-Vis spectroscopy (Figure C3.11), showing different performances in terms of TMB oxidation depending on the surface modification. No signs of TMB oxidation were observed when AuNSt were stabilised with 11-MUA, while a varying degree of TMB oxidation took place with the other coating layers.

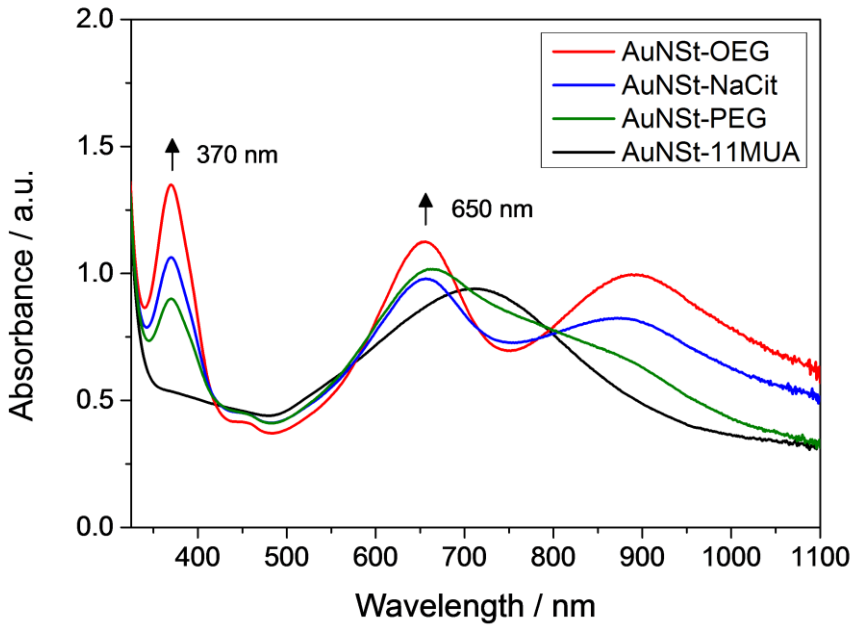

Figure C3. 11 UV-Vis spectroscopy analysis of TMB oxidation. 200 pM AuNSt coated with different molecules were mixed with 0.1 mM TMB in an aqueous solution containing 6% H_2O_2. The spectra were collected after 20 min of reaction.

After these preliminary observations, a more detailed analysis was performed to quantify the nanozyme activity of different AuNSt. In this line, a solution containing 100 pM AuNSt synthesised with different optical properties (thus different sizes) was added to different concentrations of TMB ranging from 0 to 0.5 mM in the presence of 6% H_2O_2 (Figure C3.12a). The oxidation of TMB into its radical cation (TMB^+) was observed after 20 min of reaction by measuring the absorbance of the solution at 370 nm [162]. This value was used to calculate first the concentration of oxTMB generated using the Beer-Lambert law and then the reaction rate as reported by McVey and co-workers [219]. The resulting data were plotted and fitted using the Hill equation (Equation C3.1), which enabled to determine several kinetic parameters (Table C3.3). Comparing the data of the three AuNSt batches with different LSPR values, it is observed that AuNSt with LSPR located at larger wavelengths lead to a larger maximum rate of reaction and therefore to a larger turnover number (calculated as the ratio between the maximum reaction rate and the catalyst concentration) (Figure C3.12b). These observations are in agreement with previous studies, where nanostructures with higher surface area-to-volume ratio see their catalytic properties enhanced [134]. As it has been discussed in Section 3.3.3.2, larger LSPR values are observed for AuNSt with a larger gold deposition during the synthesis,

which provide the AuNSt with sharper and longer tips and therefore a larger gold surface acting as catalyst centre.

On the other hand, a similar study was performed using AuNSt with similar optical properties but stabilised with different coating molecules (i.e. citrate-, PEG-, OEG- and 11-MUA-capped AuNSt). This analysis (Figure C3.12c and C3.12d) showed differences in the turnover number for oxidising TMB, which implies that the 3-dimensional configuration of the SAMs onto the gold surface and the degree of surface coating play an important role in the capability of AuNPs to act as nanozymes [59]. This way, 11-MUA is expected to form a highly dense SAM exposing the carboxylic groups to the outside, due to the hydrophobic interactions between the aliphatic chains. This would impede the substrate (TMB) to reach the gold surface, thus explaining the virtually non-existent peroxidase-like activity measured. In the case of AuNSt-PEG, the hydrophilicity of the chains would avoid the formation of highly dense SAMs, leading to increased catalytic rates as a result of a better surface accessibility by the substrate. Surprisingly, AuNSt-OEG showed a significantly higher peroxidase-like activity: a 10-fold increase is observed. Several hypotheses can be posed explaining this. First, recent studies have shown that long polymeric chains are arranged following the dumbbell model [337], resulting in a random coil adjacent to the gold surface which would reduce the substrate adsorption rate. However, the smaller length of OEG SAMs could result in a helical conformation where two consecutive O atoms of the OEG chain would orientate with an angle of 90 ˚, generating an electrostatic field enhancement in the region next to them and forming strong hydrogen bond structures with surrounding H atoms from water molecules [338]. Consequently, helical OEG layers strongly absorb water, serving as a template for water nucleation and enabling a faster diffusion of TMB molecules towards the gold surface, which results in a much higher catalytic rate.

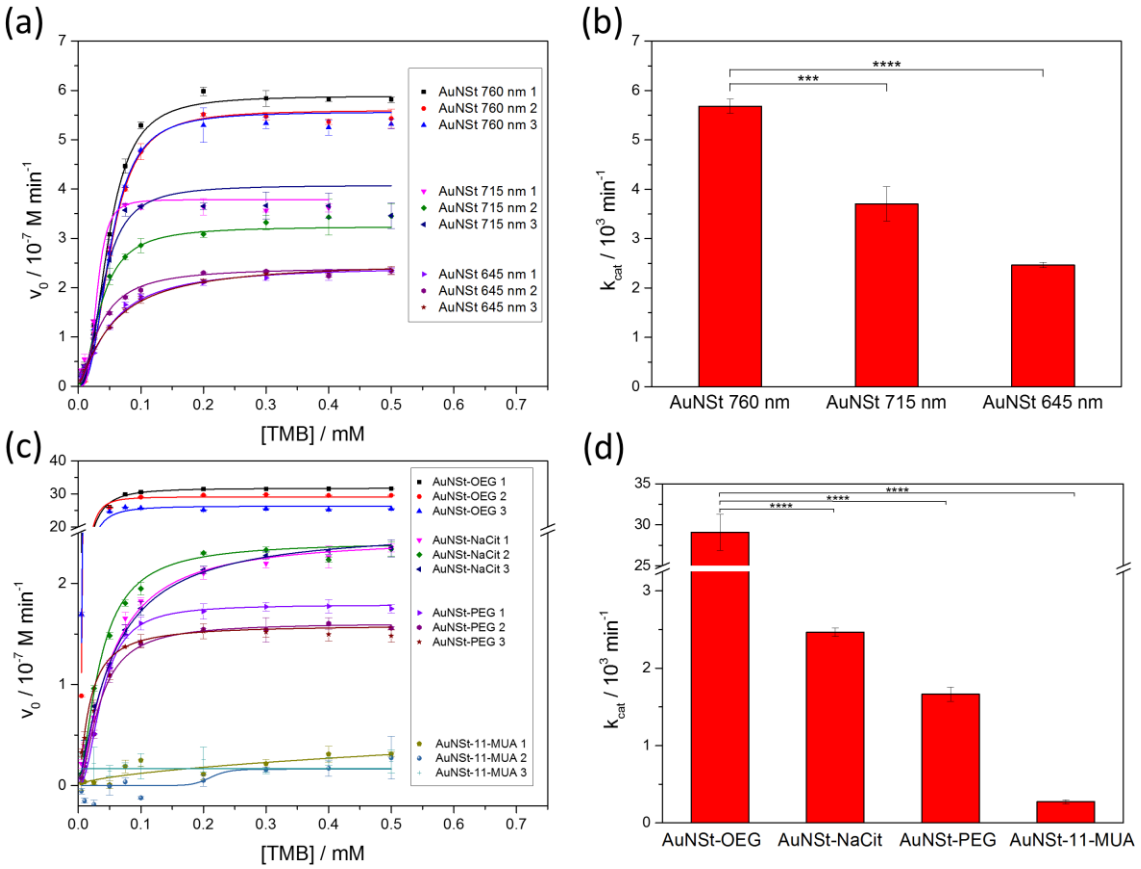

Figure C3. 12 Characterisation of the peroxidase-like activity of AuNSt depending on the size and surface modifications. (a) Kinetic analysis of AuNSt-NaCit with different sizes in the presence of varying concentrations of TMB (0 – 0.5 mM) and 6% H_2O_2. (b) Comparison of the turnover number observed for AuNSt-NaCit with different sizes. (c) Kinetic analysis of AuNSt coated with different stabilising molecules in the presence of varying concentrations of TMB (0 – 0.5 mM) and 6% H_2O_2. (d) Comparison of the turnover number observed for AuNSt coated with different stabilising molecules. Data in a and c are fitted to a Hill equation while a one-way ANOVA is performed to analyse data in b and d.

$$v_0 = \frac{v_{max}\,[S]^n}{K_M^n + [S]^n} \qquad (Equation\ C3.1)$$

v_{max} and K_M were automatically calculated using Origin software, after fitting the results obtained in the kinetic analysis (Figure C3.12a and C3.12c) to a Hill model. The turnover number (K_{cat}) was calculated as $v_{max}/[E]$, where [E] is the enzyme concentration used (in this case, the concentration of AuNSt used for the assay, which equals 100 pM). Finally, the catalytic efficiency is calculated as K_{cat}/K_M, reflecting both binding and catalytic effects, which indicates how the velocity varies depending on the frequency of enzyme-substrate combination events.

		v_{max} / 10^{-7} M min^{-1}	K_M / µM	K_{cat} / min^{-1}	K_{cat}/K_M / μM^{-1} min^{-1}
LSPR Variation	AuNSt 760	5.7 ± 0.18	50 ± 2.1	5680 ± 180	114 ± 8.2
	AuNSt 715	3.7 ± 0.43	35 ± 4.8	3700 ± 427	107 ± 18
	AuNSt 645	2.47 ± 0.07	46 ± 10.5	2470 ± 67	55 ± 13
Surface Variation	AuNSt-OEG	29.1 ± 2.72	18.8 ± 1.19	29070 ± 2715	1550 ± 186
	AuNSt-NaCit	2.47 ± 0.07	46 ± 10.48	2470 ± 67	55 ± 13.0
	AuNSt-PEG	1.66 ± 0.11	30 ± 10.8	1660 ± 110	61 ± 24.6
	AuNSt-MUA	0.30 ± 0.12	233 ± 94.2	300 ± 121	1.5 ± 1.0

Table C3. 3 Michaelis-Menten parameters obtained from the kinetic analyses of different types of AuNSt in relation to their peroxidase-like properties. The data shown in the table are the average of triplicate values.

3.4 Conclusions

The main parameters affecting the synthesis of AuNSt have been discussed in this Chapter, which need to be controlled for achieving a good reproducibility in biosensing applications. A seed-mediated approach has been successfully used for synthesising these NPs, whose optical properties have also been tuned in the NIR region of the spectra, from 600 to 800 nm. In order to do so, the volume of seeds used in the second step of the synthesis has been varied, while the nucleation process is avoided to induce the reduction of gold only on the surface of existent gold nuclei. Afterwards, the stabilisation step has been thoroughly studied, using 5 different coating molecules from which all but one (16-MHA) were successfully attached to the AuNSt surface while preventing their aggregation. The resulting nanostructures have been characterised using a diverse range of techniques, including UV-Vis spectroscopy, TEM or Zetasizer. This way, it was possible to observe by TEM the morphological changes happening during the seeds' growth process. It was determined that not only the size increases as the seeds' volume is decreased, but also that the more they grow, the more they end up resembling a star. Alternatively, a large seeds' volume will lead to a small growth and the NPs end up looking more spherical. Regarding the NPs size, it was changed from the initial 13 nm diameter seeds until up to 105 ± 29 nm for the largest AuNSt. However, it was found a high polydispersity within the AuNSt obtained following this protocol and individual AuNSt measuring over 200 nm from tip to tip have been observed as well. Finally, further characterisation has been done regarding their refractive index sensitivity, a value that indicates how suitable nanomaterials are for plasmonic spectroscopy applications which, for the case of AuNSt, resulted in 386 nm/RIU. This value is higher than that observed for spheres, rods or even some types of bipyramids, which brings hope in terms of their performance for biosensing.

On the other hand, the peroxidase-mimicking activity of AuNSt has been elucidated in this Chapter. First studying how morphological/plasmonic changes affect their efficiency as catalysts and then studying how different surface modifications hinder or promote such activity. Considering that the coloured product generated after applying this step is the basis of any future sensing assay, it is critical to understand how any change in the nanomaterials will affect it. Using TMB as substrate, AuNSt have shown potential to replace enzymes like HRP in certain applications where extreme conditions (such as temperature or pH) do not allow proteins to be used, or simply where their low-cost, stability or versatility may suppose an advantage against their biological counterparts. Further discussion related to POC application of nanozymes can be found in a recently published review [339].

All this information related to the synthesis, stability and nanozyme properties of AuNSt is of paramount importance for successfully developing biosensors that can be applied in real situations, like the development of a *M. bovis* sensor reported in Chapter 5 using smartphones as readout systems. In such a situation, the presence of different molecules within the sample matrix can cause the AuNSt aggregation and prevent the sensor from being functional, therefore being essential to ensure the stability of the nanomaterials. On the other hand, this stabilising layer deposited onto the AuNSt surface must not interfere with their nanozyme properties, as it is based on this phenomenon that the colourimetric signal is generated in such a sensor. Consequently, the AuNSt characterisation discussed in this Chapter not only provides a theoretical framework, but also direct guidelines for a practical application of AuNSt in biosensing.

Chapter 4 Colourimetric applications of AuNSt and smartphone-based quantification

4.1 Introduction

Food analyses require both rapidity and reliability while satisfying the sensitivity thresholds legally established for each contaminant. POC assays have emerged as the alternative to archaic methodologies involving sample collection, sending to the lab and waiting for the test results to arrive before making an informed decision on its security. POC market, thus, is expected to reach USD 25.4 million by 2022, expanding at a Compound Annual Growth Rate of 5.7% [340]. Some current limitations in this regard include the difficulties in miniaturising analytical equipment, the need of trained personnel for performing the assay and the generally high cost of reliable tests. The wide distribution of smartphones worldwide and their increasingly powerful data processing software have opened a path for using them as bioassay readers. In this context, colourimetric approaches can be easily combined with smartphones considering that they are all provided with an excellent camera serving the purpose of a spectrophotometer. Several review articles have been published in the last decade discussing the potential of smartphones for biosensor development [144,145], mainly revolving around optical or electrochemical detection. However, while smartphone cameras can be used for data acquisition in the case of optical sensors, an external device needs to be bought and connected to the smartphone for electrochemical analyses. This is why optical biosensors may have a greater short-term potential for POC analysis, especially if sensing in low-income parts of the world is considered.

Immunochromatographic assays (ICA) are among the most common approaches for colourimetric biosensor development using AuNPs. They were initially thought as qualitative approaches, where the immobilisation of antibody-conjugated AuNPs in a specific area of the paper strip (test line) would result in a coloured line in the presence of the target analyte that could be visually detected. The success of this simple colourimetric approach spread over many working areas, including clinical analyses for detecting thrombin [341], miRNA [342] or cancer cells [343]; water samples analysis for detection of contaminant ions such as Cd^{2+} [344], Cr^{3+} and Cr^{6+} [345] or Hg^{2+} [346]; pesticides detection including carbaryl and endosulfan [347] or carbofuran and triazophos [348]; toxins and pathogens detection in food samples such as aflatoxin [349], aminohydantoin [350], clenbuterol [351] or *S. enteritidis* [352]; or drugs monitoring including sulphonamides [353], enrofloxacin residues [354] or morphine [355]. Nowadays, many of these examples have moved to the next stage, existing 3D-printed simple accessories that attach to smartphones and enable fast and sensitive POC quantification of LFA, while maintaining consistency between different measurements [356]. In parallel, smartphone

application algorithms have also evolved to enable quantification of these coloured samples [357], achieving inter-phone repeatability.

Other approaches leading to the generation of a colourimetric signal using AuNPs that have been widely exploited include aggregation of NPs in liquid-based assays or catalytic systems where AuNPs are used as nanozymes together with a chromogenic substrate. The former has been used for detecting lectins [358], foodborne pathogens [220] or cocaine [359] among others. These assays are based in the colour change undergone by AuNPs, from red to blue, as they form clusters during the aggregation process. Moreover, due to the extremely high extinction coefficients of AuNPs, they are highly sensitive and can be used at very low concentrations (nanomolar range). Nanozyme based systems, on the other hand, lead to a colour signal generally after oxidising a chromogenic substrate (such as TMB, ABTS, OPD or similar). Therefore, as opposed to the previous approaches, the colour is not generated by the AuNPs themselves. All the possibilities offered by nanozymes, including colourimetric assays, are discussed in Section 1.3. In these cases, where the assay is performed in solution rather than in a solid substrate, similar smartphone gadgets and applications for colour quantification have already been developed adapting the measurement to 96-well microtiter plates [360].

4.1.1 Colour quantification through smartphones

Despite existing several alternatives for colour quantification, none of them has shown a clear dominance over the others for satisfying the demands of colourimetric analyses through smartphones. Hence, there is still controversy around which colour space is best to use, what type of image correction is needed, or how to standardise the colour analyses with different phones. That is to say, a universal approach is needed for quantifying a colourimetric signal. Some of the main colour spaces used nowadays are “Red, Green, Blue” (RGB), “Hue, Saturation, Value” (HSV) and “Lightness, Chromatic axes A/B” (LAB). A recent study used a scoring system for comparing the performance of each one of these colour channels for measuring colour variation and colour intensity in pH strips, filter paper with dropped AuNPs and coloured solutions [361]. It was concluded that HSV and LAB colour space channels never outperformed the best RGB channels in any test. At the same time, inter-phone variability was studied, which ended up being significant for colour intensity quantification but minimal for colour change measurements. This is a key aspect in the development of smartphone-based biosensors, as any limitation regarding the type of smartphone needed for the assay would offset the benefits of a wide distribution of smartphones for biosensing.

4.1.2 Objectives

In this Chapter, the nanozyme activity of AuNSt studied in Chapter 3 is used to generate a colourimetric signal that can be read with a smartphone. The negative effects of functionalising AuNSt with biorecognition elements (mandatory step for developing most biosensing assays) are studied and several alternatives are proposed for overcoming this challenge (Scheme C4.1). On the other hand, a commercially existing smartphone application (RGB Color Detector) was used to extract colour raw data from pictures acquired with the smartphone of AuNSt colourimetric assays. RGB colour space was characterised to find the colour channel that showed the best fit for the system based on peroxidase-mimicking activity of AuNSt. Finally, an in-house developed smartphone box and application were used to measure the colour of pH strips used for milk and wine analyses, to help elucidate how coloured solutions affect the accuracy of these approaches.

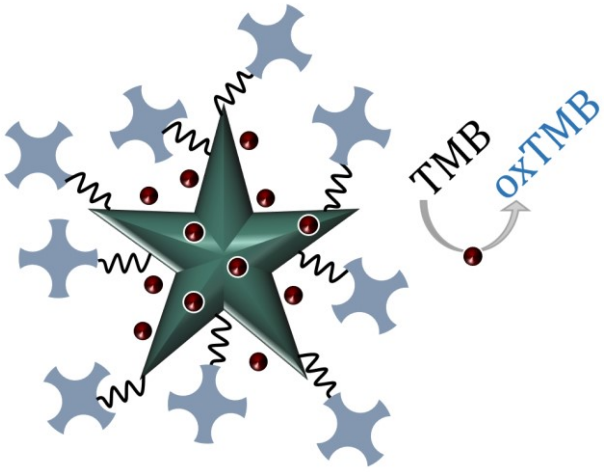

Scheme C4. 1 Streptavidin-functionalised AuNSt after performing a gold enlargement step to restore their peroxidase-mimicking activity, enabling them to generate a colourimetric signal.

4.2 Methods

4.2.1 Reagents and chemicals

O-(3-Carboxypropyl)-O'-[2-(3-mercaptopropionylamino)ethyl]-polyethylene glycol (Mw 5000), Streptavidin from *Streptomyces avidinii*, 4-Morpholineethanesulfonic acid (MES), N-(3-Dimethylaminopropyl)-N'-ethylcarbodiimide hydrochloride (EDC), EZ-Link™ Sulfo NHS-LC-LC-Biotin No-Weigh™ Format, Horseradish peroxidase, TMB/E Single Reagent – Blue color – Horseradish Peroxidase Substrate (soluble), Hydrogen peroxide solution 30 % (w/w), Gold(III) chloride trihydrate ($HAuCl_4 \cdot 3H_2O$, 99.9%), L-ascorbic acid ($C_6H_8O_6$), Silver nitrate (≥ 99.0%), Silver Enhancement Kit, Phosphate buffered saline, Greiner 96 well microplates (flat bottom clear polystyrene) and Nunc-Immuno™ 96 well MicroWell™ MaxiSorp™ (flat bottom) were all purchased from Sigma Aldrich (UK). α-mercapto-ω-amino-polyethylene glicol (Mw 5000) was purchased from RAPP Polymere. TEM Formvar carbon films on nickel grids were purchased from Agar Scientific (UK).

4.2.2 AuNSt functionalisation with streptavidin

AuNSt synthesised as described in Section 3.2.2 were stabilised with a mixture of bifunctional PEG (either α-mercapto-ω-carboxy or α-mercapto-ω-amino) at a final concentration of $2.5 \cdot 10^{-5}$ M and α-methoxy-ω-mercapto PEG at a concentration of $7.5 \cdot 10^{-5}$ M, thus using the neutral methoxy groups to separate the negative charges provided by PEG chains containing carboxylic groups. Then, a one-pot carbodiimide approach was followed to functionalise streptavidin onto AuNSt. In brief, an aqueous solution containing PEGylated AuNSt 500 pM buffered in MES 10 mM were mixed with EDC at different concentrations (0, 10, 100, 500 µM) and streptavidin (100 µg/mL). The samples were left stirring for 2 hours, centrifuged at 1200 rcf and 10 ˚C for 25 min and then the supernatant analysed using an immunoassay to determine the concentration of streptavidin unbound. The supernatant was diluted 1/10 in coating buffer (carbonate/bicarbonate 0.1 M, pH 9.6), added to a microplate (MaxiSorp) and left O/N at 4 ˚C for immobilising any unbound streptavidin. Then, the plate was washed 4 times with PBST and 100 µL of biotin-HRP (dilution 1/6000) added to each well and incubated for 30 min. Finally, the plate was washed another 4 times with PBST and 100 µl of TMB 0.3 mM in citrate solution containing H_2O_2 (0.004%) were added to each well and incubated at RT for 10 min. The oxidation

process was stopped adding 50 µl of H_2SO_4 4 M, and the oxidized product measured using a microplate reader (Multiskan FC microplate photometer from ThermoFisher) set at 450 nm.

4.2.3 Gold enlargement of AuNSt

A growth solution containing $HAuCl_4$ $2 \cdot 10^{-4}$ M and L-AA $5 \cdot 10^{-6}$ M was added to a AuNSt solution buffered with PB 10 mM and incubated for 30 min at RT prior to the addition of the substrate (TMB 0.3 mM in citrate buffer containing H_2O_2 0.004%). The reaction was followed measuring the A_{370nm} (corresponding to the radical cation TMB^+) during the first 10 minutes of reaction.

4.2.4 Silver enlargement of AuNSt

A varying concentration of AuNSt was enlarged using a silver enhancement kit purchased from Sigma Aldrich (SE100) which contains a solution A (silver salt) and a solution B (initiator) that are mixed 1:1 in volume. For achieving the best results, the growth solution containing A and B needs to be diluted 10 times in dH_2O before adding it to the AuNSt. After 10 minutes, TMB was added to a final concentration of 0.3 mM and the $A_{370\,nm}$ measured with the spectrophotometer.

4.2.5 HR-TEM

500 pM of AuNSt were enlarged following the protocol detailed in Section 4.2.3 and 4 µL of these deposited onto a formvar/carbon supported nickel grid by drop-casting and dried O/N. The sample was sent to the Ewald Microscopy Facilities (School of Mathematics and Physics) where it was analysed using a TALOS F200X G2: Scanning/Transmission Electron Microscope.

4.2.6 Colour analysis using “RGB Color Detector”

After exploiting the peroxidase-like activity of AuNSt to oxidise chromogenic substrate TMB, a picture of the coloured solution is taken with a smartphone (Samsung Galaxy J5) from a 10 cm distance while placing the microplate on a white-illuminated screen to reduce the appearance of shadows leading to variations in the light conditions during this critical step. This image is uploaded to the application, which provides Red, Green and Blue values for each spot selected in the picture, as well as values for several other colour spaces including HSL (Hue, Saturation,

Lightness) or HSV (Hue, Saturation, Value). These values are corrected using the background signal generated by an empty well illuminated by the white screen and used to quantify the colour intensity.

4.2.7 Colour analysis using "QuantColorimetryApp"

The microplate containing the coloured solutions (i.e. oxTMB generated by AuNSt) is placed onto the white-illuminated screen of a smartphone while a second smartphone is used for collecting a picture and running the App. Then, the testing images are background subtracted using the algorithm proposed in [362]: $R_T = R_B{}^{\mathcal{F}^{-1}(D_T)}\Big/_{\mathcal{F}^{-1}(D_B)}$, where R_T and R_B are the colour corrected testing and background image respectively, D_T and D_B are the original images taken by camera, and $\mathcal{F}^{-1}$ is the inverse camera response function. The processed LUV colour feature of each solution sample is collected using manually placed label markers in the smartphone App. Finally, the testing result is interpreted using the polynomial model: $\mathrm{h}_\theta(\mathrm{l},\mathrm{u},\mathrm{v}) = \left(\sum_{\mathrm{i}=0}^{4}\sum_{\mathrm{j}=0}^{4-\mathrm{i}}\sum_{\mathrm{k}=0}^{4-\mathrm{i}-\mathrm{j}}\theta_{\mathrm{ijk}}\mathrm{l}^i\mathrm{u}^j\mathrm{v}^k\right)^{10}$, where l, u, v are the three colour channels of the LUV colour feature and θ is the feature vector [363].

React Native [364] is an open software framework used to construct the smartphone App for data generation and user interfaces, while Flask [365] is a web framework that was used to develop the cloud service for image pre-processing and result interpretation. Tensorflow [366] is an open software library used as the machine learning framework. Finally, Adam Optimiser [367] was used to perform the global optimisation and calculate the optimal feature vector.

4.3 Results and discussion

4.3.1 Inhibition of peroxidase-like activity of streptavidin-functionalised AuNSt

Most diagnostic assays involving AuNPs require them to be functionalised with biorecognition elements to target specifically the desired analyte. However, as it has been described in Chapter 3, any surface modification might affect their catalytic and plasmonic properties. In order to characterise this effect, 10 different PEGylated AuNSt samples were functionalised with streptavidin varying the type of PEG used for stabilising them and the amount of EDC used, following the protocol described in Section 4.2.2 and as summarised in Table C4.1. The supernatant (SN) obtained after washing the AuNSt was collected, used to immobilise any unbound streptavidin in a microplate and analysed by a direct immunoassay as described in Section 4.2.2. To quantify the amount of streptavidin present in each supernatant (and therefore estimate the amount of streptavidin bound to the AuNSt), a calibration curve was prepared immobilising different concentrations of streptavidin ranging from 0 to 10 µg/mL thus reaching the maximum concentration possible in the supernatants after diluting them 10 times for performing the immunochemical assay. It is shown in Figure C4.1a that a *plateau* effect is reached at a streptavidin concentration of 3 µg/mL, being higher concentrations undistinguishable among them. A linear trend is observed between 0.1 and 3 µg/mL, which enables for quantification in this range (Figure C4.1b).

	F1	F2	F3	F4	F5	F6	F7	F8	F9	F10
PEG type	ω-Carboxy (C)				ω-Amino (A)				C	A
EDC / µM	0	10	100	500	0	10	100	500	-	-
Strept / µg mL^{-1}	100	100	100	100	100	100	100	100	-	-

Table C4. 1 Set of conditions used for functionalising AuNSt with streptavidin following a one-pot approach.

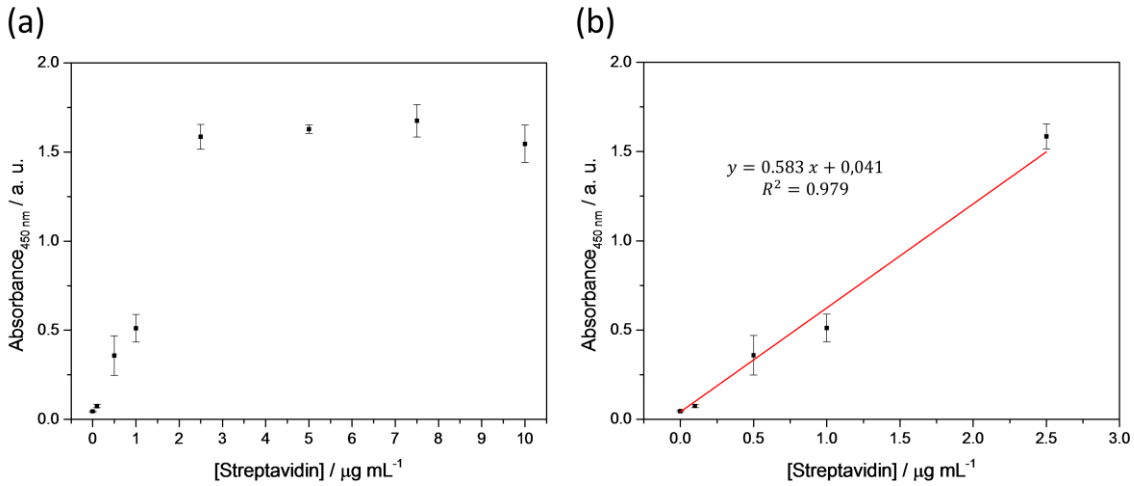

Figure C4. 1 Direct immunoassay for streptavidin detection fitted to a calibration line between 0 – 3 µg/mL range.

The analysis of the supernatant solution after centrifuging the functionalised AuNSt showed that samples where a lower EDC concentration was used had a slightly higher amount of streptavidin attach to the AuNSt (Table C4.2). That seems to indicate that EDC did not play a significant role in the functionalisation and electrostatic interactions were the main forces leading to the coverage of AuNSt surface with streptavidin. Less than 5% of the initial streptavidin concentration was detected in any supernatant after washing the functionalised AuNSt, probably due to the high concentration of NPs used for this step (500 pM).

Finally, a peroxidase-like study similar to what was discussed in Section 3.3.4 was performed. However, no absorbance signal at 370 nm was observed whatsoever after mixing streptavidin-coated AuNSt with TMB and H_2O_2 (see Figure C4.6 in Section 4.3.2.4), which can be explained by the formation of a protein-layer onto the AuNSt hindering the free diffusion of TMB towards their surface. Gu and co-workers also arrived to a similar conclusion after functionalising AuNS with antibodies and trying to exploit their peroxidase-like activity [368].

	$Abs_{450\ nm}$ / a. u.	$[Strept]_{dil\ SN}$ / µg mL^{-1}	$[Strept]_{SN}$ / µg mL^{-1}	$[Strept]_{SN\text{-}Blank}$ / µg mL^{-1}	Strept. Bound / %
F1	0.1697 ± 0.013	0.221	2.21	2.18	97.8
F2	0.1616 ± 0.013	0.207	2.07	2.04	98.0
F3	0.2016 ± 0.021	0.275	2.75	2.73	97.3
F4	0.2280 ± 0.009	0.321	3.21	3.18	96.8
F5	0.1488 ± 0.001	0.185	1.85	1.82	98.2
F6	0.1501 ± 0.005	0.187	1.87	1.85	98.2
F7	0,1743 ± 0,007	0.229	2.29	2.26	97.7
F8	0,1818 ± 0,003	0.241	2.41	2.39	97.6
F9	0,0421 ± 0,000	0.002	-	-	-
F10	0,0425 ± 0,001	0.003	-	-	-

Table C4. 2 Analysis of the supernatant of streptavidin functionalised AuNSt using a direct immunochemical assay.

4.3.2 Autocatalytic enlargement of AuNSt

To restore the peroxidase-like activity of AuNSt lost after functionalising them with streptavidin, an autocatalytic enlargement is proposed following successful previous studies [369,370]. Herein, the intrinsic property of metallic NPs to catalyse the reduction of metallic ions is exploited to overcome the limitations caused by their surface functionalisation. Au^{3+} ions are used as a gold source for the enlargement and L-AA as a weak reducing agent to promote the reduction to Au^0 only in the presence of pre-existent AuNSt. Previous studies using AuNPs and H_2O_2 as reducing agent have proved not only the deposition of gold on nanocrystalline faces, but also the growth of nanocrystals taking place at the intersection of faces to form new seeds after detaching from the surface [369]. Several parameters, however, needed to be optimised for applying this approach to restore the peroxidase-like activity of protein-functionalised AuNSt specifically and thus retrieve their potential for biosensing applications.

4.3.2.1 Optimisation of reagent concentration for autocatalytic enlargement

600 pM AuNSt were mixed in a 10 mM PB solution with $AuCl_4^-$ $2{\cdot}10^{-4}$ M and a varying concentration of L-AA (ranging from $5{\cdot}10^{-3}$ to $5{\cdot}10^{-7}$ M), following the conditions optimised by Zayats and co-workers for AuNS with minor modifications. Considering that H_2O_2 affects the

peroxidase performance of AuNSt, this reducing agent was not used and L-AA was used instead, as previously reported elsewhere [370]. The solution was left for 10 min to perform the enlargement and then TMB was added at 0.3 mM to characterise the peroxidase-like activity of enlarged AuNSt. Figure C4.2a shows that high concentrations of L-AA led to nucleation and formation of new Au clusters where no AuNSt had been added, as the colour solution changed to red and further UV-Vis analyses showed a characteristic AuNS peak (Appendix, Figure A2). However, no TMB oxidation was observed, which might be explained by the strong reducing conditions where TMB was added. When L-AA was reduced, on the other hand, no AuNP formation was observed and evident colour differences were observed after adding TMB, especially for L-AA concentration at $5 \cdot 10^{-6}$ M. To further characterise the effect of L-AA concentrations, a lower range was tested (from $5 \cdot 10^{-5}$ to $5 \cdot 10^{-9}$ M) keeping the rest of parameters constant (Figure C4.2b). Only the highest L-AA concentration showed some indications of AuNP generation translated as a slight colour change to purple tonalities. However, L-AA concentrations down to $5 \cdot 10^{-7}$ showed signs of TMB oxidation where no AuNSt had been added, meaning that either new nucleation was still happening at low scale or that an excess of other reagents was causing this effect. Considering the high colour intensities observed after performing the TMB oxidation step for samples containing AuNSt, it was suggested that other reagents concentration (i.e. Au ions) might be higher than necessary, explaining these observations.

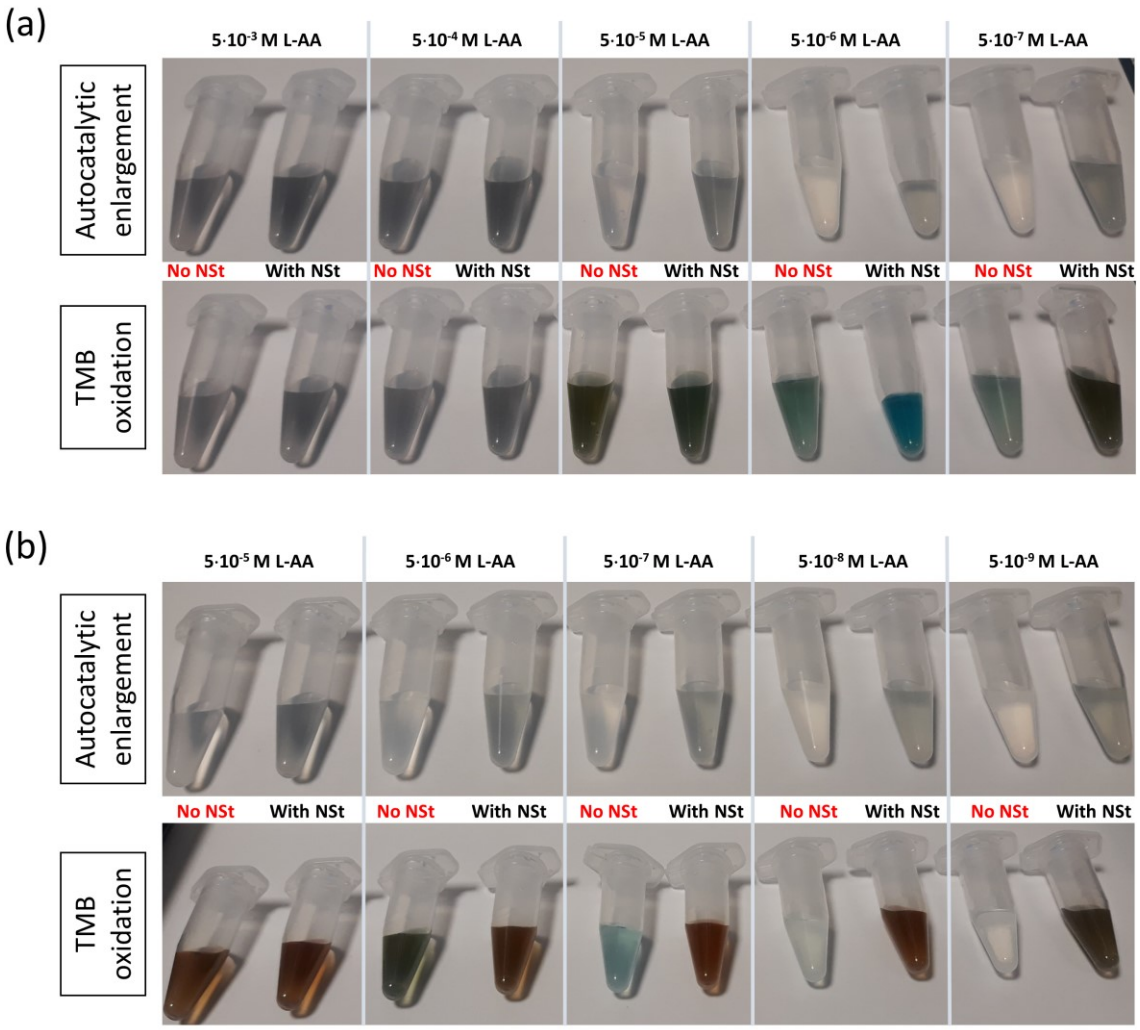

Figure C4. 2 Colour signal generated after mixing fixed concentrations of AuNSt and $AuCl_4^-$ with a varying concentration of L-AA in a high (a) and low (b) concentration range. TMB was added to all samples to determine their potential as peroxidase-mimics.

After realising that a high concentration of $AuCl_4^-$ mixed with commercial TMB (containing small amounts of H_2O_2) led to the formation of gold clusters and, therefore, to the oxidation of TMB (Figure C4.3a), it was proposed to reduce its concentration 10 and 100 times while keeping L-AA concentration fixed at $5{\cdot}10^{-6}$ M (since it was the highest concentration that did not lead to a colour change in the solution after the enlargement step). Figure C4.3b shows both visually and spectroscopically that reducing the Au ions concentration 10 times was enough to avoid the nucleation of gold where no AuNSt had been added, thus being Au^{3+} only reduced onto AuNSt which subsequently led to TMB oxidation (red graph in Figure C4.3b). A further decrease of Au ions down to $2{\cdot}10^{-6}$ M, on the other hand, did not provide Au enough to achieve enough AuNSt enlargement to generate a colourimetric signal after incubating the sample with TMB (blue graph in Figure C4.3b).

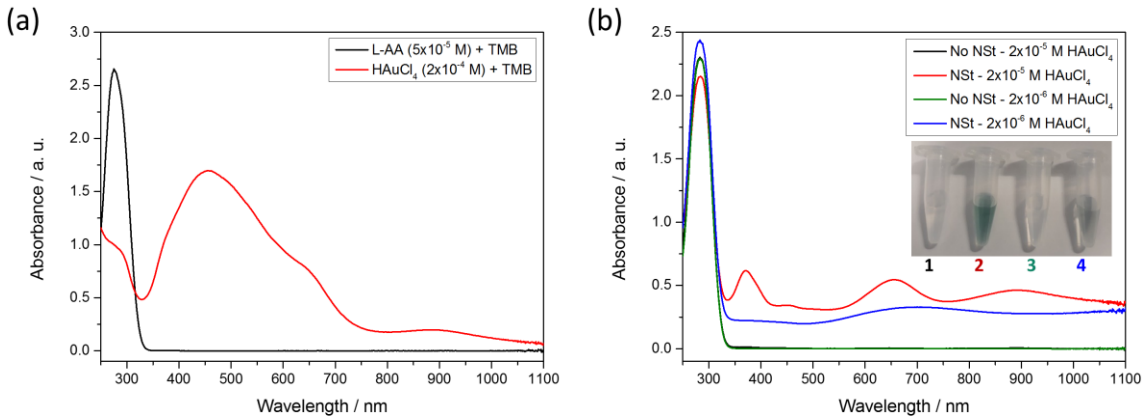

Figure C4. 3 (a) Spectroscopic characterisation of upper threshold concentrations for L-AA and $HAuCl_4$ mixed with TMB 0.3 mM to discard signal generation in negative samples. (b) Effect of the gold salt concentration in the restoration of the peroxidase-like activity of enlarged AuNSt (500 pM).

In summary, it was concluded that a L-AA concentration higher than $5 \cdot 10^{-5}$ M led to nuclei formation in the absence of AuNSt, therefore a smaller amount needs to be used to avoid false positives. On the other hand, $AuCl_4^-$ concentration was fixed at $2 \cdot 10^{-5}$ M, as higher concentrations would also lead to the formation of AuNPs after incubating the samples with TMB and lower concentrations did not provide Au ions enough to generate the sufficient colourimetric signal.

4.3.2.2 Growth time

Further analysing the effects that the gold salt concentration has in the autocatalytic enlargement, it was observed that concentrations equal or higher than 10^{-4} M led to the formation of AuNPs, which eventually would lead to the oxidation of TMB. Interestingly, this effect only happened in the negative samples where no AuNSt were present, easily surpassing the signal generated when enlarged AuNSt were used for oxidising TMB (Figure C4.4a). On the other hand, there was no doubt that a higher gold concentration led to a better performance of the assay, rising the signal generated by the peroxidase-like activity of enlarged AuNSt (measured as the $A_{370\ nm}$) from 1 to 1.5 a. u. by doubling the amount of gold used in the enlargement step. Therefore, the main problem yet to solve was the unspecific nucleation taking place in the negative samples. Varying the enlargement incubation time, it was observed that this phenomenon diminished as the growth time increases. Figure C4.4b shows that if TMB is added after 5 minutes of gold growth, it favours the nucleation of unreacted gold to form AuNPs and oxTMB quickly forms. However, when this growth time is increased to 30 min (Figure C4.4c)

gold is not reduced to form AuNPs and no TMB oxidation happens unless AuNSt were present in the solution.

This manner, the concentration of gold salt used for the enlargement step could be increased from $2 \cdot 10^{-5}$ M to $2 \cdot 10^{-4}$ M, rising the signal coming from the oxidation of TMB by 500 pM of enlarged AuNSt from 0.6 (Figure C4.3b) to 1.5 a. u (Figure C4.4c), while avoiding the nucleation issue in negative samples.

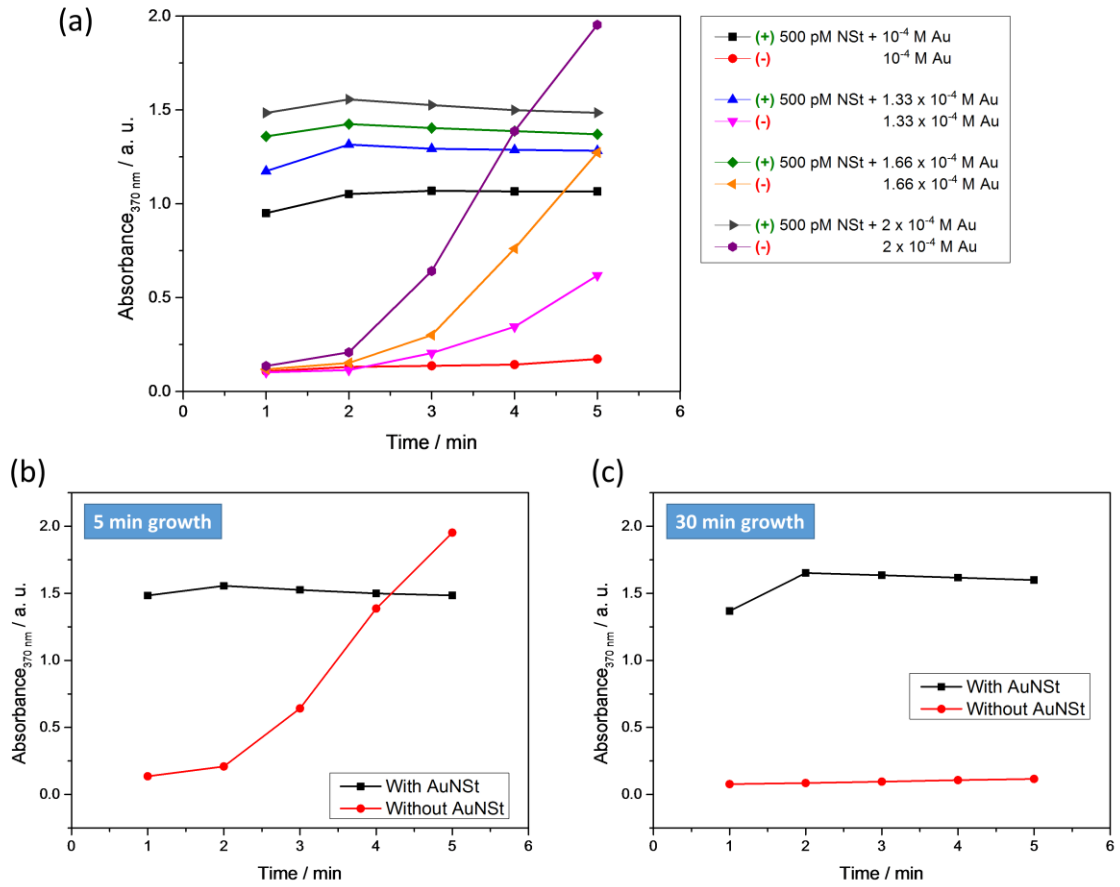

Figure C4. 4 (a) 500 pM AuNSt were enlarged with a fixed concentration of L-AA ($5 \cdot 10^{-6}$ M) and a varying concentration of Au^{3+} (from 10^{-4} to $2 \cdot 10^{-4}$ M) prior to the addition of TMB 0.3 mM. oxTMB formation is characterised by measuring A_{370nm}. (b) Samples enlarged for 5 minutes with the highest concentration of Au^{3+} ($2 \cdot 10^{-4}$ M) and $5 \cdot 10^{-6}$ M L-AA led to TMB oxidation regardless of the presence of AuNSt, whereas only samples containing AuNSt led to oxTMB when the enlargement time was increased to 30 minutes (c).

4.3.2.3 HR-TEM

Previous studies had shown that crystal growth can happen following two different mechanisms: either the original NPs are used as seeds and become larger as new metallic ions get reduced in their surface or they favour the nucleation process at their surface and then the formed nuclei get detached [371]. The former situation leads to a plasmon redshift, due to the morphological

changes in the NPs, while the latter situation sees no plasmon shift, retaining the NPs their original morphological properties.

A sample of enlarged AuNSt was prepared and analysed by HR-TEM as described in Section 4.2.5 and it was observed that, despite retaining their star-like morphology, some growth had happened at their surface (Figure C4.5), displaying round and less spiky tips if compared to those from AuNSt shown in Figure C3.8. Moreover, a closer look at the sample indicates the presence of small Au clusters around 2 nm in diameter which seem to have formed at the AuNSt surface and get detached from there.

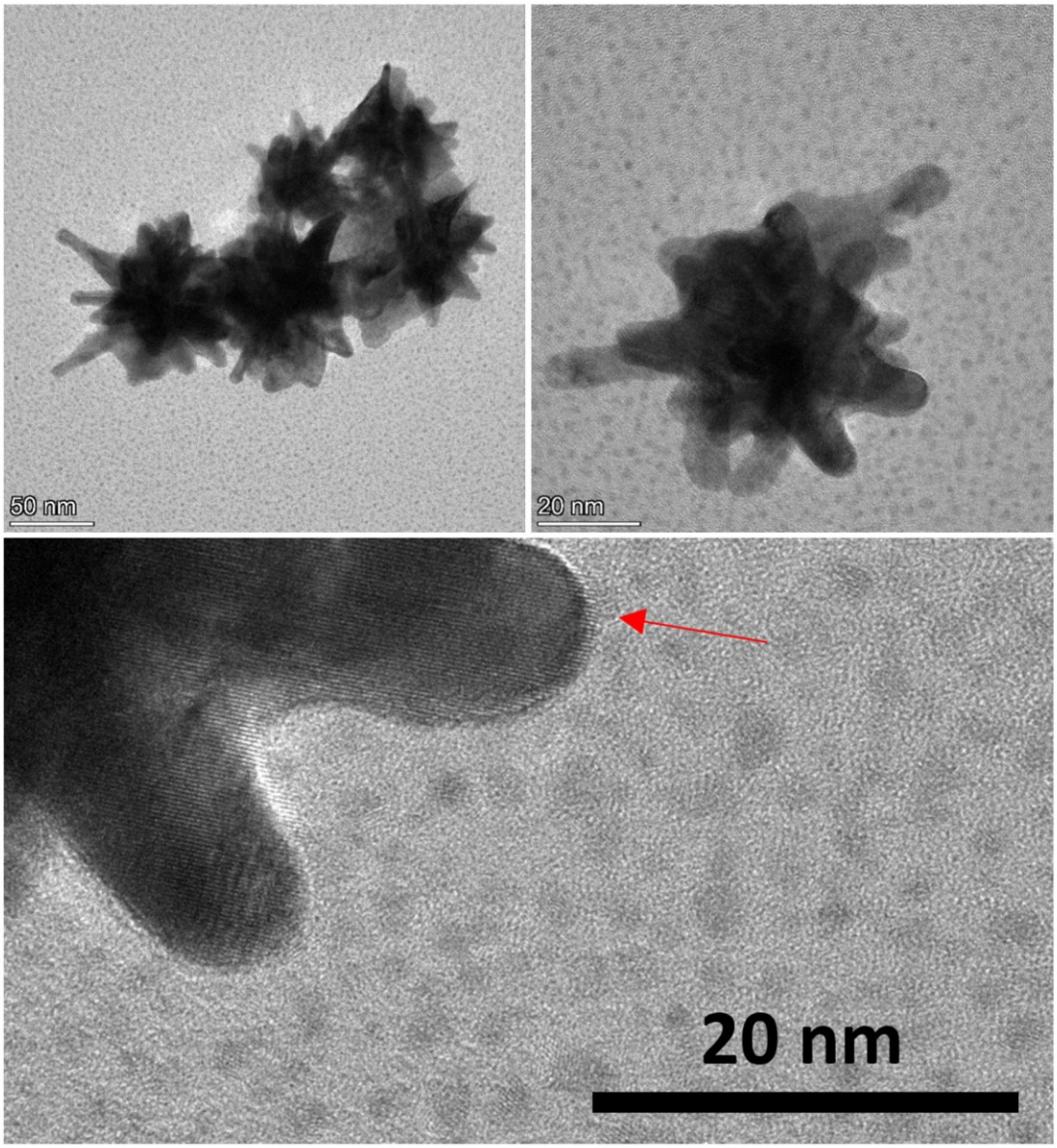

Figure C4. 5 HR-TEM image of AuNSt after 30 min of reaction with $HAuCl_4$ $2{\cdot}10^{-4}$ M and L-AA $5{\cdot}10^{-6}$ M in PB 10 mM.

4.3.2.4 Restoration of peroxidase-like activity of streptavidin-functionalised AuNSt

A growth solution containing $AuCl_4^-$ $2 \cdot 10^{-5}$ M and L-AA $5 \cdot 10^{-6}$ M buffered in PB 10 mM was incubated 30 minutes with different AuNSt samples prior to the addition of the substrate (TMB 0.3 mM). The reaction was followed measuring the $A_{370\ nm}$ to determine the presence of the radical cation TMB^+. In parallel, AuNSt samples that did not undergo the enlargement step (i.e. they were not incubated with the growth solution) were also analysed to discard any residual nanozyme activity. Figure C4.6 shows that both PEGylated AuNSt and streptavidin-functionalised AuNSt successfully restored their peroxidase-like activity and were capable of oxidising TMB and generating a colourimetric signal. Additionally, and following previous observations, the oxidation process happened very quickly, reaching saturation after 2 minutes of reaction. Streptavidin-functionalised AuNSt that were not enlarged, on the other hand, did not show any sign of TMB oxidation.

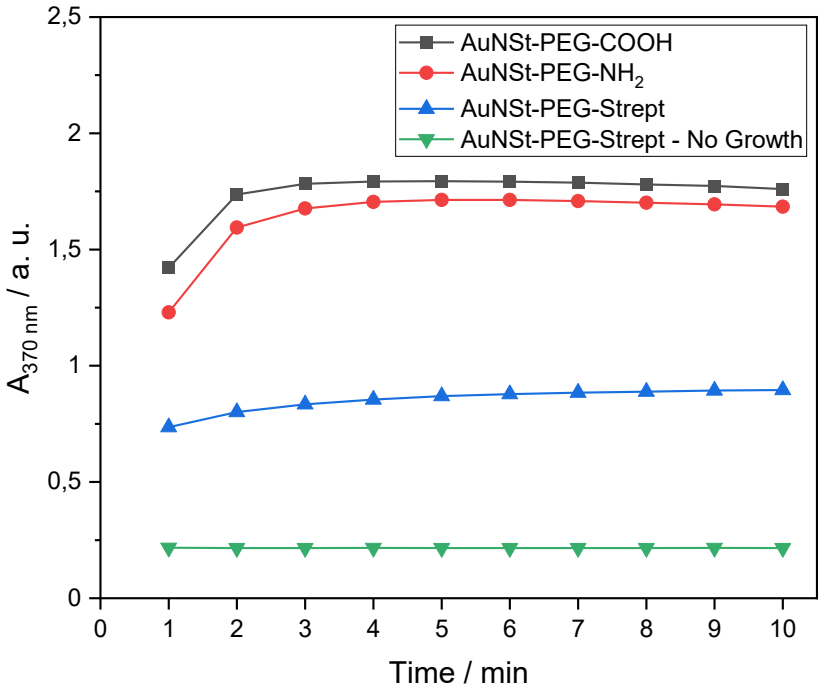

Figure C4. 6 UV-Vis analysis of oxTMB generated by AuNSt after undergoing or skipping an enlargement step. All samples contained 500 pM AuNSt.

4.3.3 Smartphone-based quantification

Once the nanozyme activity of protein-coated AuNSt had been restored, and prior to their application in a biosensor, the colour signal quantification through smartphones was characterised and optimised for this approach. The RGB colour space was used as previous studies had shown it was the most promising among the different possibilities [361], and the freely-available smartphone application "RGB Color Detector" used to extract raw data from the images taken with the smartphone.

4.3.3.1 Catalytic autoenlargement of AuNSt

Firstly, a range of AuNSt at different concentrations ranging from 0 to 500 pM was enlarged using a gold growth solution as previously described (Section 4.2.3) and, after 30 min of enlargement, TMB was added. A picture is then taken with a smartphone as described in Section 4.2.6, thus avoiding reflection issues and keeping consistency between different measurements. Before further analysing the data extracted from the picture using the application "RGB Color Detector", it can be visually appreciated that the intensity of the blue colour generated from the TMB oxidation is proportional to the AuNSt concentration, therefore enabling the qualitative determination of protein-coated AuNSt. In addition, deeper analyses using "RGB Color Detector" allows for the quantitative determination of AuNSt after extracting Red, Green and Blue values from each well (Figure C4.7). The image was first uploaded to the application, which provides values for Red, Green and Blue channels for the selected area within the image (in this case, the specific well that is being analysed, Figure C4.7a). Then, three separate spots of each well are analysed as shown in Figure C4.7b, obtaining raw data that are further processed taking into account the background noise coming from the microplate. The RGB model uses an intensity system in which the three primary colours are considered (i.e. Red, Green and Blue). Zero intensity for each component gives the darkest colour (black), whereas the addition of all three primary colours yields white at its maximum intensity. Considering that the analyses are performed placing the microplate over a screen emitting white light, empty wells (or colourless wells) will result in a maximum intensity value for each colour channel, while these values will be reduced as more intense colours develop. Finally, ΔRGB values are calculated following the Equation shown in Figure C4.7b, as the root sum square of each separate component. The resulting calibration curves (Figure C4.7c) showed that the Red channel was the most accurate among the three, displaying fairly small error bars while providing a large intensity range between the sample with the lowest concentration of AuNSt and the highest. This range was

increased using ΔRGB values, but the accuracy in this case dropped as it also takes into account the Green and Blue values, which displayed large error bars. Therefore, the Red channel was chosen as the optimum one for calculating the concentration of AuNSt present in a sample after performing an enlargement step and exploiting their peroxidase-like activity to oxidise chromogenic TMB. Thereby, a LOD of 10.6 pM of AuNSt is calculated from the Red channel calibration curve, as the Negative Control sample value minus 3 times its standard deviation. This approach (NC ± 3σ) includes 99.7% of data drawn from a normal distribution set of values, being generally considered as robust enough to determine the LOD of an assay. Regarding the Green and Blue channels, these values increased to 40.6 and 36.7 pM, respectively.

This same analysis was run in parallel using the spectrophotometer to measure $A_{370\,nm}$, obtaining a linear fit when plotted against the AuNSt concentration. It is interesting to note that this approach led to a LOD of 22.9 pM of AuNSt. Therefore, the smartphone-based method was not outperformed by lab-based equipment, revealing the potential smartphone cameras have for POC analyses.

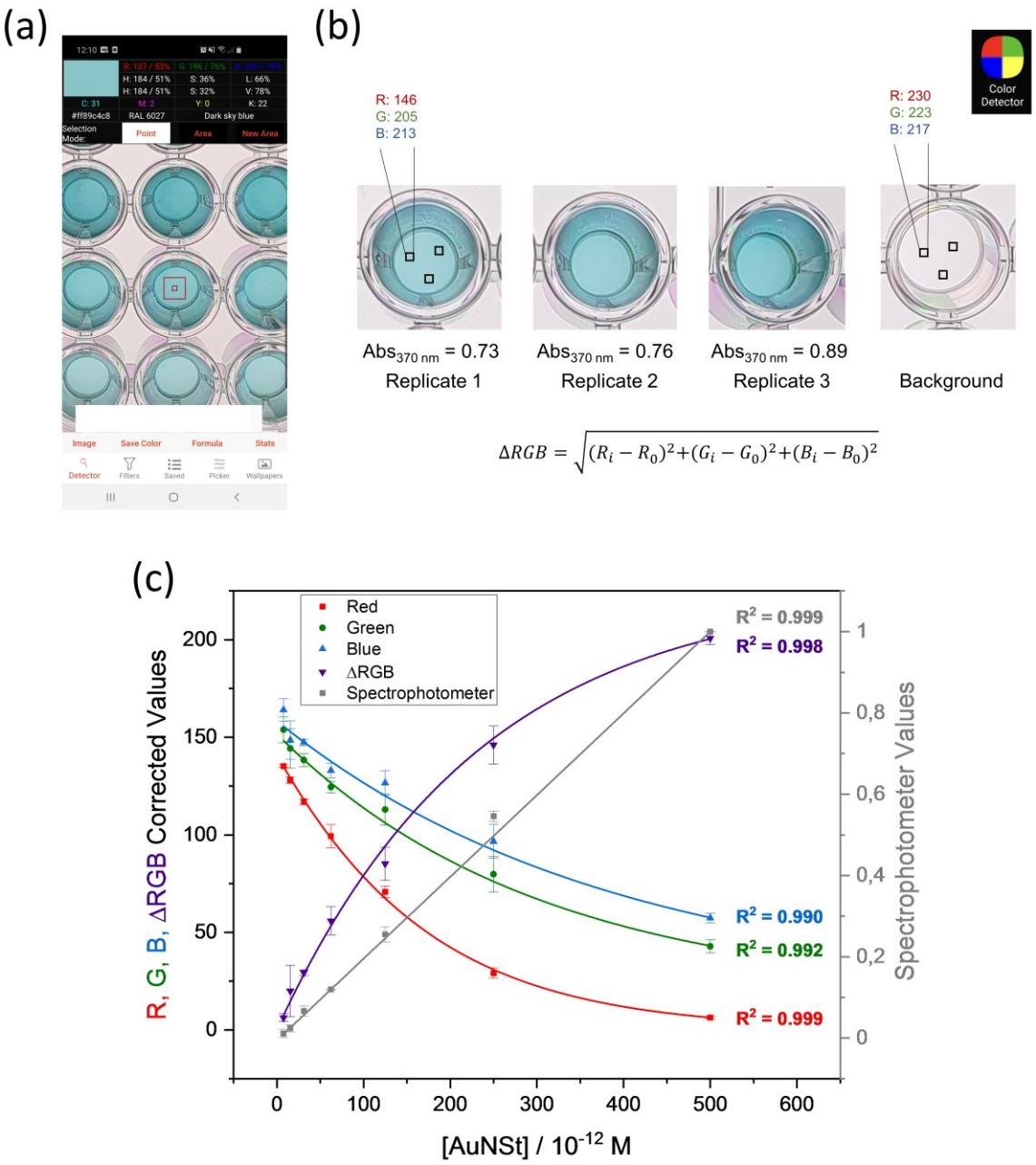

Figure C4. 7 (a) RGB app layout after uploading a picture taken with the smartphone for analysis. The red square limits the area to be measured, while the results are shown on top in different colour spaces. (b) Data acquisition approach for each AuNSt concentration, analysing each replica in 3 separate areas of the well. ΔRGB values were calculated as shown in the Equation. (c) Calibration curves obtained using a Dose-Response model from Red, Green and Blue channel values and ΔRGB to quantify the presence of AuNSt are compared with the linear fit obtained using lab-based spectrophotometer equipment to measure $A_{370\ nm}$.

4.3.3.2 Catalytic silver enhancement of AuNSt

Following previous studies claiming that a silver enhancement step can lead to an improvement in plasmonic and catalytic properties of NPs, and attempting to maximise the signal generated by AuNSt, silver was proposed as an alternative to gold for the enlargement step. First, different concentrations of $AgNO_3$ (as silver ions source) and L-AA (as reducing agent) were mixed together with 50 pM of AuNSt in dH_2O or HEPES 10 mM pH 7.4 to emulate the use of a silver enhancement kit. The concentrations included 10^{-3}, 10^{-4}, 10^{-5} and 10^{-6} M for both $AgNO_3$ and L-AA, which were combined in all sixteen possible ways. Unfortunately, the resulting silver-containing nanostructures displayed little to none peroxidase-like activity after the addition of TMB 0.3 mM, resulting in $A_{370\,nm}$ values that did not reach 0.4 a. u. in any case (Table C4.3).

	1	2	3	4	5	6	7	8	9	10	11	12	13	14	15	16
L-AA / M	10^{-3}	10^{-3}	10^{-3}	10^{-3}	10^{-4}	10^{-4}	10^{-4}	10^{-4}	10^{-5}	10^{-5}	10^{-5}	10^{-5}	10^{-6}	10^{-6}	10^{-6}	10^{-6}
$AgNO_3$ / M	10^{-3}	10^{-4}	10^{-5}	10^{-6}	10^{-3}	10^{-4}	10^{-5}	10^{-6}	10^{-3}	10^{-4}	10^{-5}	10^{-6}	10^{-3}	10^{-4}	10^{-5}	10^{-6}
50 pM AuNSt in dH_2O																
$A_{370\,nm}$	0.266	0.149	0.108	0.095	0.232	0.160	0.103	0.099	0.198	0.142	0.107	0.093	0.200	0.149	0.099	0.098
50 pM AuNSt in HEPES 10 mM pH 7.4																
$A_{370\,nm}$	0.266	0.141	0.117	0.102	**0.337**	0.137	0.103	0.105	0.214	0.165	0.117	0.101	**0.390**	0.195	0.151	0.114

Table C4. 3 The capability of silver-enlarged AuNSt to oxidise TMB and generate a blue colour was characterised spectrophotometrically.

Therefore, a silver enhancement kit was used, as described in Section 4.2.4, and after 10 min TMB was added. Figure C4.8a shows that using undiluted kit reagents leads to silver reduction regardless of whether AuNSt are present or not in the sample. The kit reagents need to be diluted 10 times to reach optimum conditions where silver is only reduced due to the AuNSt action, thereby restoring the peroxidase-like activity and generating a blue colour coming from TMB oxidation. Using these conditions, different concentrations of AuNSt in the lower scale (ranging from 0 to 50 pM) were used to study whether a silver enlargement enabled a more sensitive quantification. As shown in Figure C4.8b, concentrations under 50 pM are barely distinguishable from the Negative Control (No AuNSt). Moreover, it is interesting to note that A_{650nm} (coming from the blue Charge Transfer Complex intermediate generated in the TMB oxidation process [162]) becomes a better indicator to quantify TMB oxidation than A_{370nm} (representing TMB^+), since the spectroscopic properties of AgNPs (whose plasmon can reach

λ_{max} as little as 400 nm) overlaps with TMB^{+} optical signal at 370 nm. Finally, "RGB Color Detector" app was used to quantify the signal generated by the TMB oxidation and, in agreement with previous results, the Red channel resulted the one performing the best for AuNSt quantification through their peroxidase-like activity (Figure C4.8c). A LOD of 5.5 pM of AuNSt was obtained using the Red channel, whereas these values increased to 7.8 and 8.8 pM for the Green and Blue channels, respectively. Given that no significant improvement was achieved using a silver enhancement kit, the gold enlargement step as discussed in Section 4.3.3.1 was proposed for developing the sensing assay shown in next Chapter.

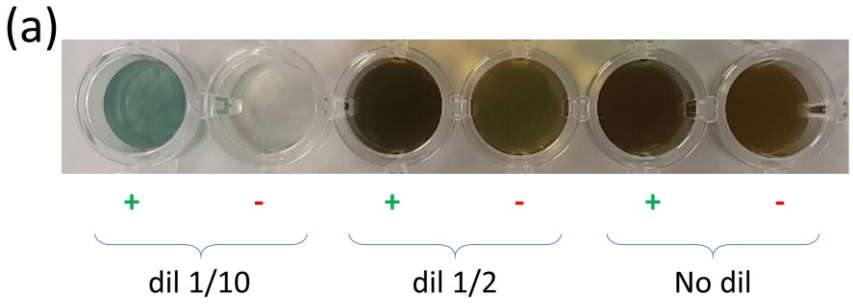

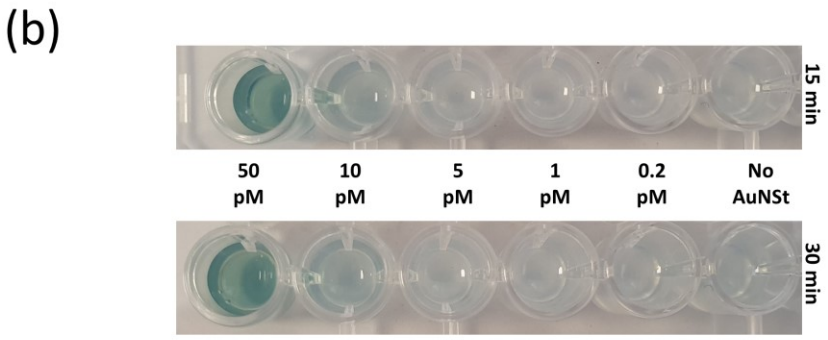

$A_{370\ nm,\ 15\ min}$	0.937	0.763	0.774	0.776	0.789	0.859
$A_{650\ nm,\ 15\ min}$	0.609	0.287	0.245	0.243	0.229	0.262
$A_{650\ nm,\ 30\ min}$	0.663	0.322	0.260	0.247	0.257	0.286

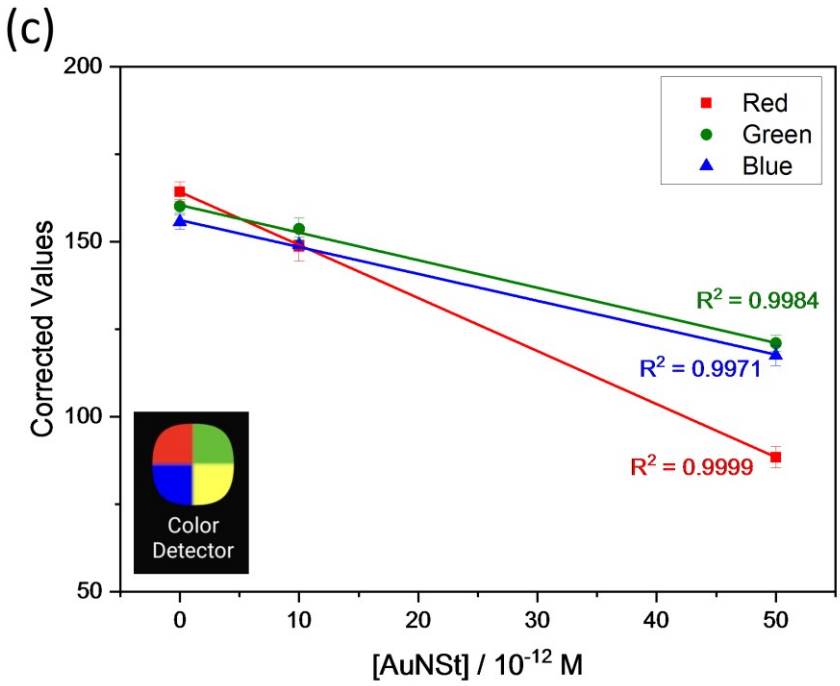

Figure C4. 8 (a) Colourimetric analysis of the peroxidase-like activity of silver enlarged AuNSt at a fixed concentration of AuNSt (50 pM) and varying the concentration of the silver enhancement solutions provided with the kit (no dilution, 2 times and 10 times dilution). (b) Images for further analysis are taken with the smartphone and the signal generated by the oxidation of TMB measured by UV-Vis spectroscopy. (c) Calibration curves obtained from Red, Green and Blue channel values to quantify the presence of AuNSt.

4.3.4 Development of a smartphone modulated colourimetric reader

Zhao, Y., Choi, S.Y., **Lou-Franco, J.**, Nelis JL, Zhou, H., Cao, C., Campbell, K., Elliott, C.T., Rafferty, K., 2019. Smartphone modulated colorimetric reader with color subtraction. *IEEE SENSORS*, 2019 Oct, pp. 1-4.

4.3.4.1 Abstract

Color analysis has been essential for the interpretation of optical readouts, e.g. colorimetry, fluorescence, spectroscopy, and scanometry. However, existing colorimetric readers can hardly eliminate the color interference of colored solutions, e.g., interpreting pH test strips to assess the pH value of red wine. This paper introduces a smartphone modulated colorimetric reader that is compatible with most smartphone models and a novel color subtraction algorithm that eliminates color interferences due to colored solutions. Experiments were conducted to validate the effectiveness of the developed reader and algorithm on evaluating pH test strips produced from transparent and colored solutions using multiple smartphone models. Applicability of the developed reader was demonstrated through its interpretation of pH test strips measuring pH values of colored and non-transparent food samples including red wine and milk.

4.3.4.2 Contribution to the project

Different buffer solutions were prepared covering a pH range from 2.6 to 8.3, mixing them with different test solutions to characterise the performance of a Smartphone Modulated Colorimetric Reader (SMCR) developed by Yunfeng Zhao at QUB (Figure C4.9). Four separate experiments were performed.

1. Project justification: many sensing devices provide a colourimetric signal that needs to be interpreted by the end user, either by the naked eye or using some sort of colour reader. This is the case of pH strips, enabling POC determination of the pH of a solution as long as the colour can be precisely identified. In some situations, it is imperative to detect the slightest pH change, as in the case of milk pH, where pH changes from its normal value (6.7) to 6.5 or 6.9 might indicate spoilage by bacterial degradation or a potential infection of cows with mastitis, respectively (https://www.mediray.co.nz/media/15606/ds_hanna_ph_ha-hi99162_1p0_0415.pdf). Thus, pH strips were used to measure the pH of transparent buffer solutions and it was observed that the average error for pH determination was 0.25 pH units by visual

detection (i.e. using the colour code provided with the pH strips), while this value dropped to well below 0.1 using the SMCR.

2. Reproducibility between smartphones: three different smartphones were used to analyse the range of colours generated by pH strips dipped into solutions with a pH ranging from 5 to 8.3. It was observed that both iPhone 6p and Samsung Galaxy S7 led to an average error in the measurement of 0.15 pH units, while an average error under 0.1 was observed for pH analysis using a Samsung Galaxy J5. This shows the interphone variability, which interestingly reports higher errors when the samples are analysed with the best equipped cameras. This might be explained by a more sophisticated image post-processing operation, which would lead to worse colourimetric analysis results in pursuit of a better image quality.
3. Colour subtraction: two coloured solutions (red and blue) were buffered at different pH values from 5 to 8.3 and then pH strips were used to perform the colourimetric analyses, both visually and using a colour subtraction algorithm incorporated in a smartphone app. In this case, the average pH errors rose to almost 0.8 pH units when the analyses were done by the naked eye. In the case of applying a colour subtracted algorithm, on the other hand, these dropped below 0.4.
4. Real application: finally, the SMCR was applied for measuring the pH of two coloured food samples of interest: milk and red wine. In the first case, milk samples were left for 6 days at RT, and their pH value was measured both using a pH-metre and the SMCR. It was observed that the differences in the pH values obtained with both approaches never differed in more than 0.2 pH units, showing the accuracy of the SMCR. In the second case, the pH of three red wine samples was analysed with and without applying the colour subtraction algorithm. In this case, the average error was set at 0.6 pH units when no colour subtraction was applied, dropping this value to 0.3 when the algorithm was applied, thus evidencing the benefits of the proposed smartphone-based system.

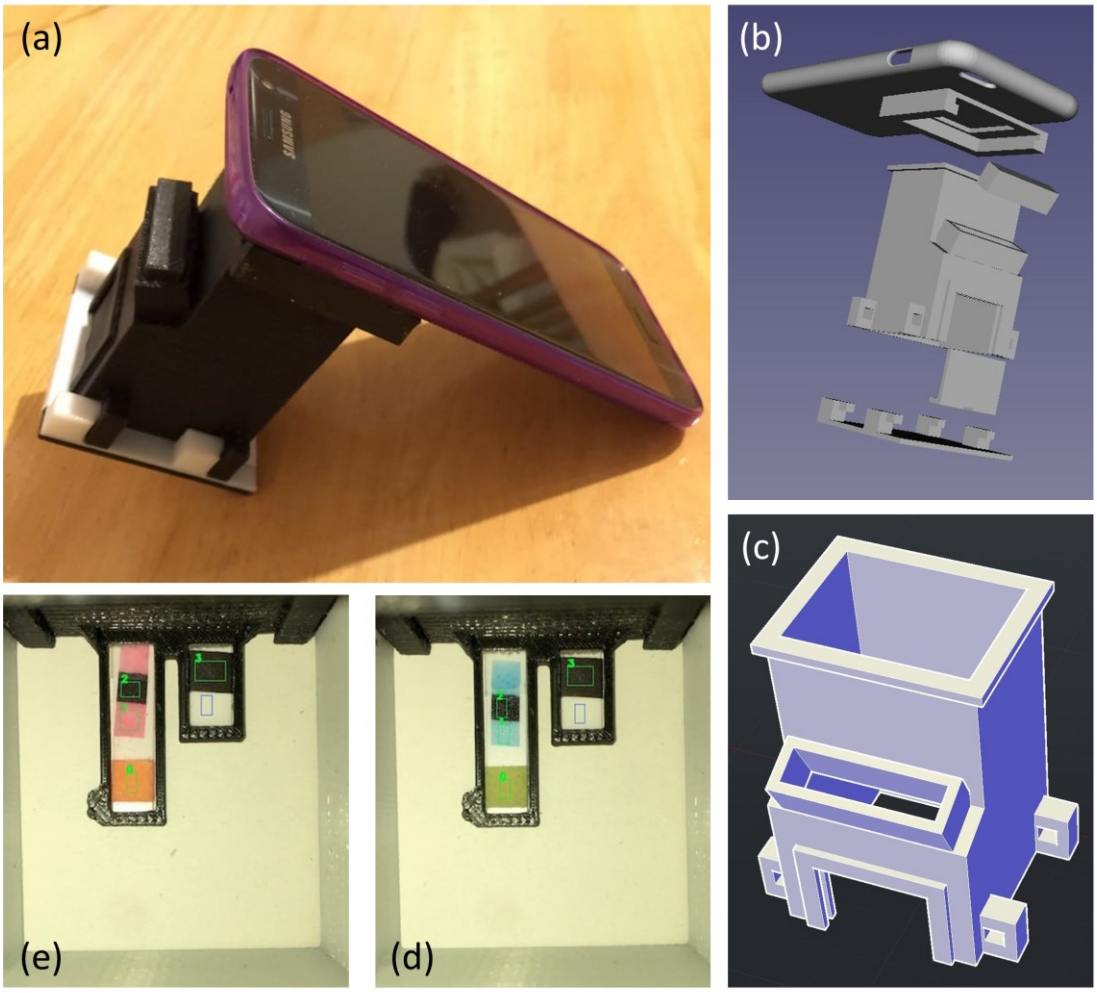

Figure C4. 9 (a) Smartphone Modulated Colorimetric Reader used for this work. (b) Components of the modulated smartphone reader, including a phone case, light-box connector, light box, assay platform adaptor and bottom panel. (c) Light box seen from the top, displaying an aperture from which an external light source can be introduced in the system. (d) Inside of the light box containing a modified pH strip prepared for analysing blue (d) and red (e) solutions.

4.4 Conclusions

Using either a gold or a silver ions source to enlarge protein-coated AuNSt has proved being an efficient manner for restoring their peroxidase-mimicking activity, enabling them to generate a colourimetric signal that can be used as transducer element in a POC biosensing assay. It has been observed that the main mechanism occurring during this step is the nucleation of gold at the AuNSt surface followed by the detachment of gold particles (Figure C4.5) whose unoccupied surface provides an excellent spot for TMB oxidation to take place. This is of especial interest considering that many spectroscopic properties are dependent on the morphological and plasmonic properties of AuNSt, like their capability to act as Raman enhancers which can be subsequently exploited for a more sensitive detection of oxTMB (see Chapter 6). Parameters such as the buffer selection, the growth time or the concentration of reagents are of paramount importance for achieving a controlled growth.

On the other hand, smartphones have been used for quantifying the colour signal generated both in liquid (microtiter plate) and in solid phase (pH test strips). Some difficulties encountered at this point included achieving a reproducible result between different operators using different smartphones, for which the consistency while acquiring the picture is essential in terms of luminosity (white-illuminated screen background), picture angle (90 ˚)and distance (10 cm). As for the data processing, the efficiency of several colour channels for quantifying the blue colour generated in a solution where the TMB oxidation process had happened was studied. In all cases (regardless of whether AuNSt had been enlarged with gold or with silver) the Red channel provided the best results, achieving better LOD values than the Green, Blue or ΔRGB channels. As little as 10 pM of protein-coated AuNSt were detected with a smartphone, hence providing a robust transducing element for biosensing.

Finally, a Smartphone Modulated Colorimetric Reader developed at QUB and fit for colour analyses in chromatographic test strips was tested as an alternative to commercially available apps that require data post-processing. This means that the SMCR can be trained thus providing a numeric result in the desired units (pH units, CFU/mL or any other used during the training), whereas most commercial apps provide a result in a specific colour space that needs to be converted into the desired unit through a calibration curve. After calibrating the system, it successfully enabled to measure pH values with a better accuracy than the naked eye while maintaining the portable character of these systems. Even more, a colour subtraction algorithm was incorporated which enabled to measure with high precision the pH of strongly coloured food samples that otherwise would lead to large inaccuracies.

Chapter 5 Smartphone-based detection of *Mycobacterium bovis*

5.1 Introduction

5.1.1 Bovine tuberculosis

Tuberculosis is an airborne infectious disease caused by the *Mycobacterium tuberculosis* complex (MTBC). It generally affects the lungs, although it can affect other parts of the body, and to date it still is one of the main causes of death worldwide [372]. The World Health Organization (WHO) estimated that there were 1.2 million TB deaths in 2018 [373]. These are mainly caused by *Mycobacterium tuberculosis* and *Mycobacterium africanum* (limited to West Africa), being both obligate human pathogens [374]. However, several animal-adapted members of MTBC exist as described in Section 1.1.4, also leading to human TB [375]. Among these, *M. bovis* is the species that has the greatest impact in human health, causing bovine TB and being responsible for up to 15% of TB cases in developing countries, where raw dairy products are commonly marketed without health inspection [50]. More importantly, even regions that have been declared bovine TB (bTB)-free for more than 10 years are reporting TB cases with zoonotic origin between 1-2% [376]. Considering that both forms of TB course with practically identical symptoms and are treated in an undifferentiated manner, the burden of bTB is thought to be underestimated, hindering many efforts to eradicate the disease. In this line, a vaccine derived from an attenuated strain of *M. bovis*, the bacille Calmette-Guérin (BCG), has been used worldwide as a TB control strategy since 1921. However, the overall protective value of BCG against all forms of TB has been reported as low as 50% [377], making the vaccine virtually non-effective for controlling the global TB epidemic. bTB is commonly transmitted to humans by cattle, which represents the main reservoir of *M. bovis*, but it can be found in other mammals like badgers [378], deer or wild boars [379,380]. Given that consumption of raw milk from infected cattle is the main transmission path to humans, pasteurization of milk prior to any use related to human consumption has resulted of paramount importance to avoid bTB infections. However, unpasteurized milk is still commercialised and consumed [381], highlighting the necessity of dairy foodstuff to be tested to detect any presence of *M. bovis* before these products reach the consumer.

5.1.2 *M. bovis* current detection approaches

To date, most attempts to detect *M. bovis* are implemented in clinical specimens, either from infected people or animals, using culture methods. These combine microbial isolation with phenotypic diagnosis which, in the case of a slow-growth species like *M. bovis*, can take up to 90 days [50,382]. Other approaches using molecular detection techniques (mainly PCR) have also been used to target *M. bovis* DNA [53]. However, nor culture nor molecular methods escape the need of trained personnel or laboratory equipment, while the latter is also incapable of distinguishing viable and non-viable bacteria. Moreover, PCR protocols lack sensitivity (since 1 CFU needs to be detected), specificity (since closely related microorganisms might not be distinguished) and reliability (induced by the presence of PCR inhibitors in food matrixes) to replace cell culture as the gold standard method. This situation has led scientific efforts to try to develop portable biosensors that can be used for rapid, on-site screening of food. Some success has been observed with electrochemical [383,384] and optoelectronic [385] biosensors, but none of them has yet achieved the level of standardisation required to be used for routine analyses. As a result, food samples at risk of being contaminated with *M. bovis* are not specifically tested, setting the control point in the cattle's health condition, often following the traditional "test and slaughter" approach. Thus, there are two tests currently approved in the EU to detect *M. bovis* infection in cattle: *in vivo* intradermal tuberculin test (skin test) and *in vitro* γ-interferon (γ-IFN) assay [54,55]. The former measures dermal swelling three days after intradermal injection of tuberculin, a purified protein derivative extracted from supernatants of mycobacterial cultures. The latter incubates heparinized whole blood with mycobacterial antigens for 18-24 hours to induce the production and release of γ-IFN by T lymphocytes, which is next quantified in a sandwich ELISA. Despite their usefulness, none of these has yet satisfied the needs of the sector, which must comply with strict regulation that leaves no space for contamination events to happen (i.e. new sensing assays must be as efficient as current prevention approaches applied to the cattle to protect the end-user from getting infected with *M. bovis*). Therefore, a rapid, effective and non-expensive technology is demanded to tackle this issue, which hinders any global effort to eradicate the TB epidemic.

5.1.3 Objectives

The overall aim of this Chapter is to develop a smartphone-based biosensor to detect the presence of *M. bovis* in a solution, potentially enabling POC analysis of dairy samples. In order to do it, AuNSt are being used as transducer elements, exploiting their properties studied in Chapter 3 as peroxidase-mimics, and smartphones as readout systems, using the apps presented in Chapter 4 for colour quantification. Firstly, the appropriate biological binder needs to be selected, as many antibodies, peptide binders, and other biorecognition elements are available, displaying diverse sensitivities and specificities towards the target bacteria. After immobilising the appropriate binder onto AuNSt, these undergo an enlargement step to restore their nanozyme activity and the colourimetric signal generated can be read using a smartphone. A representation of the assay mechanism is illustrated in Scheme C5.1. Very few examples have been described in the literature combining nanozyme activity and smartphone-based detection [161,386], an approach that paves the way for POC analyses not only in the field of food safety, but also in biomedicine or environmental analyses among others.

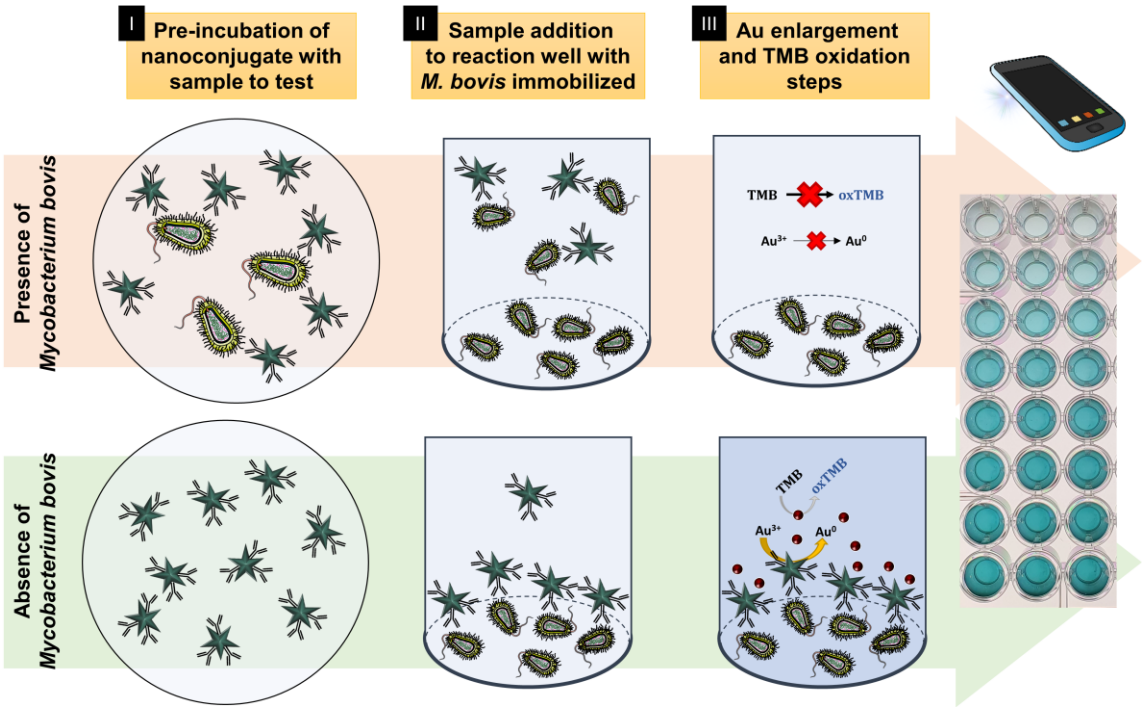

Scheme C5. 1 Assay mechanism proposed for the smartphone-based colourimetric detection of *M. bovis*.

5.2 Methods

5.2.1 Reagents and chemicals

Gold(III) chloride trihydrate ($HAuCl_4 \cdot 3H_2O$, 99.9%), L-ascorbic acid ($C_6H_8O_6$), silver nitrate ($AgNO_3$), hydrochloric acid (HCl), O-(3-Carboxypropyl)-O'-[2-(3-mercaptopropionylamino)ethyl]-polyethylene glycol (Mw 5000), 3,3',5,5'-tetramethybenzidine (TMB), hydrogen peroxide (H_2O_2 30% (w/w) in H_2O), dithiothreitol (DTT), phosphate buffer saline (PBS, pH 7.4) were all purchased from Sigma Aldrich (UK).

Biological materials, including *Mycobacterium bovis*, *Mycobacterium smegmatis*, *Escherichia coli* K12, *Escherichia coli* BL21, α-*M. bovis* antibodies and *M. bovis* peptide binders were all kindly provided by the Microbiology Department from Queen's University Belfast.

5.2.2 Binding immunoassay 1D

Different *M. bovis* concentrations were immobilised in a treated ELISA plate (Nunc-Immuno™ 96 MicroWell™ MaxiSorp™) in a 100 μl solution of coating buffer (carbonate/bicarbonate 0.05 M, pH 9.6). The coating solution was kept overnight (O/N) at 4 °C and then washed 4 times with PBST 0.05%. The biorecognition element (either antibody or peptide binder) was added in PBST 10 mM, pH 7.5 at 1 μg/mL and incubated for 30 min at 600 rpm and RT. Then 100 μl of the secondary element (α-mouse IgG, α-rabbit IgG or streptavidin bound to peroxidase) were added after another washing cycle, using a 1/6000 dilution for IgGs and 1/1000 dilution for streptavidin, and incubated as described before. 100 μl of TMB in citrate solution containing H_2O_2 (0.004%) were added to each well (after a final washing cycle) and incubated at RT for 30 min. The oxidation process was stopped adding 50 μl of H_2SO_4 4 M, and the oxidized product measured using a microplate reader (Multiskan FC microplate photometer from ThermoFisher) set at 450 nm.

5.2.3 Sandwich immunochemical assay

1 μg/mL of capture antibody was immobilised in a treated ELISA plate (Nunc-Immuno™ 96 MicroWell™ MaxiSorp™) in a 100 μl solution of coating buffer (carbonate/bicarbonate 0.05 M, pH 9.6). The coating solution was kept overnight (O/N) at 4 °C and then washed 4 times with

PBST 0.05%. 100 µL samples containing a varying *M. bovis* concentration were added in PBST 10 mM, pH 7.5 and incubated for 30 min at 600 rpm and RT. The rest of the protocol follows exactly as described in Section 5.2.2, adding the primary antibody (1F11) at 5 µg/mL and the secondary antibody (goat α-mouse – peroxidase, GAM-PO) using a 1/6000 dilution.

5.2.4 DTT reduction

The dithiothreitol (DTT) reduction was the method used to prepare IgG antibodies containing sulfhydryl groups (see Scheme C5.2), with minor modifications from previously reported protocols [387]. DTT can be employed for the covalent conjugation of AuNSt through the formation of a strong Au – S bond, as it partially reduces the disulphide bonds of the IgG and the resulting thiol groups can bind the antibody to AuNSt. This method, however, does not control the orientation of antibodies linked to the AuNSt surface, since DTT does not enable to cleave a certain antibody's disulphide bond preferentially. In short, a 200 µl solution of IgG antibody 1 mg/mL was prepared in PBS 0.1 M – EDTA 2 mM buffer. 8 µl of DTT 0.5 M prepared in aqueous solution were then added and the mixture was incubated under minor stirring conditions for 25 min at RT. The solution was immediately washed 4 times with an Amicon Ultra-0.5 Centrifugal Filter (50 KDa) at 14000 rcf for 10 min, resuspending the IgG in PBS – EDTA buffer. This was done to remove the excess of DTT thus limiting the cleavage of disulphide bridges between the heavy and light chains of the IgG and maintaining their functional binding sites [388]. The IgG was collected spinning the container upside-down at 100 rcf for 2 min. The resulting solution was added to freshly prepared and unmodified AuNSt (see Section 3.2.2), together with PEG to a final concentration of 10 µM, leaving them to react under minor stirring conditions for 30 min at RT. It has been suggested that sulphur atoms bind to the threefold hollow sites of the Au {1,1,1} surface, in agreement with observations that sulphur atoms bind to highly coordinated sites on transition metal surfaces [389]. Finally, the functionalised AuNSt were centrifugated at 10 ˚C and 1200 rcf for 25 min to remove any unbound IgG/PEG molecules.

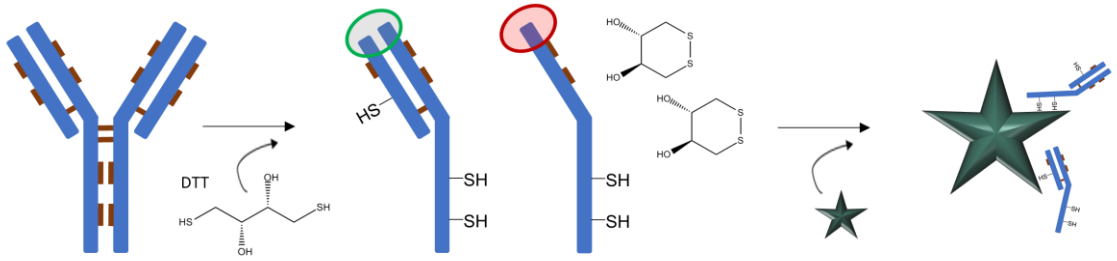

Scheme C5. 2 DTT reduction method used to conjugate AuNSt to 1F11 antibodies. The antibody fragments generated lead to functional (green) and non-functional (red) binding sites.

5.2.5 Indirect immunochemical assay

M. bovis AF2122/97 cell suspensions were produced in-house as detailed by Stewart and co-workers [57]. Briefly, they were cultured in a Middlebrook 7H9-based broth to stationary phase (which generally implies a growth of 42 days) [390], harvested by centrifugation and washed in PBS pH 7.4. Prior to any use, cell suspensions were subjected to a 10 kGy dose of gamma radiation using a Gammabeam 650 cobalt irradiator to inactivate the bacteria without damaging cell surface antigens. A *M. bovis* suspension concentrated at 10^5 CFU/mL was immobilised in a treated microplate (Nunc-ImmunoTM 96 MicroWell™ MaxiSorp™) in a 100 µL solution of coating buffer (carbonate/bicarbonate 0.1 M, pH 9.6). The coating solution was kept O/N at 4 ˚C and then washed 4 times with washing buffer (PBS 10 mM / Tween 0.05 %). Simultaneously, different concentrations of *M. bovis* (10^3 – 10^6 cfu/ml) were incubated with the functionalised AuNSt-1F11 in washing buffer for 30 min, under minor stirring and RT. The resulting AuNSt-1F11-*M. bovis* are then added to the microplate (100 µl per well) and incubated again for 30 min under minor stirring at RT. After 4 washings with washing buffer, 150 µL of growth solution ($2 \cdot 10^{-4}$ M $HAuCl_4$, $5 \cdot 10^{-6}$ M L-AA and 10^{-6} M CTAB in 10^{-2} M phosphate buffer pH 7.4) were added to each well and incubated for 30 min, undisturbed at RT. Finally, 150 µL of TMB (0.3 mM) were added to each well and the absorption at 370 nm measured after 20 min of TMB oxidation.

5.3 Results and discussion

5.3.1 Characterisation of *M. bovis* binders

The first step in the development of a biosensor consists in selecting an appropriate binder, which specifically targets the analyte at issue enabling for a robust and sensitive detection. For this purpose, five antibodies and one peptide binder provided by a collaborator at QUB were tested using *M. bovis* samples as whole cell antigens. Namely, R43, R44, Genosphere *Mycobacterium bovis* (GMB) and Genosphere *Mycobacterium tuberculosis* (GMTB) (all of them polyclonal antibodies produced in rabbit), 1F11 (monoclonal antibody produced in mouse) and a chemically synthesised peptide binder (EEA302) produced by phage display biopanning. All these elements have been tested by Stewart and co-workers as binders for *M. bovis*, displaying different specificities and sensitivities [391]. This last parameter was measured through a direct immunoassay following the protocol described in Section 5.2.2. The results (Figure C5.1) showed a varying performance for the different antibodies (Figure C5.1a) which deteriorates when biotinylated peptide binders are tested (Figure C5.1b). R43 and R44 display a higher avidity for *M. bovis*, being able to detect less than 100 CFU/mL, whereas the rest of antibodies could barely distinguish the samples containing 10^4 CFU/mL from the negative control samples. It must be highlighted that 1F11, despite not showing a great avidity like R43 and R44, had previously shown the smallest rate for nonspecific binding to 12 *Mycobacterium* spp. other than *M. bovis*, as reported by Stewart and co-workers. Therefore, depending on the needs of the final application, either the avidity or the selectivity could tilt the balance in favour of one or another antibody. As for the peptide binder, several concentrations of both HRP-Streptavidin and the peptide itself were used, none of these leading to suitable results due to a non-specific binding of the enzyme to the microplate that generated a high background noise.

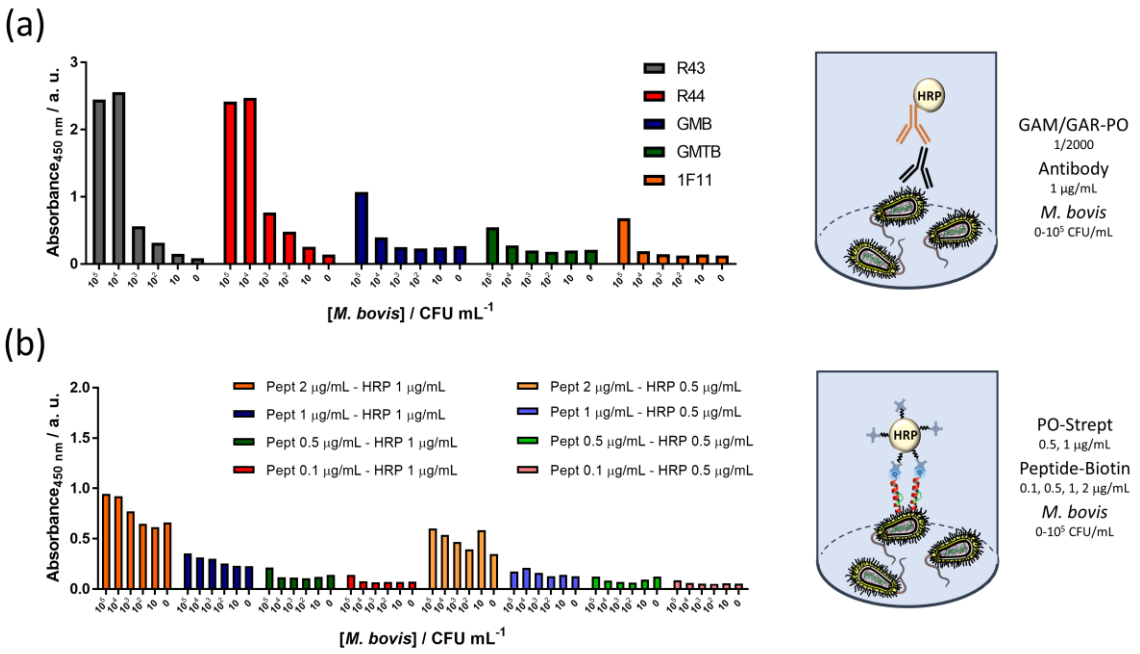

Figure C5. 1 Immunochemical assay used to select suitable biorecognition elements to include in the biosensing assay for *M. bovis* detection. (a) Antibodies tests. (b) Peptide-binder tests.

5.3.2 Immunochemical assay for *M. bovis* detection

Both R43 and R44 antibodies showed a very good performance in terms of binding their target. However, since they have both been produced in rabbit, a combination of the two of them in a sandwich assay that uses an α-rabbit peroxidase (PO)-labelled secondary antibody was not possible. Therefore, an initial screening was done testing each of the polyclonal antibodies as capture and 1F11 as detection antibody, and vice versa. The results showed that R44 – 1F11 as capture – detection antibody pair was the best combination. It must be added that, despite not displaying the best antigen avidity, 1F11 had previously reported excellent results for specifically recognising an *M. bovis* cell wall-associated protein [391].

The protocol described in Section 5.2.3 was thus followed to perform a sandwich-like immunochemical assay, using *M. bovis* samples ranging from 10^3 to 10^5 CFU/mL and resulting in a calibration curve whose linear range is shown in Figure C5.2. The linear range, however, could not be fully observed due to a lack of highly concentrated *M. bovis* samples, which did not enable to reach the saturation point (*plateau* effect) of the assay at high concentrations. This did not happen at low concentrations, being samples with 10^3 CFU/mL of *M. bovis* already indistinguishable from the negative control (PBS buffer). According to the data obtained, it was possible to determine the LOD of the system as $8.2 \cdot 10^3$ CFU/mL (*M. bovis* in PBS buffer). This

result is in accordance with other results previously reported in the literature for immunoassays targeting bacteria [392,393].

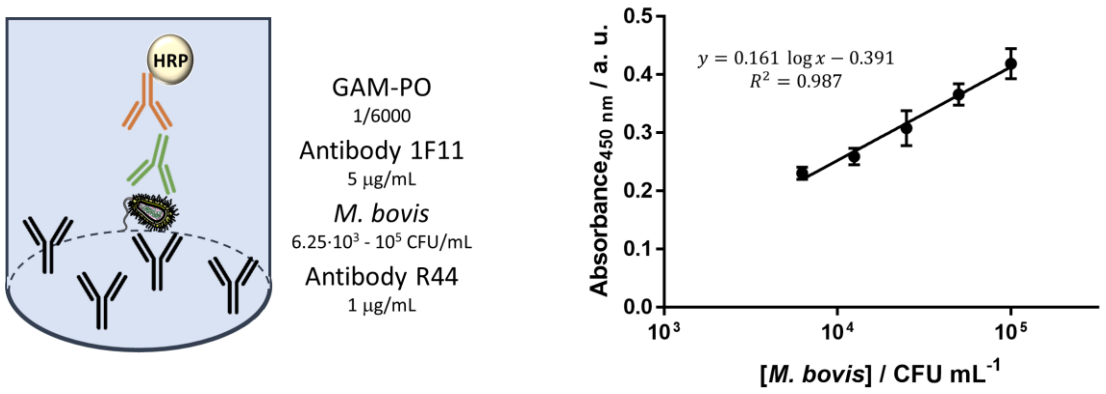

Figure C5. 2 Calibration line obtained for the sandwich immunoassay developed to detect *M. bovis* using R44 as capture antibody and 1F11 as detection antibody.

5.3.3 AuNSt conjugation to 1F11

Moving to the final biosensor format (as described in Scheme C5.1), AuNSt need first to be modified following the DTT reduction method (Section 5.2.4), which generates free sulfhydryl groups by cleaving antibodies' disulphide bonds, subsequently interacting with the AuNPs surface to form covalent bonds. Other methods were also explored to achieve this conjugation, such as the Traut's Reagent Modification Method, where 2-iminothiolane reacts with primary amines of proteins to create an amidine compound with an exposed sulfhydryl group that enables the attachment of antibodies to AuNSt [387]. This method, however, led to the aggregation of AuNSt and could not be applied. This is why the DTT reduction method was chosen, where several antibody fragments are obtained due to the indiscriminate disulphide bridge cleavage occurring when using this approach (Scheme C5.2). Thus, either light chains (25 KDa) or heavy chains (50 KDa) can be obtained, containing each of them half of the binding site and leading to non-functional antibody fragments. Only partially cleaved antibodies (75 kDa) will maintain functional binding sites while exhibiting reduced thiol groups that can directly bind AuNSt. This method, whose effectiveness has thoroughly been characterised elsewhere [388], was used to modified freshly prepared AuNSt and a spectroscopic characterisation of the AuNSt before and after the addition of the resulting antibody fragments showed a plasmon redshift (Figure C5.3) while no signs of NP aggregation were observed. Nevertheless, the surface modification of AuNSt with proteins leads to the inexorable collapse of their nanozyme nature,

which needs to be circumvented by performing a gold enlargement step as reported in Chapter 4.

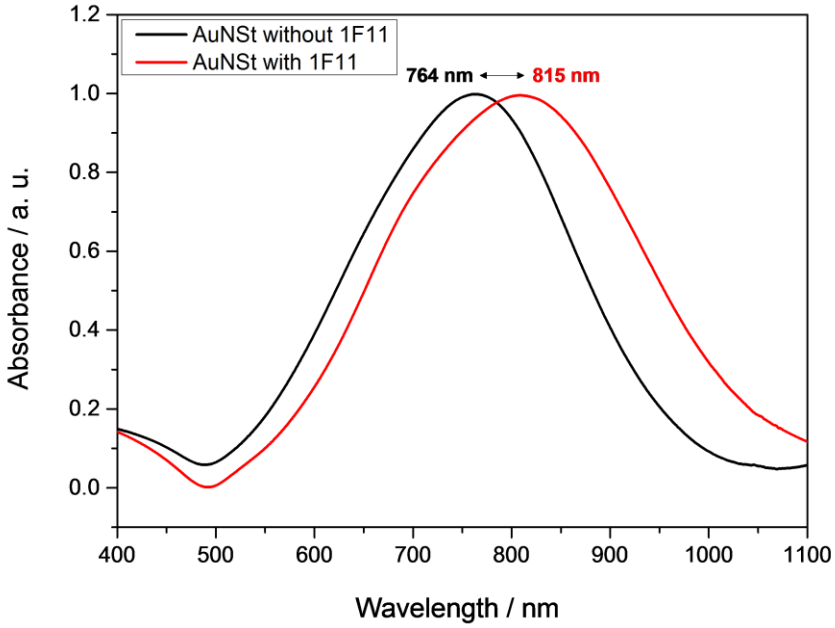

Figure C5. 3 UV-Vis analysis of AuNSt prior and after their surface modification with 1F11 antibody using the DTT reduction method.

5.3.4 Retrieving peroxidase-like activity of AuNSt for *M. bovis* detection

Prior to the smartphone-based analysis, an indirect immunochemical assay was first optimised and characterised using a spectrophotometer to measure the generated signal (see Section 5.2.5). This enabled to determine the sensitivity of the assay and ensure the selectivity towards *M. bovis*. Different concentrations of *M. bovis* were tested ranging from 10^3 to 10^6 CFU/mL. The oxidation of TMB was followed by measuring the A_{370nm} with a spectrophotometer after 20 min of reaction. The results showed a decreasing signal proportional to the increase in the concentration of *M. bovis* (Figure C5.4a). These data were plotted and fitted to a Dose-Response curve, showing a limit of detection (LOD) of $7.2 \cdot 10^3$ CFU/mL, calculated as 3 times the standard deviation of the negative sample. A linear trend is observed in the range 10^4 – 10^6 CFU/mL, although due to cell culture limitations, larger bacterial concentrations were not available to reach a *plateau* effect to determine the saturation point of the assay. These results are similar to those reported in the literature using an amperometric immunosensor capable of detecting $3.5 \cdot 10^3$ CFU/mL of *M. bovis* in milk samples [383], or using a LFD to detect *M. bovis* cells in badger faeces at concentrations equal or above 10^4 CFU/mL [57]. The former uses glassy carbon electrodes whose surface has been modified with AuNPs conjugated to Alkaline Phosphatase

(ALP) and antibodies α-*M. bovis*. The dephosphorylation process catalysed by ALP leads to an electrochemical signal that decreases as the *M. bovis* concentration increases, binds to its specific antibody and shields the active site of ALP. The latter, on the other hand, uses a filter and a cell strainer in combination with a LFD to detect the bacteria.

As for the assay's selectivity, several bacteria were tested to prove that the signal differences observed in the sensitivity assay were due to an effective IgG-bacteria binding event and not to an unspecific attachment of the AuNSt to the bacteria surface. Three different bacteria and a negative control were analysed and compared to *M. bovis*, including *Escherichia coli* K12, *Escherichia coli* BL21(DE3) and intra-genus species *Mycobacterium smegmatis*. All of them were prepared at 10^5 CFU/mL and the A_{370nm} measured with a spectrophotometer (Figure C5.4b). One-way ANOVA analyses were performed to compare the significance in the signal differences, resulting the negative sample and the 3 non-specific samples non significantly different (p-value > 0.5) whereas all these four are significantly different when compared to the *M. bovis* result (p-value ≤ 0.001). Therefore, the assay can be considered specific for *M. bovis*, while reaching a sensitivity similar to that observed in other studies.

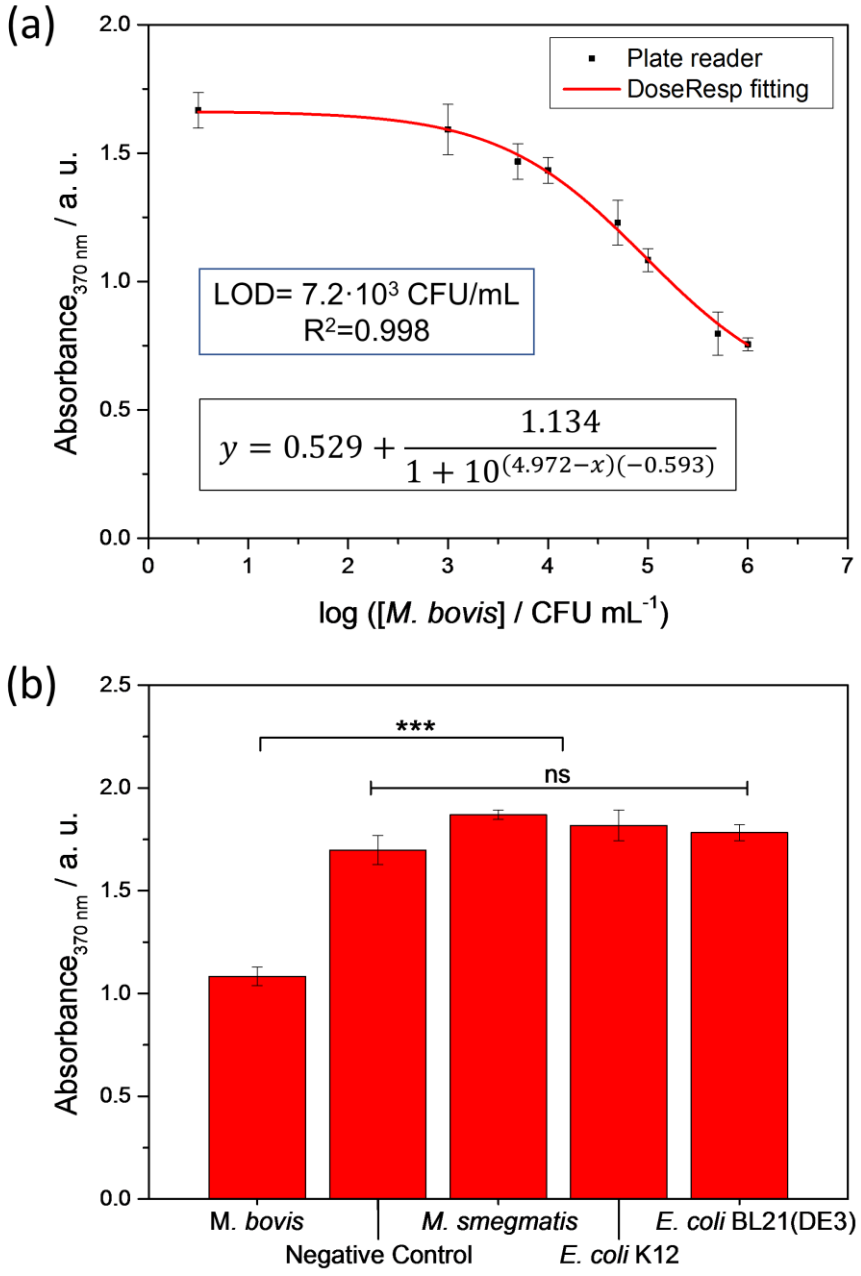

Figure C5. 4 Sensitivity and selectivity analyses of the proposed system to detect *M. bovis*. (a) Calibration curve of the assay. *M. bovis* samples ranging from 10^3 to 10^6 CFU/mL were tested and the A_{370} values measured, plot and fitted to a Dose-Response curve. (b) Selectivity assay where different bacteria at the same concentration (10^5 CFU/mL) were analysed and the results compared through a one-way ANOVA.

5.3.5 Smartphone calibration for colour analysis

Once the sensitivity and specificity of the assay were characterised, both smartphone apps analysed in the previous chapter (i.e. “RGB Color Detector” and “QuantColorimetry”) were used as readout systems to predict *M. bovis* concentrations from the colourimetric signal generated by the nanozyme activity of AuNSt. In both cases the apps are fed with an image of the assay taken with the smartphone (as reported in Section 4.2.6 and 4.2.7) which is used for calibrating the system. In the case of “RGB Color Detector” app, data obtained using the RGB colour space are used, specifically the Red channel data as they show greater accuracy than Green and Blue channels, and greater robustness towards errors than ΔRGB. Thus, each bacterial concentration tested using the indirect immunochemical assay optimised in Section 5.3.4 was associated to a specific R value, being every new measurement interpolated to a certain bacterial concentration through a Dose-Response fitting equation. In the second case, using the in-house developed application “QuantColorimetry”, the image of the calibration assay (Figure C5.5a) needs to be uploaded and then each colour intensity must be selected in the image and a specific value (i.e. *M. bovis* concentration) associated to that colour (Figure C5.5b). This way, and using a polynomial regression fitting model incorporated in the app [363], the trained system (Figure C5.5c) can be saved and new pictures of different *M. bovis* tests can be analysed with the smartphone app to predict the concentration of target bacteria present in the samples (Figure C5.5d).

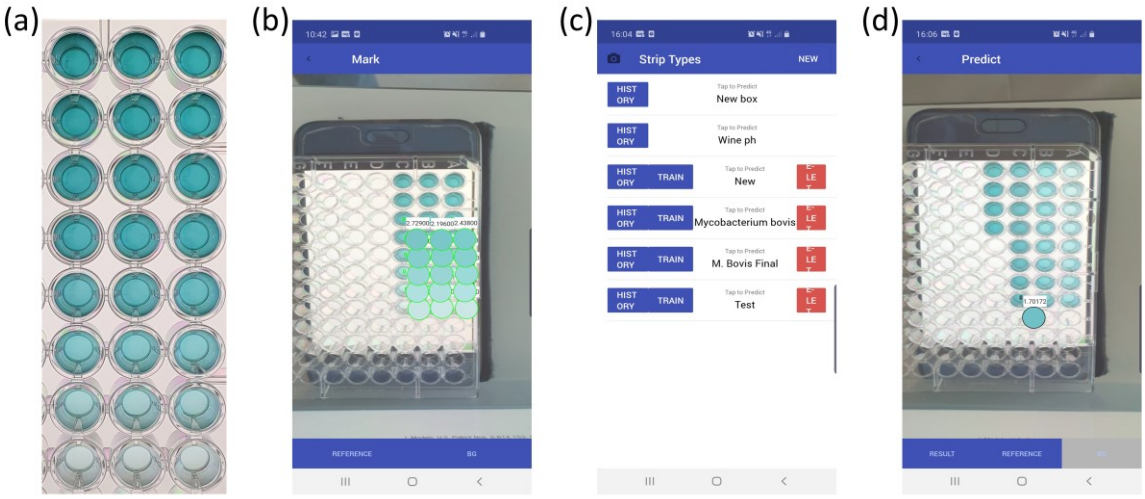

Figure C5. 5 Operating steps using “QuantColorimetryApp”. (a) A calibration image needs to be fed to the app first. (b) Each colour is associated to a certain known bacterial concentration. (c) The trained system is saved in the app, which coexists with systems for different applications. (d) A new image from a different assay is uploaded to the app for predicting the concentration of target analyte.

5.3.6 Smartphone-based detection of *M. bovis*

Lastly, an indirect immunochemical assay for *M. bovis* detection as reported in Section 5.3.4 was performed using three different readout systems: "RGB Color detector" app, "QuantColorimetryApp" and a lab-based spectrophotometer. All three systems had previously been calibrated, resulting either in a calibration curve (Figure C5.4a) or in a trained smartphone app ready to predict *M. bovis* concentrations from unknown samples (Figure C5.5). Buffered samples containing *M. bovis* at known concentrations ranging from 10^3 to 10^6 CFU/mL were analysed following the protocol described in Section 5.2.5, measuring the coloured signal with the spectrophotometer and taking a picture of the result following the conditions detailed in Sections 4.2.6 and 4.2.7. Both smartphone apps were then used to predict the *M. bovis* concentration present in the sample under analysis, in order to analyse how accurate their predictions are if compared to the real concentration of the sample. It is observed in Figure C5.6a that "RGB Color Detector" app shows a good accuracy and linearity in the predictions (slope of linear fit close to 1), when the real *M. bovis* concentration is plotted against the smartphone-predicted one. The same study, however, using the in-house developed app (i.e. "QuantColorimetryApp") resulted in a similar trend in terms of analyte detection, but both the accuracy and linearity of the predictions were outperformed by the commercially available smartphone app (translated as larger error bars and a linear fit of almost 1.5, respectively). This indicates that further optimisation is required in the latter app development if a quantitative approach, rather than a qualitative one, is expected. On the other hand, "QuantColorimetryApp" benefits from a direct *M. bovis* concentration prediction with no need of data processing, whereas "RGB Color Detector" only provides a Red Value that needs to be manually interpolated in a calibration curve to extract the *M. bovis* concentration in the desired units. This strengthens the potential of the in-house developed app for POC analysis despite still needing further optimisation to achieve accurate predictions.

All these results were compared with the predictions made using the spectrophotometer (Figure C5.6b), where a linear fitting slope of 0.99 and an equal coefficient of determination manifest the accuracy lab-based readout systems possess. The mean absolute error (MAE) of each readout system was compared, showing the spectrophotometer a MAE of 4.5±2.4 %, "RGB Color Detector" app 6.4±1.5 % and "QuantColorimetryApp" 15.4±5.9 %. From these data, it can be concluded that smartphone-based readout systems are already catching up in terms of the accuracy reached by lab-based technologies, while providing portability and accessibility to the end-user.

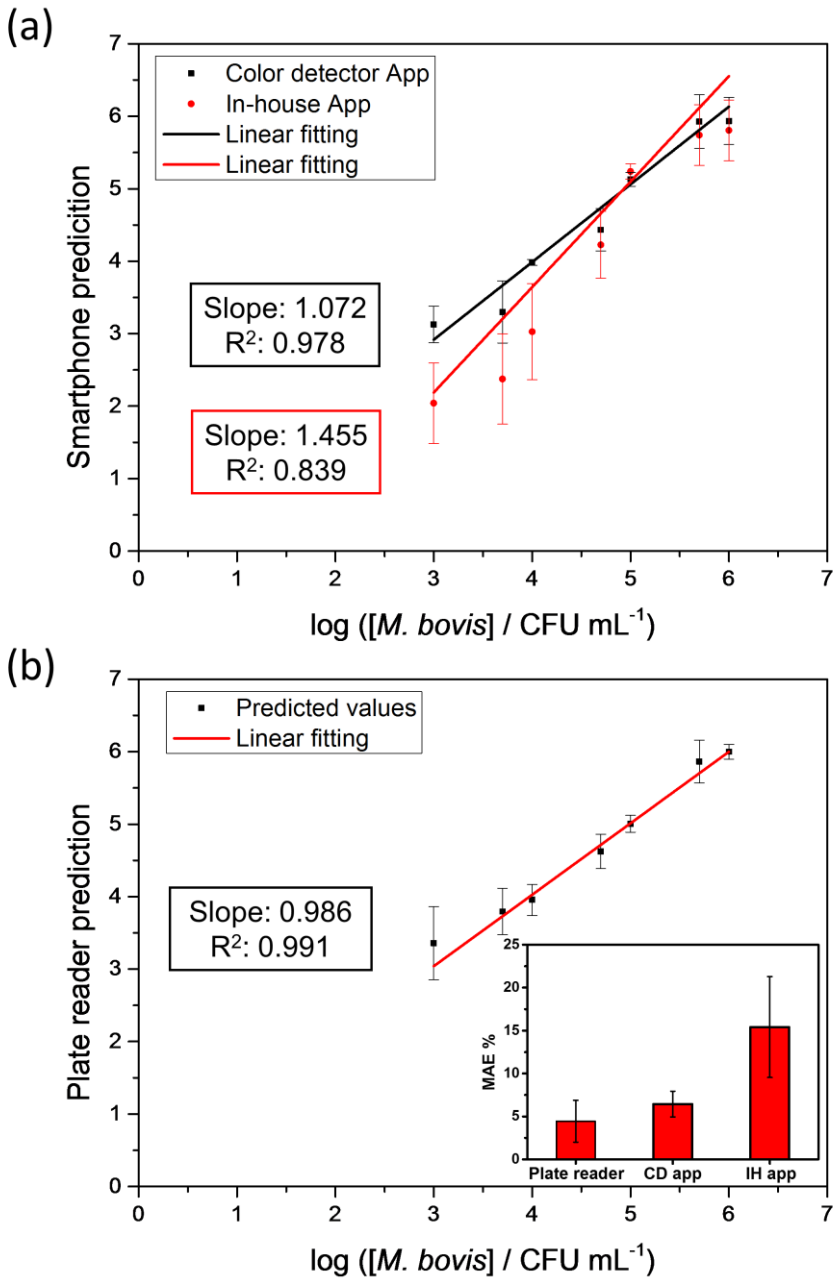

Figure C5. 6 Smartphone-based detection of *M. bovis*. (a) Two different smartphone apps are used to analyse the images taken with the smartphone. After calibrating them, both apps were capable of predicting the concentration of *M. bovis* present in several samples ranging from 10^3 to 10^6 CFU/mL. (b) Predictions observed using the spectrophotometer and comparison of the accuracy in the predictions with both smartphone apps.

5.4 Conclusions

Putting together several key aspects discussed in previous chapters has led to the development of a biosensor to detect food contaminants with potential for POC analyses. This includes the characterisation of the peroxidase-like activity of AuNSt discussed in Chapter 3, its suppression after functionalising their surface and restoration performing a gold enlargement step discussed in Chapter 4, or the potential smartphones have for quantifying a colourimetric signal. However, as important as keeping in mind all this information, it is imperative to select the appropriate biological binder to develop a successful biosensor. Some binders tested in this Chapter, like antibodies R43 and R44 showed a very good sensitivity, whereas antibody 1F11 displayed a decent sensitivity but a much higher selectivity towards *M. bovis* species within the MTBC. On the other hand, the peptide binder tested had previously reported a very good selectivity (less than 0.63% capture of non-*M. bovis Mycobacterium* spp.) but did not show positive results regarding background noise and sensitivity when tested in the 1D binding assay configuration. Overall, and without further optimisation of the nanozyme- and smartphone-based detection system, the proposed system slightly outperformed the LOD reached using an immunochemical sandwich assay for *M. bovis* detection ($7.2 \cdot 10^3$ vs $8.2 \cdot 10^3$ CFU/mL, respectively). Moreover, non-specific binding events between the modified nanomaterials and the bacteria did not occur, being the specific antigen-antibody interaction the only binding source. Thus, combining the restored peroxidase activity of 1F11 antibody modified AuNSt with smartphone apps for colour quantification provides a novel and effective semi-quantitative approach for detecting *M. bovis* in a portable (and potentially user-friendly) manner. It has been observed that “RGB Color Detector” app is second to none in terms of accuracy and sensitivity for solution-based colour quantification, even when compared to lab-based spectrophotometers. On the other hand, “QuantColorimetryApp” requires further optimisation of its fitting model to provide better predictions that can compete with current methodologies. All in all, this approach helps paving the way for the development of POC systems to be used in the food chain to discard contaminated food at any stage and prevent from wasting adequate foodstuff waiting for a lab result under the suspicion of a contamination event.

Chapter 6 Gold nanostars and SERS

6.1 Introduction

6.1.1 Raman Spectroscopy, SERS and SERRS

Raman spectroscopy (RS) was first theoretically predicted using classical quantum theory and then experimentally observed in the 1920s [394,395]. Fifty years after, it started to become a prominent analysis technique complementing those based in infrared light, as they were not ideal for samples containing polar solvents that typically absorb light in the infrared region [396]. RS is based in the inelastic scattering of light by matter, also known as *Raman effect*. As opposed to the predominant elastic scattering effect (also referred to as *Rayleigh scattering*) where the energy of the scattered photon is equal to that of the incident photon, the inelastic scattering leads to photons being scattered with a different energy. This energy difference carries a shift in wavelength of the fraction of radiation that is inelastically scattered, dependant on the chemical structure of the molecules responsible for the scattering [397]. Therefore, RS provides an interesting approach for identifying molecules through spectroscopic fingerprints. Unfortunately, the spontaneous Raman effect is very weak, as typically just 1 in 10^8 photons of the incident light undergoes spontaneous Raman scattering [396]. This poses a huge limitation in terms of the sensitivity achievable by any approach using RS. Several approaches have ever since arisen to overcome this limitation. Among these, Surface-Enhanced Raman Scattering (SERS) and Tip-Enhanced Raman Scattering (TERS). The former relies on placing the analyte on a rough metal surface or onto a nanostructure surface for achieving the Raman enhancement, whereas the latter uses a near atomically sharp pin to enhance the Raman effect at its vicinity (Figure C6.1). Considering that the relative size of the probed signal volume is much smaller in the case of TERS, the resulting enhancement will also be lower as compared to SERS (enhancement always relative to that of spontaneous Raman scattering). Thus, and due to its potential for POC analyses, SERS has been studied to a wider extent.

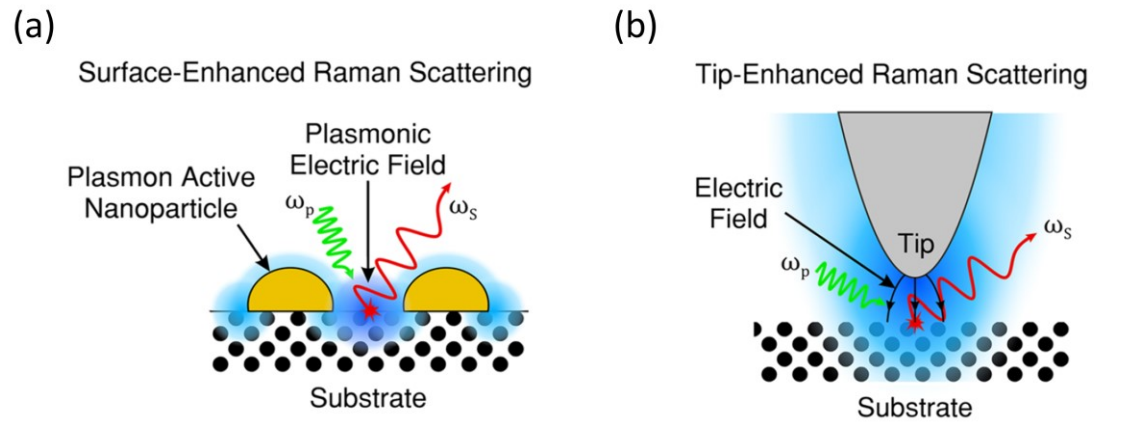

Figure C6. 1 (a) SERS. The incident light induces a surface plasmon resonance, resulting in an enhanced electromagnetic field at the vicinity of AuNPs leading to an augmented scattering effect. (b) TERS. A plasmonic tip enhances the electromagnetic field within a confined volume at the tip-sample junction, creating a lightning rod effect. ω_p: plasmon frequency, ω_S: scattered frequency. Figure reproduced from [396].

The mechanism underlaying the SERS effect has not been fully clarified yet, existing two field enhancement mechanisms thought to be involved in this effect: the electromagnetic (EM) and the chemical enhancement. The EM theory of SERS states that an amplification of the magnetic field due to the response of the metallic material surface to the incoming wave underlies the enhancement [398,399]. This happens when the exciting laser light is resonant with the dipolar plasmon of the metallic structure, that is to say, the wavelength of the incident light matches that of the plasmonic absorption peak of the nanostructure used as substrate. The chemical enhancement theory, on the other hand, states that a charge transfer between the metal surface and the analyte causes the enhancement of the Raman scattering effect. This is caused by the formation of new electronic states possessing intermediate energies resonating with the plasmonic frequency of the metal, generally due to a charge transfer transition between the highest occupied molecular orbital (HOMO) of analyte molecules and the fermi level of the metal [400]. Thus, the former involves enhancements in the field intensity as a result of plasmon resonance excitation, while the latter involves an enhancement in the polarizability of the analyte due to chemical effects such as charge-transfer excited states [399,401]. There seems to be scientific agreement though that the chemical enhancement only applies to specific molecules and contributes to the overall enhancement in a much lower extent than the EM enhancement which, besides, applies for all analytes [396]. Overall, the SERS enhancement factor (EF) can be large enough to observe single molecules (SM) [402]. However, despite remarkably high EF of the order of 10^{14} being described in the literature to explain for these SM observations, recent revisions claim that values around 10^4-10^8 are more reasonable and that

improper normalisation with respect to a non-resonant Raman signal during SERS EF calculations were on the basis of such misleading initial results [401–403]. The contribution of the resonance Raman enhancement of the bare cross section, which accounts for an additional factor of 10^5, helps supporting the possibility of detecting SM [404], although practical demonstration on this point is still controversial.

Lastly, Surface-Enhanced Resonance Raman Spectroscopy (SERRS) arises when a molecule has a chromophore close in energy to that of the light used to excite the plasmon to generate the SERS effect [405]. Thus, both the enhancement from SERS and from the analyte molecular resonance contribute to generate a very intense scattering effect, phenomenon that has long been studied [406]. Therefore, the main practical difference between SERS and SERRS is that the latter offers an additional enhancement as long as the chromophore energy and that of the light source can be matched.

6.1.2 AuNPs as Raman enhancers

Metallic NPs exhibit plasmonic features as it has been discussed in Section 1.2, leading to enhanced spectroscopic properties. Hence, these nanostructures have largely been studied for SERS applications. In pursuit of better sensitivities, many studies have tried to shed some light on how to increase the local EM field generated at the surface of metallic NPs. It is well established now that SERS signals can be intensified by assembling plasmonic NPs into dimers or small clusters, creating junctions known as “SERS hot spots” where a high confinement of the EM energy leads to a large enhancement of the Raman effect [116,407,408]. In addition to this, high confinement of EM energy has also been reported at sharp edges, tips or protrusions of anisotropic NPs, including nanorods [409,410], nanocubes [411], nanoprisms [412] or nanostars [92,413,414]. Logically, this potential has already been exploited for developing sensing approaches that combine anisotropic NPs and SERS, targeting a wide range of analytes such as mercury ions [415], aflatoxin [416], or the pesticide thiram [417]. In this line, many researches have investigated in the last years how different parameters of AuNPs affect their potential as Raman enhancers, by varying the size of gold nanospheres [418], comparing the enhancement generated by AuNPs with different shapes [419], or combining Au and Ag ions to synthesise bimetallic NPs with enhanced SERS properties [420].

6.1.3 Objectives

In this Chapter, the potential of AuNSt as Raman enhancers will be studied. Considering the lack of portability still faced by most Raman-based approaches, their performance needs to be critically compared with the traditional colourimetric systems in order to justify the need of SERS systems to develop ultra-sensitive sensors. A thorough characterisation will follow, similar to that performed in Section 3.3.4 where the peroxidase-like activity of AuNSt was studied. As different stabilising agents or LSPR variations could interfere in the nanozyme activity, they also affect the potential of AuNSt as Raman enhancers. To finish with this first section, the maximum enhancement factor reachable using AuNSt is calculated and compared to other values described in the literature.

Then, a second section of this Chapter includes a study using Au-Ag bimetallic nanostars which, depending on the nature of the nanostructure (formation of either core/shell or core/satellites structures), lead to significant differences in the Raman enhancement. Finally, two original research lines combining AuNSt and SERS for Hg^{2+} detection are analysed and compared to showcase the potential of this approach for developing ultra-sensitive biosensing devices.

Hence, this Chapter completes the fourth thesis aim (Section 1.4) “Characterise the peroxidase-like activity of AuNSt and their capability to act as Raman enhancers” and also covers the seventh thesis aim “Study the potential of bimetallic NPs for the development of ultra-sensitive sensors using SERS”.

6.2 Methods

6.2.1 Reagents and chemicals

Sodium citrate tribasic dehydrate ($HOC(COONa)(CH_2COONa)_2 \cdot aq$), gold (III) chloride trihydrate ($HAuCl_4 \cdot 3H_2O$, 99.9%), *O*-(3-Carboxypropyl)-*O*'-[2-(3-mercaptopropionylamino)ethyl]-polyethylene glycol, 11-mercaptoundecanoic acid, *O*-(2-Carboxyethyl)-*O*'-(2-mercaptoethyl)heptaethylene glycol, sodium hydroxide (NaOH), hydrochloric acid (HCl), rhodamine 6G, 3,3',5,5'-tetramethybenzidine (TMB), hydrogen peroxide (H_2O_2), silver nitrate ($AgNO_3$), ascorbic acid (L-AA), benzene-1,4-dithiol (BDT, 99%), 4-mercaptobenzoic acid (4-MBA, 99%) and cetyltrimethylammonium chloride (CTAC, ≥98%) were purchased from Sigma Aldrich (UK).

6.2.2 Raman Microscopy Analyses

RS measurements were carried out using a DXR2 Raman Microscope operated with an excitation laser light at 785 nm (Thermo Fisher Scientific, UK). The liquid samples were analysed in microtiter plate, focusing the Raman microscope prior to the measurement. This was done using the "Autofocus" function available with OMNIC™ series software in a positive control sample and then applying the same conditions throughout the rest of samples. The laser power used for the measurements has been varied along different experiments in this Chapter (between 1 – 20 mW), just as the microscope objective lens (x4 or x10). The exposure number (10) and integration time (5s), on the other hand, have been kept unvaried along all measurements.

6.2.3 Synthesis of Au-Ag bimetallic NPs

AuNSt were synthesised as discussed in Section 3.2.2 and then stabilised with CTAC 1 mM and a varying concentration of BDT (0.1 – 100 µM). The AuNSt solution was stirred for 30 min at RT and then centrifuged twice at 10 ˚C and 1200 rcf for 25 min and resuspended in an aqueous solution of CTAC 5 mM. 5 µL of $AgNO_3$ 100 mM, 5 µL of L-AA 100 mM and 2 µL of NaOH 2 M were subsequently added to 1 mL of the synthesised AuNSt-BDT and the mixture was left stirring for 2 min at RT. The resulting bimetallic nanostructures were washed once by centrifugation at 10 ˚C and 1200 rcf for 25 min and resuspended in CTAC 5 mM.

6.3 Results and discussion

6.3.1 Potential of SERS for biosensing

Along this thesis, AuNSt have been studied in relation to their potential for biosensing. Colourimetric approaches are the most interesting systems for achieving portability and user-friendliness, however they are far from ideal in terms of the sensitivity they can reach. SERS based approaches, on the other hand, are well known for reaching ultra-sensitive LOD values, but to date they still lack portability (although this aspect is expected to being solved in the near future with recent development in portable Raman spectrometers) and require trained personnel and expensive equipment as readout systems. Recent development in this direction has led to the commercialisation of handheld devices like Ocean HDX Raman Series Spectrometers (provided by Ocean Insight), BRAVO handheld Raman Spectrometer (Bruker) or ReactRaman 785 (Mettler Toledo). All these devices have been developed aiming at being user-friendly, small and portable, while maintaining the robustness and sensitivity of the method. However, they remain costly, explaining why their use has not been spread yet.

In order to introduce the potential advantages of SERS approaches for improving LOD values respect to colourimetric systems, an assay was planned to compare how AuNSt behave in each situation. Thus, 100 pM AuNSt-PEG and 0.01 mM TMB were prepared in an aqueous solution containing H_2O_2 6% and, after 20 minutes, the solution $A_{370\ nm}$ was read using a microplate spectrophotometer. It was observed that the solution containing TMB and the negative control containing AuNSt but not TMB showed very similar absorbance values, below 0.25 a.u. (Figure C6.2a). This indicates either that the colourimetric approach is not sensitive for detecting such a low concentration of oxTMB, or that AuNSt do not exhibit peroxidase-like activity under these conditions and therefore do not generate the required oxTMB for producing the spectroscopic signal. However, when these same samples were analysed with the Raman microscope, it was interesting to observe a clear difference between the sample containing TMB and the negative control sample (without TMB) (Figure C6.2b). Further analysing the spectra generated, three main bands located at specific wavenumbers (1608 cm^{-1}, 1336 cm^{-1} and 1190 cm^{-1}) indicated that the Raman signal had been generated by oxTMB. These three bands were attributed to ring stretching and C-H bending (overlapping bands at ~1608 cm^{-1}), inter-ring C-C stretching and CH_3 bending [162], respectively, and provided evidence that a blue Charge Transfer Complex (CTC) had been generated by the oxidation of TMB [421], therefore proving that AuNSt were still peroxidase-active. Additionally, another Raman band at 1401 cm^{-1} was observed, corresponding

to the stretching vibration of N=N, as a result of azo compound or unoxidized TMB [422]. These results demonstrate that SERS is a much more sensitive technique than any colourimetric approach, even if both are based in detecting the presence of the same molecule (oxTMB) in the very same sample.

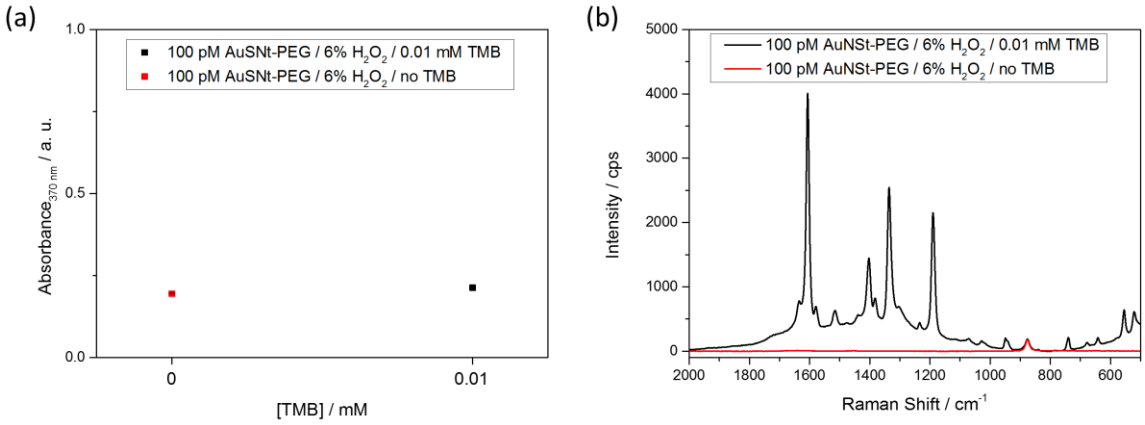

Figure C6. 2 (a) UV-Vis analyses measuring $A_{370\ nm}$ after 20 min of reaction of AuNSt in the presence of a minimal concentration of TMB and in the absence of TMB (negative control). The samples are analysed in triplicate. (b) Raman spectroscopy analyses of the same samples analysed by UV-Vis spectroscopy. Raman measurements were performed using a laser power of 20 mW, wavelength source 785 nm, 10 exposures with an integration time of 5 s and a 10x objective lens.

6.3.2 Characterisation of AuNSt as Raman enhancers

The goodness of a certain nanostructure to act as Raman enhancer is determined by many different parameters, resembling the observations discussed in Chapter 3 in relation to their peroxidase-like activity, which was affected by both the AuNSt optical properties and surface nature (Section 3.3.4). Thereby, the morphological properties of a specific NP will determine the amount of SERS hot spots, its surface nature will control the chances of a certain analyte to be located in the vicinity of the NP where the EM field has been enhanced, and the plasmonic properties of the NP will enable or not a resonance phenomenon with the incident light. The study of these parameters allows to better control the enhancement properties of AuNSt for SERS, which ultimately will result in a more sensitive approach for biosensing.

6.3.2.1 SERS dependence on AuNSt coating layer

AuNSt synthesised as described in Section 3.2.2 and functionalised with the same four coating molecules as shown in Section 3.2.3 (i.e. sodium citrate, PEG, OEG and 11-MUA) were used to

study how any surface modification affects their potential to act as Raman enhancers. Two Raman active molecules were used for this study: Rhodamine-6-G (R6G), a well-known and widely documented Raman probe [423,424], and oxTMB, a Raman active chromophore commonly used in enzymatic assays [162]. The main Raman bands belonging to each probe are listed in Table C6.1 and associated to their wavenumbers.

Wavenumber / cm^{-1}	Rhodamine-6-G	oxTMB
613	C-C-C ring in plane vibration	
1191		CH_3 bending
1312	N-H in plane bending	
1337		C-C inter-ring stretching
1364	C-H in plane bending	
1512	Aromatic C-C stretching C-N stretching C-H bending	
1605		Ring stretching and C-H bending
1651	Aromatic C-C stretching C-H in plane bending	

Table C6. 1 Assignment for the main Raman bands [162,423] obtained for two Raman active probes used in this Chapter: R6G and oxTMB.

It was interesting to note that, for both R6G and oxTMB, only AuNSt-PEG and AuNSt-NaCit based solution led to such Raman signals, whilst little to none was observed in every other situation (Figure C6.3). A plausible explanation for these observations could lie in the 3 dimensional organisation of the coating layer onto the AuNSt, which could hinder or boost the diffusion of a certain Raman probe towards the vicinity of AuNSt hot spots where the enhanced EM field is located. This would explain why AuNSt-OEG, which had shown a strong peroxidase-like activity (Figure C3.12), do not lead to a similarly strong Raman signal (peaks under 100 cps in Figure C6.3b).

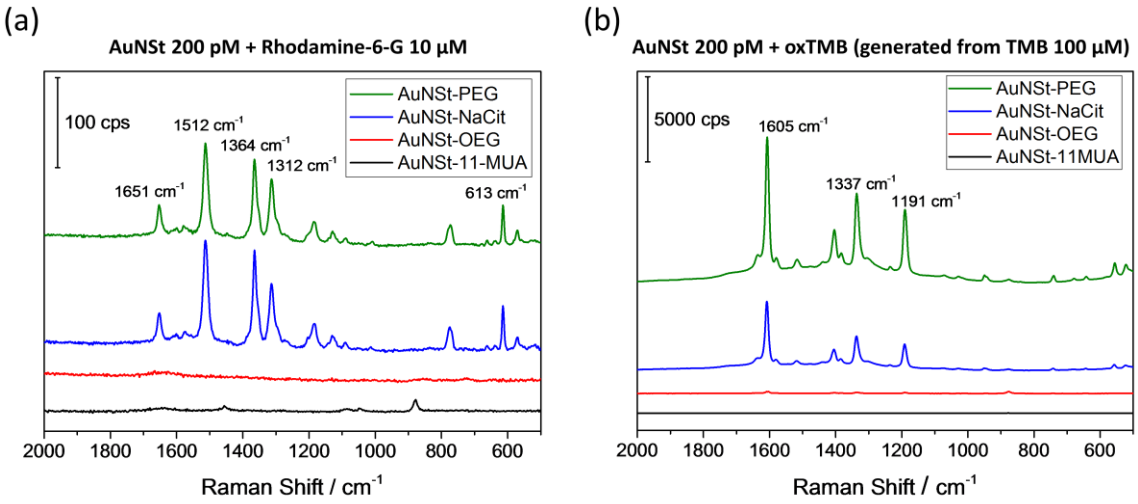

Figure C6. 3 (a) 10 µM of R6G were mixed with AuNSt stabilised with different moieties and measured by Raman spectroscopy. (b) oxTMB generated by AuNSt was measured by Raman spectroscopy. Raman measurements were performed using a laser power of 10 mW, wavelength source 785 nm, 10 exposures with an integration time of 5 s and a 10x objective lens.

6.3.2.2 SERS dependence on AuNSt LSPR

The capability of AuNSt to enhance the Raman signal is not only dependent on the nature of any surface modification, but also on their LSPR wavelength [425,426]. Therefore, it is essential to understand how plasmonic properties behave in this aspect for improving sensing assays and reaching lower LOD values.

AuNSt with LSPR values distributed along the visible spectrum (from 592 to 779 nm) were prepared as described in Section 3.2.2 and citrate capped as described in Section 3.2.3. 200 pM of each of them were incubated with 0.1 mM TMB in an aqueous solution containing 6% H_2O_2 to produce through their nanozyme activity a controlled and fixed concentration of oxTMB (i.e. 7 ± 1 µM). These solutions were subsequently analysed by Raman spectroscopy to characterise the effect of a LSPR shift in the Raman effect, using a 785 nm wavelength excitation laser (Figure C6.4a). The results clearly showed that the closer the plasmonic frequency of the AuNSt gets to that of the excitation laser, the larger the enhancement observed. This can be explained from two perspectives: either the transformation of the AuNPs from spherical- to star-like (plasmon redshift) leads to a greater number of hot spots and to a larger enhancement, or a wavelength match between the plasmonic and the laser frequencies produces a resonance that introduces a SERRS phenomenon. Further analysis on this is shown in Figure C6.4b, where UV-Vis spectroscopy results from all six samples is collected to discard any difference in the oxTMB concentration lying behind the observed SERS differences.

(a)

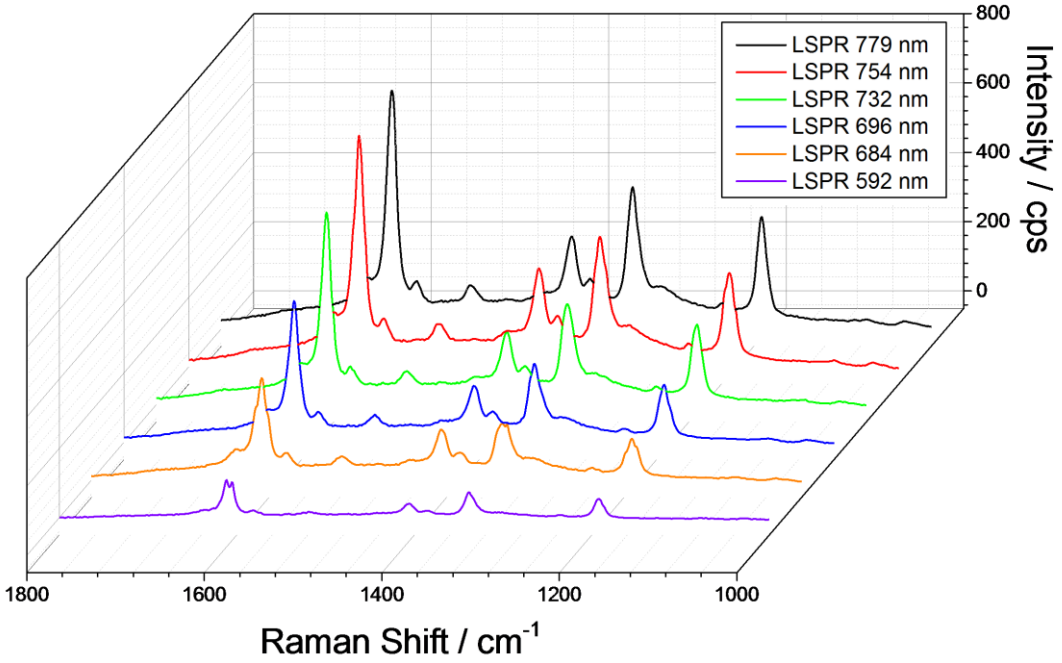

(b)

LSPR / nm	$A_{370\ nm}$ / a. u.	[oxTMB] / µM	$SERS_{1605\ cm^{-1}}$ / cps
779	0.378	6.1	686
754	0.415	6.7	665
732	0.397	6.4	553
696	0.435	7.1	406
684	0.452	7.3	294
592	0.560	9.1	88

Figure C6. 4 (a) AuNSt-NaCit with different plasmonic properties were analysed by Raman spectroscopy to detect the presence of oxTMB. Raman measurements were performed using a laser power of 2 mW, wavelength source 785 nm, 10 exposures with an integration time of 5 s and a 10x objective lens. (b) Table summarising the amount of oxTMB generated by each AuNSt sample and the Raman signal produced.

6.3.2.3 AuNSt enhancement factor

One of the most interesting parameters determining the goodness of a certain nanostructure for SERS is the enhancement factor (EF). However, no consensus has been reached yet on how to best calculate this factor in a standardised manner, making virtually not possible to critically compare the performance of different SERS substrates reported in the literature. Various review studies on this topic agree that the difficulty in unambiguously knowing the actual number of Raman active molecules residing in the scattering volume remains the main limitation for a robust EF calculation [427,428]. Therefore, the analytical enhancement factor (AEF) emerges as a rough alternative providing information on how much more signal can be expected from SERS as compared to spontaneous Raman under certain given experimental conditions. AEF is calculated as follows:

$$AEF = \frac{I_{SERS}/c_{SERS}}{I_{RS}/c_{RS}},$$

where an analyte solution with concentration (c_{RS}) generates a Raman signal (I_{RS}) under non-SERS conditions or normal Raman scattering. As opposed to the signal generated (I_{SERS}) by a certain concentration of analyte (c_{SERS}), in the presence of the SERS substrate.

R6G has been used for characterising the potential of AuNSt as Raman enhancers following this approach. Samples containing a range of R6G concentrations from 10^{-3} to 10^{-9} M were prepared and measured in two different conditions: in the presence of 200 pM AuNSt and on their own (Figure C6.5). The stronger band belonging to R6G observed by Raman spectroscopy (i.e. that located at 1512 cm^{-1}) has been used as diagnostic band and its intensity compared in all different samples. Then, the AEF was calculated using the data extracted from the sample containing the lowest detectable concentration of R6G for both the SERS and non-SERS conditions, as shown below:

$$AEF = \frac{I_{SERS}/c_{SERS}}{I_{RS}/c_{RS}} = \frac{13.2/1 \cdot 10^{-8}}{6.4/1 \cdot 10^{-3}} = \mathbf{2.1 \cdot 10^{5}}$$

Thus, the Raman enhancement provided by AuNSt is of 5 orders of magnitude, similar to other observations reported somewhere else [242,429,430], and clearly positioning them as interesting nanostructures for SERS-based sensing assays.

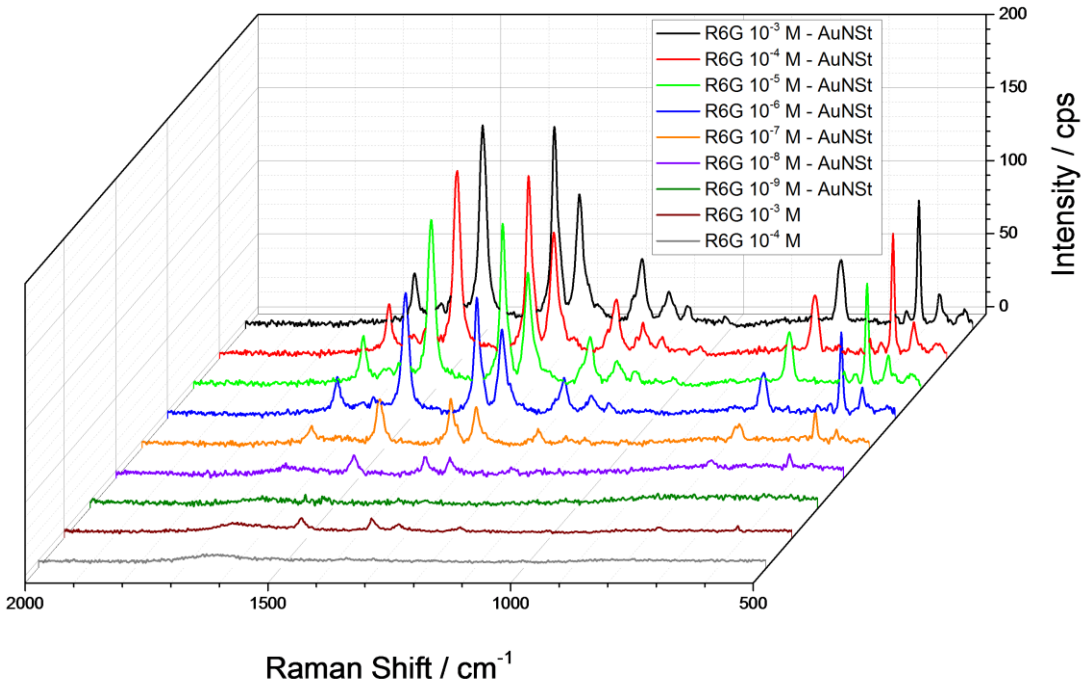

Figure C6. 5 Raman spectra of decreasing concentrations of Rhodamine 6G in the presence and absence of AuNSt-NaCit. Raman measurements were performed using a laser power of 5 mW, wavelength source 785 nm, 10 exposures with an integration time of 5 s and a 10x objective lens.

6.3.3 Au-Ag bimetallic NPs

Traditional SERS studies tended to use monometallic nanostructures such as gold or silver based, being considered the latter a better substrate than gold [431,432]. These claims are based on empirical evidence, suggesting that an analyte would interact differently with different substrates and this would lead to a particular molecular electronic density redistribution, thus producing different Raman intensities and slight band shifts. Therefore, past studies commonly focused just in varying the shape towards anisotropic nanostructures with a higher density of SERS hot spots, claiming that the SERS effectiveness of Au-Ag bimetallic nanostructures sit between that of Ag and Au colloids on their own [432]. It is well documented now that such bimetallic nanostructures can reach better AEF than their monometallic counterparts due to synergistic effects [431,433]. However, it still is uncertain whether the pin hole theory (stating that the local EM field can increase by a factor of 4 within pin holes in core-shell NPs) or the adsorbate-induced aggregation (applying to core-shell NPs in liquid) lie behind these observations [434]. In this Section, Au-Ag bimetallic nanostars are synthesised following various approaches, characterised, and their potential for SERS applications investigated. To this end,

bifunctional ligands such as 1,4-benzenedithiol (BDT) and 4-mercaptobenzoic acid (4-MBA) are used along this section as Raman probes (Table C6.2) and as Au-Ag linkers.

Wavenumber / cm^{-1}	1,4-BDT	4-MBA
350	C-C-S bending	
362		C-C-S bending
733	C-S stretching	
1060	Aromatic C-S stretching	
1078		Aromatic C-C stretching Aromatic C-S stretching
1182	C-H in plane bending	
1564	Aromatic C-C stretching	
1589		Aromatic C-C stretching

Table C6. 2 Assignment for the main Raman bands [435,436] obtained for two Raman active probes embedded in Au-Ag bimetallic NPs.

6.3.3.1 BDT-embedded Au-Ag bimetallic NSt

Previous studies had already shown that a mixture composed of the bifunctional ligand 1,4-benzenedithiol (BDT) and hexadecyltrimethylammonium chloride (CTAC) could not only provide AuNSt with long-term stability, but also enable to create a Au-BDT-Au structure where the Raman probe stays embedded in a core/shell-like structure [437]. Such stability is mainly provided by CTAC molecules, whereas BDT is involved in the formation of the core/shell like structure and has little implication in the stability process. In an attempt to increase the SERS AEF provided by AuNSt, they were used as seeds following the protocol described in Section 6.2.3 to create Au-Ag bimetallic NPs. It was observed that the reduction step of Ag onto the AuNSt surface varied depending on the concentration of BDT used to coat the AuNSt. As shown in Figure C6.6a, BDT final concentrations equal or higher than 10 µM led to a plasmon redshift, whereas concentrations under that value led to a plasmon blueshift. The observed plasmon blueshift can be associated to a silver growth on top of the AuNSt surface, a phenomenon that has been reported elsewhere [371]. The plasmon redshift, on the other hand, has been associated to the formation of silver satellites (AgSAT) attached to the AuNSt tips rather than a Au-Ag core/shell structure (unpublished results). In all cases, after the silver reduction step, a UV-Vis peak located between 400-450 nm can be observed corresponding to the plasmonic

properties of spherical AgNPs produced during this growth step. These, however, are washed off the solution by centrifugation, resulting in a yellowish supernatant and displaying no Raman activity. The pellet concentrates the Au-Ag bimetallic nanostructures, whether they are AuNSt-AgSAT or Au-Ag core/shell NSt, visualised as a dark black-yellowish solution or a clearer brown solution, respectively (Figure C6.6b).

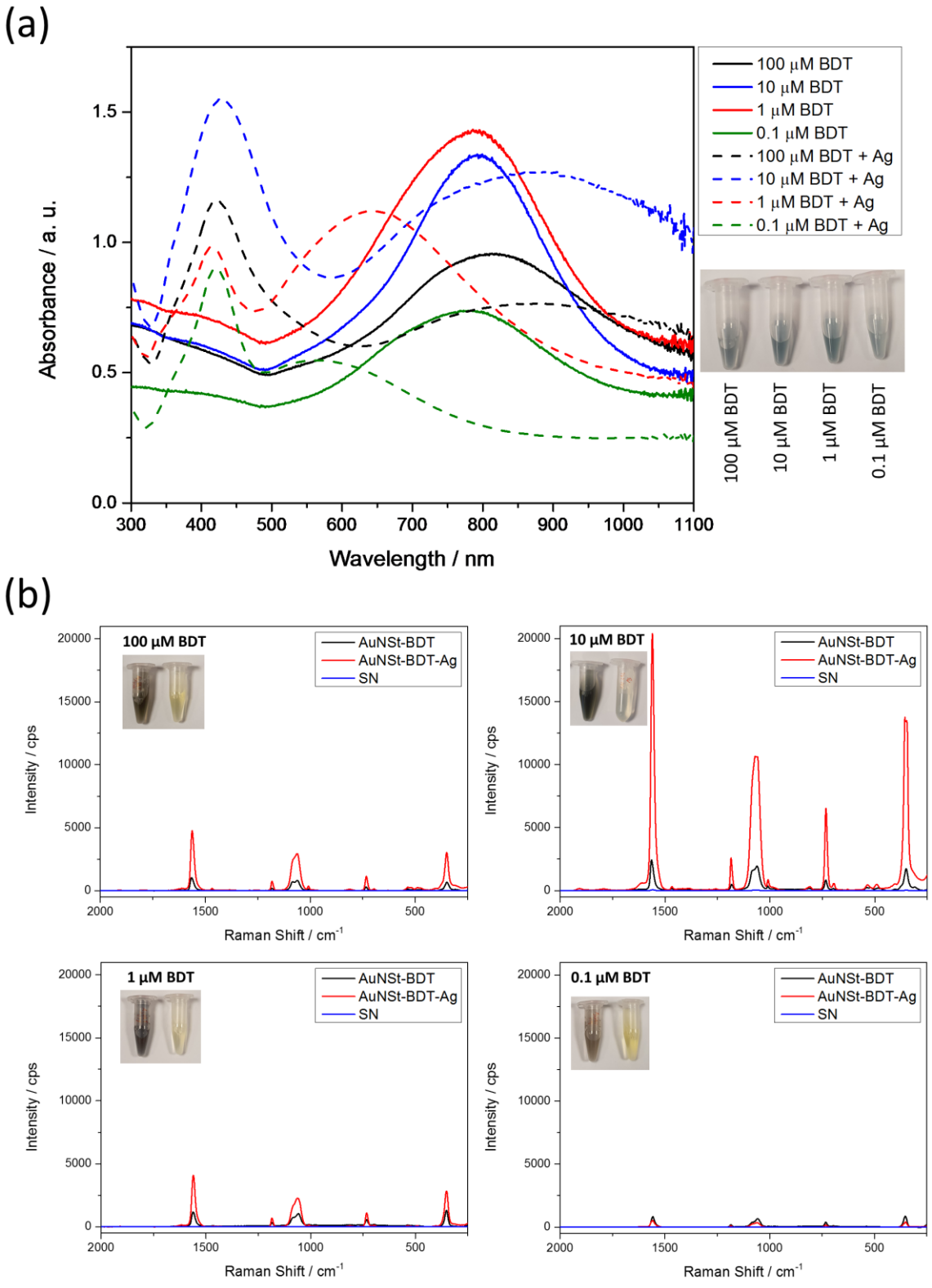

Figure C6. 6 (a) AuNSt samples coated with a varying concentration of BDT are shown in an image and further UV-Vis spectroscopy analyses shown in the graph, together with spectra obtained after adding Ag to produce Au-Ag bimetallic NPs. (b) Spectra obtained by Raman spectroscopy for each of the BDT-based nanostructures. Raman measurements were performed using a laser power of 25 mW, wavelength source 785 nm, 10 exposures with an integration time of 5 s and a 10x objective lens. (*SN: Supernatant)*

It can be observed that a BDT concentration of 10 µM results optimum for achieving the best AEF, producing a Raman signal almost 10 times larger than that generated by AuNSt-BDT on their own (20,392 vs. 2,425 cps, as seen in Figure C6.6b top right). It is interesting to note that an increase in BDT concentration to 100 µM leads to a worse stability of AuNSt-BDT, as visually appreciated in the image inserted in Figure C6.6a, probably due to some cross-linking taking place between AuNSt which causes their partial aggregation. Thus, despite showing a plasmon redshift after the Ag addition step, which indicates that the highly SERS active AuNSt-AgSAT have been formed, the enhancement is lower than that observed for AuNSt stabilised with 10 µM BDT. On the other hand, BDT concentrations under 10 µM used to coat AuNSt do not produce AgSAT, being a silver shell the most probable structure formed onto AuNSt, as expected from the plasmon blueshift observed. Figure C6.6b also shows that the Raman enhancement is not as good as that observed for AuNSt-AgSAT and decreases as the amount of BDT used to coat AuNSt drops.

6.3.3.2 4-MBA

4-Mercaptobenzoic acid (4-MBA), a similar bifunctional linker to BDT that replaces one of the thiol groups by a carboxyl group, was also tested to create Au-Ag bimetallic NPs and characterise the Raman AEF of the embedded probe. Previous studies had also shown promising results for sensing using this approach [438]. A final concentration of 100 µM of 4-MBA was used to coat AuNSt together with CTAC as described in Section 6.2.3. A UV-Vis analysis showed that the resulting nanostructures underwent a plasmon blueshift, implying the formation of a silver shell onto the AuNSt together with spherical AgNPs that are washed off the sample by centrifugation (Figure C6.7a). Even so, a large enhancement was observed by Raman spectroscopy (Figure C6.7b) which, despite not reaching absolute values as large as those observed by AuNSt-AgSAT analyses, still resulted in an 8 times increase if compared to the original AuNSt-4-MBA used as seeds.

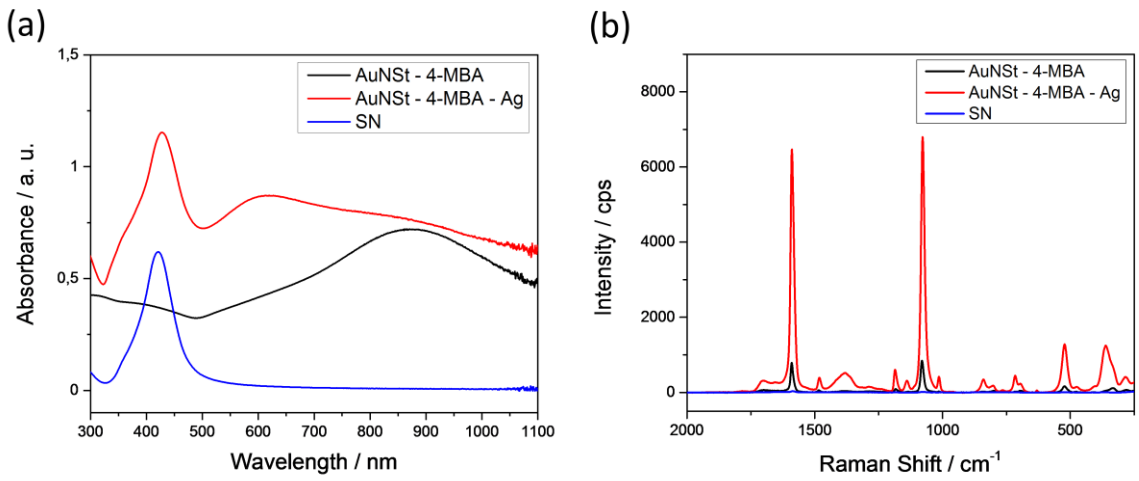

Figure C6. 7 AuNSt coated with 4-MBA before and after performing the silver reduction step were analysed by (a) UV-Vis spectroscopy and (b) Raman spectroscopy. Raman measurements were performed using a laser power of 25 mW, wavelength source 785 nm, 10 exposures with an integration time of 5 s and a 10x objective lens. (*SN: Supernatant)*

In conclusion, AuNSt-AgSAT were obtained after coating AuNSt with a high enough concentration of BDT, but not with 4-MBA. The mechanism by which these conformation takes place, however, has not been elucidated yet and further research in this line is needed. Anyhow, only these nanostructures led to a Raman signal over 20000 cps, enhancing the signal almost 10 times if compared to the AuNSt on their own (Table C6.3).

[BDT] / µM	LSPR / nm	Abs_{LSPR} / a.u.	$SERS_{1567\ cm^{-1}}$ / cps	LSPR (Ag) / nm	Abs (Ag) $_{LSPR}$ / a.u.	SERS (Ag) $_{1567\ cm^{-1}}$ / cps
100	813	0.957	1032	874 (→)	0.767	4756 **(x4.6)**
10	795	1.338	2425	887 (→)	1.274	20392 **(x8.4)**
1	790	1.432	1176	642 (←)	1.123	4082 **(x3.5)**
0.1	782	0.738	820	559 (←)	0.547	519 **(x0.6)**
[4-MBA] / µM	**LSPR / nm**	**Abs_{LSPR} / a.u.**	**$SERS_{1078\ cm^{-1}}$ / cps**	**LSPR (Ag) / nm**	**Abs (Ag) $_{LSPR}$ / a.u.**	**SERS (Ag) $_{1078\ cm^{-1}}$ / cps**
100	862	0.721	848	626 (←)	0.871	6797 **(x8.0)**

Table C6. 3 Compilation of spectroscopic data obtained from AuNSt coated with several concentrations of Raman probes BDT and 4-MBA, before and after (Ag) applying a silver growth step. (→) indicates plasmon redshift, (←) indicates plasmon blueshift.

6.3.4 Published studies

As indicated by the foregoing, AuNSt have shown great potential for the development of Raman-based biosensing approaches. This has been exploited for the detection of Hg^{2+} ions, a health-threatening environmental contaminant, following two different mechanisms: combination of their nanozyme activity (i.e. peroxidase mimicking) to generate the Raman active probe oxTMB (Mechanism 1), and use of the enhanced Raman signal provided by Au-Ag bimetallic NPs (specifically, AuNSt-AgSAT) (Mechanism 2). The study involving the former mechanism has just been published as an original article [439], whilst the latter has been submitted and it is in track for publication.

6.3.4.1 Mechanism 1

It has been observed that PEGylated AuNSt show an adequate peroxidase-like activity (Figure C3.12) and a strong Raman enhancement (Figure C6.3), making them ideal candidates both as colourimetric and spectroscopic reporters. On the other hand, Hg ions are well known for forming amalgams with most metals, including gold, which leads to a AuNSt shape truncation if present together in a sample. As shown in Scheme C6.1, the resulting spherification of AuNSt increases with the concentration of Hg^{2+} ions and carries a drop in the Raman enhancement, but not in the nanozyme activity [215]. Thus, oxTMB (acting as Raman probe) is still generated but the loss of hot spots leads to a signal decrease that can be correlated to a certain Hg concentration. This approach enabled a Hg^{2+} detection down to 0.2 ppb in seawater samples (MRL of 2 ppb as set by the Environmental Protection Agency [440]), being further analytical parameters of this assay shown in Table C6.4.

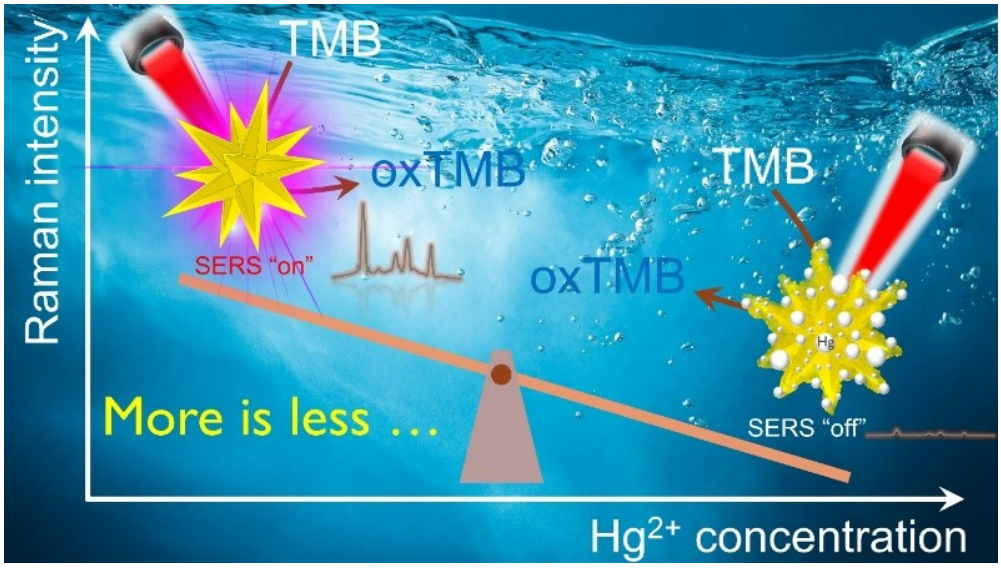

Scheme C6. 1 Mechanism for Hg^{2+} sensing in environmental water samples [439].

6.3.4.2 Mechanism 2

AuNSt-AgSAT prepared as discussed in Section 6.2.3 using a BDT concentration of 10 µM were exploited in this study to provide a better Raman enhancement in pursuit of a better sensitivity for Hg^{2+} ions detection. Recent characterisation of these nanostructures had shown that the Raman signal provided by BDT was almost 10 times greater than that obtained using AuNSt on their own (Section 6.3.3). This signal increase is generated due to the synergism of Au and Ag atoms, while retaining an anisotropic nanostructure rich in Raman hot spots. As the Hg^{2+} ions concentration increases, a morphological disruption of the AuNSt-BDT-AgSAT is observed, causing the SERS signal to drop (unpublished results). Therefore, the mechanism followed here differs from the approach above in the Raman probe (BDT instead of oxTMB) and the amplification strategy (Au-Ag synergism instead of nanozyme activity of AuNSt). Thus, a Hg^{2+} concentration as little as 0.1 ppb was successfully detected in deionised water (Scheme C6.2).

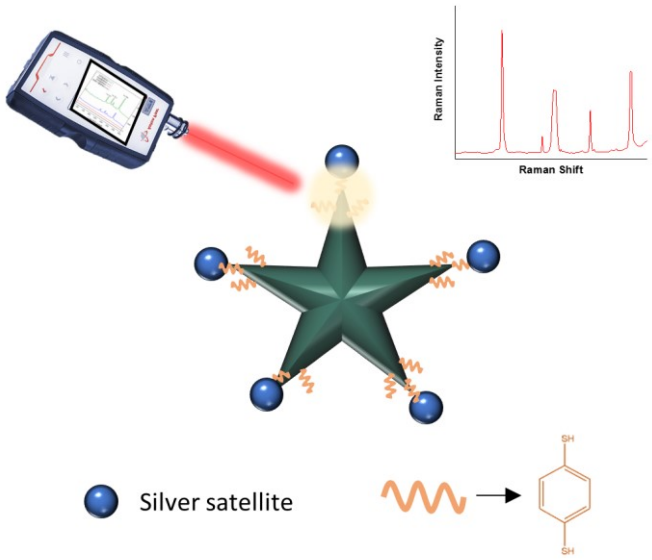

Scheme C6. 2 Mechanism for Hg^{2+} sensing through SERS using AuNSt-BDT-AgSAT.

Both mechanisms have exposed the potential that anisotropic and bimetallic nanoparticles possess in terms of Raman enhancement and their applicability for developing ultra-sensitive sensors. While the second reaches a slightly better limit of detection, it has not been as thoroughly validated with real samples as the first mechanism, therefore further research in this line could strengthen the approach based in the synergism of bimetallic NPs for SERS. More sensitive methods for the detection of Hg^{2+} ions exist, naturally, including confirmatory techniques such as cold-vapor atomic absorption spectrometry (CV-AAS) or inductively coupled plasma-mass spectrometry (ICP-MS), detecting 0.008 ppb [441] and 0.001 ppb [442],

respectively. However, few examples exist in the literature reporting novel methods potentially applicable for POC scenarios with such low LODs [439].

	Mechanism 1	Mechanism 2
Assay mechanism	AuNSt oxidation of TMB (nanozyme) & SERS detection	AuNSt-BDT-AgSAT SERS detection
Target analyte	Hg^{2+} ions	Hg^{2+} ions
Matrix	Seawater CRM	dH_2O
Selectivity	Tested against 13 other ions (K^{+}, Zn^{2+}, Na^{+}, Mn^{2+}, Ag^{+}, Al^{3+}, Co^{2+}, Ca^{2+}, Fe^{2+}, Mg^{2+}, Bi^{3+}, Li^{4+}, Sn^{4+})	Tested against 9 other ions (Mg^{2+}, Bi^{3+}, Sn^{4+}, Fe^{2+}, Mn^{2+}, Co^{2+}, Na^{+}, Al^{3+}, Ag^{+})
Sensitivity	0.2 ppb	0.1 ppb
Recovery	95.2 – 104.5 %	-

Table C6. 4 Comparison of analytical performance of two different approaches discussed in this Section for Hg sensing in water samples exploiting SERS activity of AuNSt.

6.4 Conclusions

In this Chapter, the potential of anisotropic AuNSt to act as Raman enhancers is demonstrated altogether with some guidance on how to improve this effect. This spectroscopic approach shares some similarities with the colourimetric approach elsewhere discussed along this thesis, such as its dependence on the optical and surface nature properties of the nanomaterials, but also shows differences as to the achievable sensitivity. Thus, given a certain laser wavelength to irradiate the AuNSt and induce the Raman effect, there is an optimum LSPR that leads to a maximum signal. Likewise, different surface modifications onto the NPs will lead to a rise or a drop in the Raman signal generated, presumably due to the hinderance degree it has over the analyte to stay close in the vicinity of the NP surface. These correlations have been studied and the optimum conditions to develop a sensor following this mechanism elucidated. On the other hand, the achievable sensitivity using SERS has been compared to that using the colourimetric approach that exploits the nanozyme activity of AuNSt. The better sensitivity reached by SERS justifies why, despite lacking the portability and user-friendliness offered by colourimetric approaches, SERS-based devices are still a competitive option in the biosensing field. Specifically, AuNSt-PEG have shown great potential for Raman enhancement, whereas other stabilising agents like OEG or 11-MUA did not display these properties. As for their optical properties, it has been observed that the closer the plasmonic properties of the AuNSt to the wavelength of the incident light, the better enhancement factors were reached. Following these conclusions, an enhancement factor higher than 10^5 was achieved for detecting Raman-active model dye Rhodamine-6-G.

In addition, the capability of different metals to act in a synergistic manner to further enhance the Raman signal was thoroughly characterised using Au-Ag bimetallic NSt. Previous studies had reported that such bimetallic nanostructures presented better SERS activity than that of the NPs made of either pure gold or silver, while retaining the benefits of each of them (i.e. higher plasmonic efficiency of silver and better chemical stability of gold-based nanostructures). BDT has been used as Raman probe for comparing SERS activity of Au-Ag bimetallic NSt to that of AuNSt on their own. A 10 times increase was observed when the Raman intensity was compared in both situations, therefore implying that bimetallic nanostructures could reach better sensitivities for the development of SERS-based biosensors. Nevertheless, attention must be paid to the type of bimetallic nanostructure formed, as varying the linker's concentration may result in core-shell structures, satellites formation, or a wide range of different morphologies that carry an equally variable Raman enhancement capability.

Finally, all the information collected along the Chapter has been put into practice for the development of two sensing mechanisms with environmental relevance: detection of mercury ions in water samples. Each system uses a different Raman probe and amplification strategy for this purpose, being their analytical features compared in a table. The first system uses the nanozyme activity of AuNSt to generate Raman-active oxTMB, while the second system detects the Raman probe BDT embedded between Au and Ag atoms in a AuNSt-BDT-AgSAT nanostructure, this exploiting the Au-Ag synergism to obtain a maximum Raman effect. In both cases the Raman signal is inversely proportional to the presence of Hg^{2+} ions, as the Au-Hg amalgamation process disrupts the anisotropic morphology of AuNSt and reduces the presence of Raman hot spots. Concentrations well below the maximum residue level (MRL) for Hg^{2+} in drinking water (2 ppb, as set by the Environmental Protection Agency [440] and the World Health Organisation [443]) were reached by both mechanisms: 0.2 and 0.1 ppb, respectively. Current detection methods include ICP-MS, enabling to detect as little as 0.001 ppb. These studies highlight the importance of further miniaturising and automatising Raman spectrophotometers, as it is evident now both the potential they have for developing ultra-sensitive assays and the limitations they present for portability with current equipment.

Chapter 7 Thesis conclusions

Gold nanoparticles have long been known and used for very diverse applications ranging from decoration, disease treatment, industrial processing and, in the last decades, biosensing. Much knowledge has been gained throughout their use in history, but an explosive development has arisen in the last years especially due to the fast development of physicochemical equipment enabling us to study them, handle them and, literally, see them in the nanoscale. This thesis reports some of the last findings related to gold nanostars, a specific type of anisotropic gold nanoparticles that hide in their shape a great potential for improving detection mechanisms that can be incorporated in biosensing devices. Their augmented surface-to-volume ratio, a simple morphological property on first sight, lies behind their capability to shift their plasmonic properties along the visible, near-infrared and infrared spectrum, their improved performance as Raman enhancers and even their nanozyme properties.

On the other hand, a growing world population demanding more food production than ever has brought the necessity to test food products to discard any health-threatening contamination (microbiological or otherwise) before the food reaches the consumer. The complexity of the global network bringing food "from farm to fork" includes producers, transporters, wholesalers, retailers and, eventually, the consumers. Such a large number of actors involved in the food production chain altogether with the equally large number of miles travelled by food leads to a higher risk of a contamination event to happen and, more importantly, to pass unnoticed if proper foodstuff track is not in place. Strict regulation applies for food contamination, naturally, but still the RASFF portal had to notify 392 cases of food contamination of milk products only in the EU in the last decade (2010-2019). Considering that a single contamination event in the EU rarely affects only one country, a large number of people is at risk of suffering any sort of food poisoning.

In consideration of the above, the present thesis aimed at applying the new technology brought by gold nanostars to solve the current food-related problems faced by modern societies. In addition, limitations of current sensors are considered, which include lack of portability, price of the test, user-friendliness, etc. That is to say, sensors need to be developed aiming at being used where they are needed and by whoever needs them. A very interesting option to bridge *the Valley of Death* in POC analyses is the use of smartphones as readout systems and data processors in new biosensing devices. They are widely spread, even within low-income regions, enable to quantify signals generated by gold nanostars and comply with POC requirements.

In this context, the key findings of this research are summarised below:

In **Chapter 1**, a literature review is presented discussing the main issues related to food contamination, while a justified explanation is given on why targeting microbiological contaminants specifically or why using gold nanomaterials for that. Besides, the main novelty of this Chapter lies in the publication of an extensive review article discussing the latest advances on gold nanozymes and their applications in the biomedical field. It showcases that metallic nanoparticles display several enzyme-mimicking activities, including oxidase-, glucose oxidase-, peroxidase-, catalase-, superoxide dismutase- or reductase-like activities. Moreover, the morphology and surface chemistry of nanoparticles play an important role in their catalytic properties, as well as external parameters including the pH or the temperature. Such versatility has opened a new path for developing novel sensing technologies in several biological fields including medical, food-related or environmental areas. This review discusses key aspects that may boost or inhibit nanozyme activities, as well as recent solutions proposed for overcoming current obstacles faced while developing biosensing devices based in this technology. The information extracted from over 200 recently published articles provides invaluable input on what can be done with nanozymes, which obstacles have already been solved and which ones remain unexplored.

In **Chapter 2**, an online sensors classification system based on a user-friendly decision tree is reported. The interactive platformed shown in this Chapter, named TEST (The End-user Sensor Tree), was prepared after analysing over 900 sensors retrieved form the literature and commercial market. This database provides a current picture of state-of-the-art sensors targeting several food contaminants, such as aquatic toxins, mycotoxins, pesticides and microorganisms. Sensors are therein classified according to their portability, capability to quantify the analyte, user-friendliness or capability to perform multiplex analyses. Nanomaterial-enhanced and electrochemical sensors came out as the preferred approaches for satisfying POC needs (i.e. portability, low cost and ease of use) while retaining an adequate sensitivity. However, an important conclusion arising from this study is that too few diagnostic devices are brought from lab prototypes to a finished commercial product. Therefore, and endless list of sensing mechanisms is reported in the literature, but just a few of them have reached the end-user (mainly immunochromatographic assays, and ELISA or PCR tests). Moreover, a fully portable and quantitative assay for microbiological contaminants in food is yet to be developed. Thus, current methodologies reaching required LODs have to disregard either the portability of the assay or the capability to quantify. Finally, while there are many studies pointing out the potential of nanozymes as transducer elements and smartphones as readout

systems, only one article using both elements has been found in the literature, indicating that further research in this line could lead to novel and successful POC sensing devices.

In **Chapter 3**, gold nanostars have been synthesised and characterised following a number of physicochemical approaches. Following previous studies, they were synthesised with different plasmonic properties and successfully stabilised with 4 coating molecules: sodium citrate, OEG, PEG and 11-MUA. Only the attempt to stabilise gold nanostars with 16-MHA led to an aggregation event, regardless of the conditions used. TEM analyses showed that gold seeds had grown from their initial 13 nm diameter to an average 105 ± 29 nm for samples reaching a maximum growth. Besides, their refractive index sensitivity was calculated as 386 nm/RIU, indicating great potential for plasmonic biosensing. However, the main novelty of this chapter lies in the extensive characterisation performed on the peroxidase-mimicking activity of gold nanostars. It showed that gold nanostars with a larger surface-to-volume ratio (i.e. those samples that had endured a larger anisotropic growth from their original spherical shape, leading to a large plasmon redshift) displayed better catalytic properties measured as their efficiency to oxidise TMB. Similarly, differences in the stabilising agent used led to enhanced or reduced capabilities to oxidise TMB, ordered form the most to the least suitable: OEG > NaCit > PEG > 11-MUA. These findings are of special relevance for the development of a biosensor, as only stable nanostars that retain nanozyme properties will be able to generate the required colourimetric signal.

In **Chapter 4**, two smartphone applications (one commercial, another developed by an in-house collaborator) are successfully used to quantify the colourimetric signal generated by the nanozyme activity of gold nanostars. Nevertheless, a recurrent obstacle had to be solved first: the inhibition of the peroxidase-like activity of gold nanostars after coating their surface with a suitable biorecognition element. A catalytic autoenlargement of gold nanostars step was proposed and optimised to generate a new, uncoated, gold surface capable to restore the peroxidase-like activity previously lost. A similar study was performed using silver ions for this secondary growth (instead of gold) but no improvement was observed. Using a commercial smartphone app for colour quantification, as little as 10 pM of protein-coated gold nanostars were detected. In order to do that, colour data were extracted using the RGB colour code and the Red channel values used for quantifying the blue colour generated by the TMB oxidation process. This system provided the basis for developing the smartphone-based colourimetric sensor reported in the next Chapter. On the other hand, the in-house developed smartphone app was calibrated to measure pH strip results with the camera with a better accuracy than that reachable by the naked eye. Besides, a successful colour subtraction algorithm was incorporated

enable the measurement of pH vales from coloured foodstuff that generally leads to large inaccuracies where no readout system is used.

In **Chapter 5**, a novel smartphone-based sensor was developed targeting *Mycobacterium bovis*, a microbiological contaminant that can be found in dairy products if these are obtained from infected animals. A set of *M. bovis* surface binders (including antibodies and peptide binders) was tested and, the best performing antibody, successfully bound to the gold nanostars surface following the DTT reduction method. These nanostructures were used in an indirect immunochemical assay, first binding specifically the target bacteria and then using their restored peroxidase-like activity to generate a colourimetric signal inversely proportional to the presence of the bacteria. This sensing approach enabled the detection of *M. bovis* at $7.2 \cdot 10^3$ CFU/ml, selectively binding it in the presence of other (closely related or not) bacteria, such as *M. smegmatis* or *E. coli* K12, respectively. Moreover, the results were measured and analysed with a smartphone, using its camera for the data acquisition and two different applications for the data quantification. Both apps were able to predict the concentration of the bacteria between 10^3 – 10^6 CFU/ml with a relatively good accuracy, although the MAE calculations showed that the commercial app "RGB Color Detector" was more accurate in its predictions than the in-house developed app "QuantColorimetryApp" (MAE of 6.4±1.5 % and 15.4±5.9 %, respectively, as compared to 4.5±2.4 % obtained using the spectrophotometer). Further optimisation of the in-house developed app could lead to a better accuracy in the predictions, while some work directed at automating the assay steps could help develop a truly POC system. To date, no rapid and portable sensor device has been developed to detect *M. bovis*, highlighting the novelty of this approach and the potential it could have for POC diagnostics.

In **Chapter 6**, an extensive SERS characterisation of gold nanostars is shown prior to the application of these findings for the development of two sensing mechanisms to detect Hg^{2+} ions in environmental water samples. It was first found the importance that the nanoparticles stabilising agent has on their capability to act as Raman enhancers. Thus, PEG-coated gold nanostars displayed very good properties for SERS, while OEG or 11-MUA did not. Moreover, the optical properties of gold nanostars also played an important role in enhancing such signal, as a plasmonic frequency closer to that of the incident light led to a larger Raman enhancement. Taking all this into account, an analytical enhancement factor of $2.1 \cdot 10^5$ was achieved using gold nanostars and R6G as model Raman probe. These findings were of paramount importance to choose adequate working conditions to develop successful sensing devices. Additionally, bimetallic Au-Ag nanostructures were synthesised and characterised as Raman enhancers following previous studies indicating the potential that such mixes could have for SERS. Both

BDT and 4-MBA were studied as Au-Ag linkers, leading to the formation of core/shell nanostructures in most cases. However, the addition of BDT concentrations equal or higher than 10 µM to the gold nanostars led to the formation of silver satellites, which curiously led to a much larger Raman enhancement than that observed for gold nanostars on their own or even that of Au-Ag core/shell nanostructures. Specifically, this additional Raman enlargement entailed a Raman intensity one order of magnitude larger than that of gold nanostars alone. This key finding was exploited for developing an ultra-sensitive sensing mechanism detecting Hg^{2+} ions at a concentration of 0.1 ppb.

Overall, this thesis reports some of the latest findings related to the optical and spectroscopic properties of gold nanostars, both through the revision of recently published articles and through new experimental analyses. Several lab-based prototypes of diagnostic devices have been developed along this thesis, which are expected to be of use to those working in the fields of nanotechnology and nanobiosensors. Besides, the publication of a scientific review discussing the latest information of gold nanozymes applied for biosensing [97] and the development of a user-friendly online database collecting the most recent information about sensing assays targeting food contaminants (http://test.foodsmartphone.net/) are anticipated to have relevance among the scientific community and the general public willing to take informed decisions, respectively. However, these pieces of work mostly literature-based have both shown that we are still far from developing diagnostic devices fit for POC use, especially if small concentrations of a certain analyte are to be detected. Excellent sensitivities can be reached using lab-based equipment, like chromatography or cell culture. Even with portable devices, like certain handheld Raman spectrometers. However, the scientific community still struggles to develop non-expensive sensors for *in situ* analyses performed by non-trained personnel and reaching the required sensitivities. Despite appearing like something unattainable, there are already some examples satisfying all these parameters, like pregnancy tests or glucose sensors. This is partly due to the relatively high limits of detection required for these specific applications, set in the millimolar range for the latter. Therefore, the search for novel technologies capable of improving sensitivity limits and the miniaturisation of already existing laboratory equipment remain the principal strategies for extending POC sensing to many different applications still neglected.

List of publications arising from this thesis

Journal Publications

Nelis, J.L.D., Tsagkaris, A.S., Zhao, Y., Lou-Franco, J., Nolan, P., Zhou, H., Cao, C., Rafferty, K., Hajslova, J., Elliott, C.T. and Campbell, K., 2019. The end user sensor tree: An end-user friendly sensor database. *Biosensors and Bioelectronics*, *130*, pp.245-253.

- JLF contributed to the writing, reviewing and editing of the original draft.
- JLF contributed to the investigation in the literature review, preparation of the supplementary tables and in the reviewing and editing of the TEST repository (microbiological contamination section).

Zhao, Y., Choi, S.Y., Lou-Franco, J., Nelis, J.L.D., Zhou, H., Cao, C., Campbell, K., Elliott, C. and Rafferty, K., 2019, October. Smartphone modulated colorimetric reader with color subtraction. In *2019 IEEE SENSORS* (pp. 1-4). IEEE.

- JLF assisted in the sample preparation and data acquisition through the smartphone-based system.
- JLF contributed to the reviewing and editing of the original draft.

Nelis, J.L., Migliorelli, D., Jafari, S., Generelli, S., Lou-Franco, J., Salvador, J.P., Marco, M.P., Cao, C., Elliott, C.T. and Campbell, K., 2020. The benefits of carbon black, gold and magnetic nanomaterials for point-of-harvest electrochemical quantification of domoic acid. *Microchimica Acta*, *187*(3), pp.1-11.

- JLF assisted regarding nanoparticle synthesis and characterization.
- JLF contributed to the reviewing and editing of the original draft.

Lou-Franco, J., Das, B., Elliott, C. and Cao, C., 2021. Gold nanozymes: from concept to biomedical applications. *Nano-Micro Letters*, *13*(1), pp.1-36.

- JLF was the main author writing the original draft.
- JLF was the main author involved in the investigation in the literature review.

Logan, N., Lou-Franco, J., Elliott, C. and Cao, C., 2021. Catalytic gold nanostars for SERS-based detection of mercury ions (Hg^{2+}) with inverse sensitivity. *Environmental Science: Nano*.

- NL & JLF contributed equally to this work
- JLF contributed to writing and reviewing the original draft.
- JLF performed the experimental assays related to the synthesis and functionalisation of gold nanostars and the SERS-related characterisation.

Das, B., Lou-Franco, J., Logan, N., Balasubramanian, P., Kim, M.I. and Cao, C., 2021. Nanozymes in Point-of-Care Diagnosis: An Emerging Futuristic Approach for Biosensing. *Nano-Micro Letters*.

- JLF contributed to the reviewing and editing of the original draft.
- JLF contributed to the investigation in the literature review

Ellis, M.G., Lou-Franco, J., ... and Cao, C., 2021. Directed Assembly of Au Nanostar@Ag Satellite Nanostructures for SERS-based Detection of Mercury Ions. (in preparation)

Lou-Franco, J., …, Elliott, C. and Cao, C., 2021. Retrieving peroxidase-like activity of gold nanostars for the smartphone-based detection of Mycobacterium bovis. (in preparation)

Conferences & Other dissemination activities

J.L.D. Nelis, A.S. Tsagkaris, Y. Zhao, **J. Lou Franco**, P. Nolan, C. Elliott, C. Cao, H.Zhou, J. Hajslova, K. Campbell. ASSET, Belfast, UK 2018: Poster presentation 'Biosensors into the limelight: Towards a user-friendly interface with The Bio End user Sensor Tree'

S. Ying-Choi, N. Logan, **J. Lou-Franco**, E. Jimenez, P. Perez-Jove, C. Cao. ASSET, Belfast, UK 2018: Poster presentation 'Isothermal amplification of nucleic acids for rapid and multiplexed detection of antibiotic-resistance in *Campylobacter jejuni*'

J. Lou-Franco, C. Elliott, C. Cao. World Congress on Biosensors, Miami, USA 2018: Poster presentation 'Tuneable Plasmonic and Catalytic Gold Nanostars for Surface-Enhanced Resonance Raman Scattering (SERRS): Synthesis, Characterization and Optimization'

J.L.D. Nelis, A.S. Tsagkaris, Y. Zhao, **J. Lou Franco**, P. Nolan, C. Elliott, C. Cao,H.Zhou, J. Hajslova, K. Campbell. World Congress on Biosensors, Miami, USA 2018: Poster presentation 'Revealing biosensor capabilities through an open source stakeholder interaction platform equipped with a user friendly decision tree'

J. Lou Franco, J.L.D. Nelis, Y. Zhao. IGFS Newsletter December 2018: Research news article 'IGFS-based FoodSmartphone Early Stage Researchers share their opinions on future technologies for food safety analysis'

J. Lou-Franco, B. Gilbride, Y. Zhao, M. Ellis, J.-Pablo Salvador, M.-Pilar Marco, L. Stewart, C. Elliott, C. Cao. Recent Advances in Food Analysis (RAFA), Prague, Czech Republic 2019: Oral presentation 'Retrieving peroxidase-like activity of ligand-capped gold nanostars for the detection of *Mycobacterium bovis*'

Joost L.D. Nelis, Davide Migliorelli, Safiye Jafari, Silvia Generelli, **Javier Lou-Franco**, J.-Pablo Salvador, M.-Pilar Marco, Cuong Cao, Christopher T. Elliott, Katrina Campbell. Recent Advances in Food Analysis (RAFA), Prague, Czech Republic 2019: Poster presentation 'Carbon black modified screen printed electrodes and magnetic beads for mass production compatible point of site detection of domoic acid in shellfish'

J. Lou-Franco, J.L.D. Nelis, C.T. Elliot. New Food Magazine, December 2020: Magazine Article 'Milk pasteurization: could tuberculosis be slipping into our breakfast bowls?'

References

1. M. Garvey, Food pollution: a comprehensive review of chemical and biological sources of food contamination and impact on human health. Nutrire. **44** (1), 1–13 (2019). https://doi.org/10.1186/s41110-019-0096-3.
2. G. Taylor, M. Millar, 'The Appliance of Science': The Politics of European Food Regulation and Reform. Public Policy Adm. **17** (2), 125–146 (2002). https://doi.org/10.1177/095207670201700208.
3. G.A. Kleter, A. Prandini, L. Filippi, H.J.P. Marvin, Identification of potentially emerging food safety issues by analysis of reports published by the European Community's Rapid Alert System for Food and Feed (RASFF) during a four-year period. Food Chem. Toxicol. **47** (5), 932–950 (2009). https://doi.org/10.1016/j.fct.2007.12.022.
4. WHO, No Title. (2020). https://www.who.int/news-room/fact-sheets/detail/food-safety.
5. F. Fung, H.S. Wang, S. Menon, Food safety in the 21st century. Biomed. J. **41** (2), 88–95 (2018). https://doi.org/10.1016/j.bj.2018.03.003.
6. FERG, WHO Estimates of the Global Burden of Foodborne Diseases, Geneva, 2015.
7. D. Playfair, DAERA, Northern Ireland Agri-Food Sector Key Statistics, Ballymiscow, 2017.
8. L.H. Ledenbach, R.T. Marshall, Compendium of the Microbiological Spoilage of Foods and Beverages. (2009). https://doi.org/10.1007/978-1-4419-0826-1.
9. J. Odumeru, Current Microbial Concerns in the Dairy Industry. FoodSafety Mag. **February** (2002).
10. R.P. Evershed, S. Payne, A.G. Sherratt, M.S. Copley, J. Coolidge, D. Urem-Kotsu, K. Kotsakis, M. Özdoğan, A.E. Özdoğan, O. Nieuwenhuyse, P.M.M.G. Akkermans, D. Bailey, R.R. Andeescu, S. Campbell, S. Farid, I. Hodder, N. Yalman, M. Özbaşaran, E. Biçakci, Y. Garfinkel, T. Levy, M.M. Burton, Earliest date for milk use in the Near East and southeastern Europe linked to cattle herding. Nature. **455** (7212), 528–531 (2008). https://doi.org/10.1038/nature07180.
11. O.E. Craig, J. Chapman, C. Heron, L.H. Willis, L. Bartosiewicz, G. Taylor, A. Whittle, M. Collins, Did the first farmers of central and eastern Europe produce dairy foods? Antiquity. **79** (306), 882–894 (2005). https://doi.org/10.1017/S0003598X00115017.
12. R.P. Evershed, Experimental approaches to the interpretation of absorbed organic residues in archaeological ceramics. World Archaeol. **40** (1), 26–47 (2008). https://doi.org/10.1080/00438240801889373.
13. C. Warinner, J. Hendy, C. Speller, E. Cappellini, R. Fischer, C. Trachsel, J. Arneborg, N. Lynnerup, O.E. Craig, D.M. Swallow, A. Fotakis, R.J. Christensen, J. V. Olsen, A. Liebert, N. Montalva, S. Fiddyment, S. Charlton, M. MacKie, A. Canci, A. Bouwman, F. Rühli, M.T.P. Gilbert, M.J. Collins, Direct evidence of milk consumption from ancient human dental calculus. Sci. Rep. **4** 1–6 (2014). https://doi.org/10.1038/srep07104.
14. P. Gerbault, M. Roffet-Salque, R.P. Evershed, M.G. Thomas, How long have adult humans been consuming milk? IUBMB Life. **65** (12), 983–990 (2013). https://doi.org/10.1002/iub.1227.
15. M. Salque, P.I. Bogucki, J. Pyzel, I. Sobkowiak-Tabaka, R. Grygiel, M. Szmyt, R.P. Evershed, Earliest evidence for cheese making in the sixth millennium BC in northern Europe.

Nature. **493** (7433), 522–525 (2013). https://doi.org/10.1038/nature11698.

16. Center for Food Safety and Applied Nutrition. Grade “A” Pasteurized Milk Ordinance: 2019 Revision, 2019. https://www.fda.gov/media/140394/download.

17. A. Coorevits, V. De Jonghe, J. Vandroemme, R. Reekmans, J. Heyrman, W. Messens, P. De Vos, M. Heyndrickx, Comparative analysis of the diversity of aerobic spore-forming bacteria in raw milk from organic and conventional dairy farms. Syst. Appl. Microbiol. **31** (2), 126–140 (2008). https://doi.org/10.1016/j.syapm.2008.03.002.

18. J.T. LeJeune, P.J. Rajala-Schultz, Unpasteurized Milk: A Continued Public Health Threat. Clin. Infect. Dis. **48** (1), 93–100 (2009). https://doi.org/10.1086/595007.

19. M. Vacheyrou, A.C. Normand, P. Guyot, C. Cassagne, R. Piarroux, Y. Bouton, Cultivable microbial communities in raw cow milk and potential transfers from stables of sixteen French farms. Int. J. Food Microbiol. **146** (3), 253–262 (2011). https://doi.org/10.1016/j.ijfoodmicro.2011.02.033.

20. L. Quigley, O. O’Sullivan, C. Stanton, T.P. Beresford, R.P. Ross, G.F. Fitzgerald, P.D. Cotter, The complex microbiota of raw milk. FEMS Microbiol. Rev. **37** (5), 664–698 (2013). https://doi.org/10.1111/1574-6976.12030.

21. G.B. de Oliveira, L. Favarin, R.H. Luchese, D. McIntosh, Psychrotrophic bacteria in milk: How much do we really know? Brazilian J. Microbiol. **46** (2), 313–321 (2015). https://doi.org/10.1590/S1517-838246220130963.

22. T. Sørhaug, L. Stepaniak, Psychrotrophs and their enzymes in milk and dairy products: Quality aspects. Trends Food Sci. Technol. **8** (2), 35–41 (1997). https://doi.org/10.1016/S0924-2244(97)01006-6.

23. V. De Jonghe, A. Coorevits, K. Van Hoorde, W. Messens, A. Van Landschoot, P. De Vos, M. Heyndrickx, Influence of storage conditions on the growth of pseudomonas species in refrigerated raw milk. Appl. Environ. Microbiol. **77** (2), 460–470 (2011). https://doi.org/10.1128/AEM.00521-10.

24. A. Mallet, M. Guéguen, F. Kauffmann, C. Chesneau, A. Sesboué, N. Desmasures, Quantitative and qualitative microbial analysis of raw milk reveals substantial diversity influenced by herd management practices. Int. Dairy J. **27** (1–2), 13–21 (2012). https://doi.org/10.1016/j.idairyj.2012.07.009.

25. L. Meng, Y. Zhang, H. Liu, S. Zhao, J. Wang, N. Zheng, Characterization of Pseudomonas spp. and associated proteolytic properties in raw milk stored at low temperatures. Front. Microbiol. **8** (NOV), 1–7 (2017). https://doi.org/10.3389/fmicb.2017.02158.

26. F. Postollec, A.G. Mathot, M. Bernard, M.L. Divanac’h, S. Pavan, D. Sohier, Tracking spore-forming bacteria in food: From natural biodiversity to selection by processes. Int. J. Food Microbiol. **158** (1), 1–8 (2012). https://doi.org/10.1016/j.ijfoodmicro.2012.03.004.

27. G. Lücking, M. Stoeckel, Z. Atamer, J. Hinrichs, M. Ehling-Schulz, Characterization of aerobic spore-forming bacteria associated with industrial dairy processing environments and product spoilage. Int. J. Food Microbiol. **166** (2), 270–279 (2013). https://doi.org/10.1016/j.ijfoodmicro.2013.07.004.

28. N.H. Martin, K.J. Boor, M. Wiedmann, Symposium review: Effect of post-pasteurization contamination on fluid milk quality. J. Dairy Sci. **101** (1), 861–870 (2018). https://doi.org/10.3168/jds.2017-13339.

29. S. Marchand, J. De Block, V. De Jonghe, A. Coorevits, M. Heyndrickx, L. Herman, Biofilm Formation in Milk Production and Processing Environments; Influence on Milk Quality

and Safety. Compr. Rev. Food Sci. Food Saf. **11** (2), 133–147 (2012). https://doi.org/10.1111/j.1541-4337.2011.00183.x.

30. V. Velusamy, K. Arshak, O. Korostynska, K. Oliwa, C. Adley, An overview of foodborne pathogen detection : In the perspective of biosensors. Biotechnol. Adv. **28** (2), 232–254 (2010). https://doi.org/10.1016/j.biotechadv.2009.12.004.

31. E.D. van Asselt, H.J. van der Fels-Klerx, H.J.P. Marvin, H. van Bokhorst-van de Veen, M.N. Groot, Overview of Food Safety Hazards in the European Dairy Supply Chain. Compr. Rev. Food Sci. Food Saf. **16** (1), 59–75 (2017). https://doi.org/10.1111/1541-4337.12245.

32. S.G. Lopez-Brea, N. Gómez-Torres, M.Á. Arribas, Spore-forming bacteria in dairy products, in: P. Poltronieri (Ed.), Microbiol. Dairy Process. Challenges Oppor., 2018th ed., John Wiley & Sons Ltd and the Institute of Food Technologists, 2017: pp. 12–36. https://doi.org/10.1002/9781119115007.ch2.

33. N. Balaban, A. Rasooly, Staphylococcal enterotoxins. Int. J. Food Microbiol. **61** (1), 1–10 (2000). https://doi.org/10.1016/S0168-1605(00)00377-9.

34. S.P. Olivier, B.M. Jayarao, R.A. Almeida, Foodborne Pathogens in Milk and the Dairy Farm Environment: Food Safety and Public Health Implications. Foodborne Pathog. Dis. **2** (2), 115–137 (2005).

35. L.E. Macdonald, J. Brett, D. Kelton, S.E. Majowicz, K. Snedeker, J.M. Sargeant, A systematic review and meta-analysis of the effects of pasteurization on milk vitamins, and evidence for raw milk consumption and other health-related outcomes. J. Food Prot. **74** (11), 1814–1832 (2011). https://doi.org/10.4315/0362-028X.JFP-10-269.

36. W.L. Claeys, S. Cardoen, G. Daube, J. De Block, K. Dewettinck, K. Dierick, L. De Zutter, A. Huyghebaert, H. Imberechts, P. Thiange, Y. Vandenplas, L. Herman, Raw or heated cow milk consumption: Review of risks and benefits. Food Control. **31** (1), 251–262 (2013). https://doi.org/10.1016/j.foodcont.2012.09.035.

37. G. Loss, S. Apprich, M. Waser, W. Kneifel, J. Genuneit, G. Büchele, J. Weber, B. Sozanska, H. Danielewicz, E. Horak, R.J. Joost van Neerven, D. Heederik, P.C. Lorenzen, E. von Mutius, C. Braun-Fahrländer, S. Apprich, A. Boznanski, C. Braun-Fahrländer, G. Büchele, W. Cookson, P. Cullinan, H. Danielewicz, A. Debińska, M. Depner, M. Ege, U. Frey, O. Fuchs, J. Genuneit, D. Heederik, E. Horak, A. Hyvärinen, S. Illi, M. Kabesch, K. Kovacs, A. Kosmeda, W. Kneifel, P. Latzin, R. Lauener, G. Loss, S. MacNeill, B. Morass, A.C. Normand, R. Piarroux, H. Rintala, M.K. Rochat, N. Sitaridis, B. Sozanska, D. Strachan, C. Strunz-Lehner, B. Sudre, E. von Mutius, M. Waser, J. Weber, I.M. Wouters, The protective effect of farm milk consumption on childhood asthma and atopy: The GABRIELA study. J. Allergy Clin. Immunol. **128** (4), (2011). https://doi.org/10.1016/j.jaci.2011.07.048.

38. W.L. Claeys, C. Verraes, S. Cardoen, J. De Block, A. Huyghebaert, K. Raes, K. Dewettinck, L. Herman, Consumption of raw or heated milk from different species: An evaluation of the nutritional and potential health benefits. Food Control. **42** 188–201 (2014). https://doi.org/10.1016/j.foodcont.2014.01.045.

39. EFSA, Scientific Opinion on the public health risks related to the consumption of raw drinking milk, 2015. https://doi.org/10.2903/j.efsa.2015.3940.

40. European Commission, Regulation (EC) N° 853/2004 of the European Parlamient and of the Council of 29 April 2004 laying down specific hygiene rules for on the hygiene of foodstuffs. Off. J. Eur. Union. **L 139** (55), (2004).

41. H. Montgomery, S.A. Haughey, C.T. Elliott, Recent food safety and fraud issues within the dairy supply chain (2015–2019). Glob. Food Sec. **26** (October), 100447 (2020).

https://doi.org/10.1016/j.gfs.2020.100447.

42. A. Kowalska, L. Manning, Using the rapid alert system for food and feed: potential benefits and problems on data interpretation. Crit. Rev. Food Sci. Nutr. **61** (6), 906–919 (2021). https://doi.org/10.1080/10408398.2020.1747978.

43. EFSA, Multi-country outbreak of Shiga toxin-producing Escherichia coli infection associated with haemolytic uraemic syndrome, 2016. https://doi.org/10.2903/sp.efsa.2016.en-1017.

44. EFSA, Multi-country outbreak of Salmonella Agona infections linked to infant formula, 2018. https://doi.org/10.2903/sp.efsa.2018.en-1365.

45. EFSA, Multi-country outbreak of Salmonella Poona infections linked to consumption of infant formula, 2019. https://doi.org/10.2903/sp.efsa.2019.en-1594.

46. A.J. Rodriguez-Morales, D.M. Castañeda-Hernández, Bacteria: Mycobacterium bovis. Encycl. Food Saf. **1** 468–475 (2014). https://doi.org/10.1016/B978-0-12-378612-8.00103-7.

47. K.. Addo, K. Owusu-darko, D. Yeboah-manu, P. Caulley, M. Minamikawa, F. Bonsu, C. Leinhardt, P. Akpedonu, D. Ofori-adjei, Mycobacterial species causing pulmonary tuberculosis at the Korle Bu Teaching hospital, Accra, Ghana. Ghana Med. J. **41** (2), 52–57 (2007). https://doi.org/10.4314/gmj.v41i2.55293.

48. A. Kiers, A. Klarenbeek, B. Mendelts, D. Van Soolingen, G. Koëter, Transmission of Mycobacterium pinnipedii to humans in a zoo with marine mammals. Int. J. Tuberc. Lung Dis. **12** (12), 1469–1473 (2008).

49. WHO, Global Tuberculosis Report 2017, 2017. http://www.who.int/tb/publications/global_report/gtbr2017_main_text.pdf?ua=1.

50. C.A.D. Bolaños, C.L. de Paula, S.T. Guerra, M.M.J. Franco, M.G. Ribeiro, Diagnosis of mycobacteria in bovine milk: An overview. Rev. Inst. Med. Trop. Sao Paulo. **59** 1–13 (2017). https://doi.org/10.1590/S1678-9946201759040.

51. WHO, Zoonotic Tuberculosis, 2017. http://www.who.int/tb/areas-of-work/zoonotic-tb/en.

52. R. De La Rua-Domenech, Human Mycobacterium bovis infection in the United Kingdom: Incidence, risks, control measures and review of the zoonotic aspects of bovine tuberculosis. Tuberculosis. **86** (2), 77–109 (2006). https://doi.org/10.1016/j.tube.2005.05.002.

53. A.P. Adams, S.R. Bolin, A.E. Fine, C.A. Bolin, J.B. Kaneene, Comparison of PCR versus culture for detection of Mycobacterium bovis after experimental inoculation of various matrices held under environmental conditions for extended periods. Appl. Environ. Microbiol. **79** (20), 6501–6506 (2013). https://doi.org/10.1128/AEM.02032-13.

54. R. de la Rua-Domenech, A.T. Goodchild, H.M. Vordermeier, R.G. Hewinson, K.H. Christiansen, R.S. Clifton-Hadley, Ante mortem diagnosis of tuberculosis in cattle: A review of the tuberculin tests, γ-interferon assay and other ancillary diagnostic techniques. Res. Vet. Sci. **81** (2), 190–210 (2006). https://doi.org/10.1016/j.rvsc.2005.11.005.

55. I. Schiller, B. Oesch, H.M. Vordermeier, M. V. Palmer, B.N. Harris, K.A. Orloski, B.M. Buddle, T.C. Thacker, K.P. Lyashchenko, W.R. Waters, Bovine tuberculosis: A review of current and emerging diagnostic techniques in view of their relevance for disease control and eradication. Transbound. Emerg. Dis. **57** (4), 205–220 (2010).

https://doi.org/10.1111/j.1865-1682.2010.01148.x.

56. I. Olsen, P. Boysen, S. Kulberg, J.C. Hope, G. Jungersen, A.K. Storset, Bovine NK cells can produce gamma interferon in response to the secreted mycobacterial proteins ESAT-6 and MPP14 but not in response to MPB70. Infect. Immun. **73** (9), 5628–5635 (2005). https://doi.org/10.1128/IAI.73.9.5628-5635.2005.

57. L.D. Stewart, N. Tort, P. Meakin, J.M. Argudo, R. Nzuma, N. Reid, R.J. Delahay, R. Ashford, W.I. Montgomery, I.R. Grant, Development of a novel immunochromatographic lateral flow assay specific for Mycobacterium bovis cells and its application in combination with immunomagnetic separation to test badger faeces. BMC Vet. Res. **13** (1), 1–12 (2017). https://doi.org/10.1186/s12917-017-1048-x.

58. P. Doran, J. Carson, E. Costello, S.J. More, An outbreak of tuberculosis affecting cattle and people on an Irish dairy farm, following the consumption of raw milk. Ir. Vet. J. **62** (6), 390–397 (2009). https://doi.org/10.1186/2046-0481-62-6-390.

59. J.C. Love, L.A. Estroff, J.K. Kriebel, R.G. Nuzzo, G.M. Whitesides, Self-Assembled Monolayers of Thiolates on Metals as a Form of Nanotechnology. Chem. Rev. **105** (4), 1103–1169 (2005).

60. M.C.M. Daniel, D. Astruc, Gold Nanoparticles: Assembly, Supramolecular Chemistry, Quantum-Size Related Properties and Applications toward Biology, Catalysis and Nanotechnology,. Chem. Rev. **104** (1), 293–346 (2004). https://doi.org/10.1021/cr030698+.

61. A.M. Alkilany, C.J. Murphy, Toxicity and cellular uptake of gold nanoparticles: What we have learned so far? J. Nanoparticle Res. **12** (7), 2313–2333 (2010). https://doi.org/10.1007/s11051-010-9911-8.

62. L. Dykman, N. Khlebtsov, Gold nanoparticles in biomedical applications: Recent advances and perspectives. Chem. Soc. Rev. **41** (6), 2256–2282 (2012). https://doi.org/10.1039/c1cs15166e.

63. I. Freestone, N. Meeks, M. Sax, C. Higgit, The Lycurgus Cup - A Roman Nanotechnology. Gold Bull. **40** (4), 270–277 (2007). https://doi.org/10.1007/BF03215599.

64. P. Fermo, G. Padeletti, The use of nano-particles to produce iridescent metallic effects on ancient ceramic objects. J. Nanosci. Nanotechnol. **12** (11), 8764–8769 (2012). https://doi.org/10.1166/jnn.2012.6464.

65. J.A. Chrestien, De la méthode ïatraleptique, ou observations pratiques sur l'efficacité des remèdes administrés par la voie, de l'absorption cutanée dans le traitement de plusieurs maladies internes et externes; et sur un nouveau remède [pour les] maladies vénériennes et, Paris, 1811.

66. M. Faraday, The correspondence of Michael Faraday, The Institution of Engineering and Technology, London, 2008.

67. R. Koch, No Title. Dtsch. Medizinische Wochenschrift. **16** 756–757 (1890).

68. J. Turkevich, P.C. Stevenson, J. Hillier, A study of the nucleation and growth processes in the synthesis of colloidal gold. Discuss. Faraday Soc. **11** 55–75 (1951).

69. R.P. Feynman, There's plenty of room at the bottom. Eng. Sci. **23** (5), 22–36 (1960). http://resolver.caltech.edu/CaltechES:23.5.1960Bottom.

70. M. a Garcia, Surface plasmons in metallic nanoparticles: fundamentals and applications. J. Phys. D. Appl. Phys. **45** (38), 1–20 (2012). https://doi.org/10.1088/0022-3727/45/38/389501.

71. S. Trudel, Unexpected magnetism in gold nanostructures: Making gold even more attractive. Gold Bull. **44** (1), 3–13 (2011). https://doi.org/10.1007/s13404-010-0002-5.

72. Y. Lin, J. Ren, X. Qu, Nano-gold as artificial enzymes: Hidden talents. Adv. Mater. **26** (25), 4200–4217 (2014). https://doi.org/10.1002/adma.201400238.

73. Y. Wang, Y. Xia, Bottom-up and top-down approaches to the synthesis of monodispersed spherical colloids of low melting-point metals. Nano Lett. **4** (10), 2047–2050 (2004). https://doi.org/10.1021/nl048689j.

74. J.F. Liu, L.G. Zhang, N. Gu, J.Y. Ren, Y.P. Wu, Z.H. Lu, P.S. Mao, D.Y. Chen, Fabrication of colloidal gold micro-patterns using photolithographed self-assembled monolayers as templates. Thin Solid Films. **327**–**329** (1–2), 176–179 (1998). https://doi.org/10.1016/S0040-6090(98)00623-3.

75. M.K. Corbierre, J. Beerens, R.B. Lennox, Gold nanoparticles generated by electron beam lithography of gold(I)-thiolate thin films. Chem. Mater. **17** (23), 5774–5779 (2005). https://doi.org/10.1021/cm051085b.

76. D. Qin, Y. Xia, G.M. Whitesides, Soft lithography for micro- and nanoscale patterning. Nat. Protoc. **5** (3), 491–502 (2010). https://doi.org/10.1038/nprot.2009.234.

77. H.W. Li, B.V.O. Muir, G. Fichet, W.T.S. Huck, Nanocontact printing: A route to sub-50-nm-scale chemical and biological patterning. Langmuir. **19** (6), 1963–1965 (2003). https://doi.org/10.1021/la0269098.

78. G. Barbillon, F. Hamouda, S. Held, P. Gogol, B. Bartenlian, Gold nanoparticles by soft UV nanoimprint lithography coupled to a lift-off process for plasmonic sensing of antibodies. Microelectron. Eng. **87** (5–8), 1001–1004 (2010). https://doi.org/10.1016/j.mee.2009.11.114.

79. B.J.Y. Tan, C.H. Sow, T.S. Koh, K.C. Chin, A.T.S. Wee, C.K. Ong, Fabrication of size-tunable gold nanoparticles array with nanosphere lithography, reactive ion etching, and thermal annealing. J. Phys. Chem. B. **109** (22), 11100–11109 (2005). https://doi.org/10.1021/jp045172n.

80. S.M. Yang, S.G. Jang, D.G. Choi, S. Kim, H.K. Yu, Nanomachining by colloidal lithography. Small. **2** (4), 458–475 (2006). https://doi.org/10.1002/smll.200500390.

81. J.C. Garno, Y. Yang, N.A. Amro, S. Cruchon-Dupeyrat, S. Chen, G.Y. Liu, Precise positioning of nanoparticles on surfaces using scanning probe lithography. Nano Lett. **3** (3), 389–395 (2003). https://doi.org/10.1021/nl025934v.

82. S.H. Kim, B.Y.H. Liu, M.R. Zachariah, Synthesis of nanoporous metal oxide particles by a new inorganic matrix spray pyrolysis method. Chem. Mater. **14** (7), 2889–2899 (2002). https://doi.org/10.1021/cm010957g.

83. S. Stopić, B. Friedrich, K. Raić, T. Volkov-Husović, M. Dimitrijević, Characterization of nano-powder morphology obtained by ultrasonic spray pyrolysis. Metalurgija. **14** (1), 41–54 (2008).

84. Jelena-Dokić, R. Rudolf, S. Tomíc, S. Stopić, B. Friedrich, B. Budič, I. Anžel, M. Čolić, Immunomodulatory properties of nanoparticles obtained by ultrasonic spray pirolysis from gold scrap. J. Biomed. Nanotechnol. **8** (3), 528–538 (2012). https://doi.org/10.1166/jbn.2012.1405.

85. V. Pareek, A. Bhargava, R. Gupta, N. Jain, J. Panwar, Synthesis and Applications of Noble Metal Nanoparticles: A Review. Adv. Sci. Eng. Med. **9** (7), 527–544 (2017). https://doi.org/10.1166/asem.2017.2027.

86. Q. Ruan, L. Shao, Y. Shu, J. Wang, H. Wu, Growth of Monodisperse Gold Nanospheres with Diameters from 20 nm to 220 nm and Their Core/Satellite Nanostructures. Adv. Opt. Mater. **2** (1), 65–73 (2014). https://doi.org/10.1002/adom.201300359.

87. B. Nikoobakht, M.A. El-Sayed, Preparation and growth mechanism of gold nanorods (NRs) using seed-mediated growth method. Chem. Mater. **15** (10), 1957–1962 (2003). https://doi.org/10.1021/cm020732l.

88. P.L. Truong, C. Cao, S. Park, M. Kim, S.J. Sim, A new method for non-labeling attomolar detection of diseases based on an individual gold nanorod immunosensor. Lab Chip. **11** (15), 2591–2597 (2011). https://doi.org/10.1039/c1lc20085b.

89. Y. Sun, Y. Xia, Shape-controlled synthesis of gold and silver nanoparticles. Science (80-.). **298** (5601), 2176–2179 (2002). https://doi.org/10.1126/science.1077229.

90. T.H. Ha, H.J. Koo, B.H. Chung, Shape-controlled syntheses of gold nanoprisms and nanorods influenced by specific adsorption of halide ions. J. Phys. Chem. C. **111** (3), 1123–1130 (2007). https://doi.org/10.1021/jp066454l.

91. X. Ma, Y. Cheng, Y. Huang, Y. Tian, S. Wang, Y. Chen, PEGylated gold nanoprisms for photothermal therapy at low laser power density. RSC Adv. **5** (99), 81682–81688 (2015). https://doi.org/10.1039/c5ra17385j.

92. P. Senthil Kumar, I. Pastoriza-Santos, B. Rodríguez-González, F. Javier García De Abajo, L.M. Liz-Marzán, High-yield synthesis and optical response of gold nanostars. Nanotechnology. **19** (1), 1–6 (2008). https://doi.org/10.1088/0957-4484/19/01/015606.

93. E.C. Cho, L. Au, Q. Zhang, Y. Xia, The effects of size, shape, and surface functional group of gold nanostructures on their adsorption and internalization by cells. Small. **6** (4), 517–522 (2010). https://doi.org/10.1002/smll.200901622.

94. F. Kim, S. Connor, H. Song, T. Kuykendall, P. Yang, Platonic Gold Nanocrystals. Angew. Chemie. **116** (28), 3759–3763 (2004). https://doi.org/10.1002/ange.200454216.

95. J. Shen, J. Su, J. Yan, B. Zhao, D. Wang, S. Wang, K. Li, M. Liu, Y. He, S. Mathur, C. Fan, S. Song, Bimetallic nano-mushrooms with DNA-mediated interior nanogaps for high-efficiency SERS signal amplification. Nano Res. **8** (3), 731–742 (2015). https://doi.org/10.1007/s12274-014-0556-2.

96. C. Fang, G. Zhao, Y. Xiao, J. Zhao, Z. Zhang, B. Geng, Facile Growth of High-Yield Gold Nanobipyramids Induced by Chloroplatinic Acid for High Refractive Index Sensing Properties. Sci. Rep. **6** (July), 1–8 (2016). https://doi.org/10.1038/srep36706.

97. J. Lou-Franco, B. Das, C. Elliott, C. Cao, Gold Nanozymes: From Concept to Biomedical Applications, Springer Singapore, 2021. https://doi.org/10.1007/s40820-020-00532-z.

98. S. Link, M.A. El-Sayed, Shape and size dependence of radiative, non-radiative and photothermal properties of gold nanocrystals, 2000. https://doi.org/10.1080/01442350050034180.

99. K.L. Kelly, E. Coronado, L.L. Zhao, G.C. Schatz, The optical properties of metal nanoparticles: The influence of size, shape, and dielectric environment. J. Phys. Chem. B. **107** (3), 668–677 (2003). https://doi.org/10.1021/jp026731y.

100. P.K. Jain, X. Huang, I.H. El-Sayed, M.A. El-Sayed, Noble metals on the nanoscale: Optical and photothermal properties and some applications in imaging, sensing, biology, and medicine. Acc. Chem. Res. **41** (12), 1578–1586 (2008). https://doi.org/10.1021/ar7002804.

101. K. Bolaños, M.J. Kogan, E. Araya, Capping gold nanoparticles with albumin to improve

their biomedical properties. Int. J. Nanomedicine. **14** 6387–6406 (2019). https://doi.org/10.2147/IJN.S210992.

102. I. Alber, W. Sigle, S. Müller, R. Neumann, O. Picht, M. Rauber, P.A. Van Aken, M.E. Toimil-Molares, Visualization of multipolar longitudinal and transversal surface plasmon modes in nanowire dimers. ACS Nano. **5** (12), 9845–9853 (2011). https://doi.org/10.1021/nn2035044.

103. Y. Hong, Y.M. Huh, D.S. Yoon, J. Yang, Nanobiosensors based on localized surface plasmon resonance for biomarker detection. J. Nanomater. **2012** (1), (2012). https://doi.org/10.1155/2012/759830.

104. S. Chen, M. Svedendahl, M. Käll, L. Gunnarsson, A. Dmitriev, Ultrahigh sensitivity made simple: Nanoplasmonic label-free biosensing with an extremely low limit-of-detection for bacterial and cancer diagnostics. Nanotechnology. **20** (43), (2009). https://doi.org/10.1088/0957-4484/20/43/434015.

105. W.S. Hwang, S.J. Sim, A strategy for the ultrasensitive detection of cancer biomarkers based on the LSPR response of a single AuNP. J. Nanosci. Nanotechnol. **11** (7), 5651–5656 (2011). https://doi.org/10.1166/jnn.2011.4346.

106. E. Polo, P. del Pino, B. Pelaz, V. Grazu, J.M. de la Fuente, Plasmonic-driven thermal sensing: ultralow detection of cancer markers. Chem. Commun. (Camb). **49** (35), 3676–8 (2013). https://doi.org/10.1039/c3cc39112d.

107. V.P. Zharov, K.E. Mercer, E.N. Galitovskaya, M.S. Smeltzer, Photothermal nanotherapeutics and nanodiagnostics for selective killing of bacteria targeted with gold nanoparticles. Biophys. J. **90** (2), 619–627 (2006). https://doi.org/10.1529/biophysj.105.061895.

108. X. Huang, I.H. El-Sayed, W. Qian, M.A. El-Sayed, Cancer cell imaging and photothermal therapy in the near-infrared region by using gold nanorods. J. Am. Chem. Soc. **128** (6), 2115–2120 (2006). https://doi.org/10.1021/ja057254a.

109. S. Laing, L.E. Jamieson, K. Faulds, D. Graham, Surface-enhanced Raman spectroscopy for in vivo biosensing. Nat. Rev. Chem. **1** 1–20 (2017). https://doi.org/10.1038/s41570-017-0060.

110. S. Pawar, A. Bhattacharya, A. Nag, Metal-Enhanced Fluorescence Study in Aqueous Medium by Coupling Gold Nanoparticles and Fluorophores Using a Bilayer Vesicle Platform. ACS Omega. **4** (3), 5983–5990 (2019). https://doi.org/10.1021/acsomega.9b00036.

111. B. Della Ventura, M. Gelzo, E. Battista, A. Alabastri, A. Schirato, G. Castaldo, G. Corso, F. Gentile, R. Velotta, Biosensor for Point-of-Care Analysis of Immunoglobulins in Urine by Metal Enhanced Fluorescence from Gold Nanoparticles. ACS Appl. Mater. Interfaces. **11** (4), 3753–3762 (2019). https://doi.org/10.1021/acsami.8b20501.

112. J.R. Lakowicz, C.D. Geddes, I. Gryczynski, J. Malicka, Z. Gryczynski, K. Aslan, J. Lukomska, E. Matveeva, J. Zhang, R. Badugu, J. Huang, Advances in Surface-Enhanced Fluorescence. J. Fluoresc. **14** (4), 425–441 (2004).

113. V. V. Thacker, L.O. Herrmann, D.O. Sigle, T. Zhang, T. Liedl, J.J. Baumberg, U.F. Keyser, DNA origami based assembly of gold nanoparticle dimers for surface-enhanced Raman scattering. Nat. Commun. **5** 1–7 (2014). https://doi.org/10.1038/ncomms4448.

114. R.W. Taylor, R. Esteban, S. Mahajan, J. Aizpurua, J.J. Baumberg, Optimizing SERS from Gold Nanoparticle Clusters: Addressing the Near Field by an Embedded Chain Plasmon Model. J. Phys. Chem. C. **120** (19), 10512–10522 (2016).

https://doi.org/10.1021/acs.jpcc.6b00506.

115. J. Reguera, J. Langer, D. Jiménez De Aberasturi, L.M. Liz-Marzán, Anisotropic metal nanoparticles for surface enhanced Raman scattering. Chem. Soc. Rev. **46** (13), 3866–3885 (2017). https://doi.org/10.1039/c7cs00158d.

116. A.S.D.S. Indrasekara, S. Meyers, S. Shubeita, L.C. Feldman, T. Gustafsson, L. Fabris, Gold nanostar substrates for SERS-based chemical sensing in the femtomolar regime. Nanoscale. **6** 8891–8899 (2014). https://doi.org/10.1039/c4nr02513j.

117. H. Wei, E. Wang, Nanomaterials with enzyme-like characteristics (nanozymes): Next-generation artificial enzymes. Chem. Soc. Rev. **42** (14), 6060–6093 (2013). https://doi.org/10.1039/c3cs35486e.

118. Y. Lin, J. Ren, X. Qu, Nano-Gold as Artificial Enzymes: Hidden Talents. Adv. Mater. **26** 4200–4217 (2014). https://doi.org/10.1002/adma.201400238.

119. D.Y. Cha, G. Parravano, Surface Reactivity of Supported Gold. I. Oxygen Transfer Between Carbon Monoxide and Carbon Dioxide. J. Catal. **18** 200–211 (1970).

120. M. Haruta, T. Kobayashi, H. Sano, N. Yamada, Novel Gold Catalysts for the Oxidation of Carbon Monoxide at a Temperature far Below 0 °C. Chem. Lett. **16** (2), 405–408 (1987). https://doi.org/10.1246/cl.1987.405.

121. D. G. Duff, A. Baiker, Preparation and Structural Properties of Ultrafine Gold Colloids for Oxidation Catalysis. Prep. Catal. VI. 505–512 (1995). https://doi.org/10.1017/CBO9781107415324.004.

122. Y. Tao, E. Ju, J. Ren, X. Qu, Bifunctionalized mesoporous silica-supported gold nanoparticles: Intrinsic oxidase and peroxidase catalytic activities for antibacterial applications. Adv. Mater. **27** (6), 1097–1104 (2015). https://doi.org/10.1002/adma.201405105.

123. M. Comotti, C. Della Pina, R. Matarrese, M. Rossi, The catalytic activity of “naked” gold particles. Angew. Chemie - Int. Ed. **43** (43), 5812–5815 (2004). https://doi.org/10.1002/anie.200460446.

124. W. Luo, C. Zhu, S. Su, D. Li, Y. He, Q. Huang, C. Fan, Self-catalyzed, self-limiting growth of glucose oxidase-mimicking gold nanoparticles. ACS Nano. **4** (12), 7451–7458 (2010). https://doi.org/10.1021/nn102592h.

125. Y. Jv, B. Li, R. Cao, Positively-charged gold nanoparticles as peroxidiase mimic and their application in hydrogen peroxide and glucose detection. Chem. Commun. **46** (42), 8017–8019 (2010). https://doi.org/10.1039/c0cc02698k.

126. W. He, Y.T. Zhou, W.G. Wamer, X. Hu, X. Wu, Z. Zheng, M.D. Boudreau, J.J. Yin, Intrinsic catalytic activity of Au nanoparticles with respect to hydrogen peroxide decomposition and superoxide scavenging. Biomaterials. **34** (3), 765–773 (2013). https://doi.org/10.1016/j.biomaterials.2012.10.010.

127. C.W. Tseng, H.Y. Chang, J.Y. Chang, C.C. Huang, Detection of mercury ions based on mercury-induced switching of enzyme-like activity of platinum/gold nanoparticles. Nanoscale. **4** (21), 6823–6830 (2012). https://doi.org/10.1039/c2nr31716h.

128. N. Pradhan, A. Pal, T. Pal, Catalytic reduction of aromatic nitro compounds by coinage metal nanoparticles. Langmuir. **17** (5), 1800–1802 (2001). https://doi.org/10.1021/la000862d.

129. F. Manea, F.B. Houillon, L. Pasquato, P. Scrimin, Nanozymes: Gold-nanoparticle-based transphosphorylation catalysts. Angew. Chemie - Int. Ed. **43** (45), 6165–6169 (2004).

https://doi.org/10.1002/anie.200460649.

130. I.M. Klotz, G.P. Royer, I.S. Scarpa, Synthetic Derivatives of Polyethyleneimine with Enzyme-Like Catalytic Activity (Synzymes). Proc. Natl. Acad. Sci. **68** (2), 263–264 (1971). https://doi.org/10.1073/pnas.68.2.263.

131. X. Cao, C. Li, Y. Lu, B. Zhang, Y. Wu, Q. Liu, J. Wu, J. Teng, W. Yan, Y. Huang, Catalysis of Au nano-pyramids formed across the surfaces of ordered Au nano-ring arrays. J. Catal. **377** 389–399 (2019). https://doi.org/10.1016/j.jcat.2019.07.038.

132. N. Lopez, T.V.W. Janssens, B.S. Clausen, Y. Xu, M. Mavrikakis, T. Bligaard, J.K. Nørskov, On the origin of the catalytic activity of gold nanoparticles for low-temperature CO oxidation. J. Catal. **223** (1), 232–235 (2004). https://doi.org/10.1016/j.jcat.2004.01.001.

133. M.C. Saint-Lager, I. Laoufi, A. Bailly, O. Robach, S. Garaudée, P. Dolle, Catalytic properties of supported gold nanoparticles: New insights into the size-activity relationship gained from in operando measurements. Faraday Discuss. **152** 253–265 (2011). https://doi.org/10.1039/c1fd00028d.

134. T. Ma, W. Yang, S. Liu, H. Zhang, F. Liang, A Comparison Reduction of 4-Nitrophenol by Gold Nanospheres and Gold Nanostars. Catalysts. **7** (38), 1–10 (2017). https://doi.org/10.3390/catal7020038.

135. C. Zheng, W. Ke, T. Yin, X. An, Intrinsic peroxidase-like activity and the catalytic mechanism of gold @ carbon dots nanocomposites. RSC Adv. **6** 35280–35286 (2016). https://doi.org/10.1039/C6RA01917J.

136. M. Drozd, M. Pietrzak, P. Parzuchowski, M. Mazurkiewicz-Pawlicka, E. Malinowska, Peroxidase-like activity of gold nanoparticles stabilized by hyperbranched polyglycidol derivatives over a wide pH range. Nanotechnology. **26** (49), (2015). https://doi.org/10.1088/0957-4484/26/49/495101.

137. J. Li, W. Liu, X. Wu, X. Gao, Mechanism of pH-switchable peroxidase and catalase-like activities of gold, silver, platinum and palladium. Biomaterials. **48** 37–44 (2015). https://doi.org/10.1016/j.biomaterials.2015.01.012.

138. Y. Lu, Y. Mei, M. Drechsler, M. Ballauff, Thermosensitive core-shell particles as carriers for Ag nanoparticles: Modulating the catalytic activity by a phase transition in networks. Angew. Chemie - Int. Ed. **45** (5), 813–816 (2006). https://doi.org/10.1002/anie.200502731.

139. S. Wang, W. Chen, A. Liu, L. Hong, H. Deng, X. Lin, Comparison of the Peroxidase-Like Activity of Unmodified, Amino-Modified and Citrate-Capped Gold Nnaoparticles. ChemPhysChem. **13** 1199–1204 (2012). https://doi.org/10.1002/cphc.201100906.

140. H.J. Chun, Y.M. Park, Y.D. Han, Y.H. Jang, H.C. Yoon, Paper-based glucose biosensing system utilizing a smartphone as a signal reader. Biochip J. **8** (3), 218–226 (2014). https://doi.org/10.1007/s13206-014-8308-7.

141. T.T. Tsai, C.Y. Huang, C.A. Chen, S.W. Shen, M.C. Wang, C.M. Cheng, C.F. Chen, Diagnosis of Tuberculosis Using Colorimetric Gold Nanoparticles on a Paper-Based Analytical Device. ACS Sensors. **2** (9), 1345–1354 (2017). https://doi.org/10.1021/acssensors.7b00450.

142. L. Zheng, G. Cai, S. Wang, M. Liao, Y. Li, J. Lin, A microfluidic colorimetric biosensor for rapid detection of Escherichia coli O157:H7 using gold nanoparticle aggregation and smart phone imaging. Biosens. Bioelectron. **124–125** (October 2018), 143–149 (2019). https://doi.org/10.1016/j.bios.2018.10.006.

143. H. Zhu, Quantum dot enabled detection of Escherichia coli using acell-phone. Analyst. **137** (11), (2012). https://doi.org/10.1039/c2an35071h.

144. A. Roda, E. Michelini, M. Zangheri, M. Di Fusco, D. Calabria, P. Simoni, Smartphone-based biosensors: A critical review and perspectives. TrAC - Trends Anal. Chem. **79** 317–325 (2016). https://doi.org/10.1016/j.trac.2015.10.019.

145. D. Zhang, Q. Liu, Biosensors and bioelectronics on smartphone for portable biochemical detection. Biosens. Bioelectron. **75** 273–284 (2016). https://doi.org/10.1016/j.bios.2015.08.037.

146. I.E. Tothill, Biosensors for cancer markers diagnosis. Semin. Cell Dev. Biol. **20** (1), 55–62 (2009). https://doi.org/10.1016/j.semcdb.2009.01.015.

147. J. Kim, A.S. Campbell, J. Wang, Wearable non-invasive epidermal glucose sensors: A review. Talanta. **177** (August 2017), 163–170 (2018). https://doi.org/10.1016/j.talanta.2017.08.077.

148. L.C. Brazaca, I. Sampaio, V. Zucolotto, B.C. Janegitz, Applications of biosensors in Alzheimer's disease diagnosis. Talanta. **210** (December 2019), 120644 (2020). https://doi.org/10.1016/j.talanta.2019.120644.

149. Y. Yang, E. Noviana, M.P. Nguyen, B.J. Geiss, D.S. Dandy, C.S. Henry, Paper-Based Microfluidic Devices: Emerging Themes and Applications. Anal. Chem. **89** (1), 71–91 (2017). https://doi.org/10.1021/acs.analchem.6b04581.

150. M. Drozd, M. Pietrzak, P.G. Parzuchowski, E. Malinowska, Pitfalls and capabilities of various hydrogen donors in evaluation of peroxidase-like activity of gold nanoparticles. Anal. Bioanal. Chem. **408** (29), 8505–8513 (2016). https://doi.org/10.1007/s00216-016-9976-z.

151. Y. Liu, D. Ding, Y. Zhen, R. Guo, Amino acid-mediated 'turn-off/turn-on' nanozyme activity of gold nanoclusters for sensitive and selective detection of copper ions and histidine. Biosens. Bioelectron. **92** (January), 140–146 (2017). https://doi.org/10.1016/j.bios.2017.01.036.

152. Y. Wu, Y. Chen, Y. Li, J. Huang, H. Yu, Z. Wang, Accelerating peroxidase-like activity of gold nanozymes using purine derivatives and its application for monitoring of occult blood in urine. Sensors Actuators, B Chem. **270** 443–451 (2018). https://doi.org/10.1016/j.snb.2018.05.057.

153. Y. Sun, J. Wang, W. Li, J. Zhang, Y. Zhang, Y. Fu, DNA-stabilized bimetallic nanozyme and its application on colorimetric assay of biothiols. Biosens. Bioelectron. **74** 1038–1046 (2015). https://doi.org/10.1016/j.bios.2015.08.001.

154. L. Long, J. Liu, K. Lu, T. Zhang, Y. Xie, Y. Ji, X. Wu, Highly sensitive and robust peroxidase-like activity of Au-Pt core/shell nanorod-antigen conjugates for measles virus diagnosis. J. Nanobiotechnology. **16** (1), (2018). https://doi.org/10.1186/s12951-018-0371-0.

155. S. Oh, J. Kim, V.T. Tran, D.K. Lee, S.R. Ahmed, J.C. Hong, J. Lee, E.Y. Park, J. Lee, Magnetic Nanozyme-Linked Immunosorbent Assay for Ultrasensitive Influenza A Virus Detection. ACS Appl. Mater. Interfaces. **10** (15), 12534–12543 (2018). https://doi.org/10.1021/acsami.8b02735.

156. S.R. Ahmed, J. Kim, T. Suzuki, J. Lee, E.Y. Park, Enhanced catalytic activity of gold nanoparticle-carbon nanotube hybrids for influenza virus detection. Biosens. Bioelectron. **85** 503–508 (2016). https://doi.org/10.1016/j.bios.2016.05.050.

157. S. Cho, H.Y. Shin, M. Il Kim, Nanohybrids consisting of magnetic nanoparticles and gold

nanoclusters as effective peroxidase mimics and their application for colorimetric detection of glucose. Biointerphases. **12** (1), 01A401 1-7 (2017). https://doi.org/10.1116/1.4974198.

158. K. Boriachek, M.K. Masud, C. Palma, H.-P. Phan, Y. Yamauchi, M.S.A. Hossain, N.-T. Nguyen, C. Salomon, M.J.A. Shiddiky, Avoiding pre-isolation step in exosome analysis: Direct isolation and sensitive detection of exosomes using gold-loaded nanoporous ferric oxide nanozymes. Anal. Chem. **91** (6), 3827–3834 (2019). https://doi.org/10.1021/acs.analchem.8b03619.

159. M. Liu, H. Zhao, S. Chen, H. Yu, X. Quan, Interface engineering catalytic graphene for smart colorimetric biosensing. ACS Nano. **6** (4), 3142–3151 (2012). https://doi.org/10.1021/nn3010922.

160. Z. Sun, Q. Zhao, G. Zhang, Y. Li, G. Zhang, F. Zhang, X. Fan, Exfoliated MoS2 supported Au-Pd bimetallic nanoparticles with core-shell structures and superior peroxidase-like activities. RSC Adv. **5** (14), 10352–10357 (2015). https://doi.org/10.1039/c4ra13575j.

161. K.N. Han, J.S. Choi, J. Kwon, Gold nanozyme-based paper chip for colorimetric detection of mercury ions. Sci. Rep. **7** (1), (2017). https://doi.org/10.1038/s41598-017-02948-x.

162. S. Laing, A. Hernandez-Santana, J. Sassmannshausen, D.L. Asquith, I.B. McInnes, K. Faulds, D. Graham, Quantitative detection of human tumor necrosis factor α by a resonance raman enzyme-linked immunosorbent assay. Anal. Chem. **83** (1), 297–302 (2011). https://doi.org/10.1021/ac1024039.

163. D. Sun, X. Lin, J. Lu, P. Wei, Z. Luo, X. Lu, Z. Chen, L. Zhang, DNA nanotetrahedron-assisted electrochemical aptasensor for cardiac troponin I detection based on the co-catalysis of hybrid nanozyme, natural enzyme and artificial DNAzyme. Biosens. Bioelectron. **142** (2019). https://doi.org/10.1016/j.bios.2019.111578.

164. P.-C. Kuo, C.-W. Lien, J.-Y. Mao, B. Unnikrishnan, H.-T. Chang, H.-J. Lin, C.-C. Huang, Detection of urinary spermine by using silver-gold/silver chloride nanozymes. Anal. Chim. Acta. **1009** 89–97 (2018). https://doi.org/10.1016/j.aca.2018.01.018.

165. X. Lin, Y. Liu, Z. Tao, J. Gao, J. Deng, J. Yin, S. Wang, Nanozyme-based bio-barcode assay for high sensitive and logic-controlled specific detection of multiple DNAs. Biosens. Bioelectron. **94** 471–477 (2017). https://doi.org/10.1016/j.bios.2017.01.008.

166. Y. Tao, Y. Lin, J. Ren, X. Qu, A dual fluorometric and colorimetric sensor for dopamine based on BSA-stabilized Au nanoclusters. Biosens. Bioelectron. **42** (1), 41–46 (2013). https://doi.org/10.1016/j.bios.2012.10.014.

167. L. Hu, H. Liao, L. Feng, M. Wang, W. Fu, Accelerating the Peroxidase-Like Activity of Gold Nanoclusters at Neutral pH for Colorimetric Detection of Heparin and Heparinase Activity. Anal. Chem. **90** (10), 6247–6252 (2018). https://doi.org/10.1021/acs.analchem.8b00885.

168. R. Das, A. Dhiman, A. Kapil, V. Bansal, T.K. Sharma, Aptamer-mediated colorimetric and electrochemical detection of Pseudomonas aeruginosa utilizing peroxidase-mimic activity of gold NanoZyme. Anal. Bioanal. Chem. **411** (6), 1229–1238 (2019). https://doi.org/10.1007/s00216-018-1555-z.

169. T. Zhang, F. Tian, L. Long, J. Liu, X. Wu, Diagnosis of rubella virus using antigen-conjugated au@pt nanorods as nanozyme probe. Int. J. Nanomedicine. **13** 4795–4805 (2018). https://doi.org/10.2147/IJN.S171429.

170. O. Adegoke, C. McKenzie, N.N. Daeid, Multi-shaped cationic gold nanoparticle-L-cysteine-ZnSeS quantum dots hybrid nanozyme as an intrinsic peroxidase mimic for the

rapid colorimetric detection of cocaine. Sensors Actuators, B Chem. **287** 416–427 (2019). https://doi.org/10.1016/j.snb.2019.02.074.

171. Y. Hu, H. Cheng, X. Zhao, J. Wu, F. Muhammad, S. Lin, J. He, L. Zhou, C. Zhang, Y. Deng, P. Wang, Z. Zhou, S. Nie, H. Wei, Surface-Enhanced Raman Scattering Active Gold Nanoparticles with Enzyme-Mimicking Activities for Measuring Glucose and Lactate in Living Tissues. ACS Nano. **11** (6), 5558–5566 (2017). https://doi.org/10.1021/acsnano.7b00905.

172. P. Weerathunge, R. Ramanathan, V.A. Torok, K. Hodgson, Y. Xu, R. Goodacre, B.K. Behera, V. Bansal, Ultrasensitive Colorimetric Detection of Murine Norovirus Using NanoZyme Aptasensor. Anal. Chem. **91** (5), 3270–3276 (2019). https://doi.org/10.1021/acs.analchem.8b03300.

173. X.X. Wang, Q. Wu, Z. Shan, Q.M. Huang, BSA-stabilized Au clusters as peroxidase mimetics for use in xanthine detection. Biosens. Bioelectron. **26** (8), 3614–3619 (2011). https://doi.org/10.1016/j.bios.2011.02.014.

174. L. Fan, X. Xu, C. Zhu, J. Han, L. Gao, J. Xi, R. Guo, Tumor Catalytic-Photothermal Therapy with Yolk-Shell Gold@Carbon Nanozymes. ACS Appl. Mater. Interfaces. **10** (5), 4502–4511 (2018). https://doi.org/10.1021/acsami.7b17916.

175. D. Zhang, Y.X. Zhao, Y.J. Gao, F.P. Gao, Y.S. Fan, X.J. Li, Z.Y. Duan, H. Wang, Anti-bacterial and in vivo tumor treatment by reactive oxygen species generated by magnetic nanoparticles. J. Mater. Chem. B. **1** (38), 5100–5107 (2013). https://doi.org/10.1039/c3tb20907e.

176. L. Gao, K.M. Giglio, J.L. Nelson, H. Sondermann, A.J. Travis, Ferromagnetic nanoparticles with peroxidase-like activity enhance the cleavage of biological macromolecules for biofilm elimination. Nanoscale. **6** (5), 2588–2593 (2014). https://doi.org/10.1039/c3nr05422e.

177. R.S. Riley, E.S. Day, Gold nanoparticle-mediated photothermal therapy: applications and opportunities for multimodal cancer treatment. Wiley Interdiscip. Rev. Nanomedicine Nanobiotechnology. **9** (4), (2017). https://doi.org/10.1002/wnan.1449.

178. Y. Liu, M. Yuan, L. Qiao, R. Guo, An efficient colorimetric biosensor for glucose based on peroxidase-like protein-Fe3O4 and glucose oxidase nanocomposites. Biosens. Bioelectron. **52** 391–396 (2014). https://doi.org/10.1016/j.bios.2013.09.020.

179. S. Maman, I.P. Witz, A history of exploring cancer in context. Nat. Rev. Cancer. **18** (6), 359–376 (2018). https://doi.org/10.1038/s41568-018-0006-7.

180. J.M. Brown, W.R. Wilson, Exploiting tumour hypoxia in cancer treatment. Nat. Rev. Cancer. **4** (6), 437–447 (2004). https://doi.org/10.1038/nrc1367.

181. Q. Chen, C. Liang, X. Sun, J. Chen, Z. Yang, H. Zhao, L. Feng, Z. Liu, H2O2-responsive liposomal nanoprobe for photoacoustic inflammation imaging and tumor theranostics via in vivo chromogenic assay. Proc. Natl. Acad. Sci. U. S. A. **114** (21), 5343–5348 (2017). https://doi.org/10.1073/pnas.1701976114.

182. M. López-Lázaro, Dual role of hydrogen peroxide in cancer: Possible relevance to cancer chemoprevention and therapy. Cancer Lett. **252** (1), 1–8 (2007). https://doi.org/10.1016/j.canlet.2006.10.029.

183. Y. Zhang, F. Wang, C. Liu, Z. Wang, L. Kang, Y. Huang, K. Dong, J. Ren, X. Qu, Nanozyme Decorated Metal-Organic Frameworks for Enhanced Photodynamic Therapy. ACS Nano. **12** (1), 651–661 (2018). https://doi.org/10.1021/acsnano.7b07746.

184. A. Zhang, S. Pan, Y. Zhang, J. Chang, J. Cheng, Z. Huang, T. Li, C. Zhang, J.M. De La Fuentea, Q. Zhang, D. Cui, Carbon-gold hybrid nanoprobes for real-time imaging, photothermal/photodynamic and nanozyme oxidative therapy. Theranostics. **9** (12), 3443–3458 (2019). https://doi.org/10.7150/thno.33266.

185. Y.-C. Ma, Y.-H. Zhu, X.-F. Tang, L.-F. Hang, W. Jiang, M. Li, M.I. Khan, Y.-Z. You, Y.-C. Wang, Au nanoparticles with enzyme-mimicking activity-ornamented ZIF-8 for highly efficient photodynamic therapy. Biomater. Sci. **7** (7), 2740–2748 (2019). https://doi.org/10.1039/c9bm00333a.

186. L. Li, Z. Yang, W. Fan, L. He, C. Cui, J. Zou, W. Tang, O. Jacobson, Z. Wang, G. Niu, S. Hu, X. Chen, In Situ Polymerized Hollow Mesoporous Organosilica Biocatalysis Nanoreactor for Enhancing ROS-Mediated Anticancer Therapy. Adv. Funct. Mater. **1907716** 1–11 (2019). https://doi.org/10.1002/adfm.201907716.

187. S.K. Maji, S. Yu, K. Chung, M. Sekkarapatti Ramasamy, J.W. Lim, J. Wang, H. Lee, D.H. Kim, Synergistic Nanozymetic Activity of Hybrid Gold Bipyramid-Molybdenum Disulfide Core@Shell Nanostructures for Two-Photon Imaging and Anticancer Therapy. ACS Appl. Mater. Interfaces. **10** (49), 42068–42076 (2018). https://doi.org/10.1021/acsami.8b15443.

188. C. Liu, L. Luo, L. Zeng, J. Xing, Y. Xia, S. Sun, L. Zhang, Z. Yu, J. Yao, Z. Yu, O.U. Akakuru, M. Saeed, A. Wu, Porous Gold Nanoshells on Functional NH2-MOFs: Facile Synthesis and Designable Platforms for Cancer Multiple Therapy. Small. **14** (35), (2018). https://doi.org/10.1002/smll.201801851.

189. S. Gao, H. Lin, H. Zhang, H. Yao, Y. Chen, J. Shi, Nanocatalytic Tumor Therapy by Biomimetic Dual Inorganic Nanozyme-Catalyzed Cascade Reaction. Adv. Sci. **6** (3), (2019). https://doi.org/10.1002/advs.201801733.

190. Z. Wang, K. Dong, Z. Liu, Y. Zhang, Z. Chen, H. Sun, J. Ren, X. Qu, Activation of biologically relevant levels of reactive oxygen species by Au/g-C3N4 hybrid nanozyme for bacteria killing and wound disinfection. Biomaterials. **113** 145–157 (2017). https://doi.org/10.1016/j.biomaterials.2016.10.041.

191. H. Koo, R.N. Allan, R.P. Howlin, P. Stoodley, L. Hall-Stoodley, Targeting microbial biofilms: Current and prospective therapeutic strategies. Nat. Rev. Microbiol. **15** (12), 740–755 (2017). https://doi.org/10.1038/nrmicro.2017.99.

192. Q. Zhang, S. Chen, H. Wang, H. Yu, Exquisite Enzyme-Fenton Biomimetic Catalysts for Hydroxyl Radical Production by Mimicking an Enzyme Cascade. ACS Appl. Mater. Interfaces. **10** (10), 8666–8675 (2018). https://doi.org/10.1021/acsami.7b18690.

193. M. hui Zhang, H. Dong, L. Zhao, D. xi Wang, D. Meng, A review on Fenton process for organic wastewater treatment based on optimization perspective. Sci. Total Environ. **670** 110–121 (2019). https://doi.org/10.1016/j.scitotenv.2019.03.180.

194. S. Kunjiappan, C. Bhattacharjee, R. Chowdhury, In vitro antioxidant and hepatoprotective potential of Azolla microphylla phytochemically synthesized gold nanoparticles on acetaminophen – induced hepatocyte damage in Cyprinus carpio L. Vitr. Cell. Dev. Biol. - Anim. **51** (6), 630–643 (2015). https://doi.org/10.1007/s11626-014-9841-3.

195. F. Wang, E. Ju, Y. Guan, J. Ren, X. Qu, Light-Mediated Reversible Modulation of ROS Level in Living Cells by Using an Activity-Controllable Nanozyme. Small. **13** (25), (2017). https://doi.org/10.1002/smll.201603051.

196. C.-P. Liu, T.-H. Wu, Y.-L. Lin, C.-Y. Liu, S. Wang, S.-Y. Lin, Tailoring Enzyme-Like Activities of Gold Nanoclusters by Polymeric Tertiary Amines for Protecting Neurons Against

Oxidative Stress. Small. **12** (30), 4127–4135 (2016). https://doi.org/10.1002/smll.201503919.

197. F. Dashtestani, H. Ghourchian, A. Najafi, Silver-gold-apoferritin nanozyme for suppressing oxidative stress during cryopreservation. Mater. Sci. Eng. C. **94** 831–840 (2019). https://doi.org/10.1016/j.msec.2018.10.008.

198. J.T. Hancock, R. Desikan, S.J. Neill, Role of reactive oxygen species in cell signalling pathways. Biochem. Soc. Trans. **29** (2), 345–350 (2001). https://doi.org/10.1042/0300-5127:0290345.

199. S. Boukhenouna, M.A. Wilson, K. Bahmed, B. Kosmider, Reactive oxygen species in chronic obstructive pulmonary disease. Oxid. Med. Cell. Longev. **2018** (2018). https://doi.org/10.1155/2018/5730395.

200. D.S. Manickam, A.M. Brynskikh, J.L. Kopanic, P.L. Sorgen, N.L. Klyachko, E. V. Batrakova, T.K. Bronich, A. V. Kabanov, Well-defined cross-linked antioxidant nanozymes for treatment of ischemic brain injury. J. Control. Release. **162** (3), 636–645 (2012). https://doi.org/10.1016/j.jconrel.2012.07.044.

201. M. Valko, D. Leibfritz, J. Moncol, M.T.D. Cronin, M. Mazur, J. Telser, Free radicals and antioxidants in normal physiological functions and human disease. Int. J. Biochem. Cell Biol. **39** (1), 44–84 (2007). https://doi.org/10.1016/j.biocel.2006.07.001.

202. Z. Chen, J.J. Yin, Y.T. Zhou, Y. Zhang, L. Song, M. Song, S. Hu, N. Gu, Dual enzyme-like activities of iron oxide nanoparticles and their implication for diminishing cytotoxicity. ACS Nano. **6** (5), 4001–4012 (2012). https://doi.org/10.1021/nn300291r.

203. X. Wang, Y. Zhang, T. Li, W. Tian, Q. Zhang, Y. Cheng, Generation 9 polyamidoamine dendrimer encapsulated platinum nanoparticle mimics catalase size, shape, and catalytic activity. Langmuir. **29** (17), 5262–5270 (2013). https://doi.org/10.1021/la3046077.

204. J.L.D. Nelis, A.S. Tsagkaris, Y. Zhao, J. Lou-Franco, P. Nolan, H. Zhou, C. Cao, K. Rafferty, J. Hajslova, C.T. Elliott, K. Campbell, The end user sensor tree: An end-user friendly sensor database. Biosens. Bioelectron. **130** (January), 245–253 (2019). https://doi.org/10.1016/j.bios.2019.01.055.

205. J. Hou, M. Vázquez-González, M. Fadeev, X. Liu, R. Lavi, I. Willner, Catalyzed and Electrocatalyzed Oxidation of l -Tyrosine and l -Phenylalanine to Dopachrome by Nanozymes. Nano Lett. **18** (6), 4015–4022 (2018). https://doi.org/10.1021/acs.nanolett.8b01522.

206. M. Diez-Castellnou, F. Mancin, P. Scrimin, Efficient phosphodiester cleaving nanozymes resulting from multivalency and local medium polarity control. J. Am. Chem. Soc. **136** (4), 1158–1161 (2014). https://doi.org/10.1021/ja411969e.

207. Y. Zhou, H. Sun, H. Xu, S. Matysiak, J. Ren, X. Qu, Mesoporous Encapsulated Chiral Nanogold for Use in Enantioselective Reactions. Angew. Chemie - Int. Ed. **57** (51), 16791–16795 (2018). https://doi.org/10.1002/anie.201811118.

208. Y.-W. Wang, Q. Liu, L. Wang, S. Tang, H.-H. Yang, H. Song, A colorimetric mercury(II) assay based on the Hg(II)-stimulated peroxidase mimicking activity of a nanocomposite prepared from graphitic carbon nitride and gold nanoparticles. Microchim. Acta. **186** (1), (2019). https://doi.org/10.1007/s00604-018-3137-3.

209. S. Zhang, H. Li, Z. Wang, J. Liu, H. Zhang, B. Wang, Z. Yang, A strongly coupled Au/Fe3O4/GO hybrid material with enhanced nanozyme activity for highly sensitive colorimetric detection, and rapid and efficient removal of Hg2+ in aqueous solutions. Nanoscale. **7** (18), 8495–8502 (2015). https://doi.org/10.1039/c5nr00527b.

210. C.-F. Peng, Y.-Y. Zhang, L.-Y. Wang, Z.-Y. Jin, G. Shao, Colorimetric assay for the simultaneous detection of Hg2+ and Ag+ based on inhibiting the peroxidase-like activity of core-shell Au@Pt nanoparticles. Anal. Methods. **9** (30), 4363–4370 (2017). https://doi.org/10.1039/c7ay01317e.

211. C.-L. Hsu, C.-W. Lien, S.G. Harroun, R. Ravindranath, H.-T. Chang, J.-Y. Mao, C.-C. Huang, Metal-deposited bismuth oxyiodide nanonetworks with tunable enzyme-like activity: Sensing of mercury and lead ions. Mater. Chem. Front. **1** (5), 893–899 (2017). https://doi.org/10.1039/c6qm00149a.

212. Y.J. Long, Y.F. Li, Y. Liu, J.J. Zheng, J. Tang, C.Z. Huang, Visual observation of the mercury-stimulated peroxidase mimetic activity of gold nanoparticles. Chem. Commun. **47** (43), 11939–11941 (2011). https://doi.org/10.1039/c1cc14294a.

213. C. Cao, J. Zhang, S. Li, Q. Xiong, Intelligent and ultrasensitive analysis of mercury trace contaminants via plasmonic metamaterial-based surface-enhanced raman spectroscopy. Small. **10** (16), 3252–3256 (2014). https://doi.org/10.1002/smll.201400165.

214. L. Zhang, Y. Yuan, X. Wen, Y. Li, C. Cao, Q. Xiong, A coordination and ligand replacement based three-input colorimetric logic gate sensing platform for melamine, mercury ions, and cysteine. RSC Adv. **5** (73), 59106–59113 (2015). https://doi.org/10.1039/c5ra09570k.

215. N. Logan, C. McVey, C. Elliott, C. Cao, Amalgamated gold-nanoalloys with enhanced catalytic activity for the detection of mercury ions (Hg2+) in seawater samples. Nano Res. **13** (4), 989–998 (2020). https://doi.org/10.1007/s12274-020-2731-y.

216. S. Biswas, P. Tripathi, N. Kumar, S. Nara, Gold nanorods as peroxidase mimetics and its application for colorimetric biosensing of malathion. Sensors Actuators, B Chem. **231** 584–592 (2016). https://doi.org/10.1016/j.snb.2016.03.066.

217. P. Weerathunge, R. Ramanathan, R. Shukla, T.K. Sharma, V. Bansal, Aptamer-controlled reversible inhibition of gold nanozyme activity for pesticide sensing. Anal. Chem. **86** (24), 11937–11941 (2014). https://doi.org/10.1021/ac5028726.

218. S. Singh, P. Tripathi, N. Kumar, S. Nara, Colorimetric sensing of malathion using palladium-gold bimetallic nanozyme. Biosens. Bioelectron. **92** (November 2016), 280–286 (2017). https://doi.org/10.1016/j.bios.2016.11.011.

219. C. McVey, N. Logan, N.T.K. Thanh, C. Elliott, C. Cao, Unusual switchable peroxidase-mimicking nanozyme for the determination of proteolytic biomarker. Nano Res. **12** (3), 509–516 (2019). https://doi.org/10.1007/s12274-018-2241-3.

220. C. McVey, F. Huang, C. Elliott, C. Cao, Endonuclease controlled aggregation of gold nanoparticles for the ultrasensitive detection of pathogenic bacterial DNA. Biosens. Bioelectron. **92** (October), 502–508 (2017). https://doi.org/10.1016/j.bios.2016.10.072.

221. C. Cao, L.C. Gontard, L.L. Thuy Tram, A. Wolff, D.D. Bang, Dual enlargement of gold nanoparticles: From mechanism to scanometric detection of pathogenic bacteria. Small. **7** (12), 1701–1708 (2011). https://doi.org/10.1002/smll.201100294.

222. Z. Zhang, L.M. Bragg, M.R. Servos, J. Liu, Gold nanoparticles as dehydrogenase mimicking nanozymes for estradiol degradation. Chinese Chem. Lett. **30** (9), 1655–1658 (2019). https://doi.org/10.1016/j.cclet.2019.05.062.

223. Y. Liu, Y.Y. Zhang, Q.W. Kou, D.D. Wang, D.L. Han, Z.Y. Lu, Y. Chen, L. Chen, Y.X. Wang, Y.J. Zhang, J.H. Yang, S. Xing, Fe3O4/Au binary nanocrystals: Facile synthesis with diverse structure evolution and highly efficient catalytic reduction with cyclability characteristics in 4-nitrophenol. Powder Technol. **338** 26–35 (2018).

https://doi.org/10.1016/j.powtec.2018.06.037.

224. B.H. Robinson, E-waste: An assessment of global production and environmental impacts. Sci. Total Environ. **408** (2), 183–191 (2009). https://doi.org/10.1016/j.scitotenv.2009.09.044.

225. G. Zhao, Y. Xu, G. Han, B. Ling, Biotransfer of persistent organic pollutants from a large site in China used for the disassembly of electronic and electrical waste. Environ. Geochem. Health. **28** (4), 341–351 (2006). https://doi.org/10.1007/s10653-005-9003-3.

226. H.-H. Deng, B.-Y. Luo, S.-B. He, R.-T. Chen, Z. Lin, H.-P. Peng, X.-H. Xia, W. Chen, Redox recycling-triggered peroxidase-like activity enhancement of bare gold nanoparticles for ultrasensitive colorimetric detection of rare-earth Ce 3+ Ion. Anal. Chem. **91** (6), 4039–4046 (2019). https://doi.org/10.1021/acs.analchem.8b05552.

227. Y. Liu, Y. Xiang, D. Ding, R. Guo, Structural effects of amphiphilic protein/gold nanoparticle hybrid based nanozyme on peroxidase-like activity and silver-mediated inhibition. RSC Adv. **6** (113), 112435–112444 (2016). https://doi.org/10.1039/C6RA23773H.

228. Z. Wu, X. Yuan, H. Zhong, H. Wang, G. Zeng, X. Chen, H. Wang, L. Zhang, J. Shao, Enhanced adsorptive removal of p-nitrophenol from water by aluminum metal-organic framework/reduced graphene oxide composite. Sci. Rep. **6** (May), 1–13 (2016). https://doi.org/10.1038/srep25638.

229. X. Kong, H. Zhu, C. Le Chen, G. Huang, Q. Chen, Insights into the reduction of 4-nitrophenol to 4-aminophenol on catalysts. Chem. Phys. Lett. **684** 148–152 (2017). https://doi.org/10.1016/j.cplett.2017.06.049.

230. R.N. Tanna, G.R. Tetreault, C.J. Bennett, B.M. Smith, L.M. Bragg, K.D. Oakes, M.E. Mcmaster, M.R. Servos, Occurrence and degree of intersex (testis-ova) in darters (Etheostoma SPP.) across an urban gradient in the Grand River, Ontario, Canada. Environ. Toxicol. Chem. **32** (9), 1981–1991 (2013). https://doi.org/10.1002/etc.2262.

231. M. Giulivo, M. Lopez de Alda, E. Capri, D. Barceló, Human exposure to endocrine disrupting compounds: Their role in reproductive systems, metabolic syndrome and breast cancer. A review. Environ. Res. **151** 251–264 (2016). https://doi.org/10.1016/j.envres.2016.07.011.

232. World Health Organization. (2020). https://www.who.int/news-room/fact-sheets/detail/food-safety.

233. T. Jiang, Y. Song, T. Wei, H. Li, D. Du, M.J. Zhu, Y. Lin, Sensitive detection of Escherichia coli O157:H7 using Pt-Au bimetal nanoparticles with peroxidase-like amplification. Biosens. Bioelectron. **77** 687–694 (2016). https://doi.org/10.1016/j.bios.2015.10.017.

234. T. Kumar Sharma, R. Ramanathan, P. Weerathunge, M. Mohammadtaheri, H. Kumar Daima, R. Shukla, V. Bansal, Aptamer-mediated “turn-off/turn-on” nanozyme activity of gold nanoparticles for kanamycin detection. Chem. Commun. **50** (100), 15856–15859 (2014). https://doi.org/10.1039/c4cc07275h.

235. C. Wang, C. Liu, J. Luo, Y. Tian, N. Zhou, Direct electrochemical detection of kanamycin based on peroxidase-like activity of gold nanoparticles. Anal. Chim. Acta. **936** 75–82 (2016). https://doi.org/10.1016/j.aca.2016.07.013.

236. X. Pei, A. Tandon, A. Alldrick, L. Giorgi, W. Huang, R. Yang, The China melamine milk scandal and its implications for food safety regulation. Food Policy. **36** (3), 412–420 (2011). https://doi.org/10.1016/j.foodpol.2011.03.008.

237. H. Xin, R. Stone, Tainted milk scandal: Chinese probe unmasks high-tech adulteration with melamine. Science (80-.). **322** (5906), 1310–1311 (2008). https://doi.org/10.1126/science.322.5906.1310.

238. C. Xiu, K.K. Klein, Melamine in milk products in China: Examining the factors that led to deliberate use of the contaminant. Food Policy. **35** (5), 463–470 (2010). https://doi.org/10.1016/j.foodpol.2010.05.001.

239. H.H. Deng, G.W. Li, L. Hong, A.L. Liu, W. Chen, X.H. Lin, X.H. Xia, Colorimetric sensor based on dual-functional gold nanoparticles: Analyte-recognition and peroxidase-like activity. Food Chem. **147** 257–261 (2014). https://doi.org/10.1016/j.foodchem.2013.09.151.

240. J. Li, G. Zhang, L. Wang, A. Shen, J. Hu, Simultaneous enzymatic and SERS properties of bifunctional chitosan-modified popcorn-like Au-Ag nanoparticles for high sensitive detection of melamine in milk powder. Talanta. **140** 204–211 (2015). https://doi.org/10.1016/j.talanta.2015.03.050.

241. N.R. Jana, T. Pal, Anisotropic metal nanoparticles for use as surface-enhanced Raman substrates. Adv. Mater. **19** (13), 1761–1765 (2007). https://doi.org/10.1002/adma.200601749.

242. E. Nalbant Esenturk, A.R. Hight Walker, Surface-enhanced Raman scattering spectroscopy via gold nanostars. J. Raman Spectrosc. **40** (1), 86–91 (2009). https://doi.org/10.1002/jrs.2084.

243. M. Varvara, G. Bozzo, G. Celano, C. Disanto, C.N. Pagliarone, G.V. Celano, The use of ascorbic acid as a food additive: Technical-legal issues. Ital. J. Food Saf. **5** (1), 7–10 (2016). https://doi.org/10.4081/ijfs.2016.4313.

244. S. Xu, X. Dong, S. Chen, Y. Zhao, G. Shan, Y. Sun, Y. Chen, Y. Liu, The preparation of high-index facet Au/Cu NRs and their application for colorimetric determination ascorbic acid. Sensors Actuators, B Chem. **281** 375–382 (2019). https://doi.org/10.1016/j.snb.2018.10.114.

245. L. Cao, P. Wang, L. Chen, Y. Wu, J. Di, A photoelectrochemical glucose sensor based on gold nanoparticles as a mimic enzyme of glucose oxidase. RSC Adv. **9** (27), 15307–15313 (2019). https://doi.org/10.1039/c9ra02088h.

246. G. Darabdhara, J. Bordoloi, P. Manna, M.R. Das, Biocompatible bimetallic Au-Ni doped graphitic carbon nitride sheets: A novel peroxidase-mimicking artificial enzyme for rapid and highly sensitive colorimetric detection of glucose. Sensors Actuators, B Chem. **285** (January), 277–290 (2019). https://doi.org/10.1016/j.snb.2019.01.048.

247. L. Liu, J. Du, W.-E. Liu, Y. Guo, G. Wu, W. Qi, X. Lu, Enhanced His@AuNCs oxidase-like activity by reduced graphene oxide and its application for colorimetric and electrochemical detection of nitrite. Anal. Bioanal. Chem. (2019). https://doi.org/10.1007/s00216-019-01655-y.

248. X. Zhu, X. Mao, Z. Wang, C. Feng, G. Chen, G. Li, Fabrication of nanozyme@DNA hydrogel and its application in biomedical analysis. Nano Res. **10** (3), 959–970 (2017). https://doi.org/10.1007/s12274-016-1354-9.

249. G.H. Jin, E. Ko, M.K. Kim, V.-K. Tran, S.E. Son, Y. Geng, W. Hur, G.H. Seong, Graphene oxide-gold nanozyme for highly sensitive electrochemical detection of hydrogen peroxide. Sensors Actuators, B Chem. **274** 201–209 (2018). https://doi.org/10.1016/j.snb.2018.07.160.

250. E.B. Bahadir, M.K. Sezgintürk, Applications of commercial biosensors in clinical, food, environmental, and biothreat/biowarfare analyses. Anal. Biochem. **478** 107–120 (2015).

https://doi.org/10.1016/j.ab.2015.03.011.

251. S.J. Oh, B.H. Park, G. Choi, J.H. Seo, J.H. Jung, J.S. Choi, D.H. Kim, T.S. Seo, Fully automated and colorimetric foodborne pathogen detection on an integrated centrifugal microfluidic device. Lab Chip. **16** (10), 1917–1926 (2016). https://doi.org/10.1039/c6lc00326e.

252. X. Liu, Y. Guan, S. Cheng, Y. Huang, Q. Yan, J. Zhang, G. Huang, J. Zheng, T. Liu, Development of a highly sensitive lateral immunochromatographic assay for rapid detection of Vibrio parahaemolyticus. J. Microbiol. Methods. **131** 78–84 (2016). https://doi.org/10.1016/j.mimet.2016.10.007.

253. E. Morales-Narváez, T. Naghdi, E. Zor, A. Merkoçi, Photoluminescent Lateral-Flow Immunoassay Revealed by Graphene Oxide: Highly Sensitive Paper-Based Pathogen Detection. Anal. Chem. **87** (16), 8573–8577 (2015). https://doi.org/10.1021/acs.analchem.5b02383.

254. J. Bhardwaj, S. Devarakonda, S. Kumar, J. Jang, Development of a paper-based electrochemical immunosensor using an antibody-single walled carbon nanotubes bio-conjugate modified electrode for label-free detection of foodborne pathogens. Sensors Actuators, B Chem. **253** 115–123 (2017). https://doi.org/10.1016/j.snb.2017.06.108.

255. K. Yamada, C.T. Kim, J.H. Kim, J.H. Chung, H.G. Lee, S. Jun, Single walled carbon nanotube-based junction biosensor for detection of Escherichia coli. PLoS One. **9** (9), (2014). https://doi.org/10.1371/journal.pone.0105767.

256. C. Schrader, A. Schielke, L. Ellerbroek, R. Johne, PCR inhibitors - occurrence, properties and removal. J. Appl. Microbiol. **113** (5), 1014–1026 (2012). https://doi.org/10.1111/j.1365-2672.2012.05384.x.

257. H.-B. Liu, Y.-X. Zang, X.-J. Du, P. Li, S. Wang, Development of an isothermal amplification-based assay for the rapid visual detection of Salmonella bacteria. J. Dairy Sci. **100** (9), 7016–7025 (2017). https://doi.org/10.3168/jds.2017-12566.

258. T.-H. Kim, J. Park, C.-J. Kim, Y.-K. Cho, Fully integrated lab-on-a-disc for nucleic acid analysis of food-borne pathogens. Anal. Chem. **86** (8), 3841–3848 (2014). https://doi.org/10.1021/ac403971h.

259. S. Santiago-Felipe, L.A. Tortajada-Genaro, S. Morais, R. Puchades, Á. Maquieira, One-pot isothermal DNA amplification - Hybridisation and detection by a disc-based method. Sensors Actuators, B Chem. **204** 273–281 (2014). https://doi.org/10.1016/j.snb.2014.07.073.

260. A. Kordas, G. Papadakis, D. Milioni, J. Champ, S. Descroix, E. Gizeli, Rapid Salmonella detection using an acoustic wave device combined with the RCA isothermal DNA amplification method. Sens. Bio-Sensing Res. **11** 121–127 (2016). https://doi.org/10.1016/j.sbsr.2016.10.010.

261. Y. Sun, T.L. Quyen, T.Q. Hung, W.H. Chin, A. Wolff, D.D. Bang, A lab-on-a-chip system with integrated sample preparation and loop-mediated isothermal amplification for rapid and quantitative detection of Salmonella spp. in food samples. Lab Chip. **15** (8), 1898–1904 (2015). https://doi.org/10.1039/c4lc01459f.

262. W.M. El-Sharoud, M.S. Darwish, C.A. Batt, A real-time PCR-based microfluidics platform for the detection of Cronobacter sakazakii in reconstituted milks. Int. Dairy J. **33** (1), 67–74 (2013). https://doi.org/10.1016/j.idairyj.2013.06.010.

263. Q. Yang, K.J. Domesle, F. Wang, B. Ge, Rapid detection of Salmonella in food and feed by coupling loop-mediated isothermal amplification with bioluminescent assay in real-time. BMC Microbiol. **16** (1), (2016). https://doi.org/10.1186/s12866-016-0730-7.

264. X.-J. Du, T.-J. Zhou, P. Li, S. Wang, A rapid Salmonella detection method involving thermophilic helicase-dependent amplification and a lateral flow assay. Mol. Cell. Probes. **34** 37–44 (2017). https://doi.org/10.1016/j.mcp.2017.05.004.

265. J. Fei, W. Dou, G. Zhao, A sandwich electrochemical immunoassay for Salmonella pullorum and Salmonella gallinarum based on a AuNPs/SiO<inf>2</inf>/Fe<inf>3</inf>O<inf>4</inf> adsorbing antibody and 4 channel screen printed carbon electrode electrodeposited gold nanoparticles. RSC Adv. **5** (91), 74548–74556 (2015). https://doi.org/10.1039/c5ra12491c.

266. M.H. Abdalhai, A.M. Fernandes, X. Xia, A. Musa, J. Ji, X. Sun, Electrochemical Genosensor to Detect Pathogenic Bacteria (Escherichia coli O157:H7) As Applied in Real Food Samples (Fresh Beef) to Improve Food Safety and Quality Control. J. Agric. Food Chem. **63** (20), 5017–5025 (2015). https://doi.org/10.1021/acs.jafc.5b00675.

267. M. Barreiros dos Santos, J.P. Agusil, B. Prieto-Simón, C. Sporer, V. Teixeira, J. Samitier, Highly sensitive detection of pathogen Escherichia coli O157: H7 by electrochemical impedance spectroscopy. Biosens. Bioelectron. **45** (1), 174–180 (2013). https://doi.org/10.1016/j.bios.2013.01.009.

268. C.K. Joung, H.N. Kim, M.C. Lim, T.J. Jeon, H.Y. Kim, Y.R. Kim, A nanoporous membrane-based impedimetric immunosensor for label-free detection of pathogenic bacteria in whole milk. Biosens. Bioelectron. **44** (1), 210–215 (2013). https://doi.org/10.1016/j.bios.2013.01.024.

269. Q. Chen, J. Lin, C. Gan, Y. Wang, D. Wang, Y. Xiong, W. Lai, Y. Li, M. Wang, A sensitive impedance biosensor based on immunomagnetic separation and urease catalysis for rapid detection of Listeria monocytogenes using an immobilization-free interdigitated array microelectrode. Biosens. Bioelectron. **74** 504–511 (2015). https://doi.org/10.1016/j.bios.2015.06.007.

270. E. Primiceri, M.S. Chiriacò, F. De Feo, E. Santovito, V. Fusco, G. Maruccio, A multipurpose biochip for food pathogen detection. Anal. Methods. **8** (15), 3055–3060 (2016). https://doi.org/10.1039/c5ay03295d.

271. F. Tian, J. Lyu, J. Shi, F. Tan, M. Yang, A polymeric microfluidic device integrated with nanoporous alumina membranes for simultaneous detection of multiple foodborne pathogens. Sensors Actuators, B Chem. **225** 312–318 (2016). https://doi.org/10.1016/j.snb.2015.11.059.

272. T. Wen, R. Wang, A. Sotero, Y. Li, A portable impedance immunosensing system for rapid detection of Salmonella Typhimurium. Sensors (Switzerland). **17** (9), (2017). https://doi.org/10.3390/s17091973.

273. X. Liu, M. Marrakchi, D. Xu, H. Dong, S. Andreescu, Biosensors based on modularly designed synthetic peptides for recognition, detection and live/dead differentiation of pathogenic bacteria. Biosens. Bioelectron. **80** 9–16 (2016). https://doi.org/10.1016/j.bios.2016.01.041.

274. P.B. Lillehoj, C.W. Kaplan, J. He, W. Shi, C.-M. Ho, Rapid, Electrical Impedance Detection of Bacterial Pathogens Using Immobilized Antimicrobial Peptides. J. Lab. Autom. **19** (1), 42–49 (2014). https://doi.org/10.1177/2211068213495207.

275. Q. Chen, D. Wang, G. Cai, Y. Xiong, Y. Li, M. Wang, H. Huo, J. Lin, Fast and sensitive detection of foodborne pathogen using electrochemical impedance analysis, urease catalysis and microfluidics. Biosens. Bioelectron. **86** 770–776 (2016). https://doi.org/10.1016/j.bios.2016.07.071.

276. M. Xu, R. Wang, Y. Li, Rapid detection of Escherichia coli O157:H7 and Salmonella Typhimurium in foods using an electrochemical immunosensor based on screen-printed interdigitated microelectrode and immunomagnetic separation. Talanta. **148** 200–208 (2016). https://doi.org/10.1016/j.talanta.2015.10.082.

277. V.C. Ozalp, G. Bayramoglu, Z. Erdem, M.Y. Arica, Pathogen detection in complex samples by quartz crystal microbalance sensor coupled to aptamer functionalized core-shell type magnetic separation. Anal. Chim. Acta. **853** (1), 533–540 (2015). https://doi.org/10.1016/j.aca.2014.10.010.

278. H. Sharma, R. Mutharasan, Rapid and sensitive immunodetection of Listeria monocytogenes in milk using a novel piezoelectric cantilever sensor. Biosens. Bioelectron. **45** (1), 158–162 (2013). https://doi.org/10.1016/j.bios.2013.01.068.

279. H. Sharma, R. Mutharasan, Hly A gene-based sensitive detection of listeria monocytogenes using a novel cantilever Sensor. Anal. Chem. **85** (6), 3222–3228 (2013). https://doi.org/10.1021/ac303561c.

280. L. Esfandiari, S. Wang, S. Wang, A. Banda, M. Lorenzini, G. Kocharyan, H.G. Monbouquette, J.J. Schmidt, PCR-independent detection of bacterial species-specific 16S rRNA at 10 fM by a pore-blockage sensor. Biosensors. **6** (3), (2016). https://doi.org/10.3390/bios6030037.

281. N.A. Masdor, Z. Altintas, I.E. Tothill, Sensitive detection of Campylobacter jejuni using nanoparticles enhanced QCM sensor. Biosens. Bioelectron. **78** 328–336 (2016). https://doi.org/10.1016/j.bios.2015.11.033.

282. C. Xue, C. Yang, T. Xu, J. Zhan, X. Li, A wireless bio-sensing microfluidic chip based on resonating "μ-divers." Lab Chip. **15** (10), 2318–2326 (2015). https://doi.org/10.1039/c5lc00361j.

283. C.M. Duarte, A.C. Fernandes, F.A. Cardoso, R. Bexiga, S.F. Cardoso, P.J.P. Freitas, Magnetic counter for Group B Streptococci detection in milk. IEEE Trans. Magn. **51** (1), (2015). https://doi.org/10.1109/TMAG.2014.2359574.

284. S. Wang, Y. Zhang, W. An, Y. Wei, N. Liu, Y. Chen, S. Shuang, Magnetic relaxation switch immunosensor for the rapid detection of the foodborne pathogen Salmonella enterica in milk samples. Food Control. **55** 43–48 (2015). https://doi.org/10.1016/j.foodcont.2015.02.031.

285. T. Banerjee, S. Sulthana, T. Shelby, B. Heckert, J. Jewell, K. Woody, V. Karimnia, J. McAfee, S. Santra, Multiparametric Magneto-fluorescent Nanosensors for the Ultrasensitive Detection of Escherichia coli O157:H7. ACS Infect. Dis. **2** (10), 667–673 (2016). https://doi.org/10.1021/acsinfecdis.6b00108.

286. H. Vaisocherová-Lísalová, I. Víšová, M.L. Ermini, T. Špringer, X.C. Song, J. Mrázek, J. Lamačová, N. Scott Lynn, P. Šedivák, J. Homola, Low-fouling surface plasmon resonance biosensor for multi-step detection of foodborne bacterial pathogens in complex food samples. Biosens. Bioelectron. **80** 84–90 (2016). https://doi.org/10.1016/j.bios.2016.01.040.

287. X. Zhang, S. Tsuji, H. Kitaoka, H. Kobayashi, M. Tamai, K.-I. Honjoh, T. Miyamoto, Simultaneous Detection of Escherichia coli O157:H7, Salmonella enteritidis, and Listeria monocytogenes at a Very Low Level Using Simultaneous Enrichment Broth and Multichannel SPR Biosensor. J. Food Sci. **82** (10), 2357–2363 (2017). https://doi.org/10.1111/1750-3841.13843.

288. X. Liu, Y. Hu, S. Zheng, Y. Liu, Z. He, F. Luo, Surface plasmon resonance immunosensor for

fast, highly sensitive, and in situ detection of the magnetic nanoparticles-enriched Salmonella enteritidis. Sensors Actuators, B Chem. **230** 191–198 (2016). https://doi.org/10.1016/j.snb.2016.02.043.

289. I.-H. Cho, P. Bhandari, P. Patel, J. Irudayaraj, Membrane filter-assisted surface enhanced Raman spectroscopy for the rapid detection of E. coli O157: H7 in ground beef. Biosens. Bioelectron. **64** 171–176 (2014). https://doi.org/10.1016/j.bios.2014.08.063.

290. H.-B. Liu, X.-J. Du, Y.-X. Zang, P. Li, S. Wang, SERS-Based Lateral Flow Strip Biosensor for Simultaneous Detection of Listeria monocytogenes and Salmonella enterica Serotype Enteritidis. J. Agric. Food Chem. **65** (47), 10290–10299 (2017). https://doi.org/10.1021/acs.jafc.7b03957.

291. Q. Guo, J.-J. Han, S. Shan, D.-F. Liu, S.-S. Wu, Y.-H. Xiong, W.-H. Lai, DNA-based hybridization chain reaction and biotin–streptavidin signal amplification for sensitive detection of Escherichia coli O157:H7 through ELISA. Biosens. Bioelectron. **86** 990–995 (2016). https://doi.org/10.1016/j.bios.2016.07.049.

292. I.-H. Cho, J. Irudayaraj, In-situ immuno-gold nanoparticle network ELISA biosensors for pathogen detection. Int. J. Food Microbiol. **164** (1), 70–75 (2013). https://doi.org/10.1016/j.ijfoodmicro.2013.02.025.

293. J.-W. Jeon, J.-H. Kim, J.-M. Lee, W.-H. Lee, D.-Y. Lee, S.-H. Paek, Rapid immuno-analytical system physically integrated with lens-free CMOS image sensor for food-borne pathogens. Biosens. Bioelectron. **52** 384–390 (2014). https://doi.org/10.1016/j.bios.2013.09.004.

294. M.H. Silla Santos, Biogenic amines: Their importance in foods. Int. J. Food Microbiol. **29** (2–3), 213–231 (1996). https://doi.org/10.1016/0168-1605(95)00032-1.

295. A. Naila, S. Flint, G. Fletcher, P. Bremer, G. Meerdink, Control of biogenic amines in food - existing and emerging approaches. J. Food Sci. **75** (7), (2010). https://doi.org/10.1111/j.1750-3841.2010.01774.x.

296. M. Decimo, M.C. Cabeza, J.A. Ordóñez, I. De Noni, M. Brasca, Volatile organic compounds associated with milk spoilage by psychrotrophic bacteria. Int. J. Dairy Technol. **71** (3), 593–600 (2018). https://doi.org/10.1111/1471-0307.12485.

297. F. Xu, P. Li, X. Ming, D. Yang, H. Xu, X. Wu, N.P. Shah, H. Wei, Detection of Cronobacter species in powdered infant formula by probe-magnetic separation PCR. J. Dairy Sci. **97** (10), 6067–6075 (2014). https://doi.org/10.3168/jds.2014-8287.

298. C.-M. Shih, C.-L. Chang, M.-Y. Hsu, J.-Y. Lin, C.-M. Kuan, H.-K. Wang, C.-T. Huang, M.-C. Chung, K.-C. Huang, C.-E. Hsu, C.-Y. Wang, Y.-C. Shen, C.-M. Cheng, Paper-based ELISA to rapidly detect Escherichia coli. Talanta. **145** 2–5 (2015). https://doi.org/10.1016/j.talanta.2015.07.051.

299. I.-H. Cho, L. Mauer, J. Irudayaraj, In-situ fluorescent immunomagnetic multiplex detection of foodborne pathogens in very low numbers. Biosens. Bioelectron. **57** 143–148 (2014). https://doi.org/10.1016/j.bios.2014.02.012.

300. H. Liu, F. Zhan, F. Liu, M. Zhu, X. Zhou, D. Xing, Visual and sensitive detection of viable pathogenic bacteria by sensing of RNA markers in gold nanoparticles based paper platform. Biosens. Bioelectron. **62** 38–46 (2014). https://doi.org/10.1016/j.bios.2014.06.020.

301. G.A.R.Y. Suaifan, S. Alhogail, M. Zourob, Rapid and low-cost biosensor for the detection of Staphylococcus aureus. Biosens. Bioelectron. **90** 230–237 (2017). https://doi.org/10.1016/j.bios.2016.11.047.

302. G. Mie, Contributions to the optics of turbid media, particularly of colloidal metal solutions. Ann. Phys. **25** (3), 377–445 (1908).

303. P.R. Sajanlal, T.S. Sreeprasad, A.K. Samal, T. Pradeep, Anisotropic nanomaterials: structure, growth, assembly, and functions. Nano Rev. **2** (1), 5883 (2011). https://doi.org/10.3402/nano.v2i0.5883.

304. Y. Zhang, W. Chu, A.D. Foroushani, H. Wang, D. Li, J. Liu, C.J. Barrow, X. Wang, W. Yang, New gold nanostructures for sensor applications: A review. Materials (Basel). **7** (7), 5169–5201 (2014). https://doi.org/10.3390/ma7075169.

305. P. Priecel, H.A. Salami, R.H. Padilla, Z. Zhong, J.A. Lopez-Sanchez, Anisotropic gold nanoparticles: Preparation and applications in catalysis. Chinese J. Catal. **37** (10), 1619–1650 (2016). https://doi.org/10.1016/S1872-2067(16)62475-0.

306. E.C. Dreaden, L.A. Austin, M.A. MacKey, M.A. El-Sayed, Size matters: Gold nanoparticles in targeted cancer drug delivery. Ther. Deliv. **3** (4), 457–478 (2012). https://doi.org/10.4155/tde.12.21.

307. C.Y. Yang, M.J. Heinemann, M.J. Yacamán, H. Poppa, A structural analysis of small vapor-deposited “multiply twinned” gold particles. Thin Solid Films. **58** 163–168 (1979).

308. A. Renou, M. Gillet, Growth of Au, Pt and Pd particles in a flowing argon system: Observations of decahedral and icosahedral structures. Surf. Sci. **106** (1–3), 27–34 (1981). https://doi.org/10.1016/0039-6028(81)90177-1.

309. J.L. Elechiguerra, J. Reyes-Gasga, M.J. Yacaman, The role of twinning in shape evolution of anisotropic noble metal nanostructures. J. Mater. Chem. **16** (40), 3906–3919 (2006). https://doi.org/10.1039/b607128g.

310. M. Grzelczak, J. Pérez-Juste, P. Mulvaney, L.M. Liz-Marzán, Shape control in gold nanoparticle synthesis. Chem. Soc. Rev. **37** (9), 1783–1791 (2008). https://doi.org/10.1039/b711490g.

311. T.K. Sau, A.L. Rogach, F. Jäckel, T.A. Klar, J. Feldmann, Properties and applications of colloidal nonspherical noble metal nanoparticles. Adv. Mater. **22** (16), 1805–1825 (2010). https://doi.org/10.1002/adma.200902557.

312. T.K. Sau, A.L. Rogach, Nonspherical noble metal nanoparticles: Colloid-chemical synthesis and morphology control. Adv. Mater. **22** (16), 1781–1804 (2010). https://doi.org/10.1002/adma.200901271.

313. U. Kreibig, M. Vollmer, Optical properties of metal clusters, Springer, Berlin, 1995.

314. F. Bonet, V. Delmas, S. Grugeon, R. Herrera Urbina, P.Y. Silvert, K. Tekaia-Elhsissen, Synthesis of monodisperse Au, Pt, Pd, Ru and Ir nanoparticles in ethylene glycol. Nanostructured Mater. **11** (8), 1277–1284 (1999). https://doi.org/10.1016/S0965-9773(99)00419-5.

315. X. Lu, M. Rycenga, S.E. Skrabalak, B. Wiley, Y. Xia, Chemical synthesis of novel plasmonic nanoparticles. Annu. Rev. Phys. Chem. **60** 167–192 (2009). https://doi.org/10.1146/annurev.physchem.040808.090434.

316. T. Klaus, R. Joerger, E. Olsson, Silver-based crystalline nanoparticles, microbially fabricated. Proc. Natl. Acad. Sci. U. S. A. **96** (24), 13611–13614 (1999). http://www.pnas.org/content/96/24/13611.short.

317. S. Brown, M. Sarikaya, E. Johnson, A genetic analysis of crystal growth. J. Mol. Biol. **299** (3), 725–735 (2000). https://doi.org/10.1006/jmbi.2000.3682.

318. S.S. Shankar, A. Rai, B. Ankamwar, A. Singh, A. Ahmad, M. Sastry, Biological synthesis of triangular gold nanoprisms. Nat. Mater. **3** (7), 482–488 (2004). https://doi.org/10.1038/nmat1152.

319. J. Xie, J.Y. Lee, D.I.C. Wang, Y.P. Ting, Identification of active biomolecules in the high-yield synthesis of single-crystalline gold nanoplates in algal solutions. Small. **3** (4), 672–682 (2007). https://doi.org/10.1002/smll.200600612.

320. H. Yuan, C.G. Khoury, H. Hwang, C.M. Wilson, G.A. Grant, T. Vo-Dinh, Gold nanostars : surfactant-free synthesis, 3D modelling, and two-photon photoluminescence imaging. Nanotechnology. **23** (7), (2012). https://doi.org/10.1088/0957-4484/23/7/075102.

321. A. Guerrero-Martínez, S. Barbosa, I. Pastoriza-Santos, L.M. Liz-Marzán, Nanostars shine bright for you. Colloidal synthesis, properties and applications of branched metallic nanoparticles. Curr. Opin. Colloid Interface Sci. **16** (2), 118–127 (2011). https://doi.org/10.1016/j.cocis.2010.12.007.

322. N.R. Jana, L. Gearheart,, C.J. Murphy, Seed-mediated growth approach for shape-controlled synthesis of spheroidal and rod-like gold nanoparticles using a surfactant template. Adv. Mater. **13** (18), 1389–1393 (2001). https://doi.org/10.1002/1521-4095(200109)13:18<1389::AID-ADMA1389>3.0.CO;2-F.

323. T.S. Ahmadi, Z.L. Wang, T.C. Green, A. Henglein, M.A. El-Sayed, Shape-Controlled Synthesis of Colloidal Platinum Nanoparticles. Science (80-.). **272** 1924–1926 (1996).

324. B. Nikoobakht, M.A. El-Sayed, Preparation and growth mechanism of gold nanorods (NRs) using seed-mediated growth method. Chem. Mater. **15** (10), 1957–1962 (2003). https://doi.org/10.1021/cm020732l.

325. S. Chen, Z.L. Wang, J. Ballato, S.H. Foulger, D.L. Carroll, Monopod, Bipod, Tripod, and Tetrapod Gold Nanocrystals. J. Am. Chem. Soc. **125** (52), 16186–16187 (2003). https://doi.org/10.1021/ja038927x.

326. C.L. Nehl, H. Liao, J.H. Hafner, Optical properties of star-shaped gold nanoparticles. Nano Lett. **6** (4), 683–688 (2006). https://doi.org/10.1021/nl052409y.

327. H.L. Wu, C.H. Chen, M.H. Huang, Seed-mediated synthesis of branched gold nanocrystals derived from the side growth of pentagonal bipyramids and the formation of gold nanostars. Chem. Mater. **21** (1), 110–114 (2009). https://doi.org/10.1021/cm802257e.

328. J.L. Burt, J.L. Elechiguerra, J. Reyes-Gasga, J.M. Montejano-Carrizales, M. Jose-Yacaman, Beyond Archimedean solids: Star polyhedral gold nanocrystals. J. Cryst. Growth. **285** (4), 681–691 (2005). https://doi.org/10.1016/j.jcrysgro.2005.09.060.

329. J. Xie, J.Y. Lee, D.I.C. Wang, Seedless, surfactantless, high-yield synthesis of branched gold nanocrystals in HEPES buffer solution. Chem. Mater. **19** (11), 2823–2830 (2007). https://doi.org/10.1021/cm0700100.

330. A.B. Serrano-Montes, J. Langer, M. Henriksen-Lacey, D. Jimenez De Aberasturi, D.M. Solís, J.M. Taboada, F. Obelleiro, K. Sentosun, S. Bals, A. Bekdemir, F. Stellacci, L.M. Liz-Marzán, Gold nanostar-coated polystyrene beads as multifunctional nanoprobes for SERS bioimaging. J. Phys. Chem. C. **120** (37), 20860–20868 (2016). https://doi.org/10.1021/acs.jpcc.6b02282.

331. N.R. Jana, L. Gearheart, C.J. Murphy, Seeding growth for size control of 5-40 nm diameter gold nanoparticles. Langmuir. **17** (22), 6782–6786 (2001). https://doi.org/10.1021/la0104323.

332. C.J. Orendorff, C.J. Murphy, Quantitation of metal content in the silver-assisted growth

of gold nanorods. J. Phys. Chem. B. **110** (9), 3990–3994 (2006). https://doi.org/10.1021/jp0570972.

333. M. Grzelczak, A. Sánchez-Iglesias, B. Rodríguez-González, R. Alvarez-Puebla, J. Pérez-Juste, L.M. Liz-Marzán, Influence of iodide ions on the growth of gold nanorods: Tuning tip curvature and surface plasmon resonance. Adv. Funct. Mater. **18** (23), 3780–3786 (2008). https://doi.org/10.1002/adfm.200800706.

334. W. Haiss, N.T.K. Thanh, J. Aveyard, D.G. Fernig, Determination of Size and Concentration of Gold Nanoparticles from UV-Vis Spectra. Anal. Chem. **79** 4215–4221 (2007).

335. H. de Puig, J.O. Tam, C.-W. Yen, L. Gehrke, K. Hamad-Schifferli, Extinction Coefficient of Gold Nanostars. J. Phys. Chem. C. **119** 17408–17415 (2015). https://doi.org/10.1021/acs.jpcc.5b03624.

336. H. Chen, X. Kou, Z. Yang, W. Ni, J. Wang, Shape- and size-dependent refractive index sensitivity of gold nanoparticles. Langmuir. **24** (10), 5233–5237 (2008). https://doi.org/10.1021/la800305j.

337. S.S. Pai, B. Hammouda, K. Hong, D.C. Pozzo, T.M. Przybycien, R.D. Tilton, The Conformation of the Poly(ethylene glycol) Chain in Mono-PEGylated Lysozyme and Mono-PEGylated Human Growth Hormone. Bioconjug. Chem. **22** 2317–2323 (2011).

338. R.L.C. Wang, H.J. Kreuzer, M. Grunze, Molecular Conformation and Solvation of Oligo(ethylene glycol)-Terminated Self-Assembled Monolayers and Their Resistance to Protein Adsorption. J. Phys. Chem. B. **101** (47), 9767–9773 (1997). https://doi.org/10.1021/jp9716952.

339. B. Das, J. Lou-Franco, N. Logan, P. Balasubramanian, Nanozymes in Point-of-Care Diagnosis: An Emerging Futuristic Approach for Biosensing. Nano-Micro Lett. (2021). https://doi.org/10.1007/s40820-021-00717-0.

340. S. Sachdeva, R.W. Davis, A.K. Saha, Microfluidic Point-of-Care Testing: Commercial Landscape and Future Directions. Front. Bioeng. Biotechnol. **8** (January 2021), 1–14 (2021). https://doi.org/10.3389/fbioe.2020.602659.

341. H. Xu, X. Mao, Q. Zeng, S. Wang, A.-N. Kawde, G. Liu, Aptamer-functionalized gold nanoparticles as probes in dry-reagent strip biosensor for DNA analysis. Anal. Chem. **81** (21), 669–675 (2009). https://doi.org/10.1039/b822582f.

342. X. Gao, H. Xu, M. Baloda, A.S. Gurung, L.P. Xu, T. Wang, X. Zhang, G. Liu, Visual detection of microRNA with lateral flow nucleic acid biosensor. Biosens. Bioelectron. **54** 578–584 (2014). https://doi.org/10.1016/j.bios.2013.10.055.

343. G. Liu, X. Mao, J.A. Phillips, H. Xu, W. Tan, L. Zeng, Aptamer-nanoparticle strip biosensor for sensitive detection of cancer cells. Anal. Chem. **81** (24), 10013–10018 (2009). https://doi.org/10.1021/ac901889s.

344. A.M. López-Marzo, J. Pons, D.A. Blake, A. Merkoçi, High sensitive gold-nanoparticle based lateral flow Immunodevice for Cd2+ detection in drinking waters. Biosens. Bioelectron. **47** 190–198 (2013). https://doi.org/10.1016/j.bios.2013.02.031.

345. X. Liu, J.J. Xiang, Y. Tang, X.L. Zhang, Q.Q. Fu, J.H. Zou, Y.H. Lin, Colloidal gold nanoparticle probe-based immunochromatographic assay for the rapid detection of chromium ions in water and serum samples. Anal. Chim. Acta. **745** 99–105 (2012). https://doi.org/10.1016/j.aca.2012.06.029.

346. F. Yang, J. Duan, M. Li, Z. Wang, Z. Guo, Visual and on-site detection of mercury(II) ions on lateral flow strips using DNA-functionalized gold nanoparticles. Anal. Sci. **28** (4), 333–

338 (2012). https://doi.org/10.2116/analsci.28.333.

347. C. Zhang, Y. Zhang, S. Wang, Development of multianalyte flow-through and lateral-flow assays using gold particles and horseradish peroxidase as tracers for the rapid determination of carbaryl and endosulfan in agricultural products. J. Agric. Food Chem. **54** (7), 2502–2507 (2006). https://doi.org/10.1021/jf0531407.

348. Y.R. Guo, S.Y. Liu, W.J. Gui, G.N. Zhu, Gold immunochromatographic assay for simultaneous detection of carbofuran and triazophos in water samples. Anal. Biochem. **389** (1), 32–39 (2009). https://doi.org/10.1016/j.ab.2009.03.020.

349. B.S. Delmulle, S.M.D.G. De Saeger, L. Sibanda, I. Barna-Vetro, C.H. Van Peteghem, Development of an immunoassay-based lateral flow dipstick for the rapid detection of aflatoxin B1 in pig feed. J. Agric. Food Chem. **53** (9), 3364–3368 (2005). https://doi.org/10.1021/jf0404804.

350. Y. Tang, X. Xu, X. Liu, X. Huang, Y. Chen, W. Wang, J. Xiang, Development of a lateral flow immunoassay (LFA) strip for the rapid detection of 1-aminohydantoin in meat samples. J. Food Sci. **76** (6), 138–143 (2011). https://doi.org/10.1111/j.1750-3841.2011.02217.x.

351. G.P. Zhang, X.N. Wang, J.F. Yang, Y.Y. Yang, G.X. Xing, Q.M. Li, D. Zhao, S.J. Chai, J.Q. Guo, Development of an immunochromatographic lateral flow test strip for detection of β-adrenergic agonist Clenbuterol residues. J. Immunol. Methods. **312** 27–32 (2006). https://doi.org/10.1016/j.jim.2006.02.017.

352. Z. Fang, W. Wu, X. Lu, L. Zeng, Lateral flow biosensor for DNA extraction-free detection of salmonella based on aptamer mediated strand displacement amplification. Biosens. Bioelectron. **56** 192–197 (2014). https://doi.org/10.1016/j.bios.2014.01.015.

353. X. Wang, K. Li, D. Shi, N. Xiong, X. Jin, J. Yi, D. Bi, Development of an immunochromatographic lateral-flow test strip for rapid detection of sulfonamides in eggs and chicken muscles. J. Agric. Food Chem. **55** (6), 2072–2078 (2007). https://doi.org/10.1021/jf062523h.

354. Y. Zhao, G. Zhang, Q. Liu, M. Teng, J. Yang, J. Wang, Development of a lateral flow colloidal gold immunoassay strip for the rapid detection of enrofloxacin residues. J. Agric. Food Chem. **56** 12138–12142 (2008). https://doi.org/10.1021/jf202213m.

355. S. Gandhi, N. Caplash, P. Sharma, C. Raman Suri, Strip-based immunochromatographic assay using specific egg yolk antibodies for rapid detection of morphine in urine samples. Biosens. Bioelectron. **25** (2), 502–505 (2009). https://doi.org/10.1016/j.bios.2009.07.018.

356. M. Zangheri, L. Cevenini, L. Anfossi, C. Baggiani, P. Simoni, F. Di Nardo, A. Roda, A simple and compact smartphone accessory for quantitative chemiluminescence-based lateral flow immunoassay for salivary cortisol detection. Biosens. Bioelectron. **64** 63–68 (2015). https://doi.org/10.1016/j.bios.2014.08.048.

357. A.K. Yetisen, J.L. Martinez-Hurtado, A. Garcia-Melendrez, F. Da Cruz Vasconcellos, C.R. Lowe, A smartphone algorithm with inter-phone repeatability for the analysis of colorimetric tests. Sensors Actuators, B Chem. **196** 156–160 (2014). https://doi.org/10.1016/j.snb.2014.01.077.

358. H. Otsuka, Y. Akiyama, Y. Nagasaki, K. Kataoka, Quantitative and reversible lectin-induced association of gold nanoparticles modified with α-lactosyl-ω-mercapto-poly(ethylene glycol). J. Am. Chem. Soc. **123** (34), 8226–8230 (2001). https://doi.org/10.1021/ja010437m.

359. J. Liu, Y. Lu, Fast colorimetric sensing of adenosine and cocaine based on a general sensor

design involving aptamers and nanoparticles. Angew. Chemie - Int. Ed. **45** (1), 90–94 (2005). https://doi.org/10.1002/anie.200502589.

360. S.K. Vashist, T. van Oordt, E.M. Schneider, R. Zengerle, F. von Stetten, J.H.T. Luong, A smartphone-based colorimetric reader for bioanalytical applications using the screen-based bottom illumination provided by gadgets. Biosens. Bioelectron. **67** 248–255 (2015). https://doi.org/10.1016/j.bios.2014.08.027.

361. J.L.D. Nelis, L. Bura, Y. Zhao, K.M. Burkin, K. Rafferty, C.T. Elliott, K. Campbell, The efficiency of color space channels to quantify color and color intensity change in liquids, pH strips, and lateral flow assays with smartphones. Sensors. **19** (23), (2019). https://doi.org/10.3390/s19235104.

362. Y. Zhao, C. Elliott, H. Zhou, K. Rafferty, Spectral Illumination Correction: Achieving Relative Color Constancy Under the Spectral Domain, in: 2018 IEEE Int. Symp. Signal Process. Inf. Technol., IEEE, 2018: pp. 690–695. https://doi.org/10.1109/ISSPIT.2018.8642637.

363. Y. Zhao, S.Y. Choi, J. Lou-Franco, J.L.D. Nelis, H. Zhou, C. Cao, K. Campbell, C. Elliott, K. Rafferty, Smartphone Modulated Colorimetric Reader with Color Subtraction. 2019 IEEE Sensors. Accept. Publ. 1–4 (2019). https://doi.org/10.1109/SENSORS43011.2019.8956565.

364. B. Eisenman, Learning react native: building native mobile apps with javascript, " O'Reilly Media, Inc.," 2015.

365. M. Grinberg, Flask web development: developing web applications with python, " O'Reilly Media, Inc.," 2018.

366. M. Abadi, A. Agarwal, P. Barham, E. Brevdo, Z. Chen, C. Citro, G.S. Corrado, A. Davis, J. Dean, M. Devin, S. Ghemawat, I. Goodfellow, A. Harp, G. Irving, M. Isard, Y. Jia, R. Jozefowicz, L. Kaiser, M. Kudlur, J. Levenberg, D. Mane, R. Monga, S. Moore, D. Murray, C. Olah, M. Schuster, J. Shlens, B. Steiner, I. Sutskever, K. Talwar, P. Tucker, V. Vanhoucke, V. Vasudevan, F. Viegas, O. Vinyals, P. Warden, M. Wattenberg, M. Wicke, Y. Yu, X. Zheng, TensorFlow: Large-Scale Machine Learning on Heterogeneous Distributed Systems. (2016).

367. D.P. Kingma, J. Ba, Adam: A method for stochastic optimization. ArXiv Prepr. ArXiv1412.6980. (2014).

368. D. Lou, Y. Tian, Y. Zhang, J. Yin, T. Yang, C. He, M. Ma, W. Yu, N. Gu, Peroxidase-like activity of gold nanoparticles and their gold staining enhanced ELISA application. J. Nanosci. Nanotechnol. **18** (2), 951–958 (2018). https://doi.org/10.1166/jnn.2018.13977.

369. M. Zayats, R. Baron, I. Popov, I. Willner, Biocatalytic growth of Au nanoparticles: From mechanistic aspects to biosensors design. Nano Lett. **5** (1), 21–25 (2005). https://doi.org/10.1021/nl048547p.

370. Z. Zhan, C. Cao, S.J. Sim, Quantitative detection of DNA by autocatalytic enlargement of hybridized gold nanoprobes. Biosens. Bioelectron. **26** (2), 511–516 (2010). https://doi.org/10.1016/j.bios.2010.07.061.

371. L. Rodríguez-Lorenzo, R. De La Rica, R.A. Álvarez-Puebla, L.M. Liz-Marzán, M.M. Stevens, Plasmonic nanosensors with inverse sensitivity by means of enzyme-guided crystal growth. Nat. Mater. **11** (7), 604–607 (2012). https://doi.org/10.1038/nmat3337.

372. R. Lozano, M. Naghavi, K. Foreman, S. Lim, K. Shibuya, V. Aboyans, J. Abraham, T. Adair, R. Aggarwal, S.Y. Ahn, M.A. AlMazroa, M. Alvarado, H.R. Anderson, L.M. Anderson, K.G. Andrews, C. Atkinson, L.M. Baddour, S. Barker-Collo, D.H. Bartels, M.L. Bell, E.J. Benjamin,

D. Bennett, K. Bhalla, B. Bikbov, A. Bin Abdulhak, G. Birbeck, F. Blyth, I. Bolliger, S. Boufous, C. Bucello, M. Burch, P. Burney, J. Carapetis, H. Chen, D. Chou, S.S. Chugh, L.E. Coffeng, S.D. Colan, S. Colquhoun, K.E. Colson, J. Condon, M.D. Connor, L.T. Cooper, M. Corriere, M. Cortinovis, K. Courville De Vaccaro, W. Couser, B.C. Cowie, M.H. Criqui, M. Cross, K.C. Dabhadkar, N. Dahodwala, D. De Leo, L. Degenhardt, A. Delossantos, J. Denenberg, D.C. Des Jarlais, S.D. Dharmaratne, E.R. Dorsey, T. Driscoll, H. Duber, B. Ebel, P.J. Erwin, P. Espindola, M. Ezzati, V. Feigin, A.D. Flaxman, M.H. Forouzanfar, F.G.R. Fowkes, R. Franklin, M. Fransen, M.K. Freeman, S.E. Gabriel, E. Gakidou, F. Gaspari, R.F. Gillum, D. Gonzalez-Medina, Y.A. Halasa, D. Haring, J.E. Harrison, R. Havmoeller, R.J. Hay, B. Hoen, P.J. Hotez, D. Hoy, K.H. Jacobsen, S.L. James, R. Jasrasaria, S. Jayaraman, N. Johns, G. Karthikeyan, N. Kassebaum, A. Keren, J.P. Khoo, L.M. Knowlton, O. Kobusingye, A. Koranteng, R. Krishnamurthi, M. Lipnick, S.E. Lipshultz, S. Lockett Ohno, J. Mabweijano, M.F. MacIntyre, L. Mallinger, L. March, G.B. Marks, R. Marks, A. Matsumori, R. Matzopoulos, B.M. Mayosi, J.H. McAnulty, M.M. McDermott, J. McGrath, Z.A. Memish, G.A. Mensah, T.R. Merriman, C. Michaud, M. Miller, T.R. Miller, C. Mock, A.O. Mocumbi, A.A. Mokdad, A. Moran, K. Mulholland, M.N. Nair, L. Naldi, K.M.V. Narayan, K. Nasseri, P. Norman, M. O'Donnell, S.B. Omer, K. Ortblad, R. Osborne, D. Ozgediz, B. Pahari, J.D. Pandian, A. Panozo Rivero, R. Perez Padilla, F. Perez-Ruiz, N. Perico, D. Phillips, K. Pierce, C.A. Pope, E. Porrini, F. Pourmalek, M. Raju, D. Ranganathan, J.T. Rehm, D.B. Rein, G. Remuzzi, F.P. Rivara, T. Roberts, F. Rodriguez De León, L.C. Rosenfeld, L. Rushton, R.L. Sacco, J.A. Salomon, U. Sampson, E. Sanman, D.C. Schwebel, M. Segui-Gomez, D.S. Shepard, D. Singh, J. Singleton, K. Sliwa, E. Smith, A. Steer, J.A. Taylor, B. Thomas, I.M. Tleyjeh, J.A. Towbin, T. Truelsen, E.A. Undurraga, N. Venketasubramanian, L. Vijayakumar, T. Vos, G.R. Wagner, M. Wang, W. Wang, K. Watt, M.A. Weinstock, R. Weintraub, J.D. Wilkinson, A.D. Woolf, S. Wulf, P.H. Yeh, P. Yip, A. Zabetian, Z.J. Zheng, A.D. Lopez, C.J.L. Murray, Global and regional mortality from 235 causes of death for 20 age groups in 1990 and 2010: A systematic analysis for the Global Burden of Disease Study 2010. Lancet. **380** (9859), 2095–2128 (2012). https://doi.org/10.1016/S0140-6736(12)61728-0.

373. WHO, Global Tuberculosis Report 2019, 2019. https://www.who.int/tb/publications/global_report/en/.

374. B.C. de Jong, M. Antonio, S. Gagneux, Mycobacterium africanum-review of an important cause of human tuberculosis in West Africa. PLoS Negl. Trop. Dis. **4** (9), (2010). https://doi.org/10.1371/journal.pntd.0000744.

375. S. Gagneux, Host-pathogen coevolution in human tuberculosis. Philos. Trans. R. Soc. B Biol. Sci. **367** (1590), 850–859 (2012). https://doi.org/10.1098/rstb.2011.0316.

376. G. Lombardi, I. Botti, M.L. Pacciarini, M.B. Boniotti, G. Roncarati, P. Dal Monte, Five-year surveillance of human tuberculosis caused by Mycobacterium bovis in Bologna, Italy: An underestimated problem. Epidemiol. Infect. **145** (14), 3035–3039 (2017). https://doi.org/10.1017/S0950268817001996.

377. M.J. Bannon, BCG and tuberculosis. Arch. Dis. Child. **80** (1), 80–83 (1999). https://doi.org/10.1136/adc.80.1.80.

378. R.J. Delahay, A.N.S. De Leeuw, A.M. Barlow, R.S. Clifton-Hadley, C.L. Cheeseman, The status of Mycobacterium bovis infection in UK wild mammals: A review. Vet. J. **164** (2), 90–105 (2002). https://doi.org/10.1053/tvjl.2001.0667.

379. A. Aranaz, L. de Juan, N. Montero, C. Sanchez, M. Galka, C. Delso, J. Alvarez, B. Romero, J. Bezos, A.I. Vela, V. Briones, A. Mateos, L. Dominguez, Bovine Tuberculosis (Mycobacterium bovis) in Wildlife in Spain. J. Clin. Microbiol. **42** (6), 2602–2608 (2004). https://doi.org/10.1128/JCM.42.6.2602.

380. A.C. Matos, L. Figueira, M.H. Martins, M.L. Pinto, M. Matos, A.C. Coelho, New Insights into Mycobacterium bovis Prevalence in Wild Mammals in Portugal. Transbound. Emerg. Dis. **63** (5), 313–322 (2016). https://doi.org/10.1111/tbed.12306.

381. J.T. LeJeune, P.J. Rajala-Schultz, Unpasteurized Milk: A Continued Public Health Threat. Clin. Infect. Dis. **48** (1), 93–100 (2009). https://doi.org/10.1086/595007.

382. I.F.S. Authority, Zoonotic Tuberculosis and Food Safety Zoonotic Tuberculosis and Food Safety 2nd Edition. (2), (2008).

383. Z. Chena, W. Wanga, H. Lib, Y. Lib, J. Chena, Rapid detection of Mycobacterium bovis in milk by a nanobiosensor. Int. J. Appl. Res. Vet. Med. **13** (2), 93–99 (2015).

384. A. Lermo, S. Liébana, S. Campoy, S. Fabiano, M. Inés García, A. Soutullo, M.J. Zumárraga, S. Alegret, M. Isabel Pividori, A novel strategy for screening-out raw milk contaminated with Mycobacterium bovis on dairy farms by double-tagging PCR and electrochemical genosensing. Int. Microbiol. **13** (2), 91–97 (2010). https://doi.org/10.2436/20.1501.01.114.

385. L.B. Silva, B. Veigas, G. Doria, P. Costa, J. Inácio, R. Martins, E. Fortunato, P. V. Baptista, Portable optoelectronic biosensing platform for identification of mycobacteria from the Mycobacterium tuberculosis complex. Biosens. Bioelectron. **26** (5), 2012–2017 (2011). https://doi.org/10.1016/j.bios.2010.08.078.

386. Y.P. Hsu, N.S. Li, Y.T. Chen, H.H. Pang, K.C. Wei, H.W. Yang, A serological point-of-care test for Zika virus detection and infection surveillance using an enzyme-free vial immunosensor with a smartphone. Biosens. Bioelectron. **151** 1–9 (2020). https://doi.org/10.1016/j.bios.2019.111960.

387. T. Ji, M.C. Muenker, R.V.L. Papineni, J.W. Harder, D.L. Vizard, W.E. Mclaughlin, Increased sensitivity in antigen detection with fluorescent latex nanosphere-IgG antibody conjugates. Bioconjug. Chem. **21** (3), 427–435 (2010). https://doi.org/10.1021/bc900295v.

388. S. Pathak, M.C. Davidson, G.A. Silva, Characterization of the functional binding properties of antibody conjugated quantum dots. Nano Lett. **7** (7), 1839–1845 (2007). https://doi.org/10.1021/nl062706i.

389. T. Bürgi, Properties of the gold-sulphur interface: from self-assembled monolayers to clusters. Nanoscale. **7** (38), 15553–15567 (2015). https://doi.org/10.1039/c5nr03497c.

390. N. Assal, B. Rennie, L. Walrond, T. Cyr, L. Rohonczy, M. Lin, Proteome characterization of the culture supernatant of Mycobacterium bovis in different growth stages. Biochem. Biophys. Reports. **28** 101154 (2021). https://doi.org/10.1016/j.bbrep.2021.101154.

391. L.D. Stewart, J. McNair, L. McCallan, S. Thompson, L.A. Kulakov, I.R. Grant, Production and evaluation of antibodies and phage display-derived peptide ligands for immunomagnetic separation of Mycobacterium bovis. J. Clin. Microbiol. **50** (5), 1598–1605 (2012). https://doi.org/10.1128/JCM.05747-11.

392. R. Chen, X. Huang, J. Li, S. Shan, W. Lai, Y. Xiong, A novel fluorescence immunoassay for the sensitive detection of Escherichia coli O157:H7 in milk based on catalase-mediated fluorescence quenching of CdTe quantum dots. Anal. Chim. Acta. **947** 50–57 (2016). https://doi.org/10.1016/j.aca.2016.10.017.

393. C. Wang, K. Xing, G. Zhang, M. Yuan, S. Xu, D. Liu, W. Chen, J. Peng, S. Hu, W.H. Lai, Novel ELISA based on fluorescent quenching of DNA-stabilized silver nanoclusters for detecting E. coli O157:H7. Food Chem. **281** (December 2018), 91–96 (2019). https://doi.org/10.1016/j.foodchem.2018.12.079.

394. A. Smekal, Zur Quantentheorie der Streuung und Dispersion. Naturwissenschaften. **16** (31), 612–613 (1923). https://doi.org/10.1007/BF01494086.

395. C.V. Raman, K.S. Krishnan, A New Type of Secondary Radiation. Nature. **121** 501–502 (1928).

396. R.R. Jones, D.C. Hooper, L. Zhang, D. Wolverson, V.K. Valev, Raman Techniques: Fundamentals and Frontiers. Nanoscale Res. Lett. **14** (1), (2019). https://doi.org/10.1186/s11671-019-3039-2.

397. R.S. Das, Y.K. Agrawal, Raman spectroscopy: Recent advancements, techniques and applications. Vib. Spectrosc. **57** (2), 163–176 (2011). https://doi.org/10.1016/j.vibspec.2011.08.003.

398. H. Xu, J. Aizpurua, M. Käll, P. Apell, Electromagnetic contributions to single-molecule sensitivity in surface-enhanced Raman scattering. Phys. Rev. E - Stat. Physics, Plasmas, Fluids, Relat. Interdiscip. Top. **62** (3 B), 4318–4324 (2000). https://doi.org/10.1103/PhysRevE.62.4318.

399. K. Kneipp, M. Moskovits, H. Kneipp, Surface-Enhanced Raman Scattering, Springer, 2006.

400. J. Kim, Y. Jang, N.J. Kim, H. Kim, G.C. Yi, Y. Shin, M.H. Kim, S. Yoon, Study of Chemical Enhancement Mechanism in Non-plasmonic Surface Enhanced Raman Spectroscopy (SERS). Front. Chem. **7** (August), 1–7 (2019). https://doi.org/10.3389/fchem.2019.00582.

401. E.C. Le Ru, P.G. Etchegoin, Quantifying SERS enhancements. MRS Bull. **38** (8), 631–640 (2013). https://doi.org/10.1557/mrs.2013.158.

402. E.C. Le Ru, P.G. Etchegoin, Single-molecule surface-enhanced raman spectroscopy. Annu. Rev. Phys. Chem. **63** 65–87 (2012). https://doi.org/10.1146/annurev-physchem-032511-143757.

403. P.G. Etchegoin, E.C. Le Ru, A perspective on single molecule SERS: Current status and future challenges. Phys. Chem. Chem. Phys. **10** (40), 6079–6089 (2008). https://doi.org/10.1039/b809196j.

404. S.L. Kleinman, E. Ringe, N. Valley, K.L. Wustholz, E. Phillips, K.A. Scheidt, G.C. Schatz, R.P. Van Duyne, Single-molecule surface-enhanced raman spectroscopy of crystal violet isotopologues: Theory and experiment. J. Am. Chem. Soc. **133** (11), 4115–4122 (2011). https://doi.org/10.1021/ja110964d.

405. G. McNay, D. Eustace, W.E. Smith, K. Faulds, D. Graham, Surface-enhanced Raman scattering (SERS) and surface-enhanced resonance raman scattering (SERRS): A review of applications. Appl. Spectrosc. **65** (8), 825–837 (2011). https://doi.org/10.1366/11-06365.

406. A.A. Stacy, R.P. Van Duyne, Surface enhanced raman and resonance raman spectroscopy in a non-aqueous electrochemical environment: Tris(2,2′-bipyridine)ruthenium(II) adsorbed on silver from acetonitrile. Chem. Phys. Lett. **102** (4), 365–370 (1983). https://doi.org/10.1016/0009-2614(83)87057-2.

407. L. Fabris, M. Dante, T.Q. Nguyen, J.B.H. Tok, G.C. Bazan, SERS aptatags: New responsive metallic nanostructures for heterogeneous protein detection by surface enhanced raman spectroscopy. Adv. Funct. Mater. **18** (17), 2518–2525 (2008). https://doi.org/10.1002/adfm.200800301.

408. C.E. Talley, J.B. Jackson, C. Oubre, N.K. Grady, C.W. Hollars, S.M. Lane, T.R. Huser, P. Nordlander, N.J. Halas, Surface-enhanced Raman scattering from individual Au nanoparticles and nanoparticle dimer substrates. Nano Lett. **5** (8), 1569–1574 (2005). https://doi.org/10.1021/nl050928v.

409. C. Zhuang, Y. Xu, N. Xu, J. Wen, H. Chen, S. Deng, Plasmonic sensing characteristics of gold nanorods with large aspect ratios. Sensors (Switzerland). **18** (10), (2018). https://doi.org/10.3390/s18103458.

410. C.J. Murphy, T.K. Sau, A.M. Gole, C.J. Orendorff, J. Gao, L. Gou, S.E. Hunyadi, T. Li, Anisotropic metal nanoparticles: Synthesis, assembly, and optical applications. J. Phys. Chem. B. **109** (29), 13857–13870 (2005). https://doi.org/10.1021/jp0516846.

411. Y. Yang, J. Liu, Z. Fu, D. Qin, Galvanic Replacement-Free Deposition of Au on Ag for Core−Shell Nanocubes with Enhanced Chemical Stability and SERS Activity. J. Am. Chem. Soc. **136** (23), 8153–8156 (2014).

412. J.E. Millstone, S. Park, K.L. Shuford, L. Qin, G.C. Schatz, C.A. Mirkin, Observation of a quadrupole plasmon mode for a colloidal solution of gold nanoprisms. J. Am. Chem. Soc. **127** (15), 5312–5313 (2005). https://doi.org/10.1021/ja043245a.

413. F. Hao, C.L. Nehl, J.H. Hafner, P. Nordlander, Plasmon Resonances of a Gold Nanostar. Nano Lett. **7** (3), 729–732 (2007). https://doi.org/10.1021/nl062969c.

414. S. Chatterjee, A.B. Ringane, A. Arya, G.M. Das, V.R. Dantham, R. Laha, S. Hussian, A high-yield, one-step synthesis of surfactant-free gold nanostars and numerical study for single-molecule SERS application. J. Nanoparticle Res. **18** (8), 1–9 (2016). https://doi.org/10.1007/s11051-016-3557-0.

415. W. Ma, M. Sun, L. Xu, L. Wang, H. Kuang, C. Xu, A SERS active gold nanostar dimer for mercury ion detection. Chem. Commun. **49** (44), 4989–4991 (2013). https://doi.org/10.1039/c3cc39087j.

416. A. Li, L. Tang, D. Song, S. Song, W. Ma, L. Xu, H. Kuang, X. Wu, L. Liu, X. Chen, C. Xu, A SERS-active sensor based on heterogeneous gold nanostar core-silver nanoparticle satellite assemblies for ultrasensitive detection of aflatoxinB1. Nanoscale. **8** (4), 1873–1878 (2016). https://doi.org/10.1039/c5nr08372a.

417. J. Zhu, M.J. Liu, J.J. Li, X. Li, J.W. Zhao, Multi-branched gold nanostars with fractal structure for SERS detection of the pesticide thiram. Spectrochim. Acta - Part A Mol. Biomol. Spectrosc. **189** 586–593 (2018). https://doi.org/10.1016/j.saa.2017.08.074.

418. S. Hong, X. Li, Optimal size of gold nanoparticles for surface-enhanced Raman spectroscopy under different conditions. J. Nanomater. **2013** (2013). https://doi.org/10.1155/2013/790323.

419. M. Li, S.K. Cushing, J. Zhang, J. Lankford, Z.P. Aguilar, D. Ma, N. Wu, Shape-dependent surface-enhanced Raman scattering in gold-Raman-probe- silica sandwiched nanoparticles for biocompatible applications. Nanotechnology. **23** (11), (2012). https://doi.org/10.1088/0957-4484/23/11/115501.

420. Y. Yang, J. Shi, G. Kawamura, M. Nogami, Preparation of Au-Ag, Ag-Au core-shell bimetallic nanoparticles for surface-enhanced Raman scattering. Scr. Mater. **58** (10), 862–865 (2008). https://doi.org/10.1016/j.scriptamat.2008.01.017.

421. Z. Yu, L. Chen, Y. Wang, X. Wang, W. Song, W. Ruan, B. Zhao, Q. Cong, A SERS-active enzymatic product used for the quantification of disease-related molecules. J. Raman Spectrosc. **45** (1), 75–81 (2014). https://doi.org/10.1002/jrs.4425.

422. K.S. McKeating, S. Sloan-Dennison, D. Graham, K. Faulds, An investigation into the simultaneous enzymatic and SERRS properties of silver nanoparticles. Analyst. **138** (21), 6347–6353 (2013). https://doi.org/10.1039/c3an01451g.

423. J. Guthmuller, B. Champagne, Resonance Raman scattering of rhodamine 6G as

calculated by time-dependent density functional theory: Vibronic and solvent effects. J. Phys. Chem. A. **112** (14), 3215–3223 (2008). https://doi.org/10.1021/jp7112279.

424. C. Wu, E. Chen, J. Wei, Surface enhanced Raman spectroscopy of Rhodamine 6G on agglomerates of different-sized silver truncated nanotriangles. Colloids Surfaces A Physicochem. Eng. Asp. **506** 450–456 (2016). https://doi.org/10.1016/j.colsurfa.2016.07.020.

425. M.K. Hossain, Y. Kitahama, G.G. Huang, X. Han, Y. Ozaki, Surface-enhanced raman scattering: Realization of localized surface plasmon resonance using unique substrates and methods. Anal. Bioanal. Chem. **394** (7), 1747–1760 (2009). https://doi.org/10.1007/s00216-009-2762-4.

426. J. Koetz, The effect of surface modification of gold nanotriangles for surface-enhanced raman scattering performance. Nanomaterials. **10** (11), 1–13 (2020). https://doi.org/10.3390/nano10112187.

427. M.J. Natan, Concluding remarks: Surface enhanced Raman scattering. Faraday Discuss. **132** 321–328 (2006). https://doi.org/10.1039/b601494c.

428. E.C. Le Ru, E. Blackie, M. Meyer, P.G. Etchegoint, Surface enhanced raman scattering enhancement factors: A comprehensive study. J. Phys. Chem. C. **111** (37), 13794–13803 (2007). https://doi.org/10.1021/jp0687908.

429. C.G. Khoury, T. Vo-Dinh, Gold Nanostars For Surface-Enhanced Raman Scattering: Synthesis, Characterization and Optimization. J. Phys. Chem. C. Nanomater. Interfaces. **112** 18849–18859 (2008).

430. Q. Su, X. Ma, J. Dong, C. Jiang, W. Qian, A reproducible SERS substrate based on electrostatically assisted aptes-functionalized surface-assembly of gold nanostars. ACS Appl. Mater. Interfaces. **3** (6), 1873–1879 (2011). https://doi.org/10.1021/am200057f.

431. Y. Cui, B. Ren, J.L. Yao, R.A. Gu, Z.Q. Tian, Synthesis of AgcoreAushell bimetallic nanoparticles for immunoassay based on surface-enhanced Raman spectroscopy. J. Phys. Chem. B. **110** (9), 4002–4006 (2006). https://doi.org/10.1021/jp056203x.

432. L. Rivas, S. Sanchez-Cortes, J. V. García-Ramos, G. Morcillo, Mixed silver/gold colloids: a study of their formation, morphology, and surface-enhanced Raman activity. Langmuir. **16** (25), 9722–9728 (2000). https://doi.org/10.1021/la000557s.

433. A. V. Girão, P.C. Pinheiro, M. Ferro, T. Trindade, Tailoring gold and silver colloidal bimetallic nanoalloys towards SERS detection of rhodamine 6G. RSC Adv. **7** (26), 15944–15951 (2017). https://doi.org/10.1039/c7ra00685c.

434. M. Fan, F.J. Lai, H.L. Chou, W.T. Lu, B.J. Hwang, A.G. Brolo, Surface-enhanced Raman scattering (SERS) from Au:Ag bimetallic nanoparticles: The effect of the molecular probe. Chem. Sci. **4** (1), 509–515 (2013). https://doi.org/10.1039/c2sc21191b.

435. S.W. Joo, S.W. Han, K. Kim, Adsorption of 1,4-benzenedithiol on gold and silver surfaces: Surface-enhanced Raman scattering study. J. Colloid Interface Sci. **240** (2), 391–399 (2001). https://doi.org/10.1006/jcis.2001.7692.

436. C.J. Orendorff, A. Gole, T.K. Sau, C.J. Murphy, Surface-enhanced Raman spectroscopy of self-assembled monolayers: Sandwich architecture and nanoparticle shape dependence. Anal. Chem. **77** (10), 3261–3266 (2005). https://doi.org/10.1021/ac048176x.

437. Y. Wang, A.B. Serrano, K. Sentosun, S. Bals, L.M. Liz-Marzán, Stabilization and Encapsulation of Gold Nanostars Mediated by Dithiols. Small. **11** (34), 4314–4320 (2015). https://doi.org/10.1002/smll.201500703.

438. X.H. Pham, E. Hahm, K.H. Huynh, B.S. Son, H.M. Kim, D.H. Jeong, B.H. Jun, 4-Mercaptobenzoic acid labeled gold-silver-alloy-embedded silica nanoparticles as an internal standard containing nanostructures for sensitive quantitative thiram detection. Int. J. Mol. Sci. **20** (19), (2019). https://doi.org/10.3390/ijms20194841.

439. N. Logan, J. Lou Franco, C. Elliott, C. Cao, Catalytic Gold Nanostars for SERS-based Detection of Mercury Ions (Hg2+) with Inverse Sensitivity. Environ. Sci. Nano. (2021). https://doi.org/10.1039/d1en00548k.

440. Environmental Protection Agency (EPA), Ground water and drinking water fact sheet: mercury. (2016). https://archive.epa.gov/water/archive/web/pdf/archived-technical-fact-sheet-on-mercury.pdf.

441. E. Kopyść, K. Pyrzyńska, S. Garboś, E. Bulska, Determination of mercury by cold-vapor atomic absorption spectrometry with preconcentration on a gold-trap. Anal. Sci. **16** (12), 1309–1312 (2000). https://doi.org/10.2116/analsci.16.1309.

442. B. Passariello, M. Barbaro, S. Quaresima, A. Casciello, A. Marabini, Determination of mercury by inductively coupled plasma - Mass spectrometry. Microchem. J. **54** (4), 348–354 (1996). https://doi.org/10.1006/mchj.1996.0110.

443. W.H.O. (WHO), Guidelines for Drinking-Water Quality, 3rd ed., Geneva, 2004. https://www.who.int/water_sanitation_health/dwq/GDWQ2004web.pdf.

Appendices

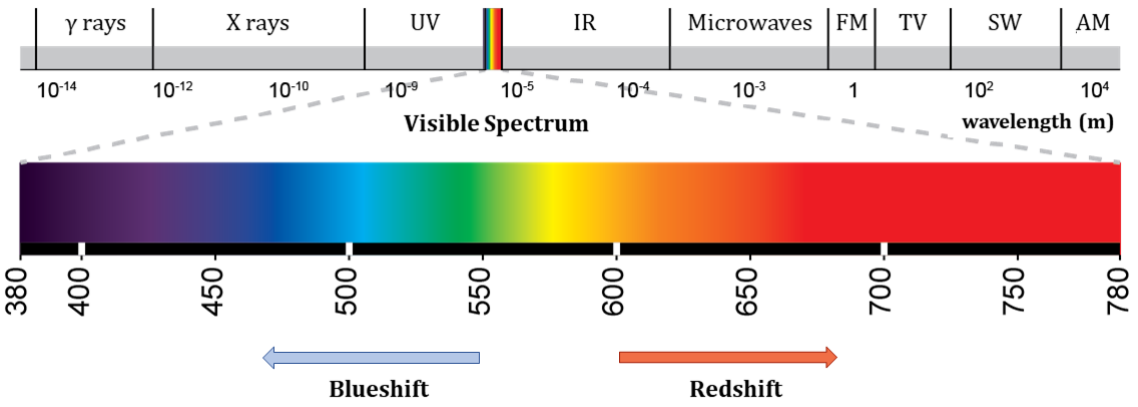

Figure A1 Electromagnetic spectrum, highlighting the Visible Spectrum to explain the terminology "blueshift" and "redshift" used along the thesis.

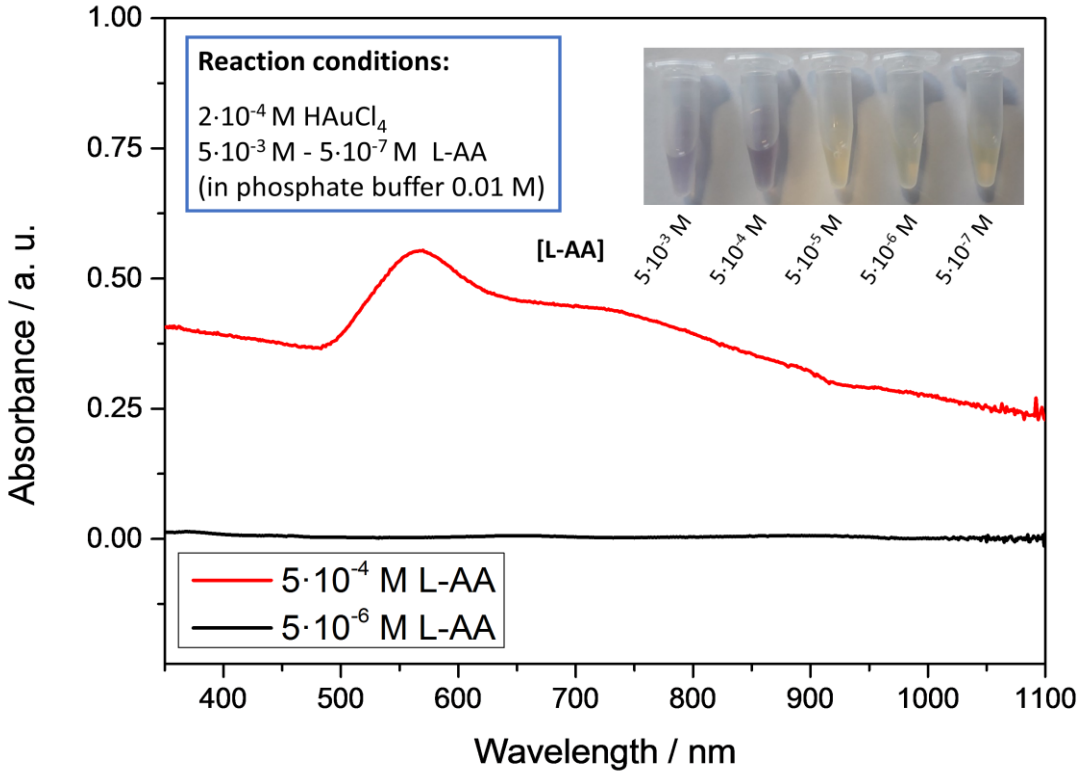

Figure A2 UV-Vis spectra of enlargement solutions containing a varying concentration of L-AA. Samples containing a L-AA concentration equal or higher than $5{\cdot}10^{-4}$ M led to a red-purple colour solution and their UV-Vis analysis displays a characteristic peak around 550 nm, indicative of the formation of AuNS, whereas none of these are observed if the L-AA concentration is reduced to $5{\cdot}10^{-5}$ M or lower concentrations.